IRON IN THE SOUTHERN OCEAN

A model study of iron sources and their impact on the phytoplankton

VIBE SCHOURUP-KRISTENSEN

March 2015

Dissertation zur Erlangung des akademischen Grades eines
Doktors der Naturwissenschaften (Dr. rer. nat)
am Fachbereich 2
der Universität Bremen

Gutachter
Prof. Dr. Dieter A. Wolf-Gladrow
Prof. Dr. Thomas Jung

Vibe Schourup-Kristensen: *Iron in the Southern Ocean,* A model study of iron sources and their impact on the phytoplankton, © March 2015

SUPERVISORS:
Prof. Dr. Dieter A. Wolf-Gladrow
Dr. Christoph Völker

LOCATION:
Alfred-Wegener-Institut Helmholtz-Zentrum für Polar- und MeeresForschung, am Handelshafen 12, 27570 Bremerhaven

CONTACT:
Vibe.schourup-kristensen@awi.de

Universität Bremen

Name: _____ Ort, Datum: _____

Anschrift: _____

ERKLÄRUNG

. Hiermit erkläre ich, dass ich die Doktorarbeit mit dem Titel:

_____

_____

_____

selbstständig verfasst und geschrieben habe und außer den angegebenen Quellen keine weiteren Hilfsmittel verwendet habe.

Ebenfalls erkläre ich hiermit, dass es sich bei den von mir abgegebenen Arbeiten um drei identische Exemplare handelt.

_____

(Unterschrift)

ABSTRACT

In the iron limited Southern Ocean, the iron sources have a large impact on the spatial distribution and magnitude of the phytoplankton blooms, and thereby also on the net primary and export production (NPP and EP). In this thesis, the Southern Ocean input of iron from the sediments and from vertical supply to the mixed layer is investigated in a new Ocean General Circlation Biogeochemical Model (OGCBM). Focus is especially on the model's representation of the iron sources, how they affect the biological production in the model and what can be learned from this about the iron sources in nature.

The first part of the thesis documents the global performance of the Regulated Ecosystem Model (REcoM2) coupled to the Finite Element Sea-ice Ocean Model (FESOM). It shows that the model does a reasonable job reproducing the large scale surface patterns of the biogeochemical fields when compared to observations and other non-eddy resolving OGCBMs. The spatial fields of chlorophyll *a* and NPP are especially good. Further analysis of the Southern Ocean shows that the total net primary and export production here fits well with previous estimates.

The second part of the thesis assesses the impact of the Ocean General Circulation Model (OGCM) on the vertical iron supply to the mixed layer of the Southern Ocean. Two similar model runs were carried out with REcoM2 coupled to two different ocean models; FESOM and MITgcm. The study shows that the modeled vertical iron fluxes, and thereby the NPP and EP, are strongly dependent on the ocean model. This is partly due to differences in the mixed layer dynamics, but is also affected by other mechanisms, such as the strength of the meridional overturning circulation. The study highlights the importance of considering the skill of the OGCM forcing the biogeochemistry. This is important for contemporary runs, but especially when predicting future changes to the biological pump using large scale OGCBMs.

The rate of iron release from the sediments in nature is not well constrained, leading to large variations in its strength between biogeochemical models. The third part of the thesis focuses on the implications of changes in the modeled strength of the sediment source, and accompanying higher scavenging rates, on the phytoplankton composition and the opal export. The study shows, that while variations in the strength of the benthic iron flux can be counteracted by an appropriate scavenging rate, thereby producing very similar values for the total NPP in the Southern Ocean, it has a large impact on the spatial distribution of the NPP, on the diatoms and on the opal export. In order to optimize the sedimentary iron input to large scale OGCBMs, it is thus important to look beyond the modeled NPP and assess the biological production by diatoms, as well as the vertical export of opal, especially for the Southern Ocean.

The general discussion focusses on the relative importance of the different iron sources in the Southern Ocean, how the different sources may change in the future and what factors modelers need consider when predicting these changes. Lastly further directions for work regarding the iron sources in the Southern Ocean as well as the new FESOM-REcoM2 model are described.

ZUSAMMENFASSUNG

Im eisenlimitierten Südpolarmeer haben Eisenquellen einen großen Einfluss auf die räumliche Verteilung und die Stärke von Phytoplanktonblüten, und dadurch auch auf die Nettoprimär- und Exportproduktion (NPP und EP). In dieser Arbeit wird der Eiseneintrag in die Deckschicht des Südpolarmeers aus Sedimenten und durch vertikalen Eintrag mit einem neuartigen Ozeanzirkulations- und Biogeochemie-Modell (OGCBM) untersucht. Der Fokus liegt hierbei besonders auf der Repräsentation der Eisenquellen im Modell, wie diese die biologische Produktion im Modell beeinflussen und was wir daraus über die Eisenquellen in der Natur lernen können.

Im ersten Teil der Arbeit werden die globalen Ergebnisse des Regulated Ecosystem Model (REcoM2), welches mit dem Finite Element Sea-ice Ocean Model (FESOM) gekoppelt wurde, dargestellt und bewertet. Die Modellevaluation zeigt, dass großskalige Oberflächenmuster der biogeochemischen Felder, verglichen mit Beobachtungen und anderen nicht-eddyauflösenden OGCBMs, relativ gut wiedergegeben werden. Die räumliche Verteilung von Chlorophyll *a* und NPP wird besonders gut wiedergegeben. Des Weiteren wird gezeigt, dass die gesamte Nettoprimär- und Exportproduktion im Südpolarmeer gut mit früheren Schätzungen übereinstimmt.

Der zweite Teil der Arbeit analysiert den Einfluss des allgemeinen Ozeanzirkulationsmodells (OGCM) auf den vertikalen Eiseneintrag in die Deckschicht des Südpolarmeers. Zwei vergleichbare Modellläufe wurden durchgeführt, in denen REcoM2 mit zwei verschiedenen Ozeanmodellen, FESOM und MITgcm, gekoppelt wurde. Die Studie zeigt, dass die simulierten vertikalen Eisenflüsse, und dadurch NPP und EP, stark vom Ozeanmodell abhängen. Der Grund dafür liegt zum Teil an Unterschieden in der Dynamik der simulierten Deckschicht, aber auch andere Mechanismen, wie z.B. die Stärke der simulierten globalen Umwälzzirkulation, spielen eine Rolle. Die Studie hebt hervor, dass es wichtig ist, die Fähigkeiten des Ozeanmodells zu kennen, welches das biogeochemische Modell antreibt. Dies ist nicht nur wichtig für die Simulation des historischen und gegenwärtigen Zustands des Ozeans, sondern auch besonders für Prognosen der zukünftigen biologischen Pumpe im Ozean unter Verwendung von OGCBMs.

Die Rate, mit der Eisen in der Natur aus Sedimenten freigesetzt wird, ist kaum bekannt, was dazu führt, dass sie auch zwischen verschiedenen biogeochemischen Modellen stark variiert. Der dritte Teil der Arbeit beschäftigt sich mit den Auswirkungen unterschiedlich starker Eisenfreisetzung und den dazugehörigen größeren Adsorptionsraten auf Partikeloberflächen auf die Phytoplanktonzusammensetzung und den Opalexport. Die Studie zeigt, dass Variationen in der Stärke des benthischen Eiseneintrags durch eine geeignete Adsorptionsrate auf Partikeloberflächen teilweise kompensiert werden, so dass trotzdem ähnliche Werte für die Gesamt-NPP im Südpolarmeer erreicht werden. Der benthische Eiseneintrag hat einen großen Einfluss auf die räumliche Verteilung der NPP, auf Diatomeen und auf den Opalexport. Um den sedimentären Eiseneintrag in großskaligen OGCBMs zu verbessern, ist es wichtig, nicht nur die simulierte NPP zu beurteilen, sondern auch die biologische Produktivität von Diatomeen und den vertikalen Opalexport im Südpolarmeer zu analysieren.

Die allgemeine Diskussion am Ende dieser Arbeit konzentriert sich auf die relative Wichtigkeit der verschiedenen Eisenquellen im Südpolarmeer, in welcher Weise diese sich in der Zukunft ändern könnten, und welche Prozesse Ökosystemmodellierer für die Vorhersage dieser Änderungen berücksichtigen müssen. Darüber hinaus wird ein Ausblick auf weiterführende Arbeiten über die Eisenquellen im Südpolarmeer und das neuartige Modell FESOM-REcoM2 gegeben.

ACKNOWLEDGMENTS

First of all, I would like to thank Dieter Wolf-Gladrow and Jens Schröter for hiring me as a PhD student and for the continuing support during the PhD.

I would also like to thank Thomas Jung and Kai Bischoff for being willing to take on the roles as reviewer of the thesis and examiner at the defense, respectively.

My supervisor, Christoph Völker, has always been ready for discussions and advice regarding the direction of my work, and has shared the knowledge about the biogeochemical model REcoM2, without which I could not have finished my work. I am grateful for this.

For the day to day work with the Finite Element Sea-Ice Ocean Model (FESOM), I very much appreciate the readiness of Dmitry Sidorenko to answer a wide variety of questions, thank you for that. And regarding FESOM, many more people have contributed their knowledge, in particular Sergey Danilov and Qiang Wang.

I also appreciate the committee meetings with Christoph Völker, Sergey Danilov, Martin Losch, Christine Klaas, Jens Schröter and Dieter Wolf-Gladrow, which greatly helped put my work into context and to see sides or problems that I had not been aware of.

Throughout my time at the AWI have been part of two working groups; Biogeoscience and Climate Dynamics. I would like to thank group members of both groups for welcoming me in them, allowing me to take advantage of both the diverse knowledge that the groups represent, but also the friendships and support that has come from it.

Christine Klaas and Dieter Wolf-Gladrow gave me the opportunity to join the RV Polarstern on a cruise in the Southern Ocean, giving me the opportunity to experience first hand how measurements of the marine biogeochemistry are obtained and how much work goes into it. It highly appreciate this opportunity and experience.

Last, but not least, my work at the AWI would never have been possible had it not been for the support and understanding of my family, and especially from my boyfriend Esben. Thank you for giving me the chance to follow my dreams by supporting our move to a new country and for putting in the extra work required to keep us all happy and healthy. Jeg elsker dig.

CONTENTS

ACRONYMS

ACC	Antarctic Circumpolar Current
AADW	Antarctic Deep Water
AAIW	Antarctic Intermediate Water
CDW	Circumpolar Deep Water
CORE	Coordinated Ocean-ice Reference Experiment
DFe	Dissolved Iron
DIC	Dissolved Inorganic Carbon
DIN	Dissolved Inorganic Nitrogen
DSi	Dissolved Inorganic Silicon
EP	Export Production
FESOM	Finite Element Sea-ice Ocean Model
HNLC	High Nutrient Low Chlorophyll
MITgcm	Massachusetts Institute of Technology general circulation model
MLD	Mixed Layer Depth
NADW	North Atlantic Deep Water
NPP	Net Primary Production
OGCBM	Ocean General Circulation Biogeochemical Model
OGCM	Ocean General Circulation Model
PF	Polar Front
REcoM	Regulated Ecosystem Model
REcoM2	Regulated Ecosystem Model with two phytoplankton classes
SACCF	Southern Antarctic Circumpolar Current Front
SAF	Subantarctic Front
SAM	Southern Annular Mode
TA	Total Alkalinity
TICZ	Temporarily Ice-Covered Zone

Part I

INTRODUCTION

1 THE SOUTHERN OCEAN

1.1 OCEANOGRAPHIC SETTING

The zonally unrestricted flow of the oceanic and atmospheric circulation is a unique property of the Southern Ocean (Fig. 1.1), allowing the strength of the Westerlies, approximately located between 45 and 55°S (Trenberth et al., 1990), to develop unhindered. This atmospheric flow drives the eastwards running Antarctic Circumpolar Current (ACC), which exists in geostrophic balance between the meridional pressure gradient and the Coriolis force. It encircles the Antarctica with an annual mean transport of approximately 130 Sv at Drake Passage (1 Sv$= 1 \times 10^6\,\mathrm{m^3\,s^{-1}}$, Cunningham et al., 2003). The ACC consists of a series of interwoven currents with multiple branches (Sokolov and Rintoul, 2009), making the flow highly complex. Three main fronts can nevertheless be identified; the Subantarctic Front (SAF), the Antarctic Polar Front (PF) and the Southern ACC Front (SACCF) (Orsi et al., 1995). Towards the north the ACC is limited by the SAF, which separates warmer saltier water in the north from the colder and fresher water towards the south (Olbers et al., 2004). The SACCF marks the southern boundary of the ACC (e.g. Orsi et al., 1995), and is frequently observed at Drake passage but does not encircle the Antarctic. The SAF and the PF, are characterized by strong zonal jets of elevated speed, as well as strong meridional gradients for temperature, density and other oceanographic properties.

The meridional gradients characterizing the area between the PF and SAF are brought on by the fact that the isopycnals rise steeply in the region (Rintoul and Trull, 2001). The southwards transported Circumpolar Deep Water (CDW) and North Atlantic Deep Water (NADW) consequently rises towards the surface south of the PF (Fig. 1.2), bringing the water properties of the deep water upwards here (Marshall and Speer, 2012). The shoaling water follows two paths dependent on density. The less dense water is transported northwards in a wind-driven Ekman flow, which is subducted north of the Antarctic PF, marking an important boundary for heat, salt and carbon fluxes. The denser shoaling water is converted to Antarctic Bottom Water (e.g. Gill, 1973; Rintoul, 1998), which is created along the ice shelves and is the densest water found in the world ocean (Orsi et al., 1999).

The steep density slopes between the PF and the SAF mean that the water column is weakly stratified, and thus easily destabilized. The area is therefore characterized by deep winter mixed layers and large seasonal variations of the mixed layer depth (MLD, de Boyer Montegut et al., 2004). The deep winter mixing, and associated subduction of Antarctic Intermediate Water (AAIW, Fig. 1.2), is key for the ventilation of the intermediate ocean, transferring physical and biogeochemical properties between the surface mixed layer and the water below (Rintoul and Trull, 2001).

The combination of the location of the Southern Ocean, the southwards shoaling pycnoclines and the deep mixed layers means that the Southern Ocean is an important area for transfer of properties such as heat, salt and biogeochemical tracers both between the southern part of the Atlantic, Indian and Pacific Oceans, and between the atmosphere and the ocean. It is therefore key to understand how the biogeochem-

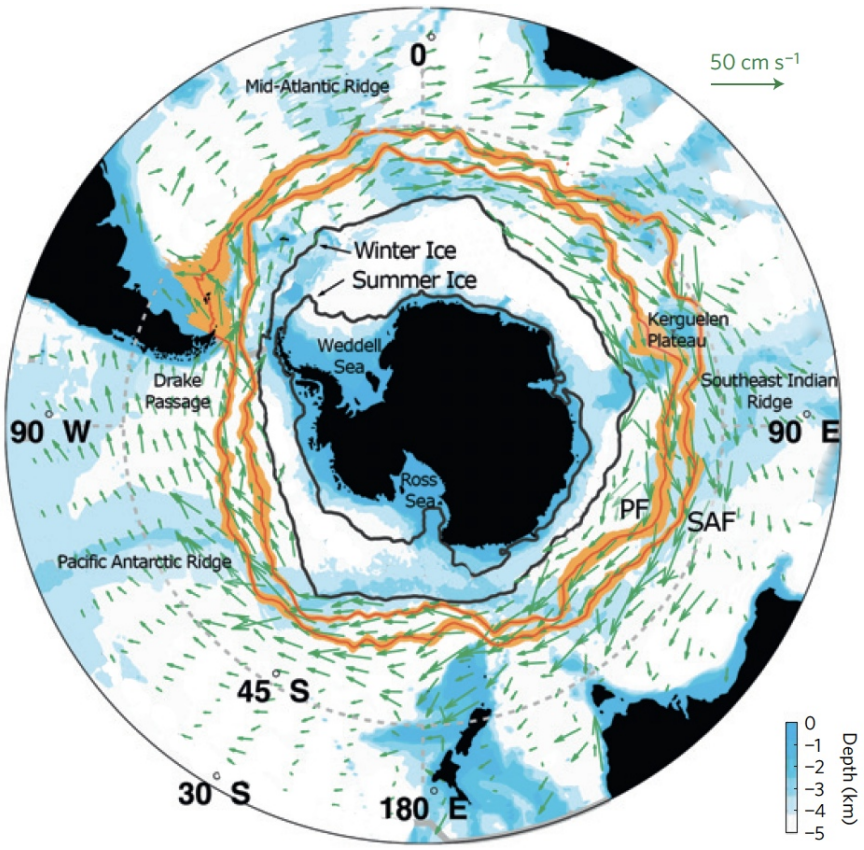

Figure 1.1: Map of the ocean south of 30° S. Green arrows denote the strength and direction of the surface currents. The mean position of the Polar Front (PF) and Subantarctic Front (SAF) are marked in orange. The mean winter and summer ice extend is marked with black lines. The background color denotes depth as shown in the colorbar (Modified from Marshall and Speer, 2012)

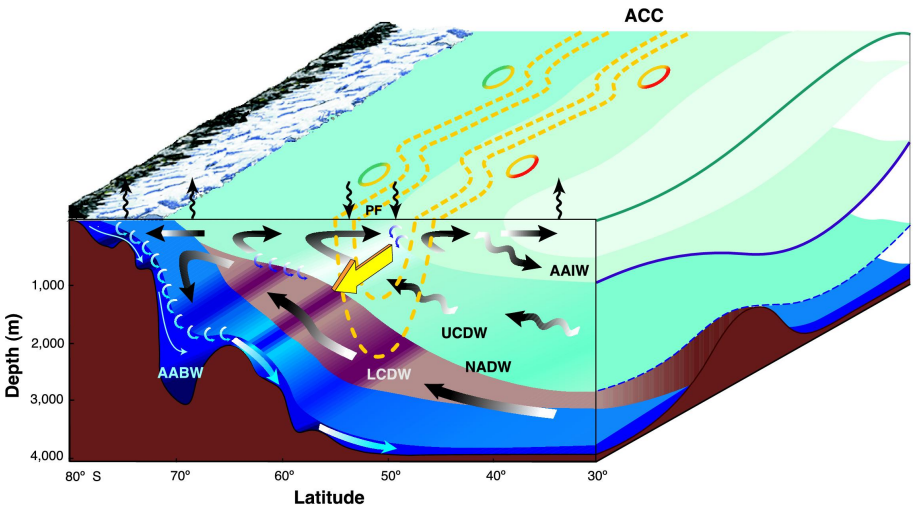

Figure 1.2: Schematic of the southern limb of the meridional overturning circulation. The meridional direction of the water flow is marked with black and blue arrows. The direction of the ACC is marked with a bold yellow arrow and the location of the ACC with a dotted orange line. The main water masses are marked: Antarctic Deep Water (AADW), Lower Circumpolar Deep Water (LCDW), Upper Circumpolar Deep Water (CDW), Antarctic Intermediate Water (AAIW) and North Atlantic Deep Water (NADW). The direction of heat exchange between the atmosphere and the ocean is marked with vertical curly arrows. (From Olbers et al., 2012, Fig. 16.3)

ical fluxes in the Southern Ocean are currently controlled and how they will respond to future climate change.

1.2 THE SOUTHERN OCEAN; AN HNLC AREA

The southward shoaling of the isopycnals in the Southern Ocean (Fig. 1.2), brings nutrient-rich water towards the surface through isopycnal and diapycnal transport (Pollard et al., 2002). But despite of a relatively high supply of macronutrients to the surface water in the Southern Ocean, they are not fully utilized by phytoplankton growth. The combination of high macronutrient concentrations and low chlorophyll levels has led to the Southern Ocean being categorized as one of the world's so-called High-Nutrient-Low-Chlorophyll (HNLC) areas (Martin et al., 1990a), a definition that it shares with the subarctic and equatorial Pacific (Martin and Fitzwater, 1988; Kolber et al., 1994). Of these areas, the Southern Ocean is by far the largest in area and in terms of the concentration of unused macronutrients (e.g. Sarmiento and Orr, 1991).

Since the early 1990'ies it has been recognized that limitation by the micronutrient iron, which is needed in the photosynthesis as well as the respiration apparatus of phytoplankton (Geider and La Roche, 1994), plays a large role in the low productivity (e.g. Martin et al., 1990a; Martin et al., 1990b). As is the case for the macronutrients, iron is supplied to the the surface water through upwelling, but due to the complicated iron chemistry in the water (See section 1.4.1), the iron-to-macronutrient ratio is too low to sustain production in the Southern Ocean. A number of experiments, ranging from laboratory to large-scale iron fertilization, have later been carried out and demonstrated that iron does indeed induce growth in the HNLC areas (e.g. Smetacek

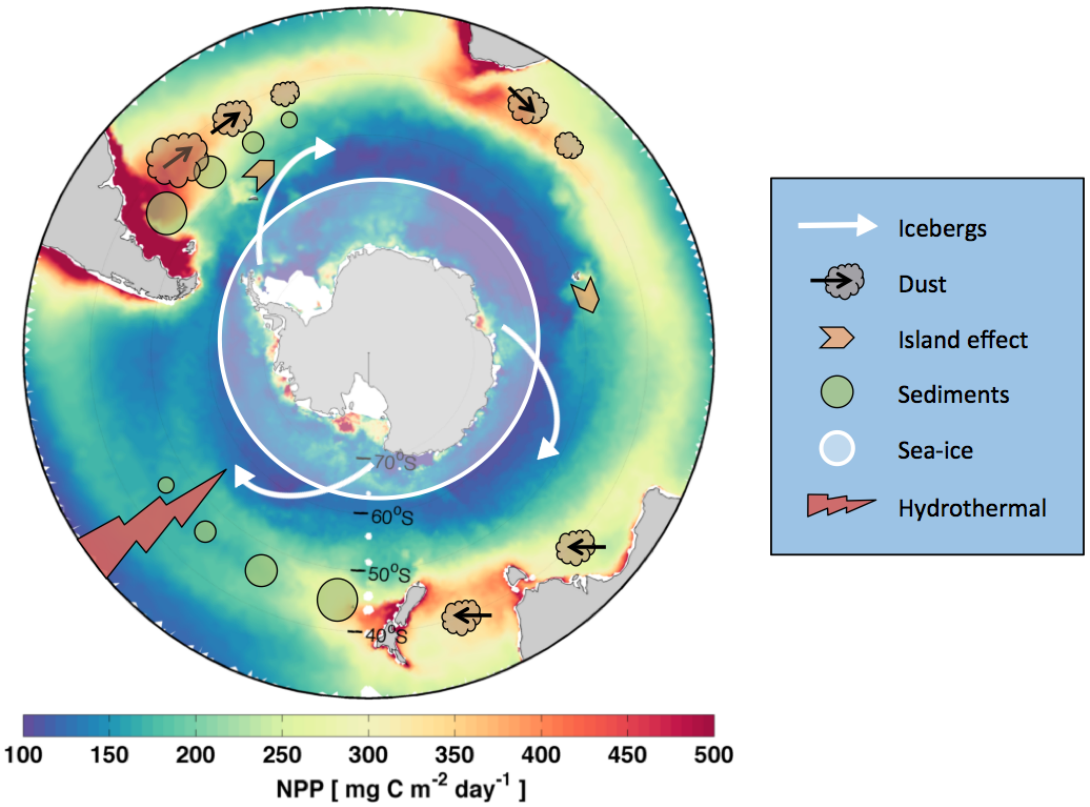

Figure 1.3: Conceptual map of iron sources to the Southern Ocean overlaid an image of mean ocean productivity (SeaWIFS and Behrenfeld and Falkowski, 1997). (After Boyd and Ellwood, 2010).

et al., 2012). But other factors, such as light limitation (Mitchell et al., 1991) and grazing (Smetacek et al., 2004) also play a role.

Despite of the overall low productivity in the Southern Ocean, recurring blooms are observed downstream of islands (e.g. Blain et al., 2001), in the vicinity of fronts (Moore and Abbott, 2002) and on the continental shelves (Fig. 1.3). This distribution largely mirrors the input of iron from external sources and indicates that they play an important role in the Southern Ocean.

1.3 SOURCES OF IRON

Traditionally, dust has been believed to be the most important source of iron to the Southern Ocean (e.g. Cassar et al., 2007), but this view has been challenged in the last decade. It is now known that other important sources include the shelf sediments (e.g. Westerlund and Öhman, 1991; Ardelan et al., 2010), melting sea-ice and icebergs (Smith et al., 2007; Raiswell et al., 2008) and hydrothermal vents (Tagliabue et al., 2010). Additionally, the iron supply from below into the mixed layer through upwelling (de Baar et al., 1995; Watson et al., 2000), entrainment (Tagliabue et al., 2014) and diffusion (Law et al., 2003) also plays a role. The magnitude of the input of iron to the Southern Ocean south of 35°S is not constrained, but a list of the current understanding of them can be found in Table (1.1).

Table 1.1: Previous estimates of iron sources to the Southern Ocean south of 35° S (From Tagliabue et al., 2010, Fig. 3)

SOURCE	MAGNITUDE [10^7 mol Fe yr^{-1}]
Dust	8 - 54
Sediment	460 - 1137
Ice	2 - 5
Hydrothermal vents	38

Quantifying the sources of the water's dissolved iron is nearly impossible from traditional measurements, and large scale estimates of the iron input to the ocean thus mainly come from modeling studies. Recently, a new technique to pin-point the origin of dissolved iron has, however, been developed, based on the isotopic composition of iron in sea water (Lacan et al., 2008; John and Adkins, 2010). The isotopic composition is a signature that can be used to identify the origin of the iron to an anoxic sedimentary source (Homoky et al., 2009; Severmann et al., 2010), a sedimentary non-reductive source (Radic et al., 2011; Homoky et al., 2013), aeolian input (Beard et al., 2003) and a hydrothermal source (Beard et al., 2003; Rouxel et al., 2008). Measurements of the isotopic fractionation in seawater are however scarce (Radic et al., 2011; Conway and John, 2014), and most large-scale estimates of the iron sources still come from modeling studies.

1.3.1 *Dust*

The earth's crust contains on average 6.3% iron based on weight (Taylor, 1964), which can be transported from arid land surfaces to the surface ocean in dust plumes. Knowledge about dust deposition is obtained locally through sampling (e.g. Wagener et al., 2008; Heimburger et al., 2012), and large scale estimates are provided by atmospheric transport models (e.g. Mahowald et al., 2003; Johnson et al., 2010).

Oceanic dust deposition predominantly takes place in the Northern Hemisphere due to the larger proportion of land sources here. Input of dust to the Southern Ocean is small (Jickells et al., 2005), but aeolian input of iron may nevertheless have a disproportional large impact on biological production in this area due to its HNLC status (Mahowald et al., 2005).

In the Southern Ocean, the aeolian iron input mainly takes place downwind of the continents (Fig. 1.3) (Cassar et al., 2007). The bulk of the dust originates in Patagonia, but studies suggest that this iron source only comprises about 10% of the total iron supply to the Atlantic sector of the Southern Ocean and that it has a small impact on biological productivity in the area (Meskhidze et al., 2007; Johnson et al., 2010). The aeolian iron deposition from Australia has likewise been shown to be of small significance for biological production in the Southern Ocean (Mackie et al., 2008). This can for example be explained by the highly episodical nature of the input and the Australian soil composition. A much smaller fraction of the total dust input to the Southern Ocean originates in South Africa, about half of which is deposited south of 70°S (Piketh et al., 2000).

The highly episodical nature of dust deposition makes the amount of iron delivered to the ocean highly dependent on the magnitude, duration and frequency of the deposition event. Dust sampling in the Southern Ocean is hindered by its remote location (Wagener et al., 2008), leading to higher uncertainties in the dust models in this area. Other uncertainties in the dust deposition models include the solubility of iron, which in reality ranges from 1 to 80% and the iron content of the dust (Mahowald et al., 2005).

1.3.2 *Ice*

During sea-ice formation, iron is incorporated from the ocean as well as from organic matter trapped into the forming ice (Lannuzel et al., 2010). The iron concentration within the sea-ice can thus be an order of magnitude higher than in the underlying water (Lannuzel et al., 2007). This iron is transported with the ice and released in the marginal ice zone during melting (Fig. 1.3), with the potential to significantly increase the water's iron concentration locally (van der Merwe et al., 2011). In the Southern Ocean, icebergs tend to drift westwards in the so-called iceberg alleys (Fig. 1.3), and they can thus be transported relatively far while releasing dissolved iron in their trajectories as they melt (Raiswell et al., 2008). Icebergs thus have the potential to affect production in remote areas of the Southern Ocean where iron limitation tends to be stronger than close to land.

Model studies show that the amount of iron released from sea-ice is minor compared to the sediment source (Lancelot et al., 2009; Wadley et al., 2014), and that adding a sea-ice iron source to a biogeochemical model changed the phytoplankton composition towards diatoms, but not the total amount of primary production (Wang et al., 2014).

1.3.3 *Sediment*

Iron measurements have revealed that the water's iron concentration is elevated in proximity to the coast (Johnson et al., 1997; Moore and Braucher, 2008), something that can be explained by release of iron from shelf sediments. Increased iron concentrations occur in the pore water of the sediment due to anoxic conditions brought on by remineralization of organic matter (e.g. Burdige, 1993). Transport of iron from the pore water to the water column through diffusion is too slow to fully explain the observed iron fluxes, and other explanations of the transport are for example enhanced flux through bio-irrigation (Elrod et al., 2004) and resuspension of particulate iron in turbulent environments (e.g. de Jong et al., 2012).

The sediment derived iron mainly increases the iron concentration in the surface water near the coast. This is because the iron release decreases with depth, as deeper sediments receive less degradable organic material (Elrod et al., 2004). The sediment derived iron can, however, also be carried far off shore. This has for example been shown in the North Pacific (Lam et al., 2006; Lam and Bishop, 2008) and in the Southern Ocean, where iron concentrations were elevated in the vicinity of the coast and the bottom of the Weddell Sea (Westerlund and Öhman, 1991; Klunder et al., 2014). The physical environment plays a large role for sediment derived iron being transported relatively far in the Southern Ocean. Several studies indicate that iron

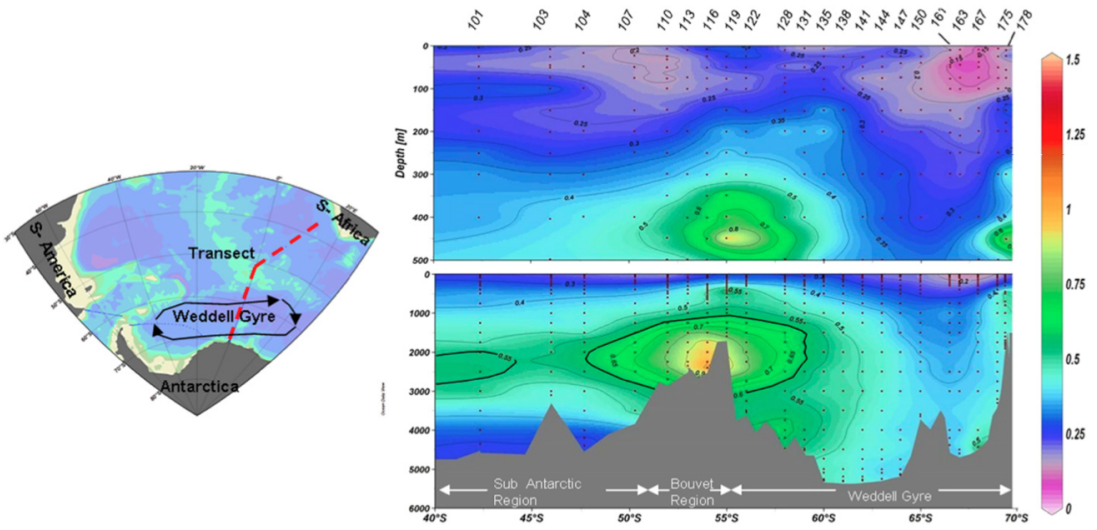

Figure 1.4: North-south transect of dissolved iron concentrations in the Atlantic sector of the Southern Ocean. The red dashed line in the left plot marks the position of the transect. (From Klunder et al., 2011).

from the Patagonian Shelf for instance is carried in the ACC over long distances (e.g. Löscher et al., 1997; de Baar et al., 1995).

In the Southern Ocean, persistent phytoplankton blooms are observed downstream of islands such as South Georgia (e.g. Korb and Whitehouse, 2004) and the Kerguelen (e.g. Blain et al., 2001; Blain et al., 2007) and Crozet (e.g. Bakker et al., 2007; Pollard et al., 2009) Islands, despite of the overall HNLC characterized ocean. This feature is known as the island mass effect, and is brought on by so-called natural iron fertilization. The mechanism behind it is not fully understood, but a number of mechanisms have been put forward as an explanation. First of all, the continental rise around the islands provides iron to the water from the sediments (e.g. Planquette et al., 2007). The iron flux from the sediments is further increased by the currents being forced upwards by the shallowing topography, gaining speed and turbulence and thereby also increasing the iron resuspension (e.g. de Jong et al., 2012). Secondly, iron has a nutrient-like vertical profile (Johnson et al., 1997). The deep water that is forced upwards by the topography in the Southern Ocean consequently already entails a higher concentration of iron than the surface water, and is hence also a potential iron source. Blain et al. (2007) did indeed show that this mechanism was important downstream of the Kerguelen Plateau.

Recent model studies have confirmed the importance of the sediment source of iron in the Southern Ocean, agreeing that it is on average more important than the dust source (Tagliabue et al., 2009a; Lancelot et al., 2009; Wadley et al., 2014).

1.3.4 *Hydrothermal supply*

Hydrothermal vents supply iron to the deep ocean (e.g. Field and Sherrell, 2000; German et al., 2002; Statham et al., 2005). While it has previously been assumed that this was a minor source of iron to the surface ocean due to rapid formation of particulates (Elderfield and Schultz, 1996), more recent studies suggest that the sig-

nificant amount of iron is protected by complexation with organic ligands (Bennett et al., 2008; Toner et al., 2009). Advection further from the source is thus possible, suggesting that hydrothermal vents supply a significant amount of iron to the deep ocean, though the exact amount is highly uncertain (Carazzo et al., 2013; Saito et al., 2013). Using the iron isotope fractionation technique, Conway and John (2014) demonstrated that hydrothermal vents added iron to the deep water of the Equatorial Atlantic Ocean which was detectable up to 1000 km away. They speculated that this iron source could serve as a buffer, continuously adding iron to the ocean also when other sources are intermittently low.

In the Southern Ocean, a model study suggests that hydrothermal vents play a role for the surface iron supply, especially in the iron depleted Pacific Ocean where the fast-spreading submarine ridges can be found (Tagliabue et al., 2010). Newer studies do, however, indicate that the hydrothermal iron supply may play a larger role in the Atlantic sector of the Southern Ocean than previously thought (Fig. 1.4) (Klunder et al., 2011; Saito et al., 2013).

1.3.5 *Supply to the mixed layer from below*

The fact that large scale wind-driven upwelling dominates south of the Polar Front means that a continuous iron flux into the mixed layer takes place here (e.g. de Baar et al., 1995; Watson et al., 2000; Hoppema et al., 2003). The deep winter mixing in the area between the Antarctic PF and SAF (de Boyer Montegut et al., 2004) transport iron into the surface water through entrainment (Tagliabue et al., 2014). Iron is also brought upwards through vertical diffusion (Law et al., 2003; Boyd et al., 2005), through horizontal advection across the base of the mixed layer (Ellwood et al., 2008) and through a transport induced by mesoscale eddies.

1.4 THE MARINE IRON CYCLE

1.4.1 *The iron cycle in nature*

Historically, advances in the knowledge of the iron cycle have been held back by the difficulties in measuring the water's concentration of dissolved iron. This was mainly caused by the trace concentrations of iron in the water combined with on-board contamination on research vessels (Achterberg et al., 2001; Bowie et al., 2006). The first reliable measurements of iron profiles ranging the entire water column were presented in the 1980'ies (e.g. Martin and Gordon, 1988; Martin et al., 1989), showing a nutrient-like profile with lower concentrations in the surface water and higher below the mixed layer. Johnson et al. (1997) presented a compilation of iron profiles from different ocean basins, confirming the nutrient-like profile and later global compilations were presented by Parekh et al. (2005) and Moore and Braucher (2008). Due to its remoteness and extreme weather, the Southern Ocean is, however, the least represented area in these compilations. But as measurement techniques have gradually improved and sampling programs, such as GEOTRACES (www.geotraces.org), have been launched, the knowledge of the iron concentrations in the Southern Ocean have improved (e.g. Klunder et al., 2011; Tagliabue et al., 2012).

Like the macronutrients, iron has a nutrient-like profile as it is taken up in the surface water and then remineralized from organic material deeper in the water col-

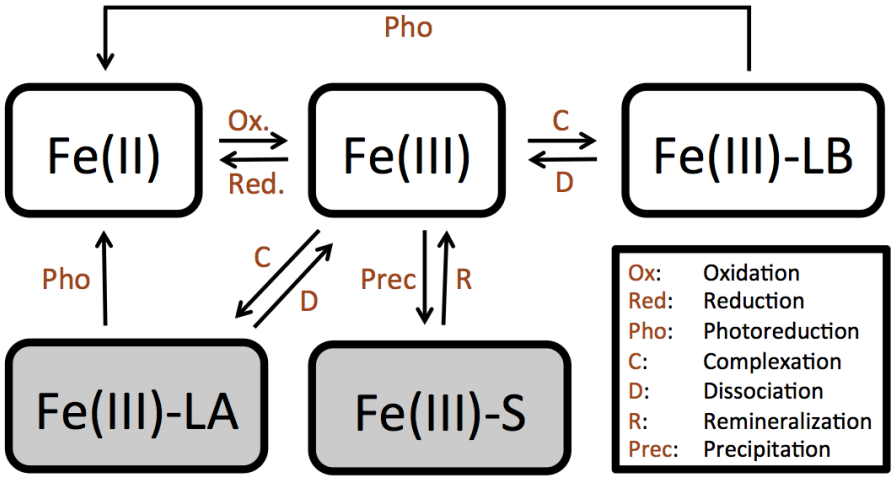

Figure 1.5: Simplified overview of the marine iron cycle. Bioavailable iron is marked in white boxes, and grey boxes represent non-available iron. Fe(III)-LB: Fe(III) complexed to organic ligands, bioavailable. Fe(III)-S: Fe(III) scavenged/precipitated to organic material, non-bioavailable. Fe(III)-LA: Fe(III) in complexation with ligands, non-bioavailable. (After Tagliabue et al., 2009a).

umn (e.g. Johnson et al., 1997). It does, however, also differ from the macronutrients because it is continuously removed from the water column through scavenging, a process converting soluble iron to colloidal or particulate forms through adsorption, precipitation and aggregation (e.g. Wu et al., 2001; Bergquist et al., 2007). This means that the deep water concentration, in contrast to the macronutrients, is lower in the Pacific and Southern Ocean than in the Atlantic as the water is older here. The removal of the water's dissolved iron also has the consequence that its residence time is relatively short, and that the vertical iron profiles are affected by local iron sources.

The marine iron cycle is highly complex and is as of now not fully understood (Gledhill and Buck, 2012). The following is a summary of the main pathways within the iron cycle, but is not a full overview.

In the ocean, the total iron can be divided into a dissolved iron pool, including ligand-bound iron, and a pool of non-labile iron, with strong interactions between these pools, making their relative contribution highly variable. The dissolved iron consists of the redox pair Fe(II) and Fe(III) (Fig. 1.5). In the oxidized ocean, Fe(II) is rapidly converted to Fe(III), a process which is faster at higher temperatures (Millero et al., 1987). Reduction of ligand-bound Fe(III) to Fe(II) is dependent on photochemical processes and thus varies with the light level in the water (e.g. Barbeau et al., 2001; Rijkenberg et al., 2005). The pool of Fe(III) is highly insoluble (Liu and Millero, 2002), and more than 99% of the dissolved iron in the ocean exists in complexation with stable organic ligands (e.g. Rue and Bruland, 1995; van den Berg, 2006). Ligand-bound iron is partly bioavailable (e.g. Hutchins et al., 1999; Maldonado et al., 2005; Tagliabue et al., 2009b). The water's concentration of ligand, which has been shown to vary between 0.2 and 10 $\mu mol\, m^{-3}$ (Gledhill and Buck, 2012), varies with depth (Ibisanmi et al., 2011) and in the horizontal domain (e.g. Thuróczy et al., 2011; Mohamed et al., 2011). Traditionally, two ligand classes have been classified, char-

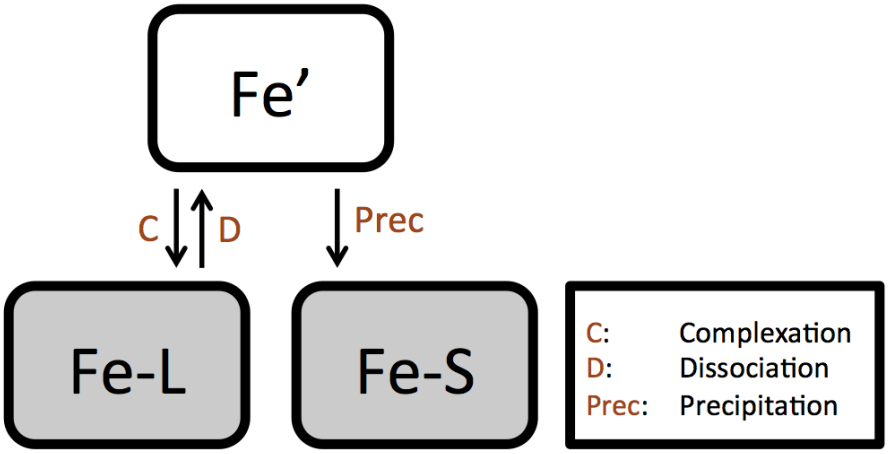

Figure 1.6: Overview of the iron cycle model from Parekh et al. (2004). Bioavailable iron is marked in white boxes, and grey boxes represent non-available iron. Fe': Free dissolved iron, bioavailable. Fe-S: Fe scavenged by organic material, non-bioavailable. Fe-L: Fe in complexation with ligands, non-bioavailable.

acterized by strong and weak binding to iron respectively (e.g. Rue and Bruland, 1995). The dissolved iron that does not form complexes with ligands is continuously removed from the water column through scavenging onto particles in the water such as detritus and phytoplankton (Fig. 1.5).

1.4.2 *The iron cycle in models*

When parameterizing a biological process in a biogeochemical model, a balance between the complexity of nature and the computational demand must be found. The relatively complex iron cycle is thus treated comparably simple in commonly used Ocean General Circulation Biogeochemical Models (OGCBMs) (e.g. Moore and Braucher, 2008; Yool et al., 2011), for example as the dissolved iron commonly is represented by a single tracer. The gradually increasing amount of iron measurements globally (Johnson et al., 1997; Parekh et al., 2005; Moore and Braucher, 2008) and in the Southern Ocean (Klunder et al., 2011; Tagliabue et al., 2012) has improved the understanding of the iron cycle and likewise its representation in models.

Johnson et al. (1997) presented an iron model in which scavenging only occurred when the iron concentration exceeded $0.6\,\mu mol\,Fe\,m^{-3}$. This was based on the assumption that the iron concentration was close to $0.6\,\mu mol\,Fe\,m^{-3}$ throughout the deep ocean, and that the dissolved iron was bound to strong ligands at lower concentrations. This assumption was incorporated in a few global models (e.g. Archer and Johnson, 2000; Aumont et al., 2003), in which the removal of iron through scavenging was balanced by aeolian iron input.

Parekh et al. (2004) were the first to introduce and interactive ligand concentration in a model, and were thereby able to reproduce the inter-ocean differences in deep water iron concentrations that newer measurements had revealed (Parekh et al., 2005); the North Atlantic had the highest and the Southern Ocean the lowest deep water iron concentrations. Newer global models adopted this approach and likewise

allowed scavenging at lower iron concentrations (e.g. Moore et al., 2004; Aumont and Bopp, 2006).

The framework for iron modeling presented by Parekh et al. (2004) and Parekh et al. (2005) is still used in a number of models (e.g. Aumont and Bopp, 2006; Dutkiewicz et al., 2009; Yool et al., 2011), including REcoM2 (Hauck et al., 2013). The iron model is relatively simple; the dissolved free iron is represented by a single iron pool and it has one ligand class of constant temporal and spatially concentration (Fig. 1.6). The pool of dissolved iron that is not bound to ligands (free iron) is continuously removed through a constant scavenging rate.

The effect of irradiance, temperature and pH on the iron cycle has been added to a global model by Tagliabue et al. (2009b), more complexity, including differentiation of Fe(II) and Fe(III) by Tagliabue and Völker (2011) and spatially varying ligand concentrations has been explored by Völker and Tagliabue (2014).

The continuous removal of dissolved iron from the water column through scavenging must be balanced by iron input in OGCBMs. The standard has been to add this through aeolian input (Archer and Johnson, 2000; Aumont et al., 2003; Parekh et al., 2005). But in the last decade, it has become clear that the sediment source of iron plays a large role, both on the global scale and especially in the Southern Ocean (e.g. Moore and Braucher, 2008; Tagliabue et al., 2009a). This source has therefore been implemented in models. Moore et al. (2004) employed a constant flux rate of $2\,\mu mol\,m^{-2}\,day^{-1}$ in sediments shallower than 1100 meters. But due to the resolution of the model grid being lower than the width of the shelfs in many places, the impact of this iron source was small in this model set-up. Aumont and Bopp (2006) therefore modulated their constant iron flux by an availability factor. This factor was controlled by the degree of anoxia in the sediments, decreasing with depth, and by the fraction of the cell that is on the shelf. Elrod et al. (2004) showed that the iron flux from the sediments is correlated with the release of carbon, and their model was incorporated into a global model by Moore and Braucher (2008). This parametrization improved the iron field in the model when it was compared to iron measurements on the global scales.

A model study by Tagliabue et al. (2010) showed that input of iron to the deep ocean by hydrothermal vents plays a role in the Pacific Ocean on long time scales, but this source has so far not been added to any other OGCBM. A couple of models have added an iron input from melting sea-ice and icebergs to the ocean (Lancelot et al., 2009; Wang et al., 2014). The mechanism behind sequestration of iron into the sea-ice is, however, complex and not fully understood.

As more knowledge is gained about the iron cycle and its effect on marine biological production it becomes possible to further add to the complexity of the iron cycle in OGCBMs. Regarding the iron cycle, the process understanding is, however, still so incomplete that adding more complexity to a model may not improve the model's representation of reality. In model runs investigating the role of climate change on biological production, it may be sensible to use an iron model in which the role of temperature, light and pH is incorporated. As is often the case in ocean biogeochemical modeling, it is therefore necessary to judge the knowledge gained by adding complexity against the increased computational demand that this complexity imposes.

REFERENCES

Achterberg, E. P., T. W. Holland, A. R. Bowie, R. F. C. Mantoura, and P. J. Worsfold (2001). "Determination of iron in seawater." *Anal. Chim. Acta* (442) 1, pp. 1–14. DOI: 10.1016/S0003-2670(01)01091-1.

Archer, D. E. and K. Johnson (2000). "A model of the iron cycle in the ocean." *Global Biogeochem. Cy.* (14) 1, pp. 269–279. DOI: 10.1029/1999GB900053.

Ardelan, M. V., O. Holm-Hansen, C. D. Hewes, C. S. Reiss, N. S. Silva, H. Dulaiova, E. Steinnes, and E. Sakshaug (2010). "Natural iron enrichment around the Antarctic Peninsula in the Southern Ocean." *Biogeosciences* (7) 1, pp. 11–25. DOI: 10.5194/bg-7-11-2010.

Aumont, O. and L. Bopp (2006). "Globalizing results from ocean in situ iron fertilization studies." *Global Biogeochem. Cy.* (20) GB2017. DOI: 10.1029/2005GB002591.

Aumont, O., E. Maier-Reimer, S. Blain, and P. Monfray (2003). "An ecosystem model of the global ocean including Fe, Si, P colimitations." *Global Biogeochem. Cy.* (17) 2. DOI: 10.1029/2001GB001745.

Bakker, D. C. E., M. C. Nielsdóttir, P. J. Morris, H. J. Venables, and A. J. Watson (2007). "The island mass effect and biological carbon uptake for the subantarctic Crozet Archipelago." *Deep Sea Res. Pt. II* (54) 18, pp. 2174–2190. DOI: 10.1016/j.dsr2.2007.06.009.

Barbeau, K., E. L. Rue, K. W. Bruland, and A. Butler (2001). "Photochemical cycling of iron in the surface ocean mediated by microbial iron(III)-binding ligands." *Nature* (413) 6854, pp. 409–413. DOI: 10.1038/35096545.

Beard, B. L., C. M. Johnson, K. L. Von Damm, and R. L. Poulson (2003). "Iron isotope constraints on Fe cycling and mass balance in oxygenated earth oceans." *Geology* (31) 7, pp. 629–632. DOI: 10.1130/0091-7613(2003)031<0629:IICOFC>2.0.CO;2.

Behrenfeld, M. J. and P. G. Falkowski (1997). "Photosynthetic rates derived from satellite-based chlorophyll concentration." *Limnol. Oceanogr.* (42) 1, pp. 1–20.

Bennett, S. A., E. P. Achterberg, D. P. Connelly, P. J. Statham, G. R. Fones, and C. R. German (2008). "The distribution and stabilisation of dissolved Fe in deep-sea hydrothermal plumes." *Earth Planet. Sc. Lett.* (270) 3, pp. 157–167. DOI: 10.1016/j.epsl.2008.01.048.

Bergquist, B. A., J. Wu, and E. A. Boyle (2007). "Variability in oceanic dissolved iron is dominated by the colloidal fraction." *Geochim. Cosmochim. Ac.* (71) 12, pp. 2960–2974. DOI: 10.1016/j.gca.2007.03.013.

Blain, S., B. Quéguiner, L. Armand, S. Belviso, B. Bombled, L. Bopp, A. Bowie, C. Brunet, C. Brussaard, F. Carlotti, U. Christaki, A. Corbiere, I. Durand, F. Ebersbach, J.-L. Fuda, N. Garcia, L. Gerringa, B. Griffiths, C. Guigue, C. Guillerm, S. Jacquet, C. Jeandel, P. Laan, D. Lefevre, C. Lo Monaco, A. Malits, J. Mosseri, I. Obernosterer, Y.-H. Park, M. Picheral, P. Pondaven, T. Remenyi, V. Sandroni, G. Sarthou, N. Savoye, L. Scouarnec, M. Souhaut, D. Huiller, K. Timmermans, T. Trull, J. Uitz, P. van Beek, M. Veldhuis, D. Vincent, E. Viollier, L. Vong, and T. Wagener (2007). "Effect of natural iron fertilization on carbon sequestration in the Southern Ocean." *Nature* (446) 7139, pp. 1070–1074. DOI: 10.1038/nature05700.

Blain, S., P. Tréguer, S. Belviso, E. Bucciarelli, M. Denis, S. Desabre, M. Fiala, V. Martin Jézéquel, J. Le Fèvre, P. Mayzaud, J.-C. Marty, and S. Razouls (2001). "A biogeochemical study of the island mass effect in the context of the iron hypothesis:

Kerguelen Islands, Southern Ocean." *Deep Sea Res. Pt. I* (48) 1, pp. 163–187. DOI: 10.1016/S0967-0637(00)00047-9.

Bowie, A. R., E. P. Achterberg, P. L. Croot, H. J. W. de Baar, P. Laan, J. W. Moffett, S. Ussher, and P. J. Worsfold (2006). "A community-wide intercomparison exercise for the determination of dissolved iron in seawater." *Mar. Chem.* (98) 1, pp. 81–99. DOI: 10.1016/j.marchem.2005.07.002.

Boyd, P. W. and M. J. Ellwood (2010). "The biogeochemical cycle of iron in the ocean." *Nat. Geosci.* (3) 10, pp. 675–682. DOI: 10.1038/ngeo964.

Boyd, P. W., C. S. Law, D. A. Hutchins, E. R. Abraham, P. L. Croot, M. Ellwood, R. D. Frew, M. Hadfield, J. Hall, S. Handy, C. Hare, J. Higgins, P. Hill, K. A. Hunter, K. LeBlanc, M. T. Maldonado, R. M. McKay, C. Mioni, M. Oliver, S. Pickmere, M. Pinkerton, K. Safi, S. Sander, S. A. Sanudo-Wilhelmy, M. Smith, R. Strzepek, A. Tovar-Sanchez, and S. Wilhelm (2005). "FeCycle: Attempting an iron biogeochemical budget from a mesoscale SF6 tracer experiment in unperturbed low iron waters." *Global Biogeochem. Cy.* (19) GB4S20. DOI: 10.1029/2005GB002494.

Burdige, D. J. (1993). "The biogeochemistry of manganese and iron reduction in marine sediments." *Earth-Sci. Rev.* (35) 3, pp. 249–284. DOI: 10.1016/0012-8252(93)90040-E.

Carazzo, G., A. M. Jellinek, and A. V. Turchyn (2013). "The remarkable longevity of submarine plumes: Implications for the hydrothermal input of iron to the deep-ocean." *Earth Planet. Sc. Lett.* (382), pp. 66–76. DOI: 10.1016/j.epsl.2013.09.008.

Cassar, N., M. L. Bender, B. A. Barnett, S. Fan, W. J. Moxim, H. Levy, and B. Tilbrook (2007). "The Southern Ocean biological response to aeolian iron deposition." *Science* (317) 5841, pp. 1067–1070. DOI: 10.1126/science.1144602.

Conway, T. M. and S. G. John (2014). "Quantification of dissolved iron sources to the North Atlantic Ocean." *Nature* (511) 7508, pp. 212–215. DOI: 10.1038/nature13482.

Cunningham, S. A., S. G. Alderson, B. A. King, and M. A. Brandon (2003). "Transport and variability of the Antarctic circumpolar current in Drake Passage." *J. Geophys. Res.* (108) C5. DOI: 10.1029/2001JC001147.

De Baar, H. J. W., J. T. M. de Jong, D. C. E. Bakker, B. M. Löscher, C. Veth, U. Bathmann, and V. Smetacek (1995). "Importance of iron for plankton blooms and carbon dioxide drawdown in the Southern Ocean." *Nature* (373). DOI: 10.1038/373412a0.

De Boyer Montegut, C., G. Madec, A. S. Fischer, A. Lazar, and D. Iudicone (2004). "Mixed layer depth over the global ocean: An examination of profile data and a profile-based climatology." *J. Geophys. Res.* (109) C12003. DOI: 10.1029/2004JC002378.

De Jong, J., V. Schoemann, D. Lannuzel, P. Croot, H. de Baar, and J.-L. Tison (2012). "Natural iron fertilization of the Atlantic sector of the Southern Ocean by continental shelf sources of the Antarctic Peninsula." *J. Geophys. Res.* (117) G1. DOI: 10.1029/2011JG001679.

Dutkiewicz, S., M. J. Follows, and J. G. Bragg (2009). "Modeling the coupling of ocean ecology and biogeochemistry." *Global Biogeochem. Cy.* (23) GB1021. DOI: 10.1029/2008GB003405.

Elderfield, H. and A. Schultz (1996). "Mid-ocean ridge hydrothermal fluxes and the chemical composition of the ocean." *Annu. Rev. Earth Planet. Sci.* (24), pp. 191–224. DOI: 10.1146/annurev.earth.24.1.191.

Ellwood, M. J., P. W. Boyd, and P. Sutton (2008). "Winter-time dissolved iron and nutrient distributions in the Subantarctic Zone from 40–52S; 155–160E." *Geophys. Res. Lett.* (35) L11604. DOI: 10.1029/2008GL033699.

Elrod, V. A., W. M. Berelson, K. H. Coale, and K. S. Johnson (2004). "The flux of iron from continental shelf sediments: A missing source for global budgets." *Geophys. Res. Lett.* (31) L12307. DOI: 10.1029/2004GL020216.

Field, M. P. and R. M. Sherrell (2000). "Dissolved and particulate Fe in a hydrothermal plume at 9° 45′ N, East Pacific Rise: Slow Fe (II) oxidation kinetics in Pacific plumes." *Geochim. Cosmochim. Ac.* (64) 4, pp. 619–628. DOI: 10.1016/S0016-7037(99)00333-6.

Geider, R. J. and J. La Roche (1994). "The role of iron in phytoplankton photosynthesis, and the potential for iron-limitation of primary productivity in the sea." *Photosynth. Res.* (39) 3, pp. 275–301. DOI: 10.1007/BF00014588.

German, C. R., S. Colley, M. R. Palmer, A. Khripounoff, and G. P. Klinkhammer (2002). "Hydrothermal plume-particle fluxes at 13°N on the East Pacific Rise." *Deep Sea Res. Pt. I* (49) 11, pp. 1921–1940. DOI: 10.1016/S0967-0637(02)00086-9.

Gill, A. E. (1973). "Circulation and bottom water production in the Weddell Sea." *Deep Sea Research and Oceanographic Abstracts* (20) 2, pp. 111–140. DOI: 10.1016/0011-7471(73)90048-X.

Gledhill, M. and K. N. Buck (2012). "The organic complexation of iron in the marine environment: a review." *Front. Microbiol.* (3) 69. DOI: 10.3389/fmicb.2012.00069.

Hauck, J., C. Völker, T. Wang, M. Hoppema, M. Losch, and D. A. Wolf-Gladrow (2013). "Seasonally different carbon flux changes in the Southern Ocean in response to the Southern Annular Mode." *Global Biogeochem. Cy.* (27), pp. 1–10. DOI: 10.1002/2013GB004600.

Heimburger, A., R. Losno, S. Triquet, F. Dulac, and N. Mahowald (2012). "Direct measurements of atmospheric iron, cobalt, and aluminum-derived dust deposition at Kerguelen Islands." *Global Biogeochem. Cy.* (26) GB4016. DOI: 10.1029/2012GB004301.

Homoky, W. B., S. G. John, T. M. Conway, and R. A. Mills (2013). "Distinct iron isotopic signatures and supply from marine sediment dissolution." *Nat. Commun.* (4). DOI: 10.1038/ncomms3143.

Homoky, W. B., S. Severmann, R. A. Mills, P. J. Statham, and G. R. Fones (2009). "Pore-fluid Fe isotopes reflect the extent of benthic Fe redox recycling: Evidence from continental shelf and deep-sea sediments." *Geology* (37) 8, pp. 751–754. DOI: 10.1130/G25731A.1.

Hoppema, M., H. J. W. de Baar, E. Fahrbach, H. H. Hellmer, and B. Klein (2003). "Substantial advective iron loss diminishes phytoplankton production in the Antarctic Zone." *Global Biogeochem. Cy.* (17) 1. DOI: 10.1029/2002GB001957.

Hutchins, D. A., A. E. Witter, A. Butler, and G. W. Luther (1999). "Competition among marine phytoplankton for different chelated iron species." *Nature* (400) 6747, pp. 858–861. DOI: 10.1038/23680.

Ibisanmi, E., S. G. Sander, P. W. Boyd, A. R. Bowie, and K. A. Hunter (2011). "Vertical distributions of iron-(III) complexing ligands in the Southern Ocean." *Deep Sea Res. Pt. II* (58) 21, pp. 2113–2125. DOI: 10.1016/j.dsr2.2011.05.028.

Jickells, T. D., Z. S. An, K. K. Andersen, A. R. Baker, G. Bergametti, N. Brooks, J. J. Cao, P. W. Boyd, R. A. Duce, K. A. Hunter, H. Kawahata, N. Kubilay, J. LaRoche, P. S. Liss, N. Mahowald, J. M. Prospero, A. J. Ridgwell, I. Tegen, and R. Torres

(2005). "Global iron connections between desert dust, ocean biogeochemistry, and climate." *Science* (308) 5718, pp. 67–71. DOI: 10.1126/science.1105959.

John, S. G. and J. F. Adkins (2010). "Analysis of dissolved iron isotopes in seawater." *Mar. Chem.* (119) 1, pp. 65–76. DOI: 10.1016/j.marchem.2010.01.001.

Johnson, K. S., R. M. Gordon, and K. H. Coale (1997). "What controls dissolved iron concentrations in the world ocean?" *Mar. Chem.* (57) 3, pp. 137–161. DOI: 10.1016/S0304-4203(97)00043-1.

Johnson, M. S., N. Meskhidze, F. Solmon, S. Gassó, P. Y. Chuang, D. M. Gaiero, R. M. Yantosca, S. Wu, Y. Wang, and C. Carouge (2010). "Modeling dust and soluble iron deposition to the South Atlantic Ocean." *J. Geophys. Res.* (115) D15. DOI: 10.1029/2009JD013311.

Klunder, M. B., P. Laan, H. J. W. De Baar, R. Middag, I. Neven, and J. Van Ooijen (2014). "Dissolved Fe across the Weddell Sea and Drake Passage: impact of DFe on nutrient uptake." *Biogeosciences* (11) 3, pp. 651–669. DOI: 10.5194/bg-11-651-2014.

Klunder, M. B., P. Laan, R. Middag, H. J. W. de Baar, and J. C. Van Ooijen (2011). "Dissolved iron in the Southern Ocean (Atlantic sector)." *Deep Sea Res. Pt. II* (58) 25, pp. 2678–2694. DOI: 10.1016/j.dsr2.2010.10.042.

Kolber, Z. S., R. T. Barber, K. H. Coale, S. E. Fitzwateri, R. M. Greene, K. S. Johnson, S. Lindley, and P. G. Falkowski (1994). "Iron limitation of phytoplankton photosynthesis in the equatorial Pacific Ocean." *Nature* (371) 6493, pp. 145–149. DOI: 10.1038/371145a0.

Korb, R. E. and M. Whitehouse (2004). "Contrasting primary production regimes around South Georgia, Southern Ocean: Large blooms versus high nutrient, low chlorophyll waters." *Deep Sea Res. Pt. I* (51) 5, pp. 721–738. DOI: 10.1016/j.dsr.2004.02.006.

Lacan, F., A. Radic, C. Jeandel, F. Poitrasson, G. Sarthou, C. Pradoux, and R. Freydier (2008). "Measurement of the isotopic composition of dissolved iron in the open ocean." *Geophys. Res. Lett.* (35) L24610. DOI: 10.1029/2008GL035841.

Lam, P. J. and J. K. B. Bishop (2008). "The continental margin is a key source of iron to the HNLC North Pacific Ocean." *Geophys. Res. Lett.* (35) L07608. DOI: 10.1029/2008GL033294.

Lam, P. J., J. K. B. Bishop, C. C. Henning, M. A. Marcus, G. A. Waychunas, and I. Y. Fung (2006). "Wintertime phytoplankton bloom in the subarctic Pacific supported by continental margin iron." *Global Biogeochem. Cy.* (20) GB1006. DOI: 10.1029/2005GB002557.

Lancelot, C., A. de Montety, H. Goosse, S. Becquevort, V. Schoemann, B. Pasquer, and M. Vancoppenolle (2009). "Spatial distribution of the iron supply to phytoplankton in the Southern Ocean: a model study." *Biogeosciences* (6) 12, pp. 2861–2878. DOI: 10.5194/bg-6-2861-2009.

Lannuzel, D., V. Schoemann, J. de Jong, B. Pasquer, P. van der Merwe, F. Masson, J.-L. Tison, and A. Bowie (2010). "Distribution of dissolved iron in Antarctic sea ice: Spatial, seasonal, and inter-annual variability." *J. Geophys. Res.* (115) G3. DOI: 10.1029/2009JG001031.

Lannuzel, D., V. Schoemann, J. de Jong, J.-L. Tison, and L. Chou (2007). "Distribution and biogeochemical behaviour of iron in the East Antarctic sea ice." *Mar. Chem.* (106) 1, pp. 18–32. DOI: 10.1016/j.marchem.2006.06.010.

Law, C. S., E. R. Abraham, A. J. Watson, and M. I. Liddicoat (2003). "Vertical eddy diffusion and nutrient supply to the surface mixed layer of the Antarctic Circumpolar Current." *J. Geophys. Res.* (108) C8. DOI: 10.1029/2002JC001604.

Liu, X. and F. J. Millero (2002). "The solubility of iron in seawater." *Mar. Chem.* (77) 1, pp. 43–54. DOI: 10.1016/S0304-4203(01)00074-3.

Löscher, B. M., H. J. W. de Baar, J. T. M. de Jong, C. Veth, and F. Dehairs (1997). "The distribution of Fe in the Antarctic circumpolar current." *Deep Sea Re. Pt. II* (44) 1, pp. 143–187. DOI: 10.1016/S0967-0645(96)00101-4.

Mackie, D. S., P. W. Boyd, G. H. McTainsh, N. W. Tindale, T. K. Westberry, and K. A. Hunter (2008). "Biogeochemistry of iron in Australian dust: From eolian uplift to marine uptake." *Geochem. Geophy. Geosy.* (9) Q03Q08. DOI: 10.1029/2007GC001813.

Mahowald, N. M., A. R. Baker, G. Bergametti, N. Brooks, R. A. Duce, T. D. Jickells, N. Kubilay, J. M. Prospero, and I. Tegen (2005). "Atmospheric global dust cycle and iron inputs to the ocean." *Global Biogeochem. Cy.* (19) GB4025. DOI: 10.1029/2004GB002402.

Mahowald, N., C. Luo, J. Del Corral, and C. S. Zender (2003). "Interannual variability in atmospheric mineral aerosols from a 22-year model simulation and observational data." *J. Geophys. Res* (108) D12. DOI: 10.1029/2002JD002821.

Maldonado, M. T., R. F. Strzepek, S. Sander, and P. W. Boyd (2005). "Acquisition of iron bound to strong organic complexes, with different Fe binding groups and photochemical reactivities, by plankton communities in Fe-limited subantarctic waters." *Global Biogeochem. Cy.* (19) GB4S23. DOI: 0.1029/2005GB002481.

Marshall, J. and K. Speer (2012). "Closure of the meridional overturning circulation through Southern Ocean upwelling." *Nat. Geosci.* (5) 3, pp. 171–180. DOI: 10.1038/ngeo1391.

Martin, J. H., S. E. Fitzwater, and R. M. Gordon (1990a). "Iron deficiency limits phytoplankton growth in Antarctic waters." *Global Biogeochem. Cy.* (4) 1, pp. 5–12. DOI: 10.1029/GB004i001p00005.

Martin, J. H., R. M. Gordon, and S. E. Fitzwater (1990b). "Iron in Antarctic waters." *Nature* (345), pp. 156–158. DOI: 10.1038/345156a0.

Martin, J. H. and S. Fitzwater (1988). "Iron deficiency limits phytoplankton growth in the north-east Pacific subarctic." *Nature* (331), pp. 341–343. DOI: 10.1038/331341a0.

Martin, J. H. and R. M. Gordon (1988). "Northeast Pacific iron distributions in relation to phytoplankton productivity." *Deep Sea Res. Pt. A* (35) 2, pp. 177–196. DOI: 10.1016/0198-0149(88)90035-0.

Martin, J. H., R. M. Gordon, S. E. Fitzwater, and W. W. Broenkow (1989). "VERTEX: phytoplankton/iron studies in the Gulf of Alaska." *Deep Sea Res. Pt. A* (36) 5, pp. 649–680. DOI: 10.1016/0198-0149(89)90144-1.

Meskhidze, N., A. Nenes, W. L. Chameides, C. Luo, and N. Mahowald (2007). "Atlantic Southern Ocean productivity: Fertilization from above or below?" *Global Biogeochem. Cy.* (21) GB2006. DOI: 10.1029/2006GB002711.

Millero, F. J., S. Sotolongo, and M. Izaguirre (1987). "The oxidation kinetics of Fe(II) in seawater." *Geochim. Cosmochim. Ac.* (51) 4, pp. 793–801. DOI: 10.1016/0016-7037(87)90093-7.

Mitchell, B. G., E. A. Brody, O. Holm-Hansen, C. McClain, and J. Bishop (1991). "Light limitation of phytoplankton biomass and macronutrient utilization in the Southern Ocean." *Limnol. Oceanogr.* (36) 8, pp. 1662–1677. DOI: 10.4319/lo.1991.36.8.1662.

Mohamed, K. N., S. Steigenberger, M. C. Nielsdottir, M. Gledhill, and E. P. Achterberg (2011). "Dissolved iron (III) speciation in the high latitude North Atlantic Ocean." *Deep Sea Res. Pt. A* (58) 11, pp. 1049–1059. DOI: 10.1016/j.dsr.2011.08.011.

Moore, J. K. and O. Braucher (2008). "Sedimentary and mineral dust sources of dissolved iron to the world ocean." *Biogeosciences* (5) 3, pp. 631–656. DOI: 10.5194/bg-5-631-2008.

Moore, J. K., S. C. Doney, and K. Lindsay (2004). "Upper ocean ecosystem dynamics and iron cycling in a global three-dimensional model." *Global Biogeochem. Cy.* (18) GB4028. DOI: 10.1029/2004GB002220.

Moore, J. K. and M. R. Abbott (2002). "Surface chlorophyll concentrations in relation to the Antarctic Polar Front: seasonal and spatial patterns from satellite observations." *J. Mar. Sys.* (37) 1, pp. 69–86. DOI: 10.1016/S0924-7963(02)00196-3.

Olbers, D., D. Borowski, C. Völker, and J.-O. Wolff (2004). "The dynamical balance, transport and circulation of the Antarctic Circumpolar Current." *Antarct. Sci.* (16) 04, pp. 439–470.

Olbers, D., J. Willebrand, and C. Eden (2012). *Ocean Dynamics*. Springer.

Orsi, A. H., G. C. Johnson, and J. L. Bullister (1999). "Circulation, mixing, and production of Antarctic Bottom Water." *Prog. Oceanogr.* (43) 1, pp. 55–109. DOI: 10.1016/S0079-6611(99)00004-X.

Orsi, A. H., T. Whitworth III, and W. D. Nowlin Jr (1995). "On the meridional extent and fronts of the Antarctic Circumpolar Current." *Deep Sea Res. I* (42) 5, pp. 641–673. DOI: 10.1016/0967-0637(95)00021-W.

Parekh, P., M. J. Follows, and E. Boyle (2004). "Modeling the global ocean iron cycle." *Global Biogeochem. Cy.* (18) GB1002. DOI: 10.1029/2003GB002061.

Parekh, P., M. J. Follows, and E. A. Boyle (2005). "Decoupling of iron and phosphate in the global ocean." *Global Biogeochem. Cy.* (19) GB2020. DOI: 10.1029/2004GB002280.

Piketh, S. J., P. D. Tyson, and W. Steffen (2000). "Aeolian transport from southern Africa and iron fertilization of marine biota in the South Indian Ocean." *S. Afr. J. Sci.* (96) 5.

Planquette, H., P. J. Statham, G. R. Fones, M. A. Charette, C. M. Moore, I. Salter, F. H. Nedelec, S. L. Taylor, M. French, A. R. Baker, N. Mahowald, and T. D. Jickells (2007). "Dissolved iron in the vicinity of the Crozet Islands, Southern Ocean." *Deep Sea Res. Pt. II* (54) 18, pp. 1999–2019. DOI: 10.1016/j.dsr2.2007.06.019.

Pollard, R. T., M. I. Lucas, and J. F. Read (2002). "Physical controls on biogeochemical zonation in the Southern Ocean." *Deep Sea Res. Pt. II* (49) 16, pp. 3289–3305. DOI: 10.1016/0198-0149(82)90058-9.

Pollard, R. T., I. Salter, R. J. Sanders, M. I. Lucas, C. M. Moore, R. A. Mills, P. J. Statham, J. T. Allen, A. R. Baker, D. C. E. Bakker, M. A. Charette, S. Fielding, G. R. Fone, M. French, A. E. Hickman, R. J. Holland, J. A. Hughes, T. D. Jickells, R. S. Lampitt, P. J. Morris, F. H. Nedelec, M. Nielsdottir, H. Planquette, E. E. Popova, A. J. Poulton, J. F. Read, S. Seeyave, T. Smith, M. Stichcombe, S. Taylor, S. Thomalla, H. J. Venables, R. Williamson, and M. V. Zubkov (2009). "Southern Ocean deep-water carbon export enhanced by natural iron fertilization." *Nature* (457) 7229, pp. 577–580. DOI: 10.1038/nature07716.

Radic, A., F. Lacan, and J. W. Murray (2011). "Iron isotopes in the seawater of the equatorial Pacific Ocean: new constraints for the oceanic iron cycle." *Earth Planet. Sc. Lett.* (306) 1, pp. 1–10. DOI: 10.1016/j.epsl.2011.03.015.

Raiswell, R., L. G. Benning, M. Tranter, and S. Tulaczyk (2008). "Bioavailable iron in the Southern Ocean: the significance of the iceberg conveyor belt." *Geochem. Trans* (9) 7, p. 9. DOI: 10.1186/1467-4866-9-7.

Rijkenberg, M. J. A., A. C. Fischer, J. J. Kroon, L. J. A. Gerringa, K. R. Timmermans, H. T. Wolterbeek, and H. J. W. de Baar (2005). "The influence of UV irradiation on the photoreduction of iron in the Southern Ocean." *Mar. Chem.* (93) 2, pp. 119–129. DOI: 10.1016/j.marchem.2004.03.021.

Rintoul, S. R. (1998). *Ocean, Ice, and Atmosphere: Interactions at the Antarctic Continental Margin*. American Geophysical Union, pp. 151–171. ISBN: 9781118668238. DOI: 10.1029/AR075p0151.

Rintoul, S. R. and T. W. Trull (2001). "Seasonal evolution of the mixed layer in the Subantarctic Zone south of Australia." *J. Geophys. Res.* (106) C12, pp. 31447–31462. DOI: 10.1029/2000JC000329.

Rouxel, O., W. C. Shanks III, W. Bach, and K. J. Edwards (2008). "Integrated Fe-and S-isotope study of seafloor hydrothermal vents at East Pacific Rise 9–10° N." *Chem. Geol.* (252) 3, pp. 214–227. DOI: 10.1016/j.epsl.2011.03.015.

Rue, E. L. and K. W. Bruland (1995). "Complexation of iron (III) by natural organic ligands in the Central North Pacific as determined by a new competitive ligand equilibration/adsorptive cathodic stripping voltammetric method." *Mar. Chem.* (50) 1, pp. 117–138. DOI: 10.1016/0304-4203(95)00031-L.

Saito, M. A., A. E. Noble, A. Tagliabue, T. J. Goepfert, C. H. Lamborg, and W. J. Jenkins (2013). "Slow-spreading submarine ridges in the South Atlantic as a significant oceanic iron source." *Nat. Geosci.* (6) 9, pp. 775–779. DOI: 10.1038/ngeo1893.

Sarmiento, J. L. and J. C. Orr (1991). "Three-dimensional simulations of the impact of Southern Ocean nutrient depletion on atmospheric CO_2 and ocean chemistry." *Limnol. Oceanogr.* (36) 8, pp. 1928–1950.

Severmann, S., J. McManus, W. M. Berelson, and D. E. Hammond (2010). "The continental shelf benthic iron flux and its isotope composition." *Geochim. Cosmochim. Ac.* (74) 14, pp. 3984–4004. DOI: 10.1016/j.gca.2010.04.022.

Smetacek, V., P. Assmy, and J. Henjes (2004). "The role of grazing in structuring Southern Ocean pelagic ecosystems and biogeochemical cycles." *Antarct. Sci.* (16) 04, pp. 541–558. DOI: 10.1017/S0954102004002317.

Smetacek, V., C. Klaas, V. H. Strass, P. Assmy, M. Montresor, B. Cisewski, N. Savoye, A. Webb, F. dÕOvidio, J. M. Arrieta, U. Bathmann, R. Bellerby, G. M. Berg, P. Croot, S. Gonzalez, J. Henjes, G. J. Herndl, L. J. Hoffmann, H. Leach, M. Losch, M. M. Mills, C. Neill, I. Peeken, R. Rottgers, O. Sachs, E. Sauter, M. M. Schmidt, J. Schwarz, A. Terbruggen, and D. Wolf-Gladrow (2012). "Deep carbon export from a Southern Ocean iron-fertilized diatom bloom." *Nature* (487) 7407, pp. 313–319.

Smith, K. L., B. H. Robison, J. J. Helly, R. S. Kaufmann, H. A. Ruhl, T. J. Shaw, B. S. Twining, and M. Vernet (2007). "Free-drifting icebergs: hot spots of chemical and biological enrichment in the Weddell Sea." *Science* (317) 5837, pp. 478–482. DOI: 10.1126/science.1142834.

Sokolov, S. and S. R. Rintoul (2009). "Circumpolar structure and distribution of the Antarctic Circumpolar Current fronts: 1. Mean circumpolar paths." *J. Geophys. Res.* (114) C11. DOI: 10.1029/2008JC005108.

Statham, P. J., C. R. German, and D. P. Connelly (2005). "Iron (II) distribution and oxidation kinetics in hydrothermal plumes at the Kairei and Edmond vent sites, Indian Ocean." *Earth Planet. Sc. Lett.* (236) 3, pp. 588–596. DOI: 10.1016/j.epsl.2005.03.008.

Tagliabue, A., L. Bopp, and O. Aumont (2009a). "Evaluating the importance of atmospheric and sedimentary iron sources to Southern Ocean biogeochemistry." *Geophys. Res. Lett.* (36) L13601. DOI: 10.1029/2009GL038914.

Tagliabue, A., L. Bopp, O. Aumont, and K. R. Arrigo (2009b). "Influence of light and temperature on the marine iron cycle: From theoretical to global modeling." *Global Biogeochem. Cy.* (23) GB2017. DOI: 10.1029/2008GB003214.

Tagliabue, A., L. Bopp, J.-C. Dutay, A. R. Bowie, F. Chever, P. Jean-Baptiste, E. Bucciarelli, D. Lannuzel, T. Remenyi, G. Sarthou, O. Aumont, M. Gehlen, and C. Jeandel (2010). "Hydrothermal contribution to the oceanic dissolved iron inventory." *Nat. Geosci.* (3) 4, pp. 252–256. DOI: 10.1038/ngeo818.

Tagliabue, A. and C. Völker (2011). "Towards accounting for dissolved iron speciation in global ocean models." *Biogeosciences* (8) 10, pp. 3025–3039.

Tagliabue, A., T. Mtshali, O. Aumont, A. R. Bowie, M. B. Klunder, A. N. Roychoudhury, and S. Swart (2012). "A global compilation of dissolved iron measurements: focus on distributions and processes in the Southern Ocean." *Biogeosciences* (9) 6, pp. 1–17. DOI: 10.5194/bg-9-2333-2012.

Tagliabue, A., J.-B. Sallée, A. R. Bowie, M. Lévy, S. Swart, and P. W. Boyd (2014). "Surface-water iron supplies in the Southern Ocean sustained by deep winter mixing." *Nat. Geosci.* (7), pp. 314–320. DOI: 10.1038/ngeo2101.

Taylor, S. R. (1964). "Abundance of chemical elements in the continental crust: a new table." *Geochim. Cosmochim. Ac.* (28) 8, pp. 1273–1285. DOI: 10.1016/0016-7037(64)90129-2.

Thuróczy, C.-E., L. Gerringa, M. Klunder, P. Laan, and H. de Baar (2011). "Observation of consistent trends in the organic complexation of dissolved iron in the Atlantic sector of the Southern Ocean." *Deep Sea Res. Pt. II* (58) 25, pp. 2695–2706. DOI: 10.1016/j.dsr2.2011.01.002.

Toner, B. M., S. C. Fakra, S. J. Manganini, C. M. Santelli, M. A. Marcus, J. W. Moffett, O. Rouxel, C. R. German, and K. J. Edwards (2009). "Preservation of iron (II) by carbon-rich matrices in a hydrothermal plume." *Nat. Geosci.* (2) 3, pp. 197–201. DOI: 10.1038/ngeo433.

Trenberth, K. E., W. G. Large, and J. G. Olson (1990). "The mean annual cycle in global ocean wind stress." *J. Phys. Oceanogr.* (20) 11, pp. 1742–1760. DOI: 10.1175/1520-0485(1990)020<1742:TMACIG>2.0.CO;2.

Van den Berg, C. M. G. (2006). "Chemical speciation of iron in seawater by cathodic stripping voltammetry with dihydroxynaphthalene." *Anal. Chem.* (78) 1, pp. 156–163. DOI: 10.1021/ac051441+.

Van der Merwe, P., D. Lannuzel, A. R. Bowie, and K. M. Meiners (2011). "High temporal resolution observations of spring fast ice melt and seawater iron enrichment in East Antarctica." *J. Geophys. Res.* (116) G3. DOI: 10.1029/2010JG001628.

Völker, C. and A. Tagliabue (2014). "Modelling organic iron-binding ligands in a three-dimensional biogeochemical ocean model." *Mar. Chem.* DOI: 10.1016/j.marchem.2014.11.008.

Wadley, M. R., T. D. Jickells, and K. J. Heywood (2014). "The role of iron sources and transport for Southern Ocean productivity." *Deep Sea Res. Pt I* (87), pp. 82–94. DOI: DOI:10.1016/j.dsr.2014.02.003.

Wagener, T., C. Guieu, R. Losno, S. Bonnet, and N. Mahowald (2008). "Revisiting atmospheric dust export to the Southern Hemisphere ocean: Biogeochemical implications." *Global Biogeochem. Cy.* (22) GB2006. DOI: 10.1029/2007GB002984.

Wang, S., D. Bailey, K. Lindsay, J. K. Moore, and M. Holland (2014). "Impact of sea ice on the marine iron cycle and phytoplankton productivity." *Biogeosciences* (11) 17, pp. 4713–4731. DOI: 10.5194/bg-11-4713-2014.

Watson, A. J., D. C. E. Bakker, A. J. Ridgwell, P. W. Boyd, and C. S. Law (2000). "Effect of iron supply on Southern Ocean CO_2 uptake and implications for glacial atmospheric CO_2." *Nature* (407) 6805, pp. 730–733. DOI: 10.1038/35037561.

Westerlund, S. and P. Öhman (1991). "Iron in the water column of the Weddell Sea." *Mar. Chem.* (35) 1, pp. 199–217. DOI: 10.1016/S0304-4203(09)90018-4.

Wu, J., E. Boyle, W. Sunda, and L.-S. Wen (2001). "Soluble and colloidal iron in the oligotrophic North Atlantic and North Pacific." *Science* (293) 5531, pp. 847–849. DOI: 10.1126/science.1059251.

Yool, A., E. E. Popova, and T. R. Anderson (2011). "Medusa-1.0: a new intermediate complexity plankton ecosystem model for the global domain." *Geosci. Model Dev.* (4), pp. 381–417. DOI: 10.5194/gmd-4-381-2011.

2 MODELS

2.1 UNSTRUCTURED GRID MODELING

Global Ocean General Circulation Biogeochemical Models (OGCBMs) are sophisticated tools, routinely used to investigate the dynamics of the earth system. They can be used to examine the mechanisms behind current trends, for example CO_2-uptake in the Southern Ocean (e.g. Hauck et al., 2013; Frölicher et al., 2015), or to evaluate the effect of future increasing temperatures on marine phytoplankton (e.g. Bopp et al., 2013; Moore et al., 2013b; Vancoppenolle et al., 2013).

The results of the biogeochemical components are sensitive to the representation of the ocean circulation, which for example influences the amount of nutrients brought to the surface water through upwelling and vertical mixing (e.g. Sinha et al., 2010). The Mixed Layer Depth (MLD) is an especially important feature because it affects the amount of radiation available for photosynthesis as well as the entrainment of nutrients to the surface water (e.g. Williams and Follows, 2003). This is particularly true for the Southern Ocean where models differ significantly regarding the mixed layer depth and biological production (e.g. Doney et al., 2004; Najjar et al., 2007).

Currently, global OGCBMs are solely applied on quasi-regular meshes, offering stable and well tested model environments (e.g. Moore et al., 2004; Aumont and Bopp, 2006). Large efforts are nevertheless continuously made to improve the representation of the ocean circulation in the models. This includes utilization of new modeling techniques. An example of this is the global isopycnal OGCBM from Bergen (Assmann et al., 2010), where the distribution of the z-coordinates depend on the density structure of the water column, allowing for a more natural vertical division than the traditionally fixed intervals (Griffies et al., 2009).

Another possibility is the usage of a model running on an unstructured grid (e.g. Danilov, 2013; Ringler et al., 2013). The core strength of a model employing an unstructured grid is the ability to highly resolve chosen areas, while providing seamless transition to areas of lower resolution (Pain et al., 2005). High resolution can for example be an advantage in places with strong ocean currents, such as the Antarctic Circumpolar Current (ACC) or around the equator. Resolving the shelf breaks could improve the description of bottom water formation around Antarctica (e.g. Matsumura and Hasumi, 2010; Haid and Timmermann, 2013). The flow through narrow straits impacts the circulation of the open ocean, and a high resolution here may therefore also be an advantage (e.g. Wekerle et al., 2013). The advantages of a multi-resolution grid makes it logical and intriguing to couple a biogeochemical model to an Ocean General Circulation Model (OGCM) employing an unstructured grid. This has already been done for coastal applications (e.g. Larsen et al., 2013), but so far not for a model covering the global domain. A reason for this is the increased computational demand an unstructured mesh model adds, especially when using the finite element method for discretization (Danilov, 2013). This is a practical feature that becomes all the more important in a global OGCBM as the biogeochemical component introduces a significant number of tracers, which makes it computationally

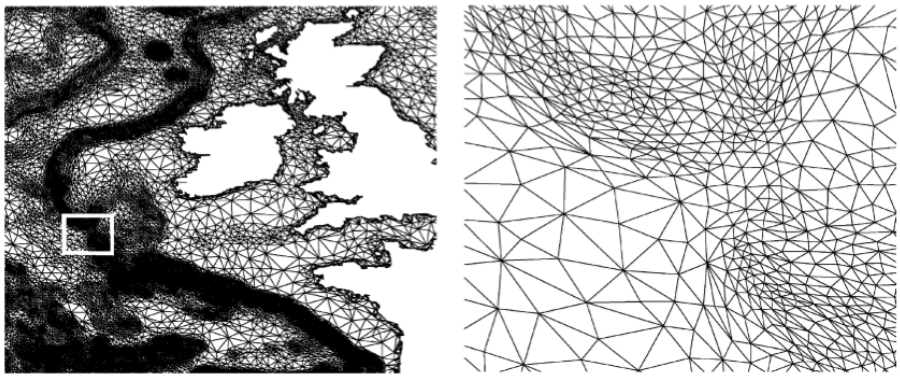

Figure 2.1: Left) Example of an unstructured and triangulated surface mesh in the North Atlantic. Right) A blow-up of the Celtic shelf break where higher resolution is applied (From Pain et al., 2005).

demanding from the outset. The ability to add high resolution locally does indeed save computer time, but it also adds the requirement of a smaller time step.

Another aspect of coupling a biogeochemical model to an ocean model based on the unstructured mesh technology is that a global OGCM with satisfying skill must exist for such a coupling. At the Alfred-Wegener-Institute, such a model exists in the Finite Element Sea-ice Ocean Model (FESOM).

2.2 THE FINITE ELEMENT SEA-ICE OCEAN MODEL

FESOM is a global 3-dimensional OGCM, coupled to a sea-ice model. Discretization is carried out employing the finite element methodology, and FESOM runs on a triangulated unstructured grid. The model has been developed in the Climate Dynamics group at the Alfred Wegener Institute in Bremerhaven, Germany. It is based on the Finite Element Model of the North Atlantic (Danilov et al., 2004), which has been further developed for the global setup and coupled to a sea-ice model (Timmermann et al., 2009). The newest version of FESOM (v. 1.4) is comprehensively described by Wang et al. (2014). FESOM is participating in the Coordinated Ocean-ice Reference Experiments (COREs) introduced by Griffies et al. (2009). Here, the performance of a number of coupled sea-ice ocean models are evaluated on the global scale (Griffies et al., 2009; Sidorenko et al., 2011) and in local ocean basins such as the North Atlantic (Danabasoglu et al., 2014) and the Southern Ocean (Downes et al., 2014).

FESOM solves the standard set of hydrostatic primitive equations under the Boussinesq approximations in a global setting. The governing equations are divided into a dynamical and a thermodynamical part, which are solved separately, divided by a lag of half a time step (Wang et al., 2008). Further information about the numerics of FESOM can be found in Danilov et al. (2004) and Wang et al. (2014), while the sea-ice component is described in detail by Timmermann et al. (2009).

FESOM is forced with the CORE-datasets, which entail the atmospheric fields needed to calculate air-sea fluxes of heat, fresh water and momentum (Large and Yeager, 2004; Large and Yeager, 2009). These datasets are based on the NCEP reanalysis data, which has been adjusted towards observations to reduce biases. The datasets were specifically developed for coupled sea-ice ocean models and therefore pay special

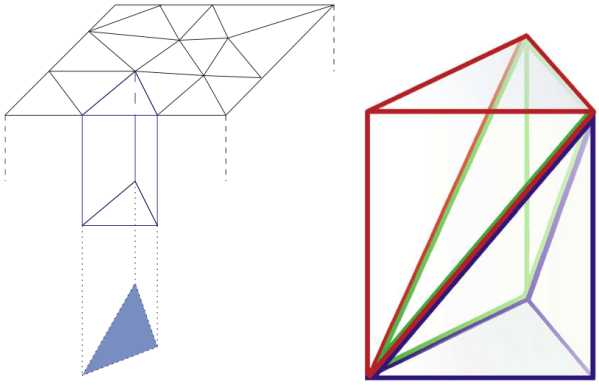

Figure 2.2: Left) Illustration of FESOM's vertically stratified and horizontally unstructured grid. Right) Division of a prism into tetrathedra (From Timmermann et al., 2009).

attention to the conservation of heat and freshwater on a global scale. The CORE-forcing used in the current thesis consists of a normal year climatology (CORE-I), which is based on the years 1948 to 2000 (Large and Yeager, 2004), and of an inter annually varying dataset (CORE-II) covering 1948 to 2008 (Large and Yeager, 2009). The forcing is provided on a grid with an approximate resolution of $1.875° \times 1.915°$. When running FESOM under the CORE forcing, it is interpolated onto the grid used by FESOM.

FESOM runs on a mesh that is vertically stratified and horizontally triangulated and unstructured. The mesh thus consist of prisms, which are further divided into tetrahedra (Fig. 2.2). This structure means that optimized meshes can be created for different studies. Recent applications of FESOM utilizing the unstructured mesh include a study of the importance of high resolution in the Canadian Arctic through-flow (Wekerle et al., 2013), a study of bottom water formation in the Weddell Sea (Haid and Timmermann, 2013) and of future melting of the Antarctic ice sheet (Hellmer et al., 2012).

2.3 THE REGULATED ECOSYSTEM MODEL

Marine phytoplankton plays an important role in the global carbon cycle as it is responsible of up to half of the global primary production (e.g. Field et al., 1998). Understanding the mechanisms behind phytoplankton growth, and thus carbon fixation, is therefore important in order to predict the response of the global carbon cycle to climate change. One way to gain further understanding is through the use of OGCBMs, which can calculate the complex interplay between biogeochemical fluxes and the oceanic and atmospheric circulation.

Biogeochemical models describe biogeochemical processes through parameterizations; mathematical equations that describe observations from the laboratory or the field to a satisfying degree. Biogeochemical processes are, however, highly complex, and the parameterizations thus represent strongly simplified versions of reality.

Marine phytoplankton growth is constrained by the availability of light (e.g. Strzepek et al., 2012) and nutrients (e.g. Moore et al., 2013a), and by the presence of grazers (e.g. Cavender-Bares et al., 1999). These factors are therefore an integral part of biogeochemical models. To simplify the dependence of the phytoplankton growth rate

on the availability of various nutrients in global OGCBMs, they commonly rely on the Redfield ratio, namely the notion that the intracellular C:N:P molar ratio in phytoplankton can be described by a constant 106:16:1 ratio (Redfield, 1958). It implies that growth is limited by a single nutrient, thereby simplifying the models substantially both in the growth parameterization and in the computational efficiency (O'Neill et al., 1989). The latter because it means that the phytoplankton concentration in the water can be described by a single value, rather than a value for each of the elements contained in the phytoplankton. The Redfield ratio can be extended to also encompass other nutrients, such as silicon and iron, which are important on the global scale; silicon is needed by diatoms (e.g. Dugdale and Wilkerson, 1998), and iron limits production in large parts of the ocean, such as the Southern and the North and Equatorial Pacific Ocean, where the external iron input is relatively small (e.g. Martin et al., 1991; Kolber et al., 1994; Martin and Fitzwater, 1988). These nutrients have therefore also been implemented into global biogeochemical models (e.g. Moore et al., 2002; Aumont et al., 2003).

In reality, however, the intracellular nutrient stoichiometry is not constant. This was first proven by Ketchum (1939) and Kuenzler and Ketchum (1962) who showed that marine phytoplankton are able perform luxury uptake of phosphorous. In his original paper, Redfield (1958) likewise pointed out that the reported C:N:P ratio was an average and that it does in fact vary significant in nature. Variable stoichiometry was first described in a biochemical model when Droop (1968) pioneered the concept of the cell quota. He showed that the growth rate of a B12-limited phytoplankton species was dependent on the cell to B12 quota, rather than just on the B12 concentration (Fig. 2.3). The cell quota model has later been shown to hold for many different nutrients and organisms (e.g. Droop, 1983, Table 1), and has thus provided the basis for later biogeochemical models including variable stoichiometry. Geider et al. (1998) developed a model with variable intracellular stoichiometry, allowing for variable C:Chl and C:N ratios. This framework has been used in a number of cell models (e.g. Armstrong, 1999; Flynn, 2001), as well in a number of global biogeochemical ocean circulation models (e.g. Moore et al., 2002; Vichi et al., 2007). For global models, the varying stoichiometry has been extended to encompass other important nutrients such as silicon and iron (Aumont and Bopp, 2006; Vichi et al., 2007).

At the Alfred Wegener Institute, the Regulated Ecosystem Model (REcoM) was first developed to reproduce conditions in mesocosm experiments (Schartau et al., 2007). It is based on the model from Geider et al. (1998) and does thus entail variable stoichiometry. The original version (Schartau et al., 2007) was based on dissolved inorganic nitrogen as the only limiting nutrient, but has later been extended to also describe the silicon cycle (Hohn, 2009) and a simple iron cycle based on Parekh et al. (2005). REcoM was extended to cover the global ocean as it was coupled to the Massachusetts Institute of Technology general circulation model (MITgcm, Hohn, 2009). In this configuration it has mainly been used to investigate the carbon cycle in the Southern Ocean (e.g. Hauck et al., 2013; Taylor et al., 2013; Losch et al., 2014)

In the Southern Ocean, variable stoichiometry is especially important as the intracellular C:Si ratio in the phytoplankton is coupled to the availability of iron (e.g. Hutchins and Bruland, 1998; Takeda, 1998), which limits production in large parts of the Southern Ocean (e.g. Martin et al., 1990; Martin et al., 1991). Adaptation in the C:Si therefore has an impact on the export of silicon to the deep ocean in the area.

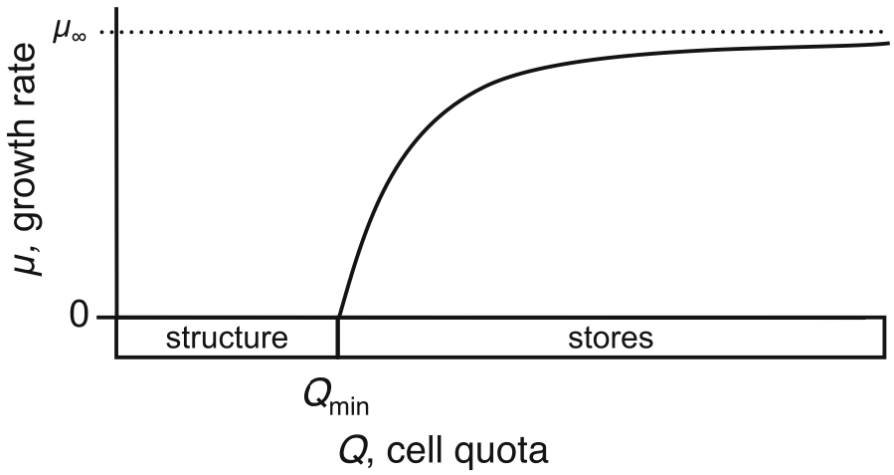

Figure 2.3: The cell quota model proposed by Droop (1968). The growth rate is dependent on the cell quota, with Q_{min} being the minimum quota necessary for life. The maximum specific growth rate (μ_∞) is asymptotically approached as the cell quota increases (From Klausmeier et al., 2008).

In a global model, the choice between variable and constant stoichiometry is however always a balance between the advantage that the complexity provides in terms of reproducing the biogeochemistry and the complexity it adds to the calculations and thus the computational burden. The latter becomes even more important when the OGCM is computationally expensive to run, such as is the case in finite element model.

REFERENCES

Armstrong, R. A. (1999). "An optimization-based model of iron-light-ammonium colimitation of nitrate uptake and phytoplankton growth." *Limnol. Oceanogr.* (44) 6, pp. 1436–1446.

Assmann, K., M. Bentsen, J. Segschneider, and C. Heinze (2010). "An isopycnic ocean carbon cycle model." *Geosci. Model Dev.* (3), pp. 143–167. DOI: 10.5194/gmd-3-143-2010.

Aumont, O. and L. Bopp (2006). "Globalizing results from ocean in situ iron fertilization studies." *Global Biogeochem. Cy.* (20) GB2017. DOI: 10.1029/2005GB002591.

Aumont, O., E. Maier-Reimer, S. Blain, and P. Monfray (2003). "An ecosystem model of the global ocean including Fe, Si, P colimitations." *Global Biogeochem. Cy.* (17) 2. DOI: 10.1029/2001GB001745.

Bopp, L., L. Resplandy, J. Orr, S. C. Doney, J. P. Dunne, M. Gehlen, P. Halloran, C. Heinze, T. Ilyina, R. Séférian, et al. (2013). "Multiple stressors of ocean ecosystems in the 21st century: projections with CMIP5 models." *Biogeosciences* (10) 10, pp. 6225–6245. DOI: 10.5194/bg-10-6225-2013.

Cavender-Bares, K. K., E. L. Mann, S. W. Chisholm, M. E. Ondrusek, and R. R. Bidigare (1999). "Differential response of equatorial Pacific phytoplankton to iron fertilization." *Limnol. Oceanogr.* (44) 2, pp. 237–246.

Danabasoglu, G., S. G. Yeager, D. Bailey, E. Behrens, M. Bentsen, D. Bi, A. Biastoch, C. Böning, A. Bozec, V. M. Canuto, C. Cassou, E. Chassignet, A. C. Coward, S. Danilo,

N. Diansky, H. Drange, R. Farneti, E. Fernandez, P. G. Fogli, G. Forget, Y. Fujii, S. M. Griffies, A. Gusev, P. Heimbach, A. Howard, T. Jung, M. Kelley, W. G. Large, A. Leboissetier, J. Lu, G. Madec, S. J. Marsland, S. Masina, A. Navarra, A. J. G. Nurser, A. Pirani, D. Salas y Mélia, B. L. Samuels, M. Scheinert, D. Sidorenko, A.-M. Treguier, H. Tsujino, P. Uotila, S. Valcke, A. Voldoire, and Q. Wang (2014). "North Atlantic simulations in coordinated ocean-ice reference experiments phase II (CORE-II). Part I: Mean states." *Ocean Model.* (73), pp. 76–107. DOI: 10.1016/j.ocemod.2013.10.005.

Danilov, S. (2013). "Ocean modeling on unstructured meshes." *Ocean Model.* (69), pp. 195–210. DOI: 10.1016/j.ocemod.2013.05.005.

Danilov, S., G. Kivman, and J. Schröter (2004). "A finite-element ocean model: principles and evaluation." *Ocean Model.* (6) 2, pp. 125–150. DOI: 10.1016/S1463-5003(02)00063-X.

Doney, S. C., K. Lindsay, K. Caldeira, J.-M. Campin, H. Drange, J.-C. Dutay, M. Follows, Y. Gao, A. Gnanadesikan, N. Gruber, A. Ishida, F. Joos, G. Madec, E. Maier-Reimer, J. C. Marshall, R. J. Matear, P. Monfray, A. Mouchet, R. Najjar, J. C. Orr, G. K. Plattner, J. L. Sarmiento, R. Schlitzer, R. D. Slater, I. J. Totterdell, M. F. Weirig, Y. Yamanaka, and A. Yool (2004). "Evaluating global ocean carbon models: The importance of realistic physics." *Global Biogeochem. Cy.* (18) GB3017. DOI: 10.1029/2003GB002150.

Downes, S., R. Farneti, P. Uotilac, S. M. Griffies, S. Marsland, D. Bailey, E. Behrens, M. Bentsen, D. Bi, A. Biastoch, C. Böning, A. Bozec, E. Chassignet, G. Danabasoglu, S. Danilov, N. Diansky, H. Drange, P. G. Fogli, A. Gusev, A. Howard, M. Illicak, T. Jung, M. Kelley, W. G. Large, A. Leboissetiero, M. Long, J. Lu, S. Masina, A. Mishra, A. Navarra, A. J. G. Nurserp, L. Patara, B. L. Samuels, D. Sidorenko, P. Spence, H. Tsujino, Q. Wang, and S. G. Yeager (2014). "An assessment of Southern Ocean water masses and sea-ice during 1988-2007 in a suite of inter-annual CORE-II simulations." *submitted to Clim. Dynam.*

Droop, M. (1968). "Vitamin B12 and marine ecology. IV. The kinetics of uptake, growth and inhibition in Monochrysis lutheri." *J. Mar. Biol. Assoc. UK* (48) 3, pp. 689–733. DOI: 10.1017/S0025315400019238.

Droop, M. (1983). "25 Years of Algal Growth Kinetics. A Personal View." *Bot. Mar.* (26) 3, pp. 99–112. DOI: 10.1515/botm.1983.26.3.99.

Dugdale, R. C. and F. P. Wilkerson (1998). "Silicate regulation of new production in the equatorial Pacific upwelling." *Nature* (391) 6664, pp. 270–273. DOI: 10.1038/34630.

Field, C. B., M. J. Behrenfeld, J. T. Randerson, and P. Falkowski (1998). "Primary production of the biosphere: integrating terrestrial and oceanic components." *Science* (281) 5374, pp. 237–240. DOI: 10.1126/science.281.5374.237.

Flynn, K. J. (2001). "A mechanistic model for describing dynamic multi-nutrient, light, temperature interactions in phytoplankton." *J. Plankton Res.* (23) 9, pp. 977–997. DOI: 10.1093/plankt/23.9.977.

Frölicher, T. L., J. L. Sarmiento, D. J. Paynter, J. P. Dunne, J. P. Krasting, and M. Winton (2015). "Dominance of the Southern Ocean in anthropogenic carbon and heat uptake in CMIP5 models." *J. Climate* (28) 2, pp. 862–886. DOI: 10.1175/JCLI-D-14-00117.1.

Geider, R. J., H. L. MacIntyre, and T. M. Kana (1998). "A dynamic regulatory model of phytoplanktonic acclimation to light, nutrients, and temperature." *Limnol. Oceanogr.* (43) 4, pp. 679–694. DOI: 10.4319/lo.1998.43.4.0679.

Griffies, S. M., A. Biastoch, C. Böning, F. Bryan, G. Danabasoglu, E. P. Chassignet, M. H. England, R. Gerdes, H. Haak, R. W. Hallberg, W. Hazeleger, J. Jungclaus, W. G. Large, G. Madec, A. Pirani, B. L. Samuels, M. Scheinert, A. S. Gupta, C. A. Severijns, H. L. Simmons, A. M. Treguier, M. Winton, S. Yeager, and J. Yin (2009). "Coordinated ocean-ice reference experiments (COREs)." *Ocean Model.* (26) 1, pp. 1–46. DOI: 10.1016/j.ocemod.2008.08.007.

Haid, V. and R. Timmermann (2013). "Simulated heat flux and sea ice production at coastal polynyas in the southwestern Weddell Sea." *J. Geophys. Res* (118), pp. 2640–2652. DOI: 10.1002/jgrc.20133.

Hauck, J., C. Völker, T. Wang, M. Hoppema, M. Losch, and D. A. Wolf-Gladrow (2013). "Seasonally different carbon flux changes in the Southern Ocean in response to the Southern Annular Mode." *Global Biogeochem. Cy.* (27), pp. 1–10. DOI: 10.1002/2013GB004600.

Hellmer, H. H., F. Kauker, R. Timmermann, J. Determann, and J. Rae (2012). "Twenty-first-century warming of a large Antarctic ice-shelf cavity by a redirected coastal current." *Nature* (485) 7397, pp. 225–228. DOI: 10.1038/nature11064.

Hohn, S. (2009). "Coupling and decoupling of biogeochemical cycles in marine ecosystems." PhD thesis. Bremen University, Germany.

Hutchins, D. A. and K. W. Bruland (1998). "Iron-limited diatom growth and Si: N uptake ratios in a coastal upwelling regime." *Nature* (393) 6685, pp. 561–564.

Ketchum, B. H. (1939). "The absorption of phosphate and nitrate by illuminated cultures of Nitzschia closterium." *Am. J. Bot.* Pp. 399–407.

Klausmeier, C. A., E. Litchman, T. Daufresne, and S. Levin (2008). "Phytoplankton stoichiometry." *Ecol. Res.* (23) 3, pp. 479–485. DOI: 10.1007/s11284-008-0470-8.

Kolber, Z. S., R. T. Barber, K. H. Coale, S. E. Fitzwateri, R. M. Greene, K. S. Johnson, S. Lindley, and P. G. Falkowski (1994). "Iron limitation of phytoplankton photosynthesis in the equatorial Pacific Ocean." *Nature* (371) 6493, pp. 145–149. DOI: 10.1038/371145a0.

Kuenzler, E. J. and B. H. Ketchum (1962). "Rate of phosphorus uptake by Phaeodactylum tricornutum." *Biol. Bull.* (123) 1, pp. 134–145.

Large, W. G. and S. G. Yeager (2004). *Diurnal to Decadal Global Forcing for Oceans and Sea-Ice Models: The Data Sets and Flux Climatologies, NCAR/TN-460+STR*. Tech. rep. Boulder, Colorado: National Center for Atmospheric Research.

Large, W. G. and S. G. Yeager (2009). "The global climatology of an interannually varying air–sea flux data set." *Clim. Dynam.* (33) 2-3, pp. 341–364. DOI: 10.1007/s00382-008-0441-3.

Larsen, J., C. Mohn, and K. Timmermann (2013). "A novel model approach to bridge the gap between box models and classic 3D models in estuarine systems." *Ecol. Model.* (266), pp. 19–29. DOI: 10.1016/j.ecolmodel.2013.06.030.

Losch, M., V. Strass, B. Cisewski, C. Klaas, and R. G. Bellerby (2014). "Ocean state estimation from hydrography and velocity observations during EIFEX with a regional biogeochemical ocean circulation model." *J. Mar. Sys.* (129), pp. 437–451. DOI: 10.1016/j.jmarsys.2013.09.003.

Martin, J. H., S. E. Fitzwater, and R. M. Gordon (1990). "Iron deficiency limits phytoplankton growth in Antarctic waters." *Global Biogeochem. Cy.* (4) 1, pp. 5–12. DOI: 10.1029/GB004i001p00005.

Martin, J. H. and S. Fitzwater (1988). "Iron deficiency limits phytoplankton growth in the north-east Pacific subarctic." *Nature* (331), pp. 341–343. DOI: 10.1038/331341a0.

Martin, J. H., R. M. Gordon, and S. E. Fitzwater (1991). "The case for iron." *Limnol. Oceanogr.* (36) 8.

Matsumura, Y. and H. Hasumi (2010). "Modeling ice shelf water overflow and bottom water formation in the southern Weddell Sea." *J. Geophys. Res.* (115) C10. DOI: 10.1029/2009JC005841.

Moore, C. M., M. M. Mills, K. R. Arrigo, I. Berman-Frank, L. Bopp, P. W. Boyd, E. D. Galbraith, R. J. Geider, C. Guieu, S. L. Jaccard, T. D. Jickells, J. La Roche, T. M. Lenton, N. M. Mahowald, E. Marañon, J. Marinov, J. K. Moore, T. Nakatsuka, A. Oschlies, M. A. Saito, T. F. Thingstad, A. Tsuda, and O. Ulloa (2013a). "Processes and patterns of oceanic nutrient limitation." *Nat. Geosci.* (6) 9, pp. 701–710. DOI: 10.1038/NGEO1765.

Moore, J. K., S. C. Doney, and K. Lindsay (2004). "Upper ocean ecosystem dynamics and iron cycling in a global three-dimensional model." *Global Biogeochem. Cy.* (18) GB4028. DOI: 10.1029/2004GB002220.

Moore, J. K., S. C. Doney, D. M. Glover, and I. Y. Fung (2002). "Iron cycling and nutrient-limitation patterns in surface waters of the World Ocean." *Deep-Sea Res. Pt. II* (49) 1, pp. 463–507. DOI: 10.1016/S0967-0645(01)00109-6.

Moore, J. K., K. Lindsay, S. C. Doney, M. C. Long, and K. Misumi (2013b). "Marine ecosystem dynamics and biogeochemical cycling in the community earth system model [CESM1 (BGC)]: comparison of the 1990s with the 2090s under the RCP4.5 and RCP8.5 Scenarios." *J. Climate* (26) 23, pp. 9291–9312. DOI: 10.1175/JCLI-D-12-00566.1.

Najjar, R. G., X. Jin, F. Louanchi, O. Aumont, K. Caldeira, S. C. Doney, J.-C. Dutay, M. Follows, N. Gruber, F. Joos, K. Lindsay, E. Maier-Reimer, R. J. Matear, K. Matsumoto, P. Monfray, A. Mouchet, J. C. Orr, G.-K. Plattner, J. L. Sarmiento, R. Schlitzer, R. D. Slater, M.-F. Weirig, Y. Yamanaka, and A. Yool (2007). "Impact of circulation on export production, dissolved organic matter, and dissolved oxygen in the ocean: Results from Phase II of the Ocean Carbon-cycle Model Intercomparison Project (OCMIP-2)." *Global Biogeochem. Cy.* (21) GB3007. DOI: 10.1029/2006GB002857.

O'Neill, R. V., D. L. DeAngelis, J. J. Pastor, B. J. Jackson, and W. M. Post (1989). "Multiple nutrient limitations in ecological models." *Ecol. Model.* (46) 3, pp. 147–163. DOI: 10.1016/0304-3800(89)90015-X.

Pain, C. C., M. D. Piggott, A. J. H. Goddard, F. Fang, G. J. Gorman, D. P. Marshall, M. D. Eaton, P. W. Power, and C. R. E. De Oliveira (2005). "Three-dimensional unstructured mesh ocean modelling." *Ocean Model.* (10) 1, pp. 5–33. DOI: 10.1016/j.ocemod.2004.07.005.

Parekh, P., M. J. Follows, and E. A. Boyle (2005). "Decoupling of iron and phosphate in the global ocean." *Global Biogeochem. Cy.* (19) GB2020. DOI: 10.1029/2004GB002280.

Redfield, A. C. (1958). "The biological control of chemical factors in the environment." *Am. sci.* 230A–221.

Ringler, T., M. Petersen, R. L. Higdon, D. Jacobsen, P. W. Jones, and M. Maltrud (2013). "A multi-resolution approach to global ocean modeling." *Ocean Model.* (69), pp. 211–232. DOI: 10.1016/j.ocemod.2013.04.010.

Schartau, M., A. Engel, J. Schröter, S. Thoms, C. Völker, and D. A. Wolf-Gladrow (2007). "Modelling carbon overconsumption and the formation of extracellular particulate organic carbon." *Biogeosciences* (4) 4, pp. 433–454. DOI: 10.5194/bg-4-433-2007.

Sidorenko, D., Q. Wang, S. Danilov, and J. Schröter (2011). "FESOM under coordinated ocean-ice reference experiment forcing." *Ocean Dynam.* (61) 7, pp. 881–890. DOI: 10.1007/s10236-011-0406-7.

Sinha, B., E. T. Buitenhuis, C. L. Quéré, and T. R. Anderson (2010). "Comparison of the emergent behavior of a complex ecosystem model in two ocean general circulation models." *Progr. Ocean.* (84) 3, pp. 204–224. DOI: 10.1016/j.pocean.2009.10.003.

Strzepek, R. F., K. A. Hunter, R. D. Frew, P. J. Harrison, and P. W. Boyd (2012). "Iron-light interactions differ in Southern O cean phytoplankton." *Limnol. Oceanogr.* (57) 4, p. 1182. DOI: 10.4319/lo.2012.57.4.1182.

Takeda, S. (1998). "Influence of iron availability on nutrient consumption ratio of diatoms in oceanic waters." *Nature* (393) 6687, pp. 774–777. DOI: 10.1038/31674.

Taylor, M. H., M. Losch, and A. Bracher (2013). "On the drivers of phytoplankton blooms in the Antarctic marginal ice zone: A modeling approach." *J. Geophys. Res* (118), pp. 63–75. DOI: 10.1029/2012JC008418.

Timmermann, R., S. Danilov, J. Schröter, C. Böning, D. Sidorenko, and K. Rollenhagen (2009). "Ocean circulation and sea ice distribution in a finite element global sea ice–ocean model." *Ocean Model.* (27) 3, pp. 114–129. DOI: 10.1016/j.ocemod.2008.10.009.

Vancoppenolle, M., L. Bopp, G. Madec, J. P. Dunne, T. Ilyina, P. R. Halloran, and N. Steiner (2013). "Future Arctic Ocean primary productivity from CMIP5 simulations: Uncertain outcome, but consistent mechanisms." *Global Biogeochem. Cy.* (27) 3, pp. 605–619. DOI: 10.1002/gbc.20055.

Vichi, M., N. Pinardi, and S. Masina (2007). "A generalized model of pelagic biogeochemistry for the global ocean ecosystem. Part I: Theory." *J. Mar. Sys.* (64) 1, pp. 89–109. DOI: 10.1016/j.jmarsys.2006.03.006.

Wang, Q., S. Danilov, and J. Schröter (2008). "Finite element ocean circulation model based on triangular prismatic elements, with application in studying the effect of topography representation." *J. Geophys. Res* (113) C0515. DOI: 10.1029/2007JC004482.

Wang, Q., S. Danilov, D. Sidorenko, R. Timmermann, C. Wekerle, X. Wang, T. Jung, and J. Schröter (2014). "The Finite Element Sea Ice-Ocean Model (FESOM) v.1.4: formulation of an ocean general circulation model." *Geosci. Model Dev.* (7) 2, pp. 663–693. DOI: 10.5194/gmd-7-663-2014.

Wekerle, C., Q. Wang, S. Danilov, T. Jung, and J. Schröter (2013). "The Canadian Arctic Archipelago throughflow in a multiresolution global model: Model assessment and the driving mechanism of interannual variability." *J. Geophys. Res* (118), pp. 4525–4541. DOI: 10.1002/jgrc.20330.

Williams, R. G. and M. J. Follows (2003). *Ocean Biogeochemistry*. Springer, pp. 19–51.

3 OUTLINE OF THESIS

In the Southern Ocean, the micronutrient iron plays a large role for the control of net primary production. Knowledge about the input of iron to the Southern Ocean mixed layer and their impact on biological production come from a wide variety of observations (e.g. Blain et al., 2001; Wagener et al., 2008; van der Merwe et al., 2011), but due to the inaccessibility and size of the Southern Ocean, Global Ocean General Circulation Biogeochemical Models (OGCBMs) are commonly used for large scale studies of the impact of the different iron sources on biological production in the Southern Ocean (e.g. Lancelot et al., 2009; Tagliabue et al., 2009; Wadley et al., 2014). But while these models are sophisticated tools that give an insight into the large scale dynamics that can not be gained through observations, they are heavily dependent on parameterization of processes that are not resolved in them as well as on tuning towards a realistic state. Understanding how the models affect the results is therefore important before drawing conclusions from the model results.

The aim of this thesis is to gain an understanding of the relative importance of the different iron sources to the Southern Ocean, and to what extend the state of the ocean model and the parameterization and tuning of the iron cycle in the biogeochemical model affects the representation of the iron sources.

To explore the significance of the input of different iron sources in a model on the phytoplankton composition, the Finite Element Sea-ice Ocean Model (FESOM) has been coupled to the Regulated Ecosystem Model (REcoM2). Before using a newly coupled model for research, the skill of the coupled model must be assessed against observational data. This assessment is first of all to see how well the model performs, but also to gain an understanding of the weaker sides of the model. In publication I, the coupled model is presented, and a skill assessment is performed with a special focus on the iron cycle and the Southern Ocean.

Traditionally, most research focussing on the iron input to the Southern Ocean has concentrated on the external sources, such as the sediment and the dust source. But as biological production occurs in the surface mixed layer, the vertical supply of iron across the base of the mixed layer may likewise play a large role (e.g. Tagliabue et al., 2014). Southern Ocean net primary and export production (NPP and EP) calculated in OGCBMs is very dependent on the state of the ocean circulation model (Doney et al., 2004; Najjar et al., 2007). One factor that may play a role in this is the vertical iron supply. Publication II presents two model runs with REcoM2 coupled to FESOM and to the Massachusetts Institute of Technology general circulation model (MITgcm). The results of the model runs are analyzed regarding the vertical iron fluxes in the seasonal and spatial domain. It is further discussed how the ocean general circulation model also has an impact on the total NPP and EP as well as on the phytoplankton composition.

The sediment source of iron has repeatedly been argued to dominate the iron input to the Southern Ocean (Lancelot et al., 2009; Tagliabue et al., 2009; Wadley et al., 2014). In publication III it is investigated to what degree the strength of the sediment source affects the modeled phytoplankton composition and distribution.

As the strength of the sediment source varies widely between measurements, it is discussed how changes in modeled phytoplankton composition and opal export can be used to determine an appropriate strength of the sediment source for OGCBMs.

In the general discussion, the relative contribution of iron from the sediments and from below to the surface mixed layer of the Southern Ocean is debated based on publication II and III. It is further discussed how future increased temperatures are likely to change the strength of all of the iron sources, thereby affecting the biological production.

For the new FESOM-REcoM2 model many future research directions are possible, both regarding the iron sources in the Southern Ocean, and regarding other topics. Some future directions are suggested in the end of the thesis.

REFERENCES

Blain, S., P. Tréguer, S. Belviso, E. Bucciarelli, M. Denis, S. Desabre, M. Fiala, V. Martin Jézéquel, J. Le Fèvre, P. Mayzaud, J.-C. Marty, and S. Razouls (2001). "A biogeochemical study of the island mass effect in the context of the iron hypothesis: Kerguelen Islands, Southern Ocean." *Deep Sea Res. Pt. I* (48) 1, pp. 163–187. DOI: 10.1016/S0967-0637(00)00047-9.

Doney, S. C., K. Lindsay, K. Caldeira, J.-M. Campin, H. Drange, J.-C. Dutay, M. Follows, Y. Gao, A. Gnanadesikan, N. Gruber, A. Ishida, F. Joos, G. Madec, E. Maier-Reimer, J. C. Marshall, R. J. Matear, P. Monfray, A. Mouchet, R. Najjar, J. C. Orr, G. K. Plattner, J. L. Sarmiento, R. Schlitzer, R. D. Slater, I. J. Totterdell, M. F. Weirig, Y. Yamanaka, and A. Yool (2004). "Evaluating global ocean carbon models: The importance of realistic physics." *Global Biogeochem. Cy.* (18) GB3017. DOI: 10.1029/2003GB002150.

Lancelot, C., A. de Montety, H. Goosse, S. Becquevort, V. Schoemann, B. Pasquer, and M. Vancoppenolle (2009). "Spatial distribution of the iron supply to phytoplankton in the Southern Ocean: a model study." *Biogeosciences* (6) 12, pp. 2861–2878. DOI: 10.5194/bg-6-2861-2009.

Najjar, R. G., X. Jin, F. Louanchi, O. Aumont, K. Caldeira, S. C. Doney, J.-C. Dutay, M. Follows, N. Gruber, F. Joos, K. Lindsay, E. Maier-Reimer, R. J. Matear, K. Matsumoto, P. Monfray, A. Mouchet, J. C. Orr, G.-K. Plattner, J. L. Sarmiento, R. Schlitzer, R. D. Slater, M.-F. Weirig, Y. Yamanaka, and A. Yool (2007). "Impact of circulation on export production, dissolved organic matter, and dissolved oxygen in the ocean: Results from Phase II of the Ocean Carbon-cycle Model Intercomparison Project (OCMIP-2)." *Global Biogeochem. Cy.* (21) GB3007. DOI: 10.1029/2006GB002857.

Tagliabue, A., L. Bopp, and O. Aumont (2009). "Evaluating the importance of atmospheric and sedimentary iron sources to Southern Ocean biogeochemistry." *Geophys. Res. Lett.* (36) L13601. DOI: 10.1029/2009GL038914.

Tagliabue, A., J.-B. Sallée, A. R. Bowie, M. Lévy, S. Swart, and P. W. Boyd (2014). "Surface-water iron supplies in the Southern Ocean sustained by deep winter mixing." *Nat. Geosci.* (7), pp. 314–320. DOI: 10.1038/ngeo2101.

Van der Merwe, P., D. Lannuzel, A. R. Bowie, and K. M. Meiners (2011). "High temporal resolution observations of spring fast ice melt and seawater iron enrichment in East Antarctica." *J. Geophys. Res.* (116) G3. DOI: 10.1029/2010JG001628.

Wadley, M. R., T. D. Jickells, and K. J. Heywood (2014). "The role of iron sources and transport for Southern Ocean productivity." *Deep Sea Res. Pt I* (87), pp. 82–94. DOI: DOI:10.1016/j.dsr.2014.02.003.

Wagener, T., C. Guieu, R. Losno, S. Bonnet, and N. Mahowald (2008). "Revisiting atmospheric dust export to the Southern Hemisphere ocean: Biogeochemical implications." *Global Biogeochem. Cy.* (22) GB2006. DOI: 10.1029/2007GB002984.

Part II

PUBLICATIONS

4 LIST OF PUBLICATIONS WITH DECLARATION OF OWN CONTRIBUTION

4.1 PUBLICATION I

V. Schourup-Kristensen, D. Sidorenko, D. A. Wolf-Gladrow and C. Völker (2014): A skill assessment of REcoM2 coupled to the Finite Element Sea-ice Ocean Model (FESOM 1.3), *Geoscientific Model Development*, 7(6), pp. 2769–2802, doi:10.5194/gmd-7-2769-2014.

A manual explaining how to run the coupled FESOM-REcoM2 model and how the exchange of information between the two models is performed, was published in the supplements of this paper along with the source code for the coupled FESOM-REcoM2 model. It can be found online at: http://www.geosci-model-dev.net/7/2769/2014/gmd-7-2769-2014-supplement.zip.

I have recoded the biogeochemical model REcoM2 and coupled it to FESOM under the guidance of Dmitry Sidorenko and Christoph Völker. During this process and the consecutive tuning of the model, results were especially discussed with Sergey Danilov and Martin Losch. I have drafted the manuscript and subsequently discussed it with the co-authors.

4.2 PUBLICATION II

V. Schourup-Kristensen, J. Hauck, M. Losch, D. A. Wolf-Gladrow and C. Völker: Vertical supply of iron to the mixed layer of the Southern Ocean: The ocean model effect. *Submitted*.

The study was planned in cooperation with Christoph Völker. I carried out the model run with REcoM2 coupled to FESOM and Judith Hauck the model run with REcoM2 coupled to MITgcm. I have performed the analysis of the model output from both models, drafted the manuscript and discussed it with the co-authors.

4.3 PUBLICATION III

V. Schourup-Kristensen, D. A. Wolf-Gladrow and C. Völker: Sensitivity of Southern Ocean phytoplankton composition to changes in model iron scavenging and sediment supply. *To be submitted*.

I have coupled the biogeochemical model REcoM2 to FESOM 1.4 and performed the model runs for the study, which were planned in cooperation with Christoph Völker. I have performed the analysis of the model output from both models, drafted the manuscript and discussed it with the co-authors.

5

PUBLICATION I

Geosci. Model Dev., 7, 2769–2802, 2014
www.geosci-model-dev.net/7/2769/2014/
doi:10.5194/gmd-7-2769-2014

Geoscientific Model Development
Open Access

A skill assessment of the biogeochemical model REcoM2 coupled to the Finite Element Sea Ice–Ocean Model (FESOM 1.3)

V. Schourup-Kristensen, D. Sidorenko, D. A. Wolf-Gladrow, and C. Völker

Alfred-Wegener-Institut Helmholtz-Zentrum für Polar- und Meeresforschung, Bremerhaven, Germany

Correspondence to: V. Schourup-Kristensen (vibe.schourup-kristensen@awi.de)

Received: 13 June 2014 – Published in Geosci. Model Dev. Discuss.: 9 July 2014
Revised: 25 September 2014 – Accepted: 26 September 2014 – Published: 25 November 2014

Abstract. In coupled biogeochmical–ocean models, the choice of numerical schemes in the ocean circulation component can have a large influence on the distribution of the biological tracers. Biogeochemical models are traditionally coupled to ocean general circulation models (OGCMs), which are based on dynamical cores employing quasi-regular meshes, and therefore utilize limited spatial resolution in a global setting. An alternative approach is to use an unstructured-mesh ocean model, which allows variable mesh resolution. Here, we present initial results of a coupling between the Finite Element Sea Ice–Ocean Model (FESOM) and the biogeochemical model REcoM2 (Regulated Ecosystem Model 2), with special focus on the Southern Ocean.

Surface fields of nutrients, chlorophyll *a* and net primary production (NPP) were compared to available data sets with a focus on spatial distribution and seasonal cycle. The model produces realistic spatial distributions, especially regarding NPP and chlorophyll *a*, whereas the iron concentration becomes too low in the Pacific Ocean. The modelled NPP is 32.5 Pg C yr^{-1} and the export production 6.1 Pg C yr^{-1}, which is lower than satellite-based estimates, mainly due to excessive iron limitation in the Pacific along with too little coastal production. The model performs well in the Southern Ocean, though the assessment here is hindered by the lower availability of observations. The modelled NPP is 3.1 Pg C yr^{-1} in the Southern Ocean and the export production 1.1 Pg C yr^{-1}.

All in all, the combination of a circulation model on an unstructured grid with a biogeochemical–ocean model shows similar performance to other models at non-eddy-permitting resolution. It is well suited for studies of the Southern Ocean, but on the global scale deficiencies in the Pacific Ocean would have to be taken into account.

1 Introduction

Primary production plays a large role in ocean carbon cycling, and understanding the drivers behind primary production is therefore of paramount importance when it comes to understanding the changes that a future warmer climate will bring. Observations, as well as coupled biogeochemical–ocean models, indicate that climate change will decrease the oceanic net primary production (NPP) (Behrenfeld et al., 2006; Steinacher et al., 2010). This would have far-reaching implications, from changes of the carbon cycle to effects on fisheries.

Coupled biogeochemical–ocean models are important tools used to analyse the net primary production in the ocean and the effects of climate change on it (e.g. Le Quéré et al., 2003; Bopp et al., 2013). The biogeochemical results of such models are highly impacted by the mixing and circulation of the ocean model as it controls processes such as horizontal advection and nutrient supply to the surface layer (Doney et al., 2004). Supply of nutrients through upwelling is especially important when it comes to modelling the equatorial Pacific (Aumont et al., 1999) and the Southern Ocean, where production is iron limited and sensitive to new supply. Results from the second Ocean Carbon-Cycle Model Intercomparison Project (OCMIP-2) highlighted the importance of the ocean model; they showed how the representation of the

ocean circulation in the Southern Ocean has a large impact on the calculations of present and future uptake of CO_2 (Doney et al., 2004), and reported that the global export production varied between 9 and 28 Gt C yr^{-1} when the same biogeochemical model was coupled to different OGCMs (Najjar et al., 2007).

Traditionally, global OGCMs employ structured grids with relatively uniform spatial resolution in the entire domain, and local refinement is done by utilizing nested models.

The unstructured-mesh technology is emerging as an alternative to nesting in ocean models, and is gradually becoming more widespread within the ocean modelling community (e.g., Chen et al., 2003; Danilov et al., 2004; Piggott et al., 2008). As solutions for the global ocean state provided by models formulated on unstructured meshes have improved (e.g., Sidorenko et al., 2011), it has become feasible to exploit the advantages offered by such models in biogeochemical modelling by coupling a biogeochemical model to an unstructured-mesh ocean model (Hill et al., 2014). One may then benefit from the possibility of aligning the grid with the bathymetry, or refining it in areas of interest without the loss of accuracy that the nesting introduces at boundaries. This is especially relevant when it comes to modelling features such as mixed layer depth, upwelling and the presence of fronts and eddies that are of vital importance for realistic modelling of ecosystems.

A drawback of the unstructured-mesh technology is that, although computer time is saved by using high resolution in chosen areas only, it still uses a substantial amount of computer time as it is less efficient per degree of freedom as compared to structured models. Furthermore, extra care must be taken for models formulated using the continuous finite elements as their local conservation of volume and tracers is formulated in the cluster-weighted sense. This brings some ambiguity into analyzing fluxes between grid cells, while divergences are well defined (Sidorenko et al., 2009).

Before using a newly coupled biogeochemical–ocean model for scientific studies, the skill of the model must be assessed (e.g. Assmann et al., 2010). Performing a skill assessment is not a trivial exercise, considering both the lack of data, especially for parameters such as dissolved iron and export production, and also the inherent uncertainty of the biogeochemical models, in which complex biochemical processes are described by comparably simple mathematical parameterizations. We have coupled the Regulated Ecosystem Model 2 (REcoM2) to the Finite Element Sea Ice–Ocean Model (FESOM), and in this paper a skill assessment of the coupled model is carried out with emphasis on the Southern Ocean. We show to what extent the results are comparable to observations and discuss how they compare to results from other models.

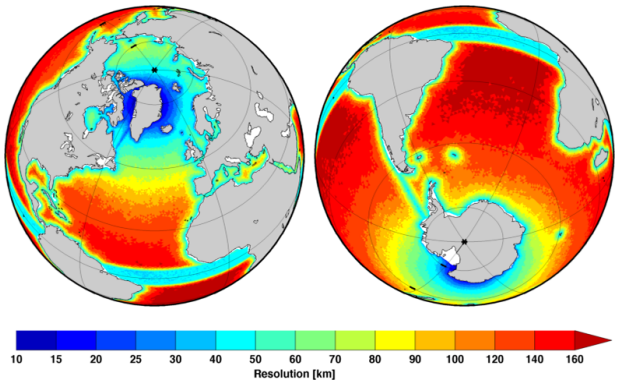

Figure 1. Horizontal resolution of FESOM's unstructured grid.

2 Method

2.1 Ocean model

The ocean component of FESOM solves the hydrostatic primitive equations under the Boussinesq approximations (Danilov et al., 2004; Wang et al., 2008). Elastic viscous plastic (EVP) sea ice dynamics is used together with the thermodynamics adopted from Parkinson and Washington (1979) as described in detail by Timmermann et al. (2009). Currently, FESOM is used for simulation of the three-dimensional global ocean with special focus on the Arctic and the Antarctic (Haid and Timmermann, 2013; Wekerle et al., 2013). The latest FESOM version is comprehensively described in Q. Wang et al. (2014).

FESOM operates on unstructured meshes that permit the main feature of the model: the capability of local grid refinement in an otherwise global set-up without nesting. The model domain is discretized by a horizontally triangulated and unstructured, but vertically stratified, mesh with tetrahedral volumes. Integration is carried out on an Arakawa A-grid, which uses vertical z coordinates for simplicity. The mesh used in this study (Fig. 1) is similar to the one used by Sidorenko et al. (2011), in which the horizontal resolution ranges from 15 km in the polar regions to 180 km in the subtropical gyres. In the vertical it has 32 layers, nine of which are located in the upper 100 m.

The bottom topography of FESOM's grid is constructed using a combination of different data products; the bulk of FESOMS bathymetry, from 60° S to 64° N, is based on topography data from the General Bathymetric Chart of the Oceans (GEBCO, 1 min resolution), south of 60° S, the bottom topography from Timmermann et al. (2010) with a resolution of 1 min (Rtopo-1) is used and north of 69° N it is based on data from the International Bathymetric Chart of the Arctic Oceans with 2 km resolution (IBCAO, version 2; Jakobsson et al., 2008). Between 64 and 69° N, a combination of the GEBCO and IBCAO data sets is used. FESOM's bottom topography is created using bilinear interpo-

lation, whereupon smoothing is performed to remove grid-scale noise. The topography data also defines the coastline using bilinear interpolation from the data to the model's grid points. For a further description of the creation of bottom topography for FESOM, please refer to Q. Wang et al. (2014).

The version of FESOM used here utilizes a linear representation on triangles (in 2-D) and tetrahedrals (in 3-D) for all model variables. The same is true for the biological tracers, which are treated similar to temperature and salinity. The temporal discretization is implicit for sea surface elevation and a second order Taylor–Galerkin method together with the flux-corrected transport (FCT) is used for advection–diffusion equations. The forward and backward Euler methods are used for lateral and vertical diffusivities, respectively, and the Coriolis force is treated with a second order Adams–Bashforth method.

The vertical mixing is calculated using the PP-scheme first described by Pacanowski and Philander (1981) with a background vertical diffusivity of $1 \times 10^{-4}\,\mathrm{m^2\,s^{-1}}$ for momentum and $1 \times 10^{-5}\,\mathrm{m^2\,s^{-1}}$ for tracers. Redi diffusion (Redi, 1982) and Gent and McWilliams parameterization of the eddy mixing (Gent et al., 1990) are applied with a critical slope of 0.004.

The skill of FESOM has been assessed within the CORE framework (Griffies et al., 2009; Sidorenko et al., 2011; Downes et al., 2014), where several sea ice–ocean models were forced with the normal year (CORE-I) and interannually varying (CORE-II) atmospheric states (Large and Yeager, 2004, 2009) and results compared. In these assessments, the full flexibility of FESOM's unstructured mesh was not utilized, but the results from FESOM were still within the spread of the other models, and it was consequently concluded that FESOM is capable of simulating the large-scale ocean circulation to a satisfactory degree.

2.2 Biogeochemical model

The Regulated Ecosystem Model 2 (REcoM2) belongs to the class of so-called quota models (Geider et al., 1996, 1998), in which the internal stoichiometry of the phytoplankton cells varies depending on light, temperature and nutrient conditions. Uptake of macronutrients is controlled by internal concentrations as well as the external nutrient concentrations, and the growth depends only on the internal nutrient concentrations (Droop, 1983). Iron uptake is controlled by Michaelis–Menten kinetics. An overview of the compartments and fluxes in REcoM2 can be seen in Fig. 2.

The model simulates the carbon cycle, including calcium carbonate as well as the nutrient elements nitrogen, silicon and iron. It has two classes of phytoplankton: nanophytoplankton and diatoms, and additionally describes zooplankton and detritus. The model's carbon chemistry follows the guidelines provided by the Ocean Carbon Model Intercomparison Project (Orr et al., 1999), and the air–sea flux calculations for CO_2 are performed using the parameterizations suggested by Wanninkhof (1992).

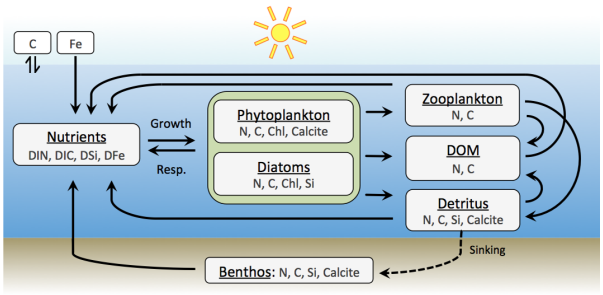

Figure 2. The pathways in the biogeochemical model REcoM2.

We do not add external sources to the macronutrient pools since the timescale of the runs is short compared to the residence time of the macronutrients in the ocean (Broecker et al., 1982).

Iron has a much shorter residence time (Moore and Braucher, 2008) and is strongly controlled by external sources as well as scavenging. Dissolved iron is taken up and remineralized by phytoplankton, it reacts with ligands and it is scavenged by detritus in the water column (Parekh et al., 2005). New iron is supplied to the ocean by dust and sedimentary input. For dust input, REcoM2 uses monthly averages (Mahowald et al., 2003; Luo et al., 2003), which have been modified to fit better to the observations from Wagener et al. (2008) (N. M. Mahowald, personal communication, 2011). The model assumes that 3.5 % of the dust field consists of iron and that 1.5 % of this iron dissolves when deposited in the surface ocean. This gives a total aeolian input of $2.65 \times 10^9\,\mathrm{mol\,DFe\,yr^{-1}}$ (DFe – dissolved iron) to the ocean on average. A flux of iron from the sediment has been added accounting for an input of $2.67 \times 10^8\,\mathrm{mol\,DFe\,yr^{-1}}$ on average. It is incorporated following Elrod et al. (2004) with the magnitude of the iron concentration released by the sediment being dependent on the rate of carbon remineralization in the sediment.

The model has 1 zooplankton class, which is the model's highest trophic level. Grazing is calculated by a sigmoidal Holling type 3 model with fixed preferences on both phytoplankton classes (Gentleman et al., 2003).

The sinking speed of detritus increases with depth, from $20\,\mathrm{m\,day^{-1}}$ at the surface, to $192\,\mathrm{m\,day^{-1}}$ at 6000 m depth (Kriest and Oschlies, 2008). Sinking detritus is subject to remineralization.

REcoM2 has sediment compartments for nitrogen, silicon, carbon and calcium carbonate, which consist of one layer into which the detritus sinks when reaching the lower-most ocean layer. Remineralization of the sunken material subsequently occurs in the benthos, and the nutrients are returned to the water column in dissolved state.

REcoM1 and 2 have previously been used for large-scale simulations with focus on the Southern Ocean in set-ups with the MITgcm (MIT general circulation model) (Hohn, 2009; Taylor et al., 2013; Hauck et al., 2013), and the purpose of the current coupling between REcoM2 and FESOM is likewise studies of the Southern Ocean.

A full description of the model equations can be found in Appendix A along with lists of parameters used in the current run.

2.3 Model experiment

We present a numerical hindcast experiment with a newly coupled biogeochemical–ocean general circulation model. The run was forced using the CORE-II data set, which was developed for the use of coupled sea ice–ocean models and gives an interannually varying forcing for the years 1949 to 2008 (Large and Yeager, 2009). As focus here is on evaluating the biological surface processes of a newly coupled model, we follow the example of Vichi and Masina (2009) and Yool et al. (2011) and let the coupled model run for a total of 38 years, from 1971 to 2008. The first 33 years are considered spin-up and we present the results for the years 2004 to 2008. Prior to activating the biogeochemical module, the ocean model had been spun up for 300 years, which is sufficient to reach a quasi-equilibrium state (Fig. 8 in Sidorenko et al., 2011). The length of the time step used throughout the run was 1800 s.

In REcoM2, the tracers for dissolved inorganic nitrogen (DIN) and dissolved silicon (DSi) were initialized with values from the Levitus World Ocean Atlas climatology of 2005 (Garcia et al., 2006), and the dissolved inorganic carbon (DIC) and total alkalinity (TA) tracers were initialized with contemporary values from the Global Ocean Data Analysis Project (GLODAP) data set (Key et al., 2004). Due to scarcity of observations for DFe, the iron field was initialized with an output from the Pelagic Interaction Scheme for Carbon and Ecosystem Studies (PISCES) model (Aumont et al., 2003), which has been modified south of 45° S with mean observed profiles from Tagliabue et al. (2012). All other tracers were initialized with arbitrary small values.

We used a constant value for the atmospheric CO_2 during the simulation. Because of the duration of the simulation, the carbon cycle is not in equilibrium at the end of the run, and we do not to focus on this part of the model here.

2.4 Data and skill metrics

The focus of this skill assessment is on the key parameters of the physical, chemical and biological surface fields, for which we examine the model behaviour on the global scale and in the ocean regions shown in Fig. 3. We have a special interest in the Southern Ocean and therefore also look further into the production and its drivers there. On the temporal scale we primarily focus on annual climatologies of the modelled fields, but also show the seasonal development for certain parameters.

The performance of the model regarding sea surface temperature (SST), sea surface salinity (SSS), mixed layer depth (MLD), DIN, DSi, chlorophyll *a* (Chl), NPP and export production (EP) is summarized in Taylor diagrams, one displaying the spatial agreement between the modelled surface multi-year means and the observations, and one also taking the seasonal variations into account. Due to a lack of monthly data, EP is only plotted in the former Taylor plot. The spatial distribution of the modelled and observed surface climatologies of these same fields, except SST and SSS, have additionally been plotted to show the bias which is not captured by the Taylor diagrams. SST and SSS were omitted as they have been evaluated elsewhere (Sidorenko et al., 2011). Global climatologies of dissolved iron concentrations do not exist, making it impossible to evaluate the modelled iron fields in the manner described above. Instead, the modelled surface climatology of the iron concentration is plotted on its own, and mean values of the ocean basins are compared to observation compilations in table form. NPP is the model's end result, and we have therefore additionally plotted the mean seasonal cycle of the NPP for each of the ocean basins defined in Fig. 3, for the model result as well as satellite-based observations. Due to the large effect the modelled mixed layer has on the prediction of the NPP, we have also chosen to illustrate the seasonal cycle of the modelled and observed mean MLD in these same ocean basins.

The Taylor diagrams (Taylor, 2001) show the correlation (r), the normalized root mean square error (RMSE) and the normalized standard deviation (SD) between the model results and the observations. The correlation between the model and the observations show whether the two data sets increase and decrease simultaneously, the SDs tells us about the magnitude of the changes in the data, but not when these changes occur and the centered RMSE reflects differences in the overall patterns of the two fields after the bias has been removed. The perfect fit between model and observations will have a correlation and a SD of 1 and a RMSE of 0.

A full list of the observations used can be seen in Table 1. For the NPP we use the Vertically Generalized Productivity Model (VGPM) product from the ocean productivity web page (http://www.science.oregonstate.edu/ocean.productivity/index.php), which is based on the Sea-viewing Wide Field-of-view Sensor (SeaWIFS, 2012) chlorophyll measurements and the VGPM NPP model (Behrenfeld and Falkowski, 1997). We have downloaded monthly values from the web page, and from these calculated the spatial and seasonal means. The EP fields from Schlitzer (2004), Siegel et al. (2014) and Laws et al. (2000) were provided as climatologies. The field from Laws et al. (2000) and Siegel et al. (2014) are satellite based, whereas the field from Schlitzer (2004) comes from an inverse model.

Satellite-based estimates of chlorophyll *a*, NPP and EP provide detailed spatial and temporal data, but obtaining

Table 1. List of the observational data sets used for the skill assessment.

Data set	Variable name	Temporal coverage	Reference
Sea surface temperature	SST	Monthly climatology	Garcia et al. (2010)
Sea surface salinity	SSS	Monthly climatology	Garcia et al. (2010)
Mixed layer depth	MLD	Monthly climatology	de Boyer Montegut et al. (2004)
Dissolved inorganic nitrogen	DIN	Monthly climatology	Garcia et al. (2010)
Dissolved inorganic silicon	DSi	Monthly climatology	Garcia et al. (2010)
Chlorophyll *a* concentration	Chl	Monthly (1998–2010)	Globcolour (2012)
Net primary production	NPP	Monthly (2003–2008)	SeaWIFS (2012), Behrenfeld and Falkowski (1997)
Export production	EP	Annual climatologies	Schlitzer (2004), Laws et al. (2000)

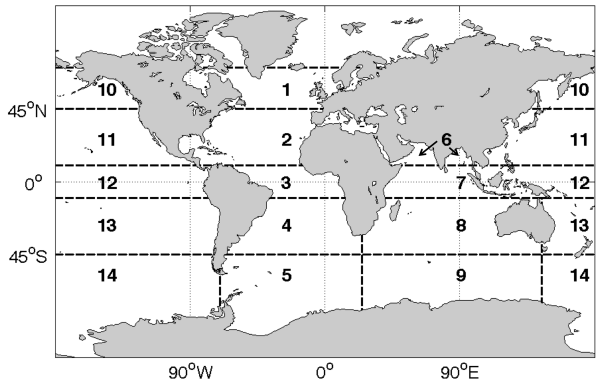

Figure 3. Map of the ocean regions used to examine the model results on a basin scale.

them is not trivial. Remotely sensed global ocean colour values are first converted to chlorophyll *a*, and under a number of assumptions about, for instance, mixed layer depth, temperature and light, NPP (Behrenfeld and Falkowski, 1997) and finally EP (e.g. Laws et al., 2000; Siegel et al., 2014) can be estimated. Increasing uncertainty is introduced during the process, and the satellite-based estimates are not as such observations, but rather another way of modelling the chlorophyll *a*, NPP and EP. The spread between the different satellite-based estimates of NPP is large. Carr et al. (2006) showed that estimates of the global NPP differed by a factor 2 between 24 models, with the largest discrepancies occurring in the high-nutrient low-chlorophyll and extreme temperature areas. The SeaWIFS (2012) algorithms have further been shown to significantly underestimate chlorophyll *a* concentrations in the Southern Ocean (Gregg and Casey, 2004), and one must consequently be aware of this when using satellite-based estimates from the Southern Ocean.

The Arctic Ocean is likewise an area in which observations are scarce, and for the seasonal Taylor diagrams the modelled results have consequently been removed in both of the polar regions when comparable observational values did not exist. As is the case in the Southern Ocean, it is especially the satellite-based observation of NPP that is affected by this during the winter months. The missing seasonal data has likewise led us to cut off the northern basins at 70° N in Fig. 3.

In addition to comparing our results to available observations, we discuss them in relation to those of other biogeochemical models. For Dfe, Chl and NPP we have plotted our bias plots to the scale used by Schneider et al. (2008). They present the results of the IPSL (Institut Pierre Simon Laplace) model, the MPI (Max Planck Institute) model and the NCAR (National Center for Atmospheric Research) model, providing a range of results to hold our model against. We additionally compare our model to the results from Assmann et al. (2010), who present the results of another non-traditional ocean model coupled to a biogeochemical model, and to Yool et al. (2011). For the export production, Moore et al. (2004) provided a thorough discussion of the export of particulate organic matter as well as opal, and our spatial plots of export production is consequently plotted to the scale used by them.

3 Model results

3.1 Physics: mixed layer depth, salinity and temperature

The fit between the spatial distributions of modelled and observed surface temperature and salinity is very good for both spatial (Fig. 4a) and monthly spatial fields (Fig. 4b), with the correlations being higher than 0.99 and the normalized SDs close to 1 for both fields. As is general practice in ocean-only models (Griffies et al., 2009), FESOM's surface salinity is weakly restored towards the Polar Science Center Hydrographic Climatology (PHC) (Steele et al., 2001) with a piston velocity of $20\,\mathrm{m\,yr^{-1}}$.

In both FESOM and the observations (de Boyer Montegut et al., 2004), the mixed layer depth is defined as the depth at which the difference between the potential density at 10 m depth and the MLD is greater than $0.03\,\mathrm{kg\,m^{-3}}$. The spatial distribution of the mean MLD has a correlation of 0.68 and a normalized SD of 0.85 when compared to the data-based estimates (Fig. 4).

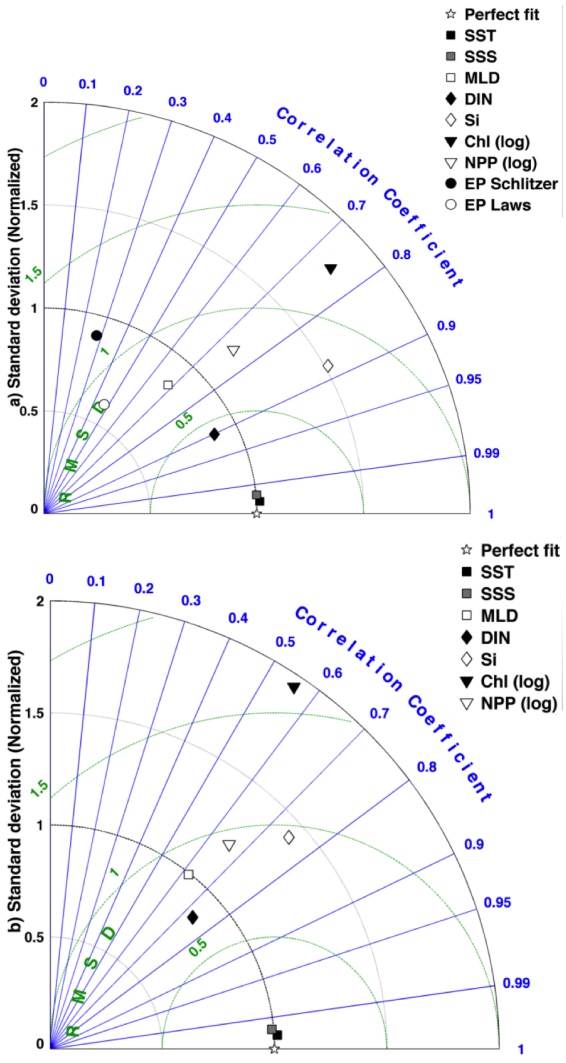

Figure 4. Taylor diagrams (Taylor, 2001) showing correlation, normalized SD and the normalized root mean square error between values of the model results and observations (Table 1), weighted by area. **(a)** Spatial distribution; **(b)** spatial–seasonal distribution. All values are surface values, except the mixed layer depth and the vertically integrated NPP. **(a)** Uses the yearly mean calculated over 2004–2008 and **(b)** uses the monthly means of the same years. All fields have been interpolated to a $1° \times 1°$ grid, using linear interpolation.

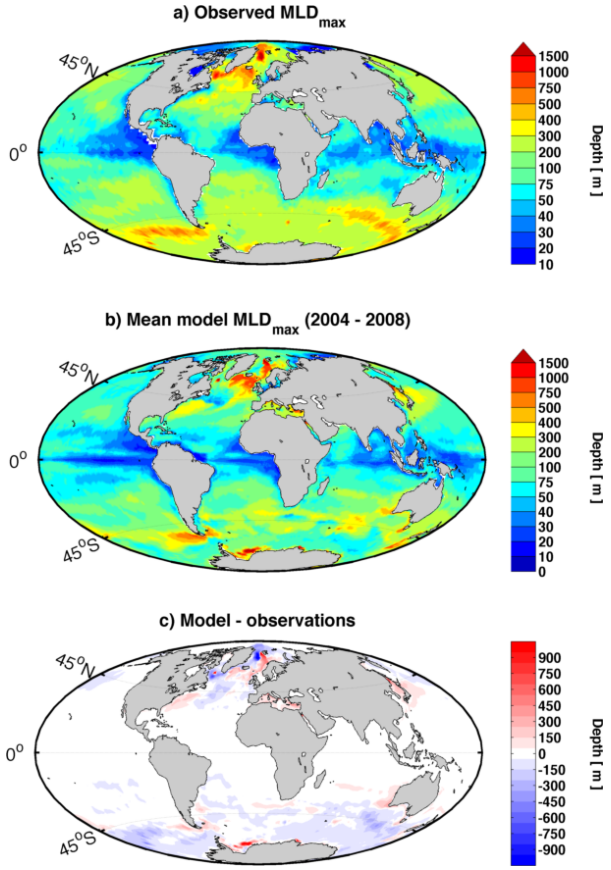

Figure 5. Mean spatial distribution of the MLD_{max} over the years 2004–2008. **(a)** Observation based (de Boyer Montegut et al., 2004). **(b)** Modelled. **(c)** Residual: modelled − observation based.

The seasonal variability of the MLD leads to entrainment of water with high nutrient concentrations to the surface water during winter, and the maximum depth of the mixed layer during the year (MLD_{max}) is therefore especially important from a biological point of view. Overall, the modelled MLD_{max} fits well with the observations, but it is generally too shallow in the Southern Ocean (Fig. 5), with the consequence that limiting nutrients are not adequately replenished during winter. This may lead to a too small NPP in the area as well as a dominance of nanophytoplankton over diatoms, as the former needs a lower iron concentration for production. This will be further discussed in Sect. 3.5.

For the monthly fields, the correlation between the modelled MLD and the observations is above 0.6 and the SD equals 1 (Fig. 4b). We investigate this further by plotting the mean depth of the mixed layer in different ocean regions defined in Fig. 3. All basins have correlations above 0.9, except the northern Indian and equatorial basins (Fig. 6), leading us to conclude that the seasonal change in the MLD is well predicted by FESOM.

3.2 Nutrients and nutrient limitation

The annual mean surface distribution of DIN and DSi have correlations between model results and observations of 0.91 and 0.86, respectively (Fig. 4a). In the Southern Ocean, the surface DIN concentrations have a negative bias for DIN (Fig. 7) and a positive for DSi (Fig. 8) when the spatial distribution of modelled and observed values are compared. The DIN concentration additionally becomes too high in the sub-

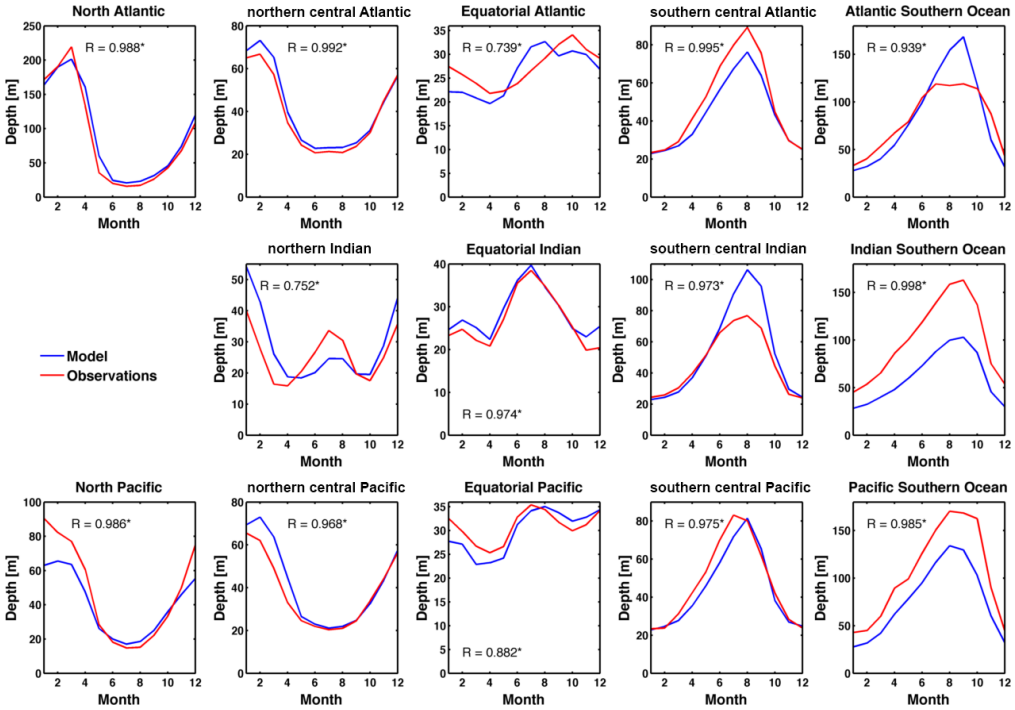

Figure 6. Mean MLD over the year in the ocean basins depicted in Fig. 3. The correlation coefficient is written in each plot, and the statistically significant correlations (p values < 0.05) are marked with *.

tropical Pacific Ocean (Fig. 7), something we will later argue happens due to a strong iron limitation in the area.

The correlation between model results and observations for the spatial–seasonal distribution of DIN and DSi is close to 0.75 for both fields (Fig. 4b). For both nutrients, the seasonal cycle has the best agreement with the observations in the polar regions (not shown).

Iron has been shown to play a large role as limiting nutrients for phytoplankton in the Southern Ocean, as well as the equatorial and subarctic Pacific (Martin et al., 1991), and is therefore a key parameter in the model. We compare the model's surface iron concentration to compilations of observations (Moore and Braucher, 2008; Tagliabue et al., 2012) and to other biogeochemical models (i.e. Schneider et al., 2008). It must be mentioned here that the model is not independent of the observations from Tagliabue et al. (2012) as they are also used for initialization of dissolved iron. But as we only compare surface values, and the residence time of iron in the Southern Ocean is much shorter than the model run, the surface iron concentrations at the end of the model run should not be affected by the initialized values.

The pattern of the surface iron concentration in the Atlantic Ocean (Fig. 9) fits well with the observations in Table 2 as well as with the results from the MPI and NCAR models in Schneider et al. (2008), with relative high concentrations in the equatorial region fed by the dust plume from the Sahara, and concentrations decreasing towards the poles. The

Table 2. Modelled mean surface iron concentrations (0–100 m) in the different ocean basins shown in Fig. 3. Observed values are from Moore and Braucher (2008), except those marked with *, which are from Tagliabue et al. (2012), Table 2. The latter is the mean of the values given for the Antarctic and Subantarctic regions.

Basin	Latitudinal extent	Model [nM]	Obs [nM]
North Atlantic	45–70° N	0.34	0.68
Northern central Atlantic	10–45° N	1.03	0.68
Southern central Atlantic	45–10° S	0.28	0.44
Northern Indian	45–10° S	1.10	1.21
North Pacific	45–70° N	0.14	0.31
Equatorial Pacific	10° S–10° N	0.02	0.84
Southern central Pacific	45–10° S	0.02	0.31
Atlantic Southern Ocean	90–45° S	0.14	0.39*
Indian Southern Ocean	90–45° S	0.08	0.33*
Pacific Southern Ocean	90–45° S	0.09	0.15*

iron concentrations in the IPSL model and Assmann et al. (2010) are somewhat lower in the equatorial and southern part of the Atlantic Ocean than our result.

In the Indian Ocean, our surface iron concentrations agree well with the IPSL and NCAR models as well as with the results from Yool et al. (2011), with values higher than 1 nM in the Arabian Sea and falling towards 0.3 nM in the main In-

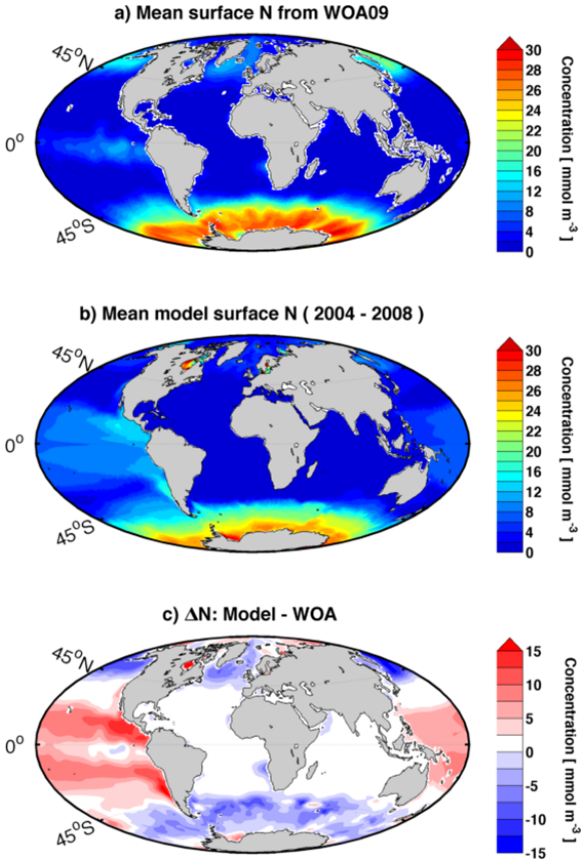

Figure 7. Spatial distribution of mean surface concentration of dissolved inorganic nitrogen. **(a)** Observed (Garcia et al., 2010) **(b)** Modelled. **(c)** Residual: modelled − observed.

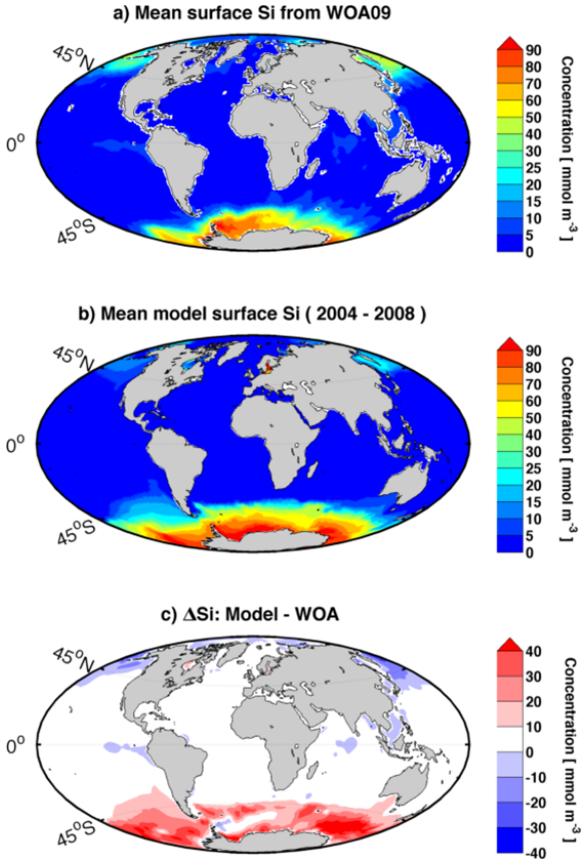

Figure 8. Spatial distribution of mean surface concentration of dissolved inorganic silicon. **(a)** Observed (Garcia et al., 2010) **(b)** Modelled. **(c)** Residual: modelled − observed.

dian Ocean. Our values also fit well with the observations in the northern Indian Ocean (Table 2), and this, along with the agreement between the models using varying magnitudes of sedimentary iron input, indicates that the coastal upwelling in the Arabian Sea is well captured in these models, and that this upwelling is responsible for the high surface iron concentrations in the area. The lower surface iron concentration in South East Asia is on the other hand evident in all of these models with the exception of the IPSL model, indicating that the sediment source plays a larger role in this area. Here, unfortunately we do not have observations to validate the models. In the Pacific Ocean, our result is closest to the one from Assmann et al. (2010), though they have a higher iron concentration along the North and South American west coast, indicating a stronger coastal upwelling in their ocean model. We have a lower surface iron concentration than all models presented by Schneider et al. (2008), even though they all have low concentrations locally. The observations in Table 2 indicate that all models underestimate the surface iron concentrations in the Pacific, especially in the equatorial region where the upwelling plays the largest

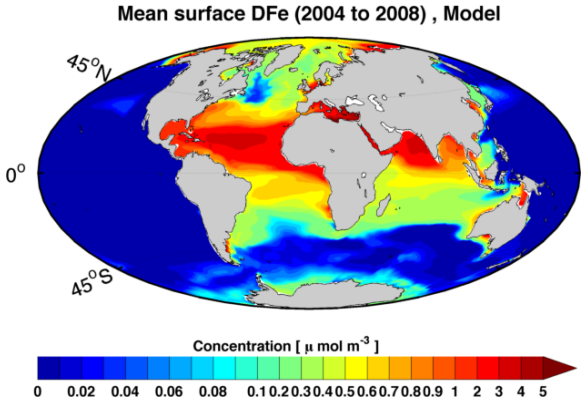

Figure 9. Spatial distribution of the mean surface concentration of dissolved iron. Plotted to the scale used by Schneider et al. (2008).

role. In the Southern Ocean, Table 2 shows that our surface iron concentration is too low, but the spatial distribution of the surface iron fits well with observed values, with the highest values found in the vicinity of the Antarctic and east of the

Patagonian shelf (Tagliabue et al., 2012). This distribution can mainly be attributed to the sediment and dust sources of iron and the seasonal ice coverage impeding iron uptake by phytoplankton near the Antarctic continent. These factors are also responsible for maintaining the relatively high surface iron concentration in the Arctic, which becomes iron limited in the absence of the sediment source of iron. Assmann et al. (2010) and Moore and Braucher (2008) also experienced this, with the latter mentioning that the missing sediment source has a modest impact on productivity and iron concentrations away from the Arctic. In the Southern Ocean, our result agrees the best with the IPSL model, with a relatively high coastal concentration, which then falls towards the north. Both the MPI and NCAR models have relatively constant higher values in the area south of 40° S of around 0.5 and 0.3 nM, respectively.

The comparison to observations is, however, hindered by the different definitions of the ocean basins. The value of the North Atlantic from Moore and Braucher (2008), for instance, roughly covers the North Atlantic as well as the northern central Atlantic of our definition (Fig. 3). For the equatorial Pacific, Moore and Braucher (2008) report the value 0.84 nM for the whole ocean, and 0.11 nM for the open ocean, where our value is closer to the latter due to the missing coastal processes in the model.

Nutrient uptake limitation is described by Michaelis–Menten kinetics in the model. The Michaelis–Menten coefficient (MM) is computed as $\mathrm{MM} = [\mathrm{Nut}]/([\mathrm{Nut}] + K_{\mathrm{Nut}})$, with [Nut] being the nutrient concentration, and K_{Nut} a nutrient and phytoplankton dependent half-saturation constant.

To plot the distribution of the mean surface limitation we follow the example of Schneider et al. (2008), where the nutrient with the lowest MM in a given place is seen as limiting and it is assumed that other factors, such as temperature and light, are limiting when all Michaelis–Menten coefficients are above 0.7 (Fig. 10).

When looking at the yearly mean, iron limits nutrient uptake for both nanophytoplankton and diatoms up to 45° S and in most of the Pacific. Nanophytoplankton is mainly nitrogen limited in the Atlantic and Indian oceans, concurring with the result by Assmann et al. (2010), Yool et al. (2011) and the IPSL model in Schneider et al. (2008). For diatoms, silicon is limited in the Atlantic and Indian oceans as well as in the Arctic, a feature that we only share with Yool et al. (2011).

In the high latitudes, the modelled nanophytoplankton become light limited during the respective winter months. For the Arctic this is most pronounced in February, where the light limitation reaches down to 45° N in the Atlantic Ocean. For the Southern Ocean, the highest degree of light limitation occurs in August when the area south of 55° S is affected. The higher nutrient demand by diatoms means that they are co-limited by iron and light during winter (not shown).

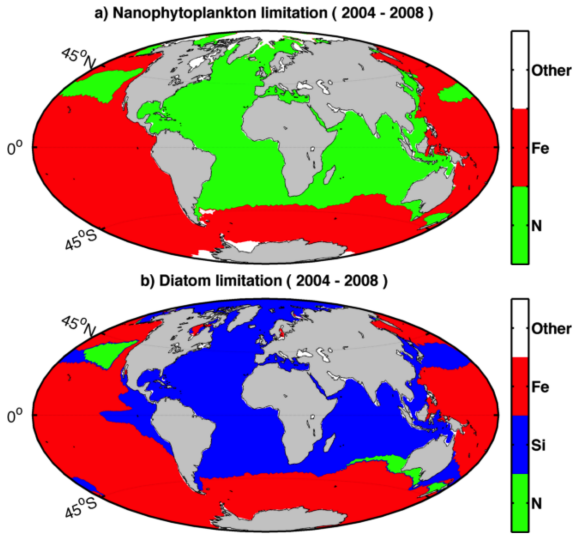

Figure 10. Following the example of Schneider et al. (2008), the spatial distribution of the annually mean limiting nutrients in the model's surface water has been calculated. **(a)** Nanophytoplankton (Fe = 56.6 %, DIN = 40.1 % of total area). **(b)** Diatoms (Fe = 53.6 %, DIN = 2.5 % and DSi = 43.8 % of total area).

3.3 Chlorophyll and net primary production

Global NPP sums up to 32.5 Pg C yr^{-1} in the model (Table 3), which is lower than the satellite-based estimate of 47.3 Pg C yr^{-1} (SeaWIFS, 2012; Behrenfeld and Falkowski, 1997) and also slightly below the estimate range of 35–70 Pg C yr^{-1} given by Carr et al. (2006), but higher than the modelled values ranging from 23.7 to 30.7 Pg C yr^{-1} reported by Schneider et al. (2008).

On a global scale, diatoms account for 25.9 % of all production in the model. In the subtropical gyres, we see close to zero percent of NPP from diatoms, whereas it constitutes close to 100 % in the Arctic Ocean (not shown).

The correlations between the spatial distribution of modelled results and satellite data are 0.75 for both chlorophyll *a* and NPP (Fig. 4a), with the mean surface chlorophyll *a* concentration being somewhat overestimated as compared to the satellite-based estimates in the high latitudes, while the equatorial regions have concentrations that are too low (Fig. 11) and the extent of the subtropical gyres is too large. Yool et al. (2011) have a higher equatorial chlorophyll *a* concentration in the equatorial regions of the Atlantic and Pacific oceans as compared to our model, but their concentration in the Southern Ocean is even higher than ours. Furthermore, when we compare our model to the IPSL model (Schneider et al., 2008), we again see that our equatorial chlorophyll *a* concentrations are lower, whereas the concentrations in the North Atlantic and Southern Ocean are fairly similar to our result.

Table 3. Net primary and export production for the global domain and the Southern Ocean south of 50° S, for REcoM2 and from literature.

	Units	FESOM–REcoM2	Previous studies
NPP_{glo}	[Pg C yr^{-1}]	32.5	35–70 (Carr et al., 2006) 23.7–30.7 (Schneider et al., 2008) 47.3 (Behrenfeld and Falkowski, 1997)
EP_{glo}	[Pg C yr^{-1}]	6.1	5.8–13.0 (Dunne et al., 2007) 6 (Siegel et al., 2014)
$Opal_{glo}$	[Tmol Si yr^{-1}]	74.5	69–185 (Dunne et al., 2007)
NPP_{SO}	[Pg C yr^{-1}]	3.1	1.1–4.9 (Carr et al., 2006)
EP_{SO}	[Pg C yr^{-1}]	1.1	1 (Schlitzer, 2002; Nevison et al., 2012)
$Opal_{SO}$	[Tmol Si yr^{-1}]	21.5	21–54 (Dunne et al., 2007)

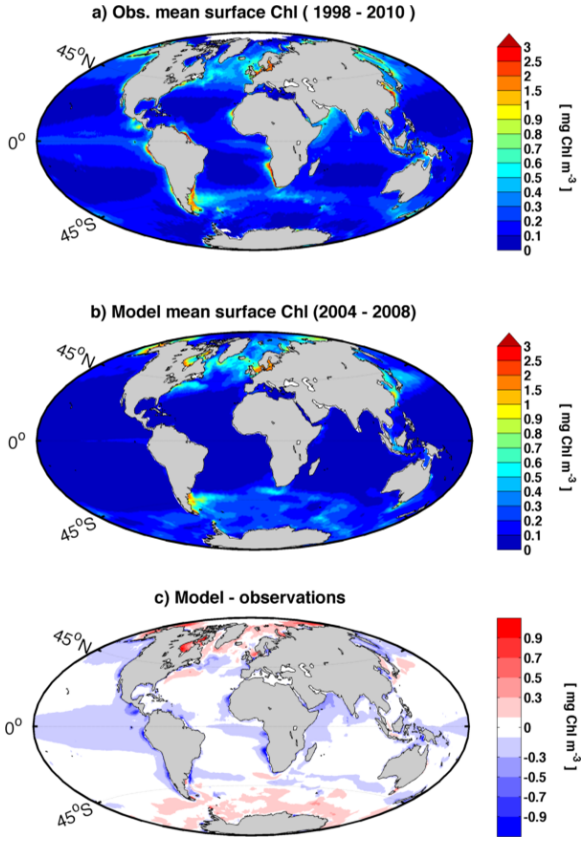

Figure 11. Spatial distribution of mean surface concentrations of chlorophyll *a* plotted to the scale used by Schneider et al. (2008). **(a)** Satellite-based estimate (www.globcolour.info). **(b)** Modelled. **(c)** Residual: modelled − satellite-based estimate.

The spatial distribution of NPP (Fig. 12), follows the same pattern as chlorophyll *a*, with low production in the oligotrophic gyres along with a higher production in the temperate regions. Production in the gyres is on the low side compared to the satellite-based estimate (Fig. 13), and as they are known to underestimate production here (Friedrichs et al., 2009), our result is most likely much too low here. An explanation may be that the nanophytoplankton in the model does not represent the smallest phytoplankton classes, such as *Prochlorococcus* and *Synechococcus*, which are important in the gyres. Even though adaption of the modelled intracellular N : C ratio is possible, this is not enough to increase production here to the level seen in satellite-based estimates.

The missing coastal primary production along the west coast of Africa and South America (Fig. 12) along with a positive temperature bias in these areas (not shown) indicate that the upwelling is too weak here. FESOM has a coastal resolution of 40 km, which is relatively high, but this resolution only covers a narrow path along the coast (Fig. 1), which may not be sufficient for the upwelling zones to be resolved properly; additionally, the low resolution further out in the subtropical gyres could play a role. Furthermore, the driving force for the upwelling is the coastal winds, and the missing upwelling may partially result from a too low resolution of the atmospheric forcing; moreover, higher resolution allows strong surface winds closer to the coast, thereby increasing the strength of the upwelling (Gent et al., 2010).

Another explanation for the low coastal NPP is the missing riverine input of macronutrients, which at least in the case of silicon plays a role locally in places like Amazonas and the Arctic (Bernard et al., 2011). Yool et al. (2011) deal with the missing riverine nutrient input by restoring the nutrient fields along the coasts. Although Yool et al. (2011) have a larger coastal production in their model (especially along the coast of West Africa), they show that the nutrient restoring only has a small influence on this.

When comparing the mean spatial distribution of NPP with other models, our result is the closest to the NCAR model presented by Schneider et al. (2008), with a relatively high production rate in the North and equatorial Atlantic as well as the Indian Ocean. Moderate production in the area of the polar front in the Southern Ocean is a feature that

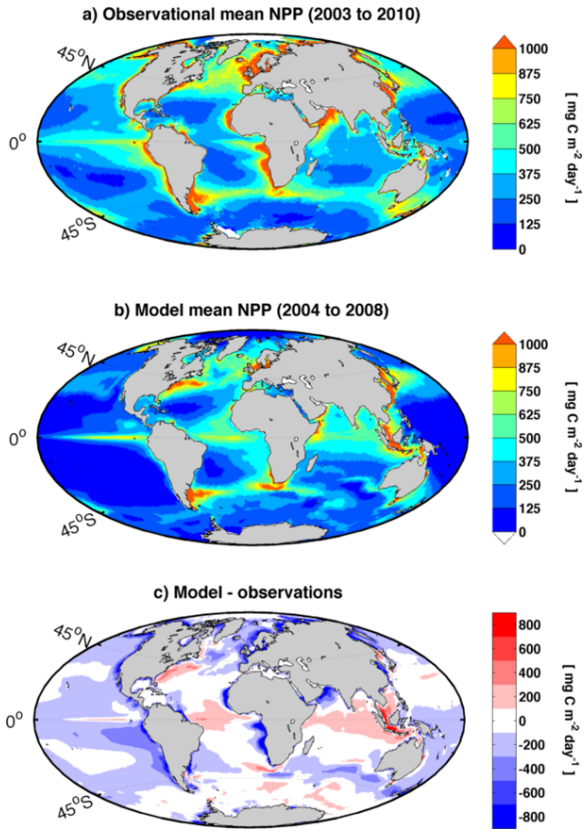

Figure 12. Mean spatial distribution of vertically integrated NPP plotted to the scale used by Schneider et al. (2008). **(a)** Satellite-based estimate (SeaWIFS, 2012; Behrenfeld and Falkowski, 1997). **(b)** Model. **(c)** Residual: modelled − satellite-based estimate.

our model shares with the satellite-based estimate (Fig. 12) and with the NCAR and IPSL models from Schneider et al. (2008). Despite our model's strong iron limitation in the Pacific Ocean, our results fit well with the IPSL model, though we have a smaller production rate in the southern Pacific.

Taking seasonal variations into account, NPP and surface chlorophyll *a* have correlations of 0.66 and 0.57, respectively, when comparing the model and the satellite-based estimate (Fig. 4b), and the normalized SDs are equal to 1.47 and 1.94 for chlorophyll *a* and NPP, respectively. Both are on the same order as the values presented by Doney et al. (2009).

The timing of the seasonal cycle of NPP is well captured in the majority of the ocean regions defined in Fig. 3 (Fig. 13). The Pearson's correlation coefficients (R) range from 0.31 in the equatorial Atlantic to 0.93 in the southern central Atlantic (Fig. 13), with significant correlations in eight of the fourteen basins. In general, the modelled seasonal cycle is closest to the satellite-based estimate between 10 and 45° N and S, where the modelled NPP is low, but the magnitude of the seasonal variations fits well with the satellite-based estimate. This is the case for all basins in the mentioned area, except the northern Indian basin.

The Southern Ocean stands out as it has a modelled NPP of the same magnitude as the satellite-based estimate, but the spring bloom occurs too early here, compared to the satellite-based estimate. This will be further discussed in Sect. 3.5.

3.4 Export production

The export of organic carbon out of the euphotic zone (export production – EP), is calculated at a reference depth, which in our case is set to the standard 100 m (e.g. Schneider et al., 2008; Doney et al., 2009). Here, we regard EP as the organic matter that sinks due to the effect of gravity, whereas the total EP also entails the vertical movement of POC by advection and diffusion plus a contribution from semi-labile DOC.

The global export production sums up to 6.1 Pg C yr^{-1} in the model (Table 3), close to the satellite-based estimate of 6 Pg C yr^{-1} from Siegel et al. (2014). It is also within the range of estimates presented by Dunne et al. (2007), but on the low side and closer to modelled estimates than to estimates based on observations or inverse models.

The modelled EP constitutes 20 % of NPP on a global scale, which is similar to the ratio predicted by Laws et al. (2000). The EP field presented by Laws et al. (2000) is calculated at 100 m depth and is based on satellite observations of ocean colour, whereas the EP field calculated by Schlitzer (2004) is based on an inverse model and is calculated at 133 m. Comparing our model to these fields can consequently be argued to be more of a model–model comparison than a model–observation comparison.

The correlation is 0.28 and 0.48, when comparing the spatial distribution of EP in our model to the fields by Schlitzer (2004) and Laws et al. (2000), respectively (Fig. 4a), indicating that our spatial distribution is closer to the field from Laws et al. (2000), and the normalized SDs are 0.90 and 0.60, respectively.

The EP fields from Schlitzer (2004) and Laws et al. (2000) both have high export along the Equator, in the upwelling regions and along 45° N and S (Fig. 14a and b). In the Southern Ocean, Schlitzer (2004) has a comparably higher export in the Indian and Pacific sector and in the North Atlantic Schlitzer (2004) has less than Laws et al. (2000).

REcoM2 captures the overall pattern with high EP around 45° N and S and along the Equator (Fig. 14c and d), and the elevated EP in the North Atlantic is a feature that REcoM2 shares with the field from Laws et al. (2000). Turning to the differences, our EP is lower in the North Atlantic, slightly lower in the gyres and higher south of 45° S when compared to the field by Laws et al. (2000) (Fig. 14e). Compared to the climatology presented by Schlitzer (2004) (Fig. 14b), our EP is generally lower in the Pacific and in the upwelling regions along West Africa and western North and South America, whereas it is higher in the North and South Atlantic (Fig. 14f). In the Southern Ocean, the differences between

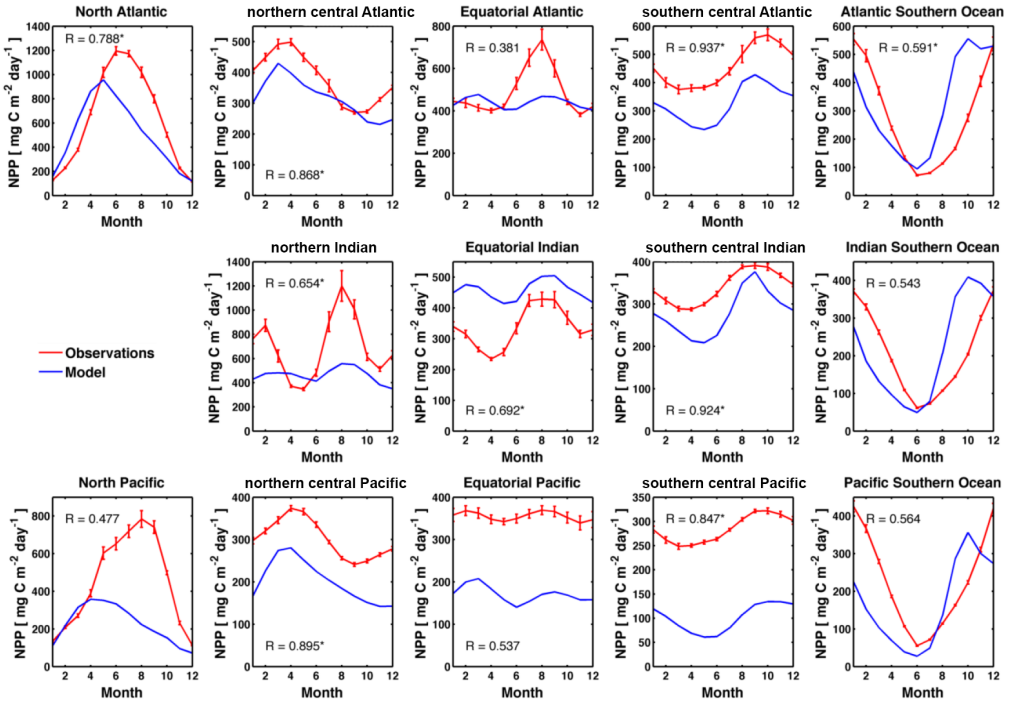

Figure 13. Mean NPP over the year in the ocean basins depicted in Fig. 3. The correlation coefficient is written in each plot, and the statistically significant correlations (p values < 0.05) are marked with *.

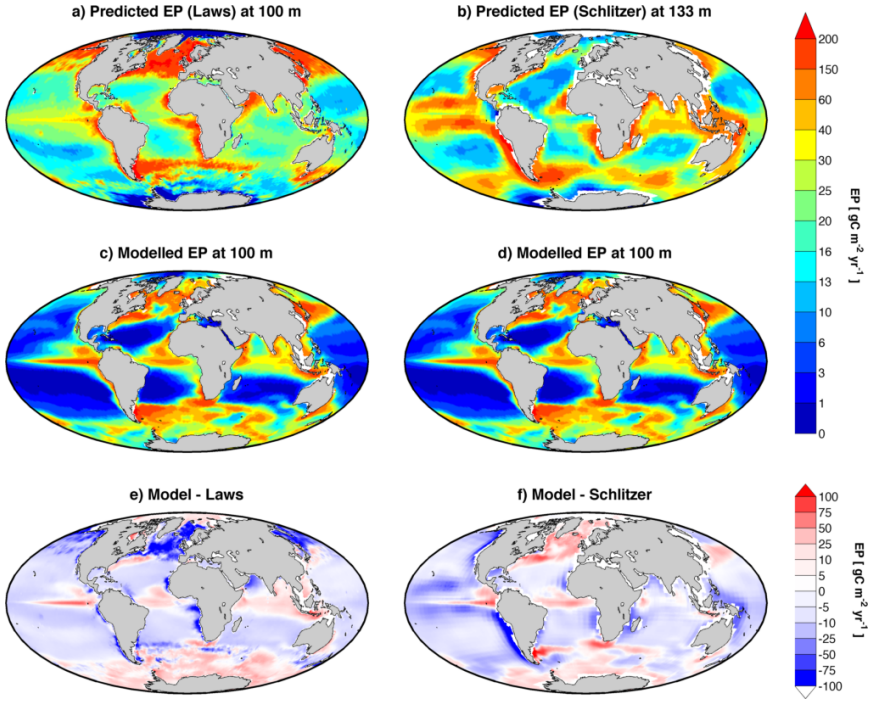

Figure 14. Spatial distribution of export of particulate organic matter plotted to the scale used by Moore et al. (2004). **(a)** Laws. **(b)** Schlitzer. **(c)** and **(d)** modelled (same figure). **(e)** Residual: modelled − Laws. **(f)** Residual: modelled − Schlitzer.

the fields are especially visible in the Indian and Pacific sectors, where Laws et al. (2000) have very low export, Schlitzer has a rather high export and REcoM2's export lies in between the two. Schlitzer argues that the satellites do not capture the deep blooms that occur in the area, thereby explaining the lack of EP in the satellite-based estimate.

Both the spatial distribution and magnitude of EP in our model are very similar to what was found by Moore et al. (2004).

Vertical export of opal is similarly calculated across a reference depth of 100 m. On a global scale we have a total opal export of 74.5 Tmol yr^{-1}. Previous estimates of global export of opal vary widely (Table 3), and our value is in the lower end of the estimates, as are our global values for NPP and EP.

3.5 The Southern Ocean

The coupled model FESOM–REcoM2, as a first step, will be used for studies regarding biogeochemical processes in the Southern Ocean south of 50° S, and we are therefore especially interested in its performance here. The reasons for this focus are further discussed in Sect. 4.

The model's surface salinity and temperature as well as the nutrient fields are well represented in the spatial domain of the Southern Ocean, with all of them having correlation coefficients above 0.9 when compared to observations (Fig. 15). The chlorophyll *a* and NPP fields both have somewhat lower correlations, with the correlation for NPP and chlorophyll *a* being equal to 0.75 and 0.48, respectively.

For the MLD, the correlation between the model results and the observational-based estimate (de Boyer Montegut et al., 2004) is 0.63 in the Southern Ocean (Fig. 15). The MLD_{max} is too shallow in the Indian and Pacific sections of the Southern Ocean, especially in the area of the polar front (Fig. 5), causing this low value. Furthermore, FESOM simulates a too deep MLD_{max} in the convection area of the Weddell Sea associated with deep-water formation. This is a common feature in sea ice–ocean models (e.g. Griffies et al., 2009) and should in itself not have a large impact on the production in the Southern Ocean.

The modelled NPP south of 50° S sums up to 3.1 Pg C yr^{-1} (Table 3). Carr et al. (2006) summarize previous studies of NPP based on ocean colour and report an average NPP of 2.6 Pg C yr^{-1} for the Southern Ocean. They also show that the largest uncertainties in satellite-based estimates regarding NPP are found in the Southern Ocean and that biogeochemical models generally predict higher NPP in the area than satellites.

The model's export production equals 1.1 Pg C yr^{-1} in the Southern Ocean, close to the 1 Pg C yr^{-1} found by both Schlitzer (2002) and Nevison et al. (2012), and the EP : NPP ratio equals 36 % in the Southern Ocean, similar to what was found by Nevison et al. (2012).

Considering the spatial distribution of EP in the Southern Ocean (Fig. 14), the model is closer to the estimate from

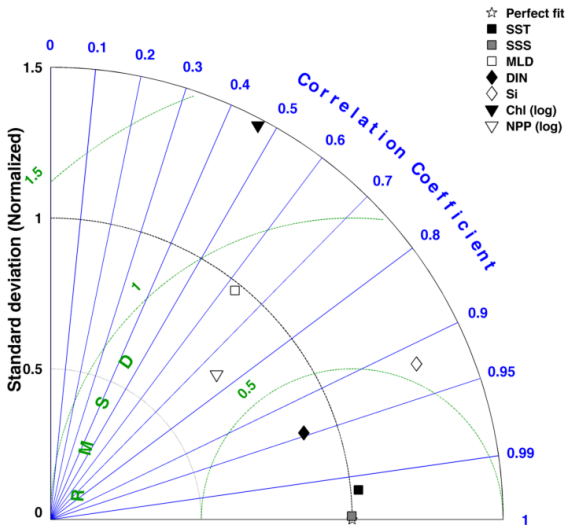

Figure 15. Taylor diagram for the Southern Ocean south of 50° S showing correlation, normalized SD and the normalized root mean square error between the spatial distribution of the model results and observed data sets, weighted by area. All values are surface values, except the mixed layer depth and the vertically integrated NPP. The fields have been linearly interpolated to a 1° × 1° grid, similar to the World Ocean Atlas. he model SD and root mean square error have been normalized by the observational SD.

Laws et al. (2000) with the highest export fluxes occurring in the northern part of the Atlantic and eastern Indian sectors of the Southern Ocean. REcoM2 does however have a larger EP closer to the Antarctic.

The fraction of the the total biomass comprised by diatoms in the Southern Ocean defers between studies (Alvain et al., 2005; Hirata et al., 2011). In the present study, the diatoms are responsible for 25 % of the NPP south of 50° S, varying from 0 % in the very iron limited waters of the South Pacific to 100 % in the iron replete regions of the Weddell Sea and on the Patagonian shelf (Fig. 16). Vogt et al. (2013) compared the results of four ecosystem models and showed that the percentage of diatom biomass in the Southern Ocean differed significantly between them, ranging from 20 to 100 %. Our diatom percentage is accordingly within the spread of other models.

Production of the silicon-containing diatoms creates a sinking flux of biogenic silica that sums up to 21.5 Tmol Si yr^{-1} south of 50° S in the model (Table 3), which is close to the satellite-based estimate of 25 ± 4 Tmol Si yr^{-1} calculated south of 45° S (Dunne et al., 2007), but estimates vary significantly between studies (e.g. Moore et al., 2004; Jin et al., 2006; Holzer et al., 2014).

In REcoM2, the opal export in the Southern Ocean accounts for 29 % of the global opal export (Table 3). This number similarly varies widely between studies, with ours being lower than the 70 % suggested by Jin et al. (2006) and

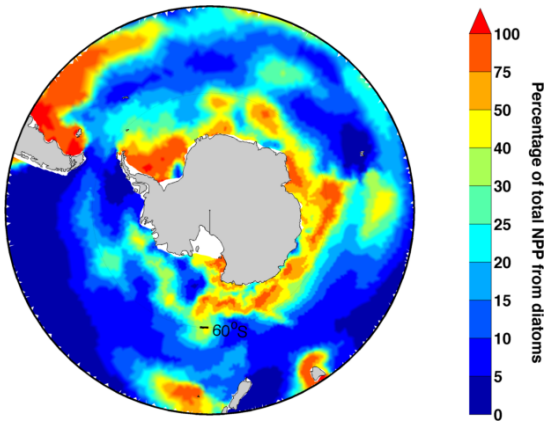

Figure 16. Contribution of diatoms to NPP in the model.

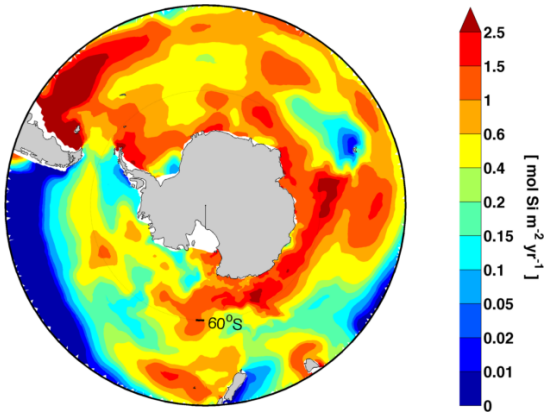

Figure 17. Modelled export of opal across 100 m depth plotted to the scale used by Moore et al. (2004).

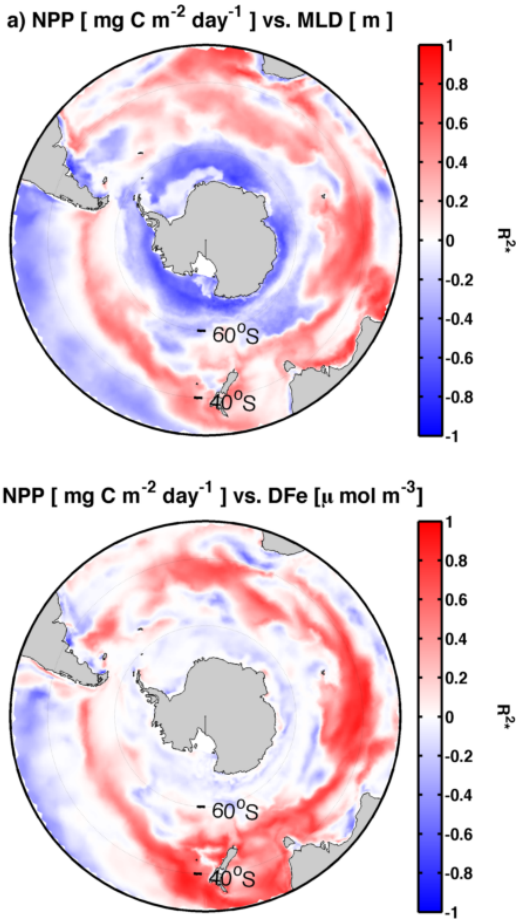

Figure 18. Maps showing coefficients of determination for cross-correlation between model results of **(a)** NPP and MLD and **(b)** NPP and DFe. DFe has been averaged over the upper 100 m of the water for the calculation. R^{2*} is defined as the temporal coefficient of correlation multiplied by the sign of the regression coefficient.

Holzer et al. (2014), but considering the area of the Southern Ocean, its contribution to the global opal flux is still large in our model.

High export fluxes of biogenic silica (Fig. 17) naturally occur in places with a corresponding high percentage of diatom production (Fig. 16). The largest values are found in the temporary ice zone between 60 and 70° S, as well as in the area east of Patagonia (Fig. 17), where dust and sediments supply iron to the surface water. A band of relatively high opal export is also present in the polar front in the Atlantic and Indian sectors of the Southern Ocean (Fig. 17). In most of the Southern Ocean, the modelled opal flux falls within a range of 0.4–2.5 mol Si m^{-2} yr^{-1}. This is slightly higher than the values given by Moore et al. (2004) and lower than the values of up to 9 mol Si m^{-2} yr^{-1} in Jin et al. (2006).

The absence of diatom production in the Pacific sector of the Southern Ocean (Fig. 16), leading to a low opal export in the area (Fig. 17), is notable and can be explained by the pronounced iron limitation of the Pacific, which also reaches into the Southern Ocean and limits production here.*

Control of bloom in the Southern Ocean

We will now examine the roles of MLD and iron concentration in explaining the seasonal variability of NPP. For this purpose we define R^{2*} as the temporal coefficient of determination multiplied by the sign of the regression slope. R^{2*} is calculated for each spatial point in the domain south of 30° S between NPP and the MLD (Fig. 18a) and between NPP and DFe (Fig. 18b), using the average iron concentration over the top 100 m of the ocean. The R^{2*} values show that the Southern Ocean is roughly divided into two zonal bands; one north of 60° S, in the area of the polar front (Moore et al., 1999), and one south of 60° S (Fig. 18).

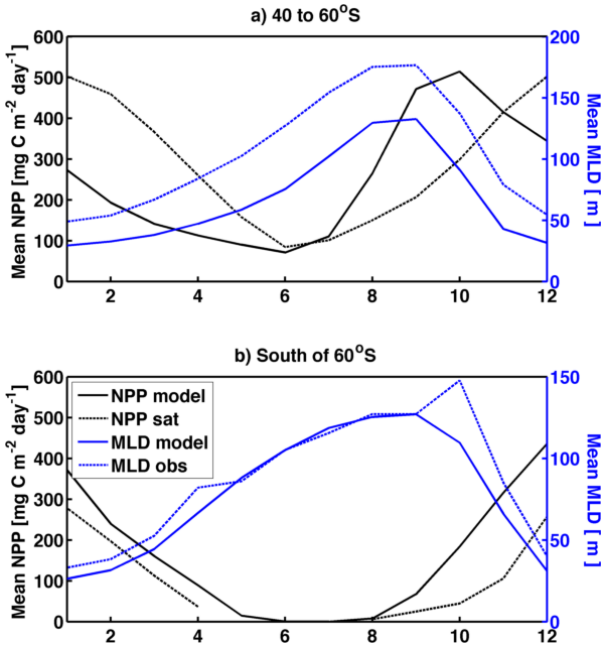

Figure 19. Seasonal change in mean modelled and observed NPP (SeaWIFS, 2012; Behrenfeld and Falkowski, 1997) and MLD (de Boyer Montegut et al., 2004) for **(a)** the Southern Ocean from 40 to 60° S and **(b)** south of 60° S.

The general picture north of 60° S is that the concentration of dissolved iron and the mixed layer depth both correlate positively with NPP (Fig. 18), indicating that production in the area mainly is iron controlled, and that production starts when the mixed layer deepens and brings iron and other nutrients to the surface. For the mean seasonal cycle of MLD and NPP north of 60° S (Fig. 19a), the magnitude of the modelled bloom fits nicely with the one from the satellite-based estimate, but the maximum occurs two months earlier. The mean MLD is well predicted by FESOM in the area (Fig. 19a), but it is consistently shallower than what is observed. This has the effect that the modelled phytoplankton receives a larger light intensity than is the case in the ocean, something that may affect the timing of the bloom. The mean iron concentration in the surface water is highly correlated with the depth of the mixed layer north of 60° S (Fig. 20a). The phytoplankton concentration starts increasing in July, when the iron concentration is high, and reaches a maximum in October, after which a combination of high grazer concentration and decreasing iron concentrations most likely causes the bloom to decline. Under nutrient and light replete conditions, the increase in biomass is a result of the balance between phytoplankton's maximum growth rate and the grazing (Behrenfeld, 2010; Hashioka et al., 2013). On the one hand, this indicates that the model's timing of the bloom could be changed by a smaller maximum growth rate, something that would change the phytoplankton dynamics on a global scale. On the other hand, the modelled zooplankton concentration is tightly coupled to the increase in phytoplankton concentration (Fig. 20a), and increasing the maximum grazing rate is another way of keeping the growth in biomass down. As modelled grazers are set to prefer nanophytoplankton over diatoms, this may further increase the diatom percentage in the Southern Ocean (Hashioka et al., 2013).

The NPP and MLD fields are negatively correlated south of 60° S, whereas correlation between NPP and DFe is close to zero here (Fig. 18). This indicates that light is the main limiting factor in this area and that iron is less important as a controlling factor. The intensity of the incoming light decreases with latitude, and is further decreased or blocked by the presence of sea ice during parts of the year, south of 60° S. The role of the sea ice for the timing of the spring bloom was highlighted by Taylor et al. (2013), who argued that the sea ice melting induces a shallower and more stable mixed layer, increasing the average light intensity received by the phytoplankton, thereby instigating growth. In our study, the modelled bloom is larger than what is estimated by the satellites south of 60° S, but the timing fits well (Fig. 19b). The difference can be explained by the aforementioned underestimation of NPP by the satellites. NPP starts increasing when the iron concentration is high and decreasing again when the iron concentration is low and the grazer concentration high (Fig. 20b).

It is worth noticing that the increase in production begins at the correct time in both areas, but that the rate of biomass increase is too high.

The sparse observations make it difficult to assess the validity of the modelled seasonal cycles of iron and zooplankton. Tagliabue et al. (2012) presented a seasonal cycle of DFe from the SR3 transect south of Tasmania. Their results indicate that the highest iron concentrations occur in January and February suggesting that our seasonal change in iron concentration, which peaks in September, is off. Our results, however, fit well with the model result from Hoppema et al. (2003), who also see a peak in the iron concentration in September.

4 Discussion

We have presented a skill assessment of an initial coupling between the biogeochemical REcoM2 and the Finite Element Sea Ice–Ocean Model (FESOM). FESOM's capability of locally increased resolution has not been fully utilized in the current study, with the smallest distance between neighbouring grid points being only a factor of about 10 smaller than the largest, and as with most biogeochemical models (e.g. Yool et al., 2011) we do not resolve eddies. The model run presented here can thus be regarded as a baseline run, from which future work that further explores the capabilities of the new coupling can proceed.

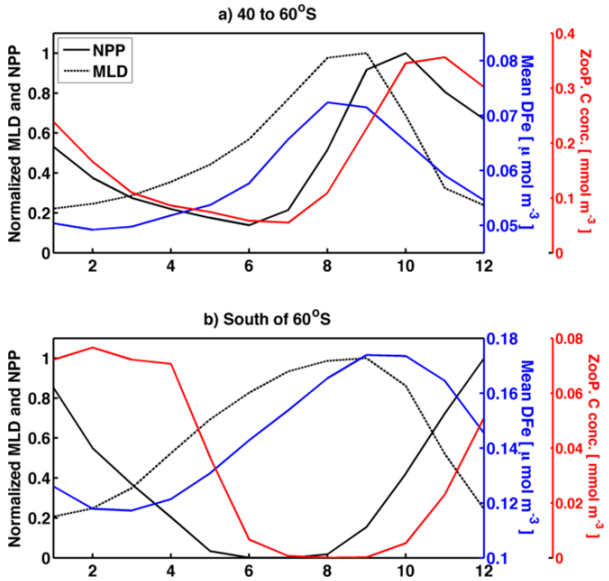

Figure 20. Seasonal change in the modelled NPP, MLD, DFe and zooplankton concentration for **(a)** the Southern Ocean from 40 to 60° S and **(b)** south of 60° S. DFe and zooplankton concentrations are averaged over the top 100 m of the ocean. NPP and MLD are normalized by the maximum of the monthly values.

Using the current resolution, the advantage of the new FESOM–REcoM2 coupling over the older MITgcm–REcoM2 coupling is not obvious, especially taking FESOM's larger demand for computer time into account. The strength of the new coupling will become clearer when new studies on specialized meshes have been carried out. We are currently looking into the effect of the ocean model on the biogeochemistry of the Southern Ocean by comparing two model runs between which only the ocean model differs. We assess the differences of the supply of iron to the surface mixed layer from below, and how it affects the NPP in the area (Schourup-Kristensen et al., 2014).

In regional models of the Southern Ocean, fixed boundary conditions must be added along the northern boundary where the Southern Ocean is connected to the Atlantic, Indian and Pacific oceans, introducing an extra potential for error in such models. Running the model in a global configuration has the advantage that the boundary conditions can be omitted.

As the dynamics of the iron supply is something we plan to study further in the future, and it is a feature we would like to improve, especially in the Pacific Ocean, we will now discuss how changes to the iron cycle may change the results of the model.

In the Southern Ocean, the spatial distribution of iron in the model is reasonable, but it tends towards low values (Table 2), something that may be explained by the crudely constrained external iron sources in the area. The strength of the sediment source varies widely between models (e.g. Moore and Braucher, 2008; Aumont and Bopp, 2006), and in REcoM2 we have an input of iron from the dust and the sediment source, which is in the smaller end of the range. Increasing the strength of the sediment source would especially impact the iron concentration locally in the Southern Ocean, though it has been shown that iron from the sediments can be carried far from the source region (Lam and Bishop, 2008). The Atlantic sector of the Southern Ocean would have an especially large input due to the presence of the Patagonian shelf and the Antarctic Peninsula (e.g. Lancelot et al., 2009), but it would most likely not change the supply to the pelagic areas in the Indian and Pacific Southern Ocean substantially. For the Southern and Pacific Oceans it would be especially important to further explore the influence of the aeolian and sedimentary iron sources as well as the input from ice in the polar areas.

In the remote parts of the Southern Ocean, the input of iron to the mixed layer from below plays a large role (De Baar et al., 1995; Löscher et al., 1997), and Tagliabue et al. (2014) showed that the entrainment of iron during deepening of the mixed layer was especially important. FESOM's MLD_{max} is too shallow in the Southern Ocean, especially in the region of the polar front in the Indian and Pacific sectors (Fig. 5), something likely affecting the degree of iron limitation in these two areas. The tight coupling between iron concentrations, NPP and MLD in the polar frontal area (Fig. 20a), further confirms the importance of entrainment as a supply mechanism of iron.

The lower iron input favors the smaller nanophytoplankton, which have a lower iron half-saturation constant, and thereby a lower requirement for iron. A larger input of iron would probably change the species composition towards more diatoms, but would not necessarily increase primary production (e.g. S. Wang et al., 2014). A higher percentage of diatoms would also possibly decrease the models surface silicon concentration, which tends towards high values in the Southern Ocean (Fig. 8). The effect on the silicon concentration is however complicated by the fact that the model's carbon and silicate cycles are decoupled under iron limitation, leading to a higher silicate uptake when the phytoplankton is iron stressed (Hohn, 2009).

In the Pacific Ocean, the surface iron concentration is very low (Fig. 9), inducing iron limitation (Fig. 10), which leads to a build-up of DIN in the surface water (Fig. 7) and low NPP (Fig. 12). The external input of iron from dust and sediment in the model is marginal in the equatorial and southern part of the Pacific and input from upwelling is consequently important here. FESOM produces a reasonable upwelling of 40 Sv along the Equator (Johnson et al., 2001), whereas upwelling is small along the west coast of South America. We have a low iron flux in the upwelled water along the equatorial Pacific in our model ($\sim 10\,\mu mol\,m^{-2}\,yr^{-1}$) compared to the values suggested by Gordon et al. (1997) and Aumont et al. (2003), who reported 44 and $68\,\mu mol\,m^{-2}\,yr^{-1}$, respectively. Our result is however higher

than the 5.1 µmol m^{-2} yr^{-1} suggested by Fung et al. (2000). The Fe : C ratio in the upwelled water in the equatorial area is 0.0015 µmol Fe mmol C^{-1} (6.66×10^6 mmol C mmol Fe^{-1}), which is significantly lower than the prescribed constant intracellular ratio of 0.005 µmol Fe mmol C^{-1} (2×10^6 mmol C mmol Fe^{-1}) in the modelled phytoplankton. The upwelled water consequently contains too little Fe to sustain growth, explaining why biological production is not able to utilize the upwelled DIN.

Allowing the model's phytoplankton to adapt to the conditions in the water with a varying intracellular Fe : C ratio would be a possible way to increase production, as the ratio would then decrease in areas with low iron concentrations. Variable intracellular Fe : C stoichiometry, as found by Sunda and Huntsman (1995) and Wilhelm et al. (2013), is used in other models (e.g. Moore et al., 2002; Aumont and Bopp, 2006). The intracellular Fe : C ratio in diatoms ranged from 0.002 µmol Fe mmol C^{-2} in the equatorial Pacific to 0.007 µmol Fe mmol C^{-2} in the subtropical gyres in Moore et al. (2002) and the former value fits remarkably well with our Fe : C ratio in the upwelled water in the Pacific. A lower intracellular Fe : C ratio in our model would lower the intracellular Fe : N ratio and bring it closer to the observed nutrient ratio in the upwelled water, indicating that implementing varying ratios would indeed improve the model's performance in the Pacific.

Other features that could potentially improve the iron cycle are spatially varying solubility of iron in the water, spatially varying ligand concentration and scavenging of iron onto dust particles in the water. The latter is present in the iron cycle used by Moore and Braucher (2008) and would likely counter the relatively high iron concentrations in the equatorial Atlantic and Indian oceans that are present in our model (Fig. 9).

5 Conclusions

In the current study we show that the newly coupled model FESOM–REcoM2 reproduces the large-scale productivity and surface nutrient patterns, with the main deficiency being the strongly iron limited Pacific Ocean. The totals NPP and EP are within the range of previous estimates, but in the lower end, mainly due to the low productivity in the Pacific. The ratio between EP and NPP is 20 %, similar to the result from Laws et al. (2000).

In the Southern Ocean, the modelled spatial mean fields are likewise reasonable, though the comparison here is hindered by the scarcity of observed data. South of 50° S, the totals NPP and EP agree well with previous estimates, as does the EP : NPP ratio of 36 %. Production is iron and light limited in the Southern Ocean making the external input of iron important as a controller of production.

On a global scale, the model provides reasonable seasonal variations of the NPP, but the main deficiency in the Southern Ocean is the early onset of the spring bloom in the area between 40 and 60° S.

Overall, the model results at the present resolution are comparable to those of other non-eddy-resolving biogeochemical models and it is well suited for studies of surface processes in the Southern Ocean on a timescale similar to the one used here.

Appendix A: Equations

In biogeochemical models, the biological state variables are subject to change by the ocean circulation through advection and turbulent mixing as well as by biological processes. Detritus further sinks vertically through the water column due to gravity, and exchange occurs across the surface and bottom boundaries for certain variables.

For a given volume of water, the change in concentration of a given biological state variable C can be expressed as follows:

$$\frac{\partial C}{\partial t} = -\boldsymbol{U} \cdot \nabla C + \nabla \cdot (\kappa \cdot \nabla C) + \mathrm{SMS}(C). \quad \text{(A1)}$$

Here, the term $-\boldsymbol{U} \cdot \nabla C$ represents the change in C due to advection, and $\boldsymbol{U} = (u, v, w)$ denotes the velocity of the water in the x, y and z directions, respectively.

For sinking state variables, the speed of vertical sinking ($\boldsymbol{V}_{\mathrm{det}} = (0, 0, w_{\mathrm{det}})$) is added to water's velocity in the advection term.

The turbulent motion is taken into account through the term $\nabla \cdot (\kappa \cdot \nabla C)$ where κ is the diffusivity tensor.

The term SMS(C), where SMS stands for sources minus sinks, represents the changes due to biological processes. This is the term that comprises the main body of biogeochemical models.

Certain state variables are subject to fluxes across the boundaries of the ocean model. For these, the flux between the ocean and the benthos (BenF) is calculated at the bottom of the ocean and the flux between the ocean and the atmosphere (AtmF) is calculated for the surface layer of the ocean.

In the following, the equations that make up the source minus sink code in the biogeochemical model REcoM2 are described.

The quota approach makes it necessary to have more tracers than in a model based on fixed ratios, as we need to know the intracellular concentration of each of the modelled elements. REcoM2 has a total of 21 oceanic state variables (Table A1) and four benthos compartments (Table A2).

Table A1. State variables; ocean

Variable	Description and unit
DIN	Dissolved inorganic nitrogen [mmol N m^{-3}]
DSi	Dissolved inorganic silicon [mmol N m^{-3}]
DFe	Dissolved inorganic iron [µmol Fe m^{-3}]
DIC	Dissolved inorganic carbon [mmol C m^{-3}]
Alk	Alkalinity [mmol C m^{-3}]
$\mathrm{PhyN_{nano}}$	Intracellular nitrogen concentration in nanophytoplankton [mmol N m^{-3}]
$\mathrm{PhyC_{nano}}$	Intracellular carbon concentration in nanophytoplankton [mmol C m^{-3}]
PhyCalc	Intracellular calcite concentration in nanophytoplankton [mmol $CaCO_3$ m^{-3}]
$\mathrm{PhyChl_{nano}}$	Intracellular chl *a* concentration in nanophytoplankton [mg Chl m^{-3}]
$\mathrm{PhyN_{dia}}$	Intracellular nitrogen concentration in diatoms [mmol N m^{-3}]
$\mathrm{PhyC_{dia}}$	Intracellular carbon concentration in diatoms [mmol C m^{-3}]
PhySi	Intracellular silicon concentration in diatoms [mmol Si m^{-3}]
$\mathrm{PhyChl_{dia}}$	Intracellular chl *a* concentration in diatoms [mg Chl m^{-3}]
ZooN	Zooplankton nitrogen concentration [mmol N m^{-3}]
ZooC	Zooplankton carbon concentration [mmol C m^{-3}]
DetN	Detritus nitrogen concentration [mmol N m^{-3}]
DetC	Detritus carbon concentration [mmol C m^{-3}]
DetCalc	Detritus calcite concentration [mmol $CaCO_3$ m^{-3}]
DetSi	Detritus silicon concentration [mmol Si m^{-3}]
DON	Extracellular dissolved organic nitrogen [mmol N m^{-3}]
DOC	Extracellular dissolved organic carbon [mmol C m^{-3}]

A1 Sources minus sinks

A1.1 DIN and DSi

$$\begin{aligned}\mathrm{SMS(DIN)} = & \underbrace{\rho_{\mathrm{N}} \cdot f_T \cdot \mathrm{DON}}_{\text{DON remineralization}} \\ & - \underbrace{V^{\mathrm{N}}_{\mathrm{nano}} \cdot \mathrm{PhyC_{nano}}}_{\text{N assimilation, nanophytoplankton}} \\ & - \underbrace{V^{\mathrm{N}}_{\mathrm{dia}} \cdot \mathrm{PhyC_{dia}}}_{\text{N assimilation, diatoms}}\end{aligned} \quad \text{(A2)}$$

$$\begin{aligned}\mathrm{SMS(DSi)} = & \underbrace{\rho^{T}_{\mathrm{Si}} \cdot \mathrm{DetSi}}_{\text{Remineralization of detritus}} \\ & - \underbrace{V^{\mathrm{Si}} \cdot \mathrm{PhyC_{dia}}}_{\text{Si assimilation, diatoms}}\end{aligned} \quad \text{(A3)}$$

The state variables DON, $\mathrm{PhyC_{nano}}$, $\mathrm{PhyC_{dia}}$ and DetSi are listed in Table A1. The value of the remineralization rate (ρ_{N}) is listed in Table A3. The temperature dependency of remineralization (f_T) is calculated in Eq. (A54) and the nitrogen and silicon assimilation rates ($V^{\mathrm{N}}_{\mathrm{nano}}$, $V^{\mathrm{N}}_{\mathrm{dia}}$ and V^{Si}, Table A4)

Table A2. State variables; benthos.

Variable	Description and unit
BenthosN	Benthos, vertically integrated N concentration [mmol N m^{-2}]
BenthosC	Benthos, vertically integrated C concentration [mmol C m^{-2}]
BenthosSi	Benthos, vertically integrated Si concentration [mmol Si m^{-2}]
BenthosCalc	Benthos, vertically integrated calcite concentration [mmol $CaCO_3$ m^{-2}]

Table A3. Degradation parameters for sources minus sinks equations.

Parameter	Value	Description and Unit
ϵ_N^{phy}	0.05	Phytoplankton excretion of organic N [day^{-1}]
ϵ_C^{phy}	0.1	Phytoplankton excretion of organic C [day^{-1}]
ϵ_N^{zoo}	0.1	Zooplankton excretion of organic N [day^{-1}]
ϵ_C^{zoo}	0.1	Zooplankton excretion of organic C [day^{-1}]
ρ_N^{ben}	0.005	Remineralization rate for benthos N [day^{-1}]
ρ_{Si}^{ben}	0.005	Remineralization rate for benthos Si [day^{-1}]
ρ_C^{ben}	0.005	Remineralization rate for benthos C [day^{-1}]
ρ_N	0.11	Temperature dependent remineralization of DON [day^{-1}]
ρ_C	0.1	Temperature dependent remineralization of DOC [day^{-1}]
ρ_{Si}	0.02	Temperature dependent remineralization of DetSi [day^{-1}]
ρ_{DetN}	0.165	Temperature dependent degradation of DetN [day^{-1}]
ρ_{DetC}	0.15	Temperature dependent degradation of DetN [day^{-1}]
deg_{Chl}	0.3	Chlorophyll *a* degradation rate [day^{-1}]

are calculated in Eqs. (A48) and (A49), respectively. ρ_{Si}^T will now be explained.

Silicon remineralization: the temperature dependent remineralization rate of silicon (ρ_{Si}^T, Table A4) is calculated following Kamatani (1982) up until a set maximum value:

$$\rho_{Si}^T = \min\left(1.32 \times 10^{16}\,\text{day}^{-1} \cdot \exp\left(\frac{-11\,200\,\text{K}}{T}\right), \rho_{Si} \cdot f_T\right). \quad \text{(A4)}$$

T is the local temperature (Table A4). The remineralization rate (ρ_{Si}) is listed in Table A3 and the temperature dependency (f_T) is calculated in Eq. (A54).

Input from benthos: the bottom grid point of the water further receives remineralized inorganic matter from the benthos:

$$\text{BenF}_{DIN} = \rho_N^{ben} \cdot \text{BenthosN} \quad \text{(A5)}$$

$$\text{BenF}_{DSi} = \rho_{Si}^{ben} \cdot \text{BenthosSi}. \quad \text{(A6)}$$

BenF_{DIN} and BenF_{DSi} (Table A5) denote the fluxes of DIN and DSi into the bottom layer of the ocean. ρ_N^{ben} and ρ_{Si}^{ben} (Table A3) are constant remineralization rates. BenthosN and BenthosSi denote the vertically integrated benthos concentration of dissolved nitrogen and silicate, respectively (Table A2).

A1.2 DFe

The intracellular iron concentration is connected to the intracellular carbon concentration through an assumed constant ratio ($q^{Fe:C}$; Table A6). Biological uptake and release of iron is likewise connected to uptake and release of carbon.

$$\begin{aligned}\text{SMS(DFe)} = &-q^{Fe:C} \cdot \underbrace{(P_{nano} - r_{nano}) \cdot \text{PhyC}_{nano}}_{\text{Nanophytoplankton net growth}} \\ &- q^{Fe:C} \cdot \underbrace{(P_{dia} - r_{dia}) \cdot \text{PhyC}_{dia}}_{\text{Diatom net growth}} \\ &+ q^{Fe:C} \cdot \underbrace{\epsilon_C^{phy} \cdot f_{lim,nano}^{N:Cmax} \cdot \text{PhyC}_{nano}}_{\text{Excretion from nanophytoplankton}} \\ &+ q^{Fe:C} \cdot \underbrace{\epsilon_C^{phy} \cdot f_{lim,dia}^{N:Cmax} \cdot \text{PhyC}_{dia}}_{\text{Excretion from diatoms}} \\ &+ q^{Fe:C} \cdot \underbrace{\rho_{DetC} \cdot f_T \cdot \text{DetC}}_{\text{Remineralization of detritus}} \\ &+ q^{Fe:C} \cdot (\underbrace{\epsilon_C^{zoo} \cdot \text{ZooC}}_{\text{Zooplankton excretion}} + \underbrace{r_{zoo} \cdot \text{ZooC}}_{\text{and respiration}}) \\ &- \underbrace{\kappa_{Fe} \cdot \text{DetC} \cdot \text{Fe}'}_{\text{Scavenging}} \end{aligned} \quad \text{(A7)}$$

The state variables PhyC_{nano}, PhyC_{dia}, DetC and ZooC are listed in Table A1. The value for the constant Fe : C ratio ($q^{Fe:C}$) is listed in Table A6 and the DOC excretion rates from phyto- and zooplankton (ϵ_C^{phy} and ϵ_C^{zoo}) and the degradation rate for detritus C (ρ_{DetC}) are listed in Table A3. The

Table A4. Model variables.

Variable	Description and unit
Agg	Aggregation rate [day^{-1}]
$\mathrm{Diss}_{\mathrm{Calc}}$	Rate of calcium carbonate dissolution [day^{-1}]
Fe'	Concentration of free iron [$\mu\mathrm{mol\,Fe\,m}^{-3}$]
f_T	Temperature dependence of rates, dimensionless
G'	Phytoplankton available for food intake [$\mathrm{mmol\,N\,m}^{-3}$]
G_{tot}	Total zooplankton grazing rate [$\mathrm{mmol\,N\,m}^{-3}\,\mathrm{day}^{-1}$]
G_{nano}	Nanophytoplankton-specific zooplankton grazing rate [$\mathrm{mmol\,N\,m}^{-3}\,\mathrm{day}^{-1}$]
G_{dia}	Diatom-specific zooplankton grazing rate [$\mathrm{mmol\,N\,m}^{-3}\,\mathrm{day}^{-1}$]
PAR	Photosynthetically available radiation [$\mathrm{W\,m}^{-2}$]
$P_{\mathrm{nano}}, P_{\mathrm{dia}}$	C-specific actual rate of photosynthesis [day^{-1}]
P_{max}	C-specific light saturated rate of photosynthesis [day^{-1}]
$r_{\mathrm{nano}}, r_{\mathrm{dia}}$	Phytoplankton respiration rate [day^{-1}]
r_{zoo}	Zooplankton respiration rate [day^{-1}]
ρ^T_{Si}	Temperature dependent remineralization rate of Si [day^{-1}]
$S^{\mathrm{chl}}_{\mathrm{nano}}, S^{\mathrm{chl}}_{\mathrm{dia}}$	Rate of chlorophyll *a* synthesis [$\mathrm{mg\,Chl\,mmol\,C}^{-1}\,\mathrm{day}^{-1}$]
T	Local temperature [K]
$V^{\mathrm{N}}_{\mathrm{nano}}, V^{\mathrm{N}}_{\mathrm{dia}}$	N assimilation rate for nanophytoplankton and diatoms, respectively [$\mathrm{mmol\,N\,mmol\,C}^{-1}\,\mathrm{day}^{-1}$]
V^{Si}	Diatom Si assimilation rate [$\mathrm{mmol\,Si\,mmol\,C}^{-1}\,\mathrm{day}^{-1}$]
w_{det}	Sinking velocity of detritus [$\mathrm{m\,day}^{-1}$]

Table A5. Benthos variables.

Variable	Description and unit
$\mathrm{BenF}_{\mathrm{Alk}}$	Flux of alkalinity from benthos to bottom water [$\mathrm{mmol\,m}^{-2}\,\mathrm{day}^{-1}$
$\mathrm{BenF}_{\mathrm{DIC}}$	Flux of C from benthos to bottom water [$\mathrm{mmol\,C\,m}^{-2}\,\mathrm{day}^{-1}$]
$\mathrm{BenF}_{\mathrm{DIN}}$	Flux of N from benthos to bottom water [$\mathrm{mmol\,N\,m}^{-2}\,\mathrm{day}^{-1}$]
$\mathrm{BenF}_{\mathrm{DSi}}$	Flux of Si from benthos to bottom water [$\mathrm{mmol\,Si\,m}^{-2}\,\mathrm{day}^{-1}$]
$\mathrm{BenF}_{\mathrm{Fe}}$	Flux of Fe from benthos to bottom water [$\mu\mathrm{mol\,Fe\,m}^{-2}\,\mathrm{day}^{-1}$]
$\mathrm{BenF}_{\mathrm{DetCalc}}$	Flux of detritus calcite from the water to the benthos [$\mathrm{mmol\,CaCO_3\,m}^{-2}\,\mathrm{day}^{-1}$]
$\mathrm{BenF}_{\mathrm{DetC}}$	Flux of detritus C from the water to the benthos [$\mathrm{mmol\,C\,m}^{-2}\,\mathrm{day}^{-1}$]
$\mathrm{BenF}_{\mathrm{DetN}}$	Flux of detritus N from the water to the benthos [$\mathrm{mmol\,N\,m}^{-2}\,\mathrm{day}^{-1}$]
$\mathrm{BenF}_{\mathrm{DetSi}}$	Flux of detritus Si from the water to the benthos [$\mathrm{mmol\,Si\,m}^{-2}\,\mathrm{day}^{-1}$]

Table A6. Parameters for iron calculations.

Parameter	Value	Description and unit
$q^{\mathrm{Fe:C}}$	0.005	Intracellular Fe : C ratio [$\mu\mathrm{mol\,Fe\,mmol\,C}^{-1}$]
K_{Fe_L}	100.0	Iron stability constant [$\mathrm{m}^{-3}\,\mu\mathrm{mol}$]
L_{T}	1.0	Total ligand concentration [$\mu\mathrm{mol\,m}^{-3}$]
κ_{Fe}	0.0312	Scavenging rate of iron [$\mathrm{m}^3\,\mathrm{mmol\,C}^{-1}\,\mathrm{day}^{-1}$]
$q^{\mathrm{Fe:C}}_{\mathrm{sed}}$	0.011	Fe : C ratio for remineralization of Fe from benthos [$\mu\mathrm{mol\,Fe\,mmol\,C}^{-1}$]

phytoplankton respiration (r_{nano} and r_{dia}) is calculated in Eq. (A45), the photosynthesis (P_{nano} and P_{dia}) in Eq. (A44), the limitation by intracellular nitrogen ($f_{\text{lim}}^{\text{N:Cmax}}$) is described in Sect. A6.1, and the temperature dependency (f_T) is calculated in Eq. (A54). The respiration by zooplankton (r_{zoo}) is calculated in Eq. (A46) and the scavenging will now be explained.

Scavenging: the calculation of the scavenging in REcoM2 is based on Parekh et al. (2004), case III. Here, the total concentration of dissolved iron (Fe_T) is divided into iron bound to ligands (Fe_L) and free iron (Fe', Table A4):

$$\text{Fe}_\text{T} = \text{Fe}_L + \text{Fe}'. \tag{A8}$$

Iron complexed with organic ligands is protected from scavenging. The total ligand concentration (L_T) can be written:

$$L_\text{T} = \text{Fe}_L + L'. \tag{A9}$$

Here L' denotes the free ligands.

We assume that the reaction between free iron and free ligand ($L' + \text{Fe}' \rightleftharpoons \text{Fe}_L$) is fast enough to be in equilibrium:

$$K_{\text{Fe}_L} = \frac{[\text{Fe}_L]}{[\text{Fe}'] \cdot [L']}. \tag{A10}$$

By prescribing the value of the conditional stability constant (K_{Fe_L}) as well as the assumed constant total ligand concentration (L_T) and combining Eqs. (A8), (A9) and (A10), we can calculate the concentration of free iron (Fe'). This is then used to calculate the scavenging of Fe', which is assumed to be correlated with the concentration of detritus carbon (Eq. A7). The values for K_{Fe_L} and L_T are listed in Table A6.

The value for the scavenging rate (κ_{Fe}, Table A6) is an important controller of deep-water iron concentrations.

Iron input from dust: the surface layer of the ocean receives an input of iron from aeolian dust deposition. Dust is assumed to contain 3.5 % iron of which 1.5 % is instantaneously dissolved in the ocean. Sea ice blocks dust, and the dust falling here is lost from the system.

Iron input from the benthos: the release of iron to the bottom layer of water is assumed to be proportional to the release of inorganic carbon. This parameterization is based on the work by Elrod et al. (2004). It is calculated as follows:

$$\text{BenF}_\text{Fe} = \rho_\text{C}^\text{ben} \cdot \text{BenthosC} \cdot q_\text{sed}^\text{Fe:C}. \tag{A11}$$

Here BenF_Fe (Table A5) is the flux of iron into the bottom layer of the ocean. ρ_C^ben (Table A3) is the remineralization rate for the benthos carbon and $q_\text{sed}^\text{Fe:C}$ (Table A6) is the iron : carbon ratio for the flux. BenthosC (Table A2) denotes the vertically integrated carbon concentration in the benthos compartment.

A1.3 DIC

$$\begin{aligned}\text{SMS(DIC)} = &\underbrace{(r_{\text{nano}} - P_{\text{nano}}) \cdot \text{PhyC}_{\text{nano}}}_{\text{Nanophytoplankton net respiration}} \\ &+ \underbrace{(r_{\text{dia}} - P_{\text{dia}}) \cdot \text{PhyC}_{\text{dia}}}_{\text{Diatom net respiration}} \\ &+ \underbrace{\rho_\text{C} \cdot f_T \cdot \text{DOC}}_{\text{Remineralization of DOC}} \\ &+ \underbrace{r_{\text{zoo}} \cdot \text{ZooC}}_{\text{Zoo respiration}} + \underbrace{\text{Diss}_{\text{calc}} \cdot \text{DetCalc}}_{\text{Calcite dissolution from detritus}} \\ &- \underbrace{\psi \cdot P_{\text{nano}} \cdot \text{PhyC}_{\text{nano}}}_{\text{Calcification}}\end{aligned} \tag{A12}$$

The state variables $\text{PhyC}_{\text{nano}}$, PhyC_{dia}, DOC, ZooC and DetCalc are described in Table A1. Respiration by nanophytoplankton (r_{nano}), diatoms (r_{dia}) and zooplankton (r_{zoo}) is calculated in Eqs. (A45) and (A46) and the photosynthesis terms (P_{nano} and P_{dia}) in Eq. (A44).

The value of the remineralization rate ρ_C is listed in Table A3 and the temperature dependency (f_T) is calculated in Eq. (A54).

The dissolution of calcite from detritus ($\text{Diss}_{\text{calc}}$) is calculated in Eq. (A34), and the value of the calcite production ratio (ψ) is listed in Table A7. ψ denotes the percentage of the nanophytoplankton that are calcifiers, and their PIC : POC ratio.

Atmospheric input: the DIC concentration of the surface grid point is affected by the air–sea flux of CO_2. It is calculated according to the guidelines provided by the Ocean Carbon Model Intercomparison Project (Orr et al., 1999). In the calculations the surface water CO_2 concentration, alkalinity, temperature and salinity are taken into account.

Input from benthos: the bottom grid point of the water further receives remineralized inorganic carbon from the benthos:

$$\text{BenF}_\text{DIC} = \rho_\text{C}^\text{ben} \cdot \text{BenthosC} + \text{Diss}_{\text{calc}} \cdot \text{BenthosCalc}\ . \tag{A13}$$

BenF_DIC (Table A5) denotes the flux of DIC into the bottom layer of the ocean and ρ_C^ben (Table A3) is a constant remineralization rate. The calcite dissolution rate ($\text{Diss}_{\text{calc}}$) is calculated in Eq. (A34). BenthosC and BenthosCalc (Table A2) denote the vertically integrated carbon and calcium carbonate concentration in the benthos compartment.

A1.4 Total alkalinity

The model's total alkalinity is changed by phytoplankton uptake of nutrients (nitrate and phosphate), precipitation and dissolution of calcium carbonate and remineralization of organic matter (Wolf-Gladrow et al., 2007). Phosphorous is not described in the model, but is taken into account using the

Table A7. Parameters for sources minus sinks equations.

Parameter	Value	Description and unit
ψ	0.1	Calcite production ratio, dimensionless
γ	0.3	Fraction of grazing flux to zooplankton pool, dimensionless
m_{zoo}	0.05	Zooplankton mortality rate $[\mathrm{m^3\,mmol\,N^{-1}\,day^{-1}}]$
ϕ_{phy}	0.02	Max aggregation loss parameter for phytoplankton N $[\mathrm{m^3\,mmol\,N^{-1}\,day^{-1}}]$
ϕ_{det}	0.22	Max aggregation loss parameter for detritus N $[\mathrm{m^3\,mmol\,N^{-1}\,day^{-1}}]$
w_0	20.0	Detritus sinking speed at surface $[\mathrm{m\,day^{-1}}]$

constant P : N ratio of 1 : 16.

$$\begin{aligned}\mathrm{SMS(Alk)} = (1+1/16)\cdot & \underbrace{V^{\mathrm{N}}_{\mathrm{nano}}\cdot \mathrm{PhyC_{nano}}}_{\text{N assimilation, nanophytoplankton}} \\ +(1+1/16)\cdot & \underbrace{V^{\mathrm{N}}_{\mathrm{dia}}\cdot \mathrm{PhyC_{dia}}}_{\text{N assimilation, diatoms}} \\ -(1+1/16)\cdot & \underbrace{\rho_{\mathrm{N}}\cdot f_T\cdot \mathrm{DON}}_{\text{Remineralization of DON}} \\ +2\cdot & \underbrace{\mathrm{Diss_{calc}}\cdot \mathrm{DetCaCO_3}}_{\text{Calcite dissolution from detritus}} \\ -2\cdot & \underbrace{\psi\cdot P_{\mathrm{nano}}\cdot \mathrm{PhyC_{nano}}}_{\text{Calcification}}\end{aligned} \tag{A14}$$

The state variables $\mathrm{PhyC_{nano}}$, $\mathrm{PhyC_{dia}}$, DON and DetCalc are described in Table A1. The N assimilation ($V^{\mathrm{N}}_{\mathrm{nano}}$ and $V^{\mathrm{N}}_{\mathrm{dia}}$) is calculated in Eq. (A48). The remineralization rate (ρ_{N}) can be found in Table A3 and the temperature dependency (f_T) is calculated in Eq. (A54).

Dissolution of calcium carbonate from detritus adds CO_3^{2-} to the water and thereby increases the alkalinity with two moles for each dissolved mole calcium carbonate. $\mathrm{Diss_{calc}}$ is calculated in Eq. (A34).

The parameter ψ, specifying the calcifying fraction of the nanophytoplankton, is listed in Table A7 and the photosynthesis (P_{nano}) is calculated in Eq. (A44).

Input from benthos: the alkalinity of the bottom grid point of the water is affected by the remineralization of DIN, and thereby also DIP as well as dissolution of calcite from the benthos:

$$\begin{aligned}\mathrm{BenF_{Alk}} = & (1+1/16)\cdot \rho^{\mathrm{ben}}_{\mathrm{N}}\cdot \mathrm{BenthosN} \\ & +2\cdot \mathrm{Diss_{calc}}\cdot \mathrm{BenthosCalc.}\end{aligned} \tag{A15}$$

$\mathrm{BenF_{Alk}}$ (Table A5) denotes the flux of alkalinity into the bottom layer of the ocean. The dissolution rate ($\mathrm{Diss_{calc}}$) is calculated in Eq. (A34), and the remineralization rate ρ^{ben}_N is listed in Table A3. BenthosN and BenthosC (Table A2) denote the vertically integrated nitrogen and carbon concentration in the benthos compartment.

A1.5 Phytoplankton N

$$\begin{aligned}\mathrm{SMS(PhyN_{nano})} = & \underbrace{V^{\mathrm{N_{nano}}}\cdot \mathrm{PhyC_{nano}}}_{\text{N assimilation}} \\ & -\underbrace{\epsilon^{\mathrm{phy}}_{\mathrm{N}}\cdot f^{\mathrm{N:Cmax}}_{\mathrm{lim,\,nano}}\cdot \mathrm{PhyN_{nano}}}_{\text{DON excretion}} \\ & -\underbrace{\mathrm{Agg}\cdot \mathrm{PhyN_{nano}}}_{\text{Aggregation loss}} - \underbrace{G_{\mathrm{nano}}}_{\text{Grazing loss}}\end{aligned} \tag{A16}$$

$$\begin{aligned}\mathrm{SMS(PhyN_{dia})} = & \underbrace{V^{\mathrm{N}}_{\mathrm{dia}}\cdot \mathrm{PhyC_{dia}}}_{\text{N assimilation}} \\ & -\underbrace{\epsilon^{\mathrm{phy}}_{\mathrm{N}}\cdot f^{\mathrm{N:Cmax}}_{\mathrm{lim,\,dia}}\cdot \mathrm{PhyN_{dia}}}_{\text{DON excretion}} \\ & -\underbrace{\mathrm{Agg}\cdot \mathrm{PhyN_{dia}}}_{\text{Aggregation loss}} - \underbrace{G_{\mathrm{dia}}}_{\text{Grazing loss}}\end{aligned} \tag{A17}$$

The state variables $\mathrm{PhyC_{nano}}$, $\mathrm{PhyN_{nano}}$, $\mathrm{PhyC_{dia}}$ and $\mathrm{PhyN_{dia}}$ are described in Table A1.

The nitrogen assimilation ($V^{\mathrm{N}}_{\mathrm{nano}}$ and $V^{\mathrm{N}}_{\mathrm{dia}}$) is calculated in Eq. (A48) and the constant excretion rate ($\epsilon^{\mathrm{phy}}_{\mathrm{N}}$) is listed in Table A3. When the N : C ratio becomes too high, excretion of DOC is downregulated by the limiter function ($f^{\mathrm{N:Cmax}}_{\mathrm{lim}}$) described in Sect. A6.1. A further loss term is phytoplankton aggregation (Agg), which transfers N to the detritus pools (Eq. A27).

The grazing loss (G_{nano} and G_{dia}) is calculated in Eqs. (A52) and (A53), respectively.

A1.6 Phytoplankton C

$$\begin{aligned}\mathrm{SMS(PhyC_{nano})} = & \underbrace{(P_{\mathrm{nano}}-r_{\mathrm{nano}})\cdot \mathrm{PhyC_{nano}}}_{\text{Net photosynthesis}} \\ & -\underbrace{\mathrm{Agg}\cdot \mathrm{PhyC_{nano}}}_{\text{Aggregation loss}} \\ & -\underbrace{\epsilon^{\mathrm{phy}}_{\mathrm{C}}\cdot f^{\mathrm{N:Cmax}}_{\mathrm{lim,\,nano}}\cdot \mathrm{PhyC_{nano}}}_{\text{Excretion of DOC}} \\ & -\underbrace{q^{\mathrm{C:N}}_{\mathrm{nano}}\cdot G_{\mathrm{nano}}}_{\text{Grazing loss}}\end{aligned} \tag{A18}$$

$$\begin{aligned}\mathrm{SMS(PhyC_{dia})} = & \underbrace{(P_{\mathrm{dia}}-r_{\mathrm{dia}})\cdot \mathrm{PhyC_{dia}}}_{\text{Net photosynthesis}} \\ & -\underbrace{\mathrm{Agg}\cdot \mathrm{PhyC_{dia}}}_{\text{Aggregation loss}} - \underbrace{\epsilon^{\mathrm{phy}}_{\mathrm{C}}\cdot f^{\mathrm{N:Cmax}}_{\mathrm{lim,\,dia}}\cdot \mathrm{PhyC_{dia}}}_{\text{Excretion of DOC}} \\ & -\underbrace{q^{\mathrm{C:N}}_{\mathrm{dia}}\cdot G_{\mathrm{dia}}}_{\text{Grazing loss}}\end{aligned} \tag{A19}$$

The state variables $\mathrm{PhyC_{nano}}$ and $\mathrm{PhyC_{dia}}$ are described in Table A1. The photosynthesis (P_{nano} and P_{dia}) is calculated

in Eq. (A44) and the respiration (r_{nano} and r_{dia}) in Eq. (A45). The constant DOC excretion rate ($\epsilon_{\mathrm{C}}^{\mathrm{phy}}$, Table A3) is downregulated by the limitation factor $f_{\mathrm{lim}}^{\mathrm{N:Cmax}}$ (Sect. A6.1) when the N : C ratio becomes too high.

Aggregation of phytoplankton (Agg) is calculated in Eq. (A27) and grazing (G_{nano} and G_{dia}) in Eqs. (A52) and (A53), respectively. $q^{\mathrm{C:N}} = \mathrm{PhyC} / \mathrm{PhyN}$, is used to convert the grazing units from mmol N to mmol C.

A1.7 Phytoplankton $CaCO_3$

Calcifiers are assumed to comprise a certain fraction of the total nanophytoplankton concentration, specified by the parameter ψ (Table A7), tying the calcite production of calcifiers to the growth of nanophytoplankton.

$$\begin{aligned}\mathrm{SMS(PhyCalc)} = {} & \underbrace{\psi \cdot P_{\mathrm{nano}} \cdot \mathrm{PhyC_{nano}}}_{\text{Calcification}} - \underbrace{r_{\mathrm{nano}} \cdot \mathrm{PhyCalc}}_{\text{Respiration}} \\ & - \underbrace{G_{\mathrm{nano}} \cdot q_{\mathrm{nano}}^{\mathrm{CaCO_3:N}}}_{\text{Grazing loss}} \\ & - \underbrace{\epsilon_{\mathrm{C}}^{\mathrm{phy}} \cdot f_{\mathrm{lim,\,nano}}^{\mathrm{N:Cmax}} \cdot \mathrm{PhyCalc}}_{\text{Excretion loss}} \\ & - \underbrace{\mathrm{Agg} \cdot \mathrm{PhyCalc}}_{\text{Aggregation loss}} \end{aligned} \tag{A20}$$

The state variables $\mathrm{PhyC_{nano}}$ and PhyCalc are described in Table A1. The value for the calcifier fraction (ψ) is listed in Table A7 and the excretion parameter ($\epsilon_{\mathrm{C}}^{\mathrm{phy}}$) in Table A3. The excretion loss is downregulated by the limiter function $f_{\mathrm{lim,\,nano}}^{\mathrm{N:Cmax}}$ (Sect. A6.1) when the intracellular N : C ratio approaches a maximum value. The photosynthesis (P_{nano}) is calculated in Eq. (A44), the respiration (r_{nano}) in Eq. (A45), the grazing on nanophytoplankton (G_{nano}) in Eq. (A52) and the aggregation rate (Agg) is calculated in Eq. (A27). $q_{\mathrm{nano}}^{\mathrm{CaCO_3:N}} = \mathrm{PhyCaCO_3} / \mathrm{PhyN_{nano}}$.

A1.8 Diatom silicon

$$\begin{aligned}\mathrm{SMS(PhySi)} = {} & \underbrace{V^{\mathrm{Si}} \cdot \mathrm{PhyC_{dia}}}_{\text{Diatom Si assimilation}} - \underbrace{\epsilon_{\mathrm{N}}^{\mathrm{phy}} \cdot f_{\mathrm{lim,\,dia}}^{\mathrm{N:Cmax}} \cdot \mathrm{PhySi}}_{\text{Excretion to detritus}} \\ & - \underbrace{\mathrm{Agg} \cdot \mathrm{PhySi}}_{\text{Aggregation loss}} - \underbrace{G_{\mathrm{dia}} \cdot q^{\mathrm{Si:N}}}_{\text{Grazing loss}} \end{aligned} \tag{A21}$$

The state variables $\mathrm{PhyC_{dia}}$ and PhySi are described in Table A1. The silicon assimilation rate (V^{Si}) is calculated in Eq. (A49), the aggregation rate (Agg) in Eq. (A27) and the grazing on diatoms (G_{dia}) is calculated in Eq. (A53). The limiter function ($f_{\mathrm{lim}}^{\mathrm{N:Cmax}}$) is described in Sect. A6.1. The value of the excretion parameter ($\epsilon_{\mathrm{N}}^{\mathrm{phy}}$) is listed in Table A3 and the intracellular ratio between diatom silicon and carbon is defined as $q^{\mathrm{Si:N}} = \mathrm{PhySi} / \mathrm{PhyN_{dia}}$.

A1.9 Phytoplankton Chl *a*

$$\begin{aligned}\mathrm{SMS(PhyChl_{nano})} = {} & \underbrace{S_{\mathrm{nano}}^{\mathrm{chl}} \cdot \mathrm{PhyC_{nano}}}_{\text{Chl } a \text{ synthesis}} - \underbrace{G_{\mathrm{nano}} \cdot q_{\mathrm{nano}}^{\mathrm{Chl:N}}}_{\text{Grazing loss}} \\ & - \underbrace{\mathrm{deg_{chl}} \cdot \mathrm{PhyChl_{nano}}}_{\text{Degradation loss}} \\ & - \underbrace{\mathrm{Agg} \cdot \mathrm{PhyChl_{nano}}}_{\text{Aggregation loss}} \end{aligned} \tag{A22}$$

$$\begin{aligned}\mathrm{SMS(PhyChl_{dia})} = {} & \underbrace{S_{\mathrm{dia}}^{\mathrm{chl}} \cdot \mathrm{PhyC_{dia}}}_{\text{Chl } a \text{ synthesis}} - \underbrace{G_{\mathrm{dia}} \cdot q_{\mathrm{dia}}^{\mathrm{Chl:N}}}_{\text{Grazing loss}} \\ & - \underbrace{\mathrm{deg_{chl}} \cdot \mathrm{PhyChl_{dia}}}_{\text{Degradation loss}} \\ & - \underbrace{\mathrm{Agg} \cdot \mathrm{PhyChl_{dia}}}_{\text{Aggregation loss}} \end{aligned} \tag{A23}$$

The state variables $\mathrm{PhyC_{nano}}$, $\mathrm{PhyC_{dia}}$, $\mathrm{PhyChl_{nano}}$ and $\mathrm{PhyChl_{dia}}$ are described in Table A1. The chlorophyll *a* synthesis (S^{chl}) is calculated in Eq. (A47), the aggregation (Agg) in Eq. (A27) and the degradation parameter ($\mathrm{deg_{chl}}$) is listed in Table A3. The grazing fluxes (G_{nano} and G_{dia}) are calculated in Eqs. (A52) and (A53), respectively. The conversion factor from mmol N to mg Chl *a* is defined as $q^{\mathrm{Chl:N}} = \mathrm{PhyChl} / \mathrm{PhyN}$.

A1.10 Zooplankton

$$\begin{aligned}\mathrm{SMS(ZooN)} = {} & \underbrace{\gamma \cdot (G_{\mathrm{nano}} + G_{\mathrm{dia}})}_{\text{Grazing on phytoplankton}} - \underbrace{m_{\mathrm{zoo}} \cdot \mathrm{ZooN}^2}_{\text{Zooplankton mortality}} \\ & - \underbrace{\epsilon_{\mathrm{N}}^{\mathrm{zoo}} \cdot \mathrm{ZooN}}_{\text{Excretion of DON}} \end{aligned} \tag{A24}$$

$$\begin{aligned}\mathrm{SMS(ZooC)} = {} & \underbrace{\gamma \cdot (G_{\mathrm{nano}} \cdot q_{\mathrm{nano}}^{\mathrm{C:N}} + G_{\mathrm{dia}} \cdot q_{\mathrm{dia}}^{\mathrm{C:N}})}_{\text{Grazing on phytoplankton}} \\ & - \underbrace{m_{\mathrm{zoo}} \cdot \mathrm{ZooN}^2 \cdot q_{\mathrm{zoo}}^{\mathrm{C:N}}}_{\text{Zooplankton mortality}} - \underbrace{r_{\mathrm{zoo}} \cdot \mathrm{ZooC}}_{\text{Respiration loss}} \\ & - \underbrace{\epsilon_{\mathrm{C}}^{\mathrm{zoo}} \cdot \mathrm{ZooC}}_{\text{Excretion of DOC}} \end{aligned} \tag{A25}$$

The state variables ZooN and ZooC are described in Table A1. It is assumed, due to sloppy feeding, that only a fraction of the grazed phytoplankton (γ, Table A7) enters the zooplankton pool. The rest is transferred to detritus.

Grazing by nanophytoplankton and diatoms (G_{nano} and G_{dia}) is calculated in Eqs. (A52) and (A53), respectively. The respiration by zooplankton (r_{zoo}) is calculated in Eq. (A46). The value of the mortality parameter (m_{zoo}) is listed in Table A7 and the DON and DOC excretion ($\epsilon_{\mathrm{N}}^{\mathrm{zoo}}$ and $\epsilon_{\mathrm{C}}^{\mathrm{zoo}}$) in Table A3.

The quotas $q_{\text{nano}}^{\text{C:N}}$ and $q_{\text{dia}}^{\text{C:N}}$ convert the units of the grazing from mmol N to mmol C and are defined as follows: $q_{\text{nano}}^{\text{C:N}} = \text{PhyC}_{\text{nano}} / \text{PhyN}_{\text{nano}}$ and $q_{\text{dia}}^{\text{C:N}} = \text{PhyC}_{\text{dia}} / \text{PhyN}_{\text{dia}}$.

A1.11 Detritus N and C

$$\begin{aligned}\text{SMS(DetN)} = &\underbrace{(G_{\text{nano}} + G_{\text{dia}}) \cdot (1-\gamma)}_{\text{Sloppy feeding}} + \underbrace{m_{\text{zoo}} \cdot \text{ZooN}^2}_{\text{Zooplankton mortality}} \\ &+ \underbrace{\text{Agg} \cdot (\text{PhyN}_{\text{nano}} + \text{PhyN}_{\text{dia}})}_{\text{Phytoplankton aggregation}} \\ &- \underbrace{\rho_{\text{DetN}} \cdot f_T \cdot \text{DetN}}_{\text{Degradation to DON}} \\ \text{SMS(DetC)} = &\underbrace{(G_{\text{nano}} \cdot q_{\text{nano}}^{\text{C:N}} + G_{\text{dia}} \cdot q_{\text{dia}}^{\text{C:N}}) \cdot (1-\gamma)}_{\text{Sloppy feeding}} \\ &+ \underbrace{m_{\text{zoo}} \cdot \text{ZooN}^2 \cdot q_{\text{zoo}}^{\text{C:N}}}_{\text{Zooplankton mortality}} \\ &+ \underbrace{\text{Agg} \cdot (\text{PhyC}_{\text{nano}} + \text{PhyC}_{\text{dia}})}_{\text{Phytoplankton aggregation}} \\ &- \underbrace{\rho_{\text{DetC}} \cdot f_T \cdot \text{DetC}}_{\text{Degradation to DOC}} \end{aligned} \quad \text{(A26)}$$

The state variables ZooN, $\text{PhyN}_{\text{nano}}$, PhyN_{dia}, DetN and DetC are described in Table A1. Due to sloppy feeding, the grazed phytoplankton partly goes to the zooplankton pool and partly to the detritus pool, depending on the grazing efficiency γ (Table A7). The grazing (G_{nano} and G_{dia}) is calculated in Eqs. (A52) and (A53), respectively.

The quadratic mortality loss from zooplankton (m_{zoo}) is listed in Table A7. The temperature dependent degradation of detritus to DOM (ρ_{DetN} and ρ_{DetC}) in Table A3, and the temperature dependency (f_T) is calculated in Eq. (A54).

The quotas $q_{\text{nano}}^{\text{C:N}} = \text{PhyC}_{\text{nano}} / \text{PhyN}_{\text{nano}}$, $q_{\text{dia}}^{\text{C:N}} = \text{PhyC}_{\text{dia}} / \text{PhyN}_{\text{dia}}$ and $q_{\text{zoo}}^{\text{C:N}} = \text{ZooC} / \text{ZooN}$ are used to convert the units from mmol N to mmol C.

Aggregation: the aggregation rate (Agg, Table A4) is proportional to the concentration of nanophytoplankton, diatoms and detritus:

$$\text{Agg} = \phi_{\text{phy}} \cdot \left(\text{PhyN}_{\text{nano}} + \text{PhyN}_{\text{dia}}\right) + \phi_{\text{det}} \cdot \text{DetN}. \quad \text{(A27)}$$

The values of the maximum aggregation loss parameters (ϕ_{phy} and ϕ_{det}) are listed in Table A7. The state variables $\text{PhyN}_{\text{nano}}$, PhyN_{dia} and DetN are described in Table A1.

Sinking: in the model the detritus is subject to sinking, which increases linearly with depth. The sinking speed (w_{det}, Table A4) is based on the work by Kriest and Oschlies (2008).

$$w_{\text{det}} = 0.0288\,\text{day}^{-1} \cdot z + w_0 \quad \text{(A28)}$$

Here z denotes the current depth and w_0 is the sinking speed at the surface (Table A7).

Loss to benthos: when the sinking detritus reaches the bottom grid point it is assumed that it continues sinking into the benthic compartment with the speed w_{det} (Eq. A28). This leads to a detrital flux ($\text{BenF}_{\text{DetN}}$ and $\text{BenF}_{\text{DetC}}$, Table A5) from the water column to the benthos:

$$\text{BenF}_{\text{DetN}} = -w_{\text{det}} \cdot \text{DetN} \quad \text{(A29)}$$

$$\text{BenF}_{\text{DetC}} = -w_{\text{det}} \cdot \text{DetC}. \quad \text{(A30)}$$

The state variables DetN and DetC are described in Table A1.

A1.12 Detritus Si

$$\begin{aligned}\text{SMS(DetSi)} = &(\underbrace{\epsilon_{\text{N}}^{\text{phy}} \cdot f_{\text{lim, dia}}^{\text{N:Cmax}}}_{\text{Diatiom excretion}} + \underbrace{\text{Agg}}_{\text{Aggregation}}) \cdot \text{PhySi} \\ &+ \underbrace{G_{\text{dia}} \cdot q^{\text{Si:N}}}_{\text{Sloppy feeding}} - \underbrace{\rho_{\text{Si}}^{T} \cdot f_T \cdot \text{DetSi}}_{\text{Remineralization to DSi}} \end{aligned} \quad \text{(A31)}$$

The state variables PhySi and DetSi are described in Table A1. The limiter function ($f_{\text{lim}}^{\text{N:Cmax}}$) is described in Sect. A6.1. The aggregation rate (Agg) is calculated in Eq. (A27), the grazing on diatoms (G_{dia}) in Eq. (A53), the remineralization rate (ρ_{Si}^{T}) in Eq. (A4) and the temperature dependency of remineralization (f_T) is calculated in Eq. (A54). The value of the excretion parameter ($\epsilon_{\text{N}}^{\text{phy}}$) is listed in Table A3. The intracellular ratio between diatom silicon and carbon is defined as $q^{\text{Si:N}} = \text{PhySi} / \text{PhyN}_{\text{dia}}$.

Loss to benthos: when the sinking detritus reaches the bottom grid point it is assumed that it continues sinking into the benthic compartment with the speed w_{det} (Eq. A28). This leads to a detrital flux ($\text{BenF}_{\text{DetSi}}$, Table A5) from the water column to the benthos:

$$\text{BenF}_{\text{DetSi}} = -w_{\text{det}} \cdot \text{DetSi}. \quad \text{(A32)}$$

The state variable DetSi is described in Table A1.

A1.13 Detritus $CaCO_3$

$$\begin{aligned}\text{SMS(DetCalc)} = &\underbrace{\epsilon_{\text{C}}^{\text{phy}} \cdot f_{\text{lim, nano}}^{\text{N:Cmax}} \cdot \text{PhyCalc}}_{\text{Nanophytoplankton excretion}} \\ &+ (\underbrace{\text{Agg}}_{\text{Aggregation}} + \underbrace{r_{\text{nano}}}_{\text{Respiration}}) \cdot \text{PhyCalc} \\ &+ \underbrace{G_{\text{nano}} \cdot q_{\text{nano}}^{\text{CaCO}_3\text{:N}}}_{\text{Grazing loss}} - \\ &\underbrace{\text{Diss}_{\text{calc}} \cdot \text{DetCalc}}_{\text{Dissolution to DIC}} \end{aligned} \quad \text{(A33)}$$

The state variables PhyCalc and DetCalc are described in Table A1. The limiter function ($f_{\text{lim}}^{\text{N:Cmax}}$) is described in Sect. A6.1. The aggregation rate (Agg) is calculated in Eq. (A27), the respiration rate (r_{nano}) in Eq. (A45) and

the nanophytoplankton grazing rate (G_{nano}) in Eq. (A52). The excretion rate ($\epsilon_{\text{C}}^{\text{phy}}$) is listed in Table A3, the ratio $q_{\text{nano}}^{\text{CaCO}_3:\text{N}} = \text{PhyCalc} / \text{PhyN}_{\text{nano}}$ and the calcite dissolution rate will now be explained.

Calcite dissolution: as the detritus calcite sinks through the water column it is subject to dissolution ($\text{Diss}_{\text{calc}}$, Table A4) occurring on a length scale of 3500 m (Yamanaka and Tajika, 1996).

$$\text{Diss}_{\text{calc}} = \frac{w_z}{3500\,\text{m}} \tag{A34}$$

w_z denotes the sinking speed at depth z and is calculated in Eq. (A28).

Loss to benthos: when the sinking detritus reaches the bottom grid point it is assumed that it continues sinking into the benthic compartment with the speed w_{det} (Eq. A28). This leads to a detrital flux ($\text{BenF}_{\text{DetCalc}}$, Table A5) from the water column to the benthos:

$$\text{BenF}_{\text{DetCalc}} = -w_{\text{det}} \cdot \text{DetCaCO}_3. \tag{A35}$$

The state variable DetCalc is described in Table A1.

A1.14 Dissolved organic material

$$\begin{aligned}\text{SMS(DON)} = &\underbrace{\epsilon_{\text{N}}^{\text{phy}} \cdot f_{\text{lim, nano}}^{\text{N:Cmax}} \cdot \text{PhyN}_{\text{nano}}}_{\text{Nanophytoplankton excretion}} \\ &+ \underbrace{\epsilon_{\text{N}}^{\text{phy}} \cdot f_{\text{lim, dia}}^{\text{N:Cmax}} \cdot \text{PhyN}_{\text{dia}}}_{\text{Diatom excretion}} \\ &+ \underbrace{\epsilon_{\text{N}}^{\text{zoo}} \cdot \text{ZooN}}_{\text{Zooplankton excretion}} + \underbrace{\rho_{\text{DetN}} \cdot f_T \cdot \text{DetN}}_{\text{Detritus degradation}} \\ &- \underbrace{\rho_{\text{N}} \cdot f_T \cdot \text{DON}}_{\text{Remineralization}}\end{aligned} \tag{A36}$$

$$\begin{aligned}\text{SMS(DOC)} = &\underbrace{\epsilon_{\text{C}}^{\text{phy}} \cdot f_{\text{lim, nano}}^{\text{N:Cmax}} \cdot \text{PhyC}_{\text{nano}}}_{\text{Nanophytoplankton excretion}} \\ &+ \underbrace{\epsilon_{\text{C}}^{\text{phy}} \cdot f_{\text{lim, dia}}^{\text{N:Cmax}} \cdot \text{PhyC}_{\text{dia}}}_{\text{Diatom excretion}} \\ &+ \underbrace{\epsilon_{\text{C}}^{\text{zoo}} \cdot \text{ZooC}}_{\text{Zooplankton excretion}} + \underbrace{\rho_{\text{DetC}} \cdot f_T \cdot \text{DetC}}_{\text{Detritus degradation}} \\ &- \underbrace{\rho_{\text{C}} \cdot f_T \cdot \text{DOC}}_{\text{Remineralization}}\end{aligned} \tag{A37}$$

The state variables are described in Table A1. The values for excretion of nitrogen and carbon from phyto- and zooplankton ($\epsilon_{\text{N}}^{\text{phy}}$, $\epsilon_{\text{C}}^{\text{phy}}$, $\epsilon_{\text{N}}^{\text{zoo}}$ and $\epsilon_{\text{C}}^{\text{zoo}}$) are listed in Table A3 along with the degradation rates for detritus (ρ_{detN} and ρ_{detC}) and remineralization rates of DON and DOC (ρ_{N} and ρ_{C}). The limitation factors ($f_{\text{lim, nano}}^{\text{N:Cmax}}$ and $f_{\text{lim, dia}}^{\text{N:Cmax}}$) are described in Sect. A6.1 and the temperature dependency (f_T) is calculated in Eq. (A54).

A2 Sources minus sinks, benthos

The model has a benthos compartment which consists of one layer. Matter is supplied to this layer through sinking detritus, and it hence has pools of nitrogen, silicon, carbon and calcite. When sinking detritus reaches the bottom it continues sinking into the benthos with the speed, w_{det}, calculated by Eq. (A28) and is thus lost from the water column. In the benthos, the detritus is assumed to be remineralized to dissolved inorganic matter. This is then re-released to the water's pools of dissolved inorganic matter (DIN, DIC, Alk and DSi):

$$\text{SMS(BenthosN)} = w_{\text{det}} \cdot \text{DetN} - \rho_{\text{N}}^{\text{ben}} \cdot \text{BenthosN} \tag{A38}$$

$$\text{SMS(BenthosSi)} = w_{\text{det}} \cdot \text{DetSi} - \rho_{\text{Si}}^{\text{ben}} \cdot \text{BenthosSi} \tag{A39}$$

$$\text{SMS(BenthosC)} = w_{\text{det}} \cdot \text{DetC} - \rho_{\text{C}}^{\text{ben}} \cdot \text{BenthosC} \tag{A40}$$

$$\begin{aligned}\text{SMS(BenthosCalc)} = &\, w_{\text{det}} \cdot \text{DetCalc} - \text{Diss}_{\text{calc}} \\ &\cdot \text{BenthosCalc.}\end{aligned} \tag{A41}$$

The state variables are described in Table A1 (DetN, DetSi, DetC and DetCalc) and Table A2 (BenthosN, BenthosSi, BenthosC and BenthosCalc). The remineralization rates ($\rho_{\text{N}}^{\text{ben}}$, $\rho_{\text{Si}}^{\text{ben}}$ and $\rho_{\text{C}}^{\text{ben}}$) are listed in Table A3 and the calcite dissolution rate ($\text{Diss}_{\text{calc}}$) is calculated in Eq. (A34).

A3 Phytoplankton growth

A3.1 Photosynthesis

The rate of the C-specific photosynthesis is calculated for both nanophytoplankton and diatoms (P_{nano} and P_{dia}, Table A4).

The calculation is based on the work by Geider et al. (1998) and differs between nanophytoplankton and diatoms in the nutrient limitation; nanophytoplankton is limited by iron and nitrogen while diatoms are additionally limited by silicon.

$$P_{\text{max}}^{\text{nano}} = \mu_{\text{C}}^{\text{max}} \cdot \min\left(f_{\text{lim, nano}}^{\text{Fe}}, f_{\text{lim, nano}}^{\text{N:Cmin}}\right) \cdot f_T \tag{A42}$$

$$P_{\text{max}}^{\text{dia}} = \mu_{\text{C}}^{\text{max}} \cdot \min\left(f_{\text{lim, dia}}^{\text{Fe}}, f_{\text{lim, dia}}^{\text{N:Cmin}}, f_{\text{lim, dia}}^{\text{Si:Cmin}}\right) \cdot f_T \tag{A43}$$

Nutrient limitation is calculated using the Liebig law of the minimum, in which the most limiting nutrient limits production (O'Neill et al., 1989).

The value of $\mu_{\text{C}}^{\text{max}}$ can be found in Table A8. The limitation terms ($f_{\text{lim}}^{\text{N:Cmin}}$, $f_{\text{lim}}^{\text{Si:Cmin}}$ and $f_{\text{lim}}^{\text{Fe}}$) differ somewhat from the formulation in Geider et al. (1998) and are described in Sect. A6.2 and the temperature dependency (f_T) is calculated in Eq. (A54).

The actual C-specific photosynthesis rate depends on how much photosynthetically available radiation (PAR, Table A4) the cell can harvest. This is controlled by the light harvesting efficiency (α) and the intracellular Chl : C ratio as well as the

Table A8. Parameters for phytoplankton growth.

Parameter	Value	Description and unit
α_{nano}	0.19	Light harvesting efficiency for nanophytoplankton [mmol C m^2 (mg Chl W day)$^{-1}$]
α_{dia}	0.23	Light harvesting efficiency for diatoms [mmol C m^2 (mg Chl W day)$^{-1}$]
$K_{\mathrm{N}}^{\mathrm{Nano}}$	0.55	Half-saturation constant for nanophyto N uptake [mmol N m^{-3}]
$K_{\mathrm{N}}^{\mathrm{Dia}}$	1.00	Half-saturation constant for diatom N uptake [mmol N m^{-3}]
K_{Si}	4.00	Half-saturation constant for diatom Si uptake [mmol Si m^{-3}]
$\mu_{\mathrm{C}}^{\mathrm{max}}$	3.0	Rate of C-specific photosynthesis [day^{-1}]
$q_{\mathrm{max}}^{\mathrm{Chl:N}}$	4.2	Maximum Chl : N ratio for phytoplankton [mg Chl mmol N^{-1}]
res	0.01	Maintenance respiration rate constant [day^{-1}]
$\sigma_{\mathrm{N:C}}$	0.2	Maximum uptake ratio N : C [mmol N mmol C^{-1}]
$\sigma_{\mathrm{Si:C}}$	0.2	Maximum uptake ratio Si : C [mmol Si mmol C^{-1}]
τ	0.01	Timescale for zooplankton respiration [day^{-1}]
V_{cm}	0.7	Scaling factor for C-specific N uptake, dimensionless
ζ	2.33	Cost of biosynthesis of N [mmol C mmol N^{-1}]

available light.

$$P = P_{\mathrm{max}} \cdot \left(1.0 - \exp\left(\frac{-\alpha \cdot q^{\mathrm{Chl:C}} \cdot \mathrm{PAR}}{P_{\mathrm{max}}}\right)\right) \tag{A44}$$

The C-specific photosynthesis rate is calculated for both nanophytoplankton and diatoms; P_{nano} and P_{dia}, respectively (Table A4).

The values for the light harvesting efficiencies (α_{nano} and α_{dia}) are listed in Table A8, the apparent maximum photosynthetic rate (P_{max}) is calculated in Eqs. (A42) and (A43) and we define $q^{\mathrm{Chl:C}} = \mathrm{PhyChl} / \mathrm{PhyC}$.

A3.2 Respiration

Phytoplankton: the phytoplankton respiration rate is calculated for both nanophytoplankton and diatoms (r_{nano} and r_{dia}, Table A4):

$$r = \underbrace{\mathrm{res} \cdot f_{\mathrm{lim}}^{\mathrm{N:Cmax}}}_{\text{Cost of maintenance}} + \underbrace{\zeta \cdot V^{\mathrm{N}}}_{\text{Cost of N assim}} \quad . \tag{A45}$$

The values for the maintenance respiration rate (res) and the cost of biosynthesis (ζ) can be found in Table A8. The limiter function ($f_{\mathrm{lim}}^{\mathrm{N:Cmax}}$) is described in Sect. A6.1 and the nitrogen assimilation rate ($V_{\mathrm{nano}}^{\mathrm{N}}$ and $V_{\mathrm{dia}}^{\mathrm{N}}$) is calculated in Eq. (A48).

Zooplankton: when the intracellular C : N ratio in zooplankton exceeds the Redfield ratio, a temperature dependent respiration (r_{zoo}, Table A4) is assumed to drive it back with a timescale τ. Otherwise, the respiration is zero.

$$r_{\mathrm{zoo}} = \max\left(0\,\mathrm{day}^{-1}, \frac{q_{\mathrm{zoo}}^{\mathrm{C:N}} - q_{\mathrm{Standard}}^{\mathrm{C:N}}}{\tau} \cdot f_T\right) \tag{A46}$$

The timescale for respiration (τ) is given in Table A8. The temperature dependence (f_T) is calculated in Eq. (A54), and we define the ratios $q_{\mathrm{zoo}}^{\mathrm{C:N}} = \mathrm{ZooC} / \mathrm{ZooN}$ and $q_{\mathrm{Standard}}^{\mathrm{C:N}} = 106\mathrm{C} / 16\mathrm{N}$.

A3.3 Chlorophyll *a* synthesis

Chlorophyll *a* synthesis is coupled to N uptake in REcoM2. The uptake of nitrogen by the phytoplankton (V^{N}) is converted to chlorophyll units with a maximum Chl : N ratio ($q_{\mathrm{max}}^{\mathrm{Chl:N}}$). This highest possible chlorophyll synthesis rate can then be downregulated by the ratio between the actual photosynthesis and the light absorption, leading to a smaller rate when photosynthesis is small.

The chlorophyll *a* synthesis is calculated for both nanophytoplankton and diatoms ($S_{\mathrm{nano}}^{\mathrm{Chl}}$ and $S_{\mathrm{dia}}^{\mathrm{Chl}}$, Table A4).

$$S^{\mathrm{chl}} = V^{\mathrm{N}} \cdot q_{\mathrm{max}}^{\mathrm{Chl:N}} \cdot \min\left(1, \frac{P}{\alpha \cdot q^{\mathrm{Chl:C}} \cdot \mathrm{PAR}}\right) \tag{A47}$$

The nitrogen assimilation ($V_{\mathrm{nano}}^{\mathrm{N}}$ and $V_{\mathrm{dia}}^{\mathrm{N}}$) is calculated in Eq. (A48), and the value for the maximum Chl : N ratio ($q_{\mathrm{max}}^{\mathrm{Chl:N}}$) can be seen in Table A8.

The C-specific photosynthesis (P_{nano} and P_{dia}) is calculated in Eq. (A44), and the values for α_{nano} and α_{dia} are listed in Table A8. PAR denotes the photosynthetically available radiation and we define $q^{\mathrm{Chl:C}} = \mathrm{PhyChl} / \mathrm{PhyC}$.

A3.4 Nitrogen and silicon assimilation

Nitrogen: the carbon-specific N assimilation rate is based on the maximum rate of carbon-specific photosynthesis (P_{max}), which is then modulated by the maximum N : C uptake ratio ($\sigma_{\mathrm{N:C}}$) and by the intracellular quota between N and C ($f_{\mathrm{lim}}^{\mathrm{N:Cmax}}$), which downregulates N assimilation when the N : C ratio approaches a maximum value (Sect. A6.1). The concentration of DIN in the surrounding water modifies the N assimilation through Michaelis–Menten kinetics.

N assimilation is calculated for both diatoms and nanophytoplankton ($V_{\mathrm{nano}}^{\mathrm{N}}$ and $V_{\mathrm{dia}}^{\mathrm{N}}$, Table A4).

$$V^{\mathrm{N}} = V_{\mathrm{cm}} \cdot P_{\mathrm{max}} \cdot \sigma_{\mathrm{N:C}} \cdot f_{\mathrm{lim}}^{\mathrm{N:Cmax}} \cdot \frac{\mathrm{DIN}}{K_{\mathrm{N}} + \mathrm{DIN}} \tag{A48}$$

The values of the parameters for V_{cm}, $\sigma_{N:C}$, K_N^{nano} and K_N^{dia} are listed in Table A8. The maximum rates of photosynthesis (P_{max}^{nano} and P_{max}^{dia}) are calculated in Eqs. (A42) and (A43), respectively, and $f_{lim}^{N:Cmax}$ is described in Sect. A6.1. DIN denotes the surrounding water's concentration of dissolved inorganic nitrogen.

Silicon: silicon assimilation (V^{Si}, Table A4) only occurs in diatoms. The maximum silicon uptake rate is calculated as the maximum photosynthetic rate (μ_C^{max}) multiplied by the maximum Si : C ratio ($\sigma_{Si:C}$) and the scaling factor for the maximum nitrogen uptake (V_{cm}) . The actual uptake depends on the surrounding water's silicon concentration through Michaelis–Menten kinetics and the temperature dependency (f_T). It is additionally downregulated when the N : C or Si : C ratios become too high ($f_{lim}^{Si:Cmax}$ and $f_{lim\,dia}^{N:Cmax}$). The N : C ratio is taken into account, as a too high ratio indicates that the intracellular concentration of energy rich carbon molecules becomes too low to use energy on silicon uptake.

$$V^{Si} = V_{cm} \cdot \mu_C^{max} \cdot f_T \cdot \sigma_{Si:C} \cdot f_{lim}^{SiCmax} \cdot f_{lim\,dia}^{NCmax} \cdot \frac{DSi}{K_{Si} + DSi} \quad \text{(A49)}$$

The scaling factor for the N uptake (V_{cm}) and the C-specific photosynthesis rate (μ_C^{max}) are listed in Table A8 along with the maximum Si : C uptake ratio ($\sigma_{Si:C}$). The temperature dependency (f_T) is calculated in Eq. (A54), and the limitation by the intracellular ratios Si : C and N : C ($f_{lim}^{Si:Cmax}$ and $f_{lim,\,dia}^{N:Cmax}$) are described in Sects. A6.3 and A6.1, respectively. K_{Si} is listed in Table , and DSi denotes the surrounding water's concentration of dissolved inorganic silicon.

A4 Grazing

REcoM2 has a single zooplankton class, which is also the highest trophic level in the model. Grazing on both nanophytoplankton and diatoms is calculated using a Type 3 Sigmoidal model as described by Gentleman et al. (2003).

The maximum grazing rate (G_{max}) is modulated by the temperature through the Arrhenius function (f_T) and by the prey availability through a quadratic Michaelis–Menten function. The model has fixed preferences for both phytoplankton classes and G' (Table A4) is the phytoplankton concentration available for food intake, in our case:

$$G' = PhyN_{nano} + PhyN_{dia} \cdot f_Z^{dia}. \quad \text{(A50)}$$

Here, the parameter f_Z^{dia} (Table A9) specifies the relative grazing preference for diatoms.

The total grazing (G_{tot}, Table A4) is calculated as follows:

$$G_{tot} = G_{max} \cdot \frac{G'^2}{K_G + G'^2} \cdot f_T \cdot ZooN. \quad \text{(A51)}$$

This total grazing can be divided into the grazing on nanophytoplankton and diatoms (G_{nano} and G_{dia}, Table A4):

$$G_{nano} = G_{tot} \cdot \frac{PhyN_{nano}}{G'} \quad \text{(A52)}$$

$$G_{dia} = G_{tot} \cdot \frac{PhyN_{dia} \cdot f_Z^{dia}}{G'}. \quad \text{(A53)}$$

The values for the maximum grazing rate (G_{max}), the half-saturation constant (K_G) and the fraction of diatoms available for grazing (f_Z^{dia}) are listed in Table A9. The temperature dependency (f_T) is calculated in Eq. (A54) and the state variables are described in Table A1.

A5 Temperature dependence of rates

Temperature dependence of metabolic rates (f_T, Table A4) is taken into account through an Arrhenius function:

$$f_T = \exp\left(-4500\,K \cdot \left(T^{-1} - T_{ref}{}^{-1}\right)\right). \quad \text{(A54)}$$

Here, T is the local temperature in Kelvin and T_{ref} is a reference temperature (Table A10). The value 4500 K is the slope of the linear part of the Arrhenius function. Figure A1 illustrates how the metabolic rates decrease for $T < T_{ref}$ and increase for $T > T_{ref}$.

A6 Nutrient limitation

One factor controlling the metabolic processes in the phytoplankton is the intracellular ratios between nutrients and carbon.

Five different limiters are used for this; one that downregulates uptake of N and release of C when the N : C ratio becomes too high ($f_{lim}^{N:Cmax}$, Sect. A6.1), three that downregulate photosynthesis when the nutrient : C ratios become too low ($f_{lim}^{N:Cmin}$, $f_{lim}^{Si:Cmin}$ and f_{lim}^{Fe}, Sect. A6.2) and one that downregulates silicon assimilation when the Si : C ratio becomes too high ($f_{lim}^{Si:Cmax}$, Sect. A6.3).

These limiters will now be described after a general explanation of the function.

The way the intracellular ratios between nutrients and carbon limit uptake in the model is based on the work by Geider et al. (1998), but has been modified to the non-linear function, which is calculated as follows:

$$f_{lim}(slope, q_1, q_2) = 1 - \exp(-slope(|\Delta q| - \Delta q)^2). \quad \text{(A55)}$$

Here, $\Delta q = q_1 - q_2$ is the difference between the intracellular nutrient : C quota and a prescribed max or min quota, which is chosen depending on the situation.

The dimensionless constant slope regulates the degree of limitation for a given Δq.

A6.1 Intracellular regulation of N uptake and C release

Here we take a closer look at the limiter $f_{lim}^{N:Cmax}$, which downregulates the metabolic processes listed in Table A11 when the intracellular N : C ratio becomes too high.

Table A9. Parameters for grazing.

Parameter	Value	Description and unit
f_Z^{dia}	0.50	Relative grazing preference for diatoms, dimensionless
G_{max}	2.40	Maximum grazing rate at 0 °C [day^{-1}]
K_G	0.35	Half-saturation constant for grazing loss [(mmol N m^{-3})^2]

Table A10. Parameters for limitation functions.

Parameter	Value	Description and unit
K_{Fe}^{nano}	0.04	Half-saturation constant for nanophytoplankton Fe uptake [µmol Fe m^{-3}]
K_{Fe}^{dia}	0.12	Half-saturation constant for diatom Fe uptake [µmol Fe m^{-3}]
$q^{N:Cmin}$	0.04	Min intracellular N : C ratio for nanophytoplankton [mmol N mmol C^{-1}]
$q^{N:Cmax}$	0.2	Max intracellular N : C ratio for nanophytoplankton [mmol N mmol C^{-1}]
$q^{Si:Cmin}$	0.04	Min intracellular Si : C ratio for diatoms [mmol Si mmol C^{-1}]
$q^{Si:Cmax}$	0.8	Max intracellular Si : C ratio for diatoms [mmol Si mmol C^{-1}]
$slope_{min}^{N}$	50	Minimum limiter regulator for N, [mmol C mmol N^{-1}]
$slope_{max}^{N}$	1000	Maximum limiter regulator for N, [mmol C mmol N^{-1}]
$slope_{min}^{Si}$	1000	Minimum limiter regulator for Si, [mmol C mmol N^{-1}]
$slope_{max}^{Si}$	1000	Maximum limiter regulator for Si, [mmol C mmol N^{-1}]
T_{ref}	288.15	Reference temperature for Arrhenius function [K]

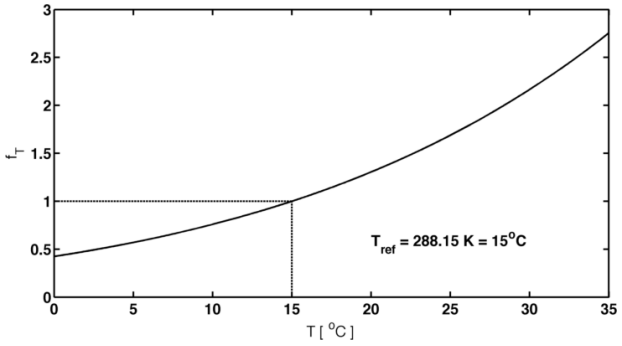

Figure A1. The Arrhenius function plotted with the parameters used in REcoM2.

It is calculated with Eq. (A55) using the following parameters:

$$\text{slope} = \text{slope}_{max}^{N}, q_1 = q^{N:Cmax}, q_2 = q^{N:C},$$

where slope_{max}^{N} is listed in Table A10 along with the prescribed maximum N : C quota ($q^{N:Cmax}$). $q^{N:C}$ is the current intracellular quota.

In Fig. A2 it is illustrated how the limiter function changes with changing intracellular N : C quota; when the intracellular concentration of nitrogen increases as compared to carbon, the rate of the processes that are affected by the limiter will be downregulated. Total limitation ($f_{lim}^{N:Cmax} = 0$) occurs when the quota becomes equal to or higher than 0.2, or the equivalent of 21.2N : 106C.

Table A11. Processes modulated by the limiter function $f_{lim}^{N:Cmax}$.

Process	Effect of $q^{N:C} \rightarrow q_{N:Cmax}$
Nitrogen assimilation	Ends uptake of N
Silicon assimilation	Ends uptake of Si
Respiration by phytoplankton	Ends release of C
Phytoplankton DOC excretion	Ends release of C
Phytoplankton DON excretion	Ends release of N
Phytoplankton calcite excretion	Ends release of C

A6.2 Intracellular regulation of C uptake

Photosynthesis is limited by the nutrients iron, nitrogen and in the case of diatoms also silicon.

Nitrogen and silicon limitation: in the case of N and Si, the regulation is controlled by the intracellular ratios N : C ($f_{lim}^{N:Cmin}$) and Si : C ($f_{lim}^{Si:Cmin}$). These limiters downregulate the rate of photosynthesis when the intracellular nutrient : C ratios become too low (Fig. A3).

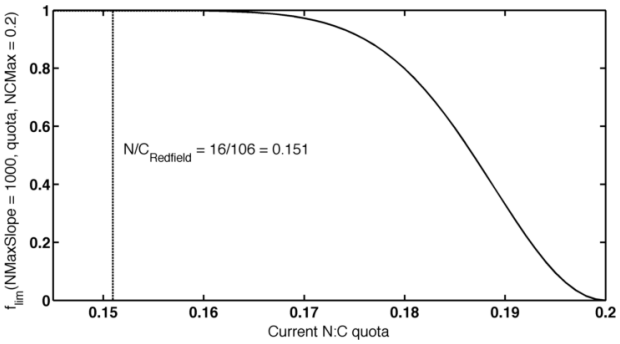

Figure A2. Change in limiter function $f_{\mathrm{lim}}^{\mathrm{N:Cmax}}$ with N : C quota.

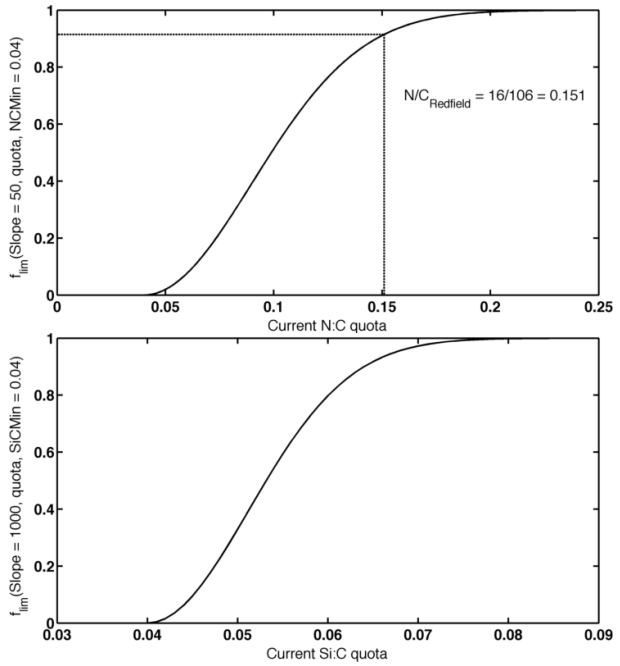

Figure A3. Change in the limiter function $f_{\mathrm{lim}}^{\mathrm{N:Cmin}}$ with N : C quota.

They are calculated with Eq. (A55) using the following parameters (Table A10):

$$\text{slope} = \text{slope}_{\mathrm{min}}^{\mathrm{N}},\quad q_1 = q^{\mathrm{N:Cmin}},\quad q_2 = q^{\mathrm{N:C}}$$
$$\text{slope} = \text{slope}_{\mathrm{min}}^{\mathrm{Si}},\quad q_1 = q^{\mathrm{Si:Cmin}},\quad q_2 = q^{\mathrm{Si:C}}.$$

Iron: for iron, the water's concentration is used to calculate the limitation. This is done using Michaelis–Menten kinetics:

$$f_{\mathrm{lim}}^{\mathrm{Fe}} = \frac{\mathrm{Fe}}{K_{\mathrm{Fe}} + \mathrm{Fe}}. \tag{A56}$$

The half-saturation constants ($K_{\mathrm{Fe}}^{\mathrm{nano}}$ and $K_{\mathrm{Fe}}^{\mathrm{dia}}$) are listed in Table A10.

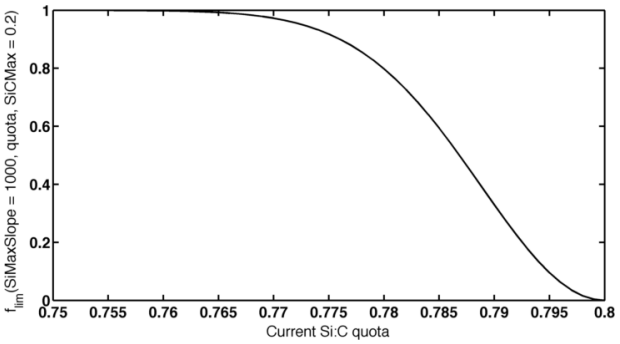

Figure A4. Change in limiter function with Si : C quota.

A6.3 Intracellular regulation of Si uptake

Diatom uptake of silicon is downregulated by the function $f_{\mathrm{lim}}^{\mathrm{Si:Cmax}}$ (Fig. A4) when the intracellular Si : C ratio exceeds a set limit. The limiter function is described in Eq. (A55) and is calculated using the following variables (Table A10):

$$\text{slope} = \text{slope}_{\mathrm{max}}^{\mathrm{Si}},\quad q_1 = q^{\mathrm{Si:C}},\quad q_2 = q^{\mathrm{Si:Cmax}}.$$

Supplementary material

The supplements contain the full code for REcoM2 along with a manual for FESOM–REcoM2, containing an overview of the code structure and instructions for running the coupled model.

The Supplement related to this article is available online at doi:10.5194/gmd-7-2769-2014-supplement.

Acknowledgements. We would like to thank Sergey Danilov for many discussions regarding the understanding and handling of the FESOM finite-element model. We also thank two anonymous reviewers for their constructive comments that helped very much to improve the manuscript. C. Völker was supported through EU FP7 project CARBOCHANGE (grant agreement no. 264879). Computational resources were made available by the "Norddeutscher Verbund für Hoch- und Höchstleistungsrechnen" (HLRN).

Edited by: J. Williams

References

Alvain, S., Moulin, C., Dandonneau, Y., and Bréon, F.: Remote sensing of phytoplankton groups in case 1 waters from global SeaWiFS imagery, Deep-Sea Res. Pt. I, 52, 1989–2004, doi:10.1016/j.dsr.2005.06.015, 2005.

Assmann, K. M., Bentsen, M., Segschneider, J., and Heinze, C.: An isopycnic ocean carbon cycle model, Geosci. Model Dev., 3, 143–167, doi:10.5194/gmd-3-143-2010, 2010.

Aumont, O. and Bopp, L.: Globalizing results from ocean in situ iron fertilization studies, Global Biogeochem. Cy., 20, GB2017, doi:10.1029/2005GB002591, 2006.

Aumont, O., Orr, J., Monfray, P., Madec, G., and Maier-Reimer, E.: Nutrient trapping in the equatorial Pacific: The ocean circulation solution, Global Biogeochem. Cy., 13, 351–369, doi:10.1029/1998GB900012, 1999.

Aumont, O., Maier-Reimer, E., Blain, S., and Monfray, F.: An ecosystem model of the global ocean including Fe, Si, P colimitations, Global Biogeochem. Cy., 17, 1060, doi:10.1029/2001GB001745, 2003.

Behrenfeld, M. J.: Abandoning Sverdrup's critical depth hypothesis on phytoplankton blooms, Ecology, 91, 977–989, doi:10.3410/f.2137018.1737130, 2010.

Behrenfeld, M. J. and Falkowski, P. G.: Photosynthetic rates derived from satellite-based chlorophyll concentration, Limnol. Oceanogr., 42, 1–20, doi:10.4319/lo.1997.42.1.0001, 1997.

Behrenfeld, M. J., O'Malley, R. T., Siegel, D. A., McClain, C. R., Sarmiento, J. L., Feldman, G. C., Milligan, A. J., Falkowski, P. G., Letelier, R. M., and Boss, E. S.: Climate-driven trends in contemporary ocean productivity, Nature, 444, 752–755, doi:10.1038/nature05317, 2006.

Bernard, C. Y., Dürr, H. H., Heinze, C., Segschneider, J., and Maier-Reimer, E.: Contribution of riverine nutrients to the silicon biogeochemistry of the global ocean – a model study, Biogeosciences, 8, 551–564, doi:10.5194/bg-8-551-2011, 2011.

Bopp, L., Resplandy, L., Orr, J. C., Doney, S. C., Dunne, J. P., Gehlen, M., Halloran, P., Heinze, C., Ilyina, T., Séférian, R., Tjiputra, J., and Vichi, M.: Multiple stressors of ocean ecosystems in the 21st century: projections with CMIP5 models, Biogeosciences, 10, 6225–6245, doi:10.5194/bg-10-6225-2013, 2013.

Broecker, W. S., Peng, T.-H., and Beng, Z.: Tracers in the Sea, Lamont-Doherty Geological Observatory, Columbia University, Palisades, New York, 1982.

Carr, M.-E., Friedrichs, M. A. M., Schmeltz, M., Noguchi Aita, M., Antoine, D., Arrigo, K. R., Asanuma, I., Aumont, O., Barber, R., Behrenfeld, M., Bidigare, R., Buitenhuis, E. T., Campbell, J., Ciotti, A., Dierssen, H., Dowell, M., Dunne, J., Esaias, W., Gentili, B., Gregg, W., Groom, S., Hoepffner, N., Ishizaka, J., Kameda, T., Le Quéré, C., Lohrenz, S., Marra, J., Mélin, F., Moore, K., Morel, A., Reddy, T. E., Ryan, J., Scardi, M., Smyth, T., Turpie, K., Tilstone, G., Waters, K., and Yamanaka, Y.: A comparison of global estimates of marine primary production from ocean color, Deep-Sea Res. Pt. II, 53, 741–770, doi:10.1016/j.dsr2.2006.01.028, 2006.

Chen, C., Liu, H., and Beardsley, R. C.: An unstructured grid, finite-volume, three-dimensional, primitive equations ocean model: application to coastal ocean and estuaries, J. Atmos. Ocean. Tech., 20, 159–186, doi:10.1175/1520-0426(2003)020<0159:AUGFVT>2.0.CO;2, 2003.

Danilov, S., Kivman, G., and Schröter, J.: A finite-element ocean model: principles and evaluation, Ocean Model., 6, 125–150, doi:10.1016/S1463-5003(02)00063-X, 2004.

De Baar, H. J. W., De Jong, J. T. M., Bakker, D. C., Löscher, B. M., Veth, C., Bathmann, U., and Smetacek, V.: Importance of iron for plankton blooms and carbon dioxide drawdown in the Southern Ocean, Nature, 373, 412–415, doi:10.1038/373412a0, 1995.

de Boyer Montegut, C., Madec, G., Fischer, A. S., Lazar, A., and Iudicone, D.: Mixed layer depth over the global ocean: An examination of profile data and a profile-based climatology, J. Geophys. Res., 109, C12003, doi:10.1029/2004JC002378, 2004.

Doney, S. C., Lindsay, K., Caldeira, K., Campin, J.-M., Drange, H., Dutay, J.-C., Follows, M., Gao, Y., Gnanadesikan, A., Gruber, N., Ishida, A., Joos, F., Madec, G., Maier-Reimer, E., Marshall, J. C., Matear, R. J., Monfray, P., Mouchet, A., Najjar, R., Orr, J. C., Plattner, G. K., Sarmiento, J. L., Schlitzer, R., Slater, R. D., Totterdell, I. J., Weirig, M. F., Yamanaka, Y., and Yool, A.: Evaluating global ocean carbon models: the importance of realistic physics, Global Biogeochem. Cy., 18, GB3017, doi:10.1029/2003GB002150, 2004.

Doney, S. C., Lima, I., Moore, J. K., Lindsay, K., Behrenfeld, M. J., Westberry, T. K., Mahowald, N., Glover, D. M., and Takahashi, T.: Skill metrics for confronting global upper ocean ecosystem-biogeochemistry models against field and remote sensing data, J. Marine Syst., 76, 95–112, doi:10.1016/j.jmarsys.2008.05.015, 2009.

Downes, S., Farneti, R., Uotilac, P., Griffies, S. M., Marsland, S., Bailey, D., Behrens, E., Bentsen, M., Bi, D., Biastoch, A., Böning, C., Bozec, A., Chassignet, E., Danabasoglu, G., Danilov, S., Diansky, N., Drange, H., Fogli, P. G., Gusev, A., Howard, A., Illicak, M., Jung, T., Kelley, M., Large, W. G., Leboissetiero, A., Long, M., Lu, J., Masina, S., Mishra, A., Navarra, A., Nurserp, A. J. G., Patara, L., Samuels, B. L., Sidorenko, D., Spence, P., Tsujino, H., Wang, Q., and Yeager, S. G.: An assessment of

Southern Ocean water masses and sea ice during 1988–2007 in a suite of inter-annual CORE-II simulations, Clim. Dynam., in preparation, 2014.

Droop, M.: 25 Years of algal growth kinetics a personal view, Bot. Mar., 26, 99–112, doi:10.1515/botm.1983.26.3.99, 1983.

Dunne, J. P., Sarmiento, J. L., and Gnanadesikan, A.: A synthesis of global particle export from the surface ocean and cycling through the ocean interior and on the seafloor, Global Biogeochem. Cy., 21, GB4006, doi:10.1029/2006GB002907, 2007.

Elrod, V. A., Berelson, W. M., Coale, K. H., and Johnson, K. S.: The flux of iron from continental shelf sediments: a missing source for global budgets, Geophys. Res. Lett., 31, L12307, doi:10.1029/2004GL020216, 2004.

Friedrichs, M. A., Carr, M.-E., Barber, R. T., Scardi, M., Antoine, D., Armstrong, R. A., Asanuma, I., Behrenfeld, M. J., Buitenhuis, E. T., Chai, F., Christian, J. R., Ciotti, A. M., Doney, S. C., Dowell, M., Dunne, J., Gentili, B., Gregg, W., Hoepffner, N., Ishizaka, J., Kameda, T., Lima, I., Marra, J., Mélin, F., Moore, J. K., Morel, A., O'Malley, R. T., O'Reilly, J., Saba, V. S., Schmeltz, M., Smyth, T. J., Tjiputra, J., Waters, K., Westberry, T. K., and Winguth, A.: Assessing the uncertainties of model estimates of primary productivity in the tropical Pacific Ocean, J. Marine Syst., 76, 113–133, doi:10.1016/j.jmarsys.2008.05.010, 2009.

Fung, I. Y., Meyn, S. K., Tegen, I., Doney, S. C., John, J. G., and Bishop, J. K. B.: Iron supply and demand in the upper ocean, Global Biogeochem. Cy., 14, 281–295, doi:10.1029/1999GB900059, 2000.

Garcia, H., Locarnini, R., Boyer, T., and Antonov, J.: World Ocean Atlas 2005, Nutrients (Phosphate, Nitrate, Silicate), Vol. 4, edited by: Levitus, S., Tech. rep., NOAA Atlas NESDIS 64, Washington DC, 2006.

Garcia, H., Locarnini, R., Boyer, T., Antonov, J., Zweng, M., Baranova, O., and Johnson, D.: World Ocean Atlas 2009, Nutrients (phosphate, nitrate, silicate), edited by: Levitus, S., Vol. 4, Tech. rep., NOAA Atlas NESDIS, Washington DC, 2010.

Geider, R. J., MacIntyre, H. L., and Kana, T. M.: A dynamic model of photoadaptation in phytoplankton, Limnol. Oceanogr., 41, 1–15, 1996.

Geider, R. J., MacIntyre, H. L., and Kana, T. M.: A dynamic regulatory model of phytoplanktonic acclimation to light, nutrients, and temperature, Limnol. Oceanogr., 43, 679–694, doi:10.4319/lo.1998.43.4.0679, 1998.

Gent, P. R. and Mcwilliams, J. C.: Isopycnal mixing in ocean circulation models, J. Phys. Oceanogr., 20, 150–155, doi:10.1175/1520-0485(1981)011<1443:POVMIN>2.0.CO;2, 1990.

Gent, P. R., Yeager, S. G., Neale, R. B., Levis, S., and Bailey, D. A.: Improvements in a half degree atmosphere/land version of the CCSM, Clim. Dynam., 34, 819–833, doi:10.1007/s00382-009-0614-8, 2010.

Gentleman, W., Leising, A., Frost, B., Strom, S., and Murray, J.: Functional responses for zooplankton feeding on multiple resources: a review of assumptions and biological dynamics, Deep-Sea Res. Pt. II, 50, 2847–2875, doi:10.1016/j.dsr2.2003.07.001, 2003.

Globcolour – Globcolour project, the European Service for Ocean Colour, available at: http://www.globcolour.info, last access: 1 December 2012.

Gordon, R. M., Coale, K. H., and Johnson, K. S.: Iron distributions in the equatorial Pacific: implications for new production, Limnol. Oceanogr., 42, 419–431, 1997.

Gregg, W. W. and Casey, N. W.: Global and regional evaluation of the SeaWiFS chlorophyll data set, Remote Sens. Environ., 93, 463–479, doi:10.1016/j.rse.2003.12.012, 2004.

Griffies, S. M., Biastoch, A., Böning, C., Bryan, F., Danabasoglu, G., Chassignet, E. P., England, M. H., Gerdes, R., Haak, H., Hallberg, R. W., Hazeleger, W., Jungclaus, J., Large, W. G., Madec, G., Pirani, A., Samuels, B. L., Scheinert, M., Gupta, A. S., Severijns, C. A., Simmons, H. L., Treguier, A. M., Winton, M., Yeager, S., and Yin, J.: Coordinated ocean-ice reference experiments (CORE s), Ocean Model., 26, 1–46, doi:10.1016/j.ocemod.2008.08.007, 2009.

Haid, V. and Timmermann, R.: Simulated heat flux and sea ice production at coastal polynyas in the southwestern Weddell Sea, J. Geophys. Res., 118, 2640–2652, doi:10.1002/jgrc.20133, 2013.

Hashioka, T., Vogt, M., Yamanaka, Y., Le Quéré, C., Buitenhuis, E. T., Aita, M. N., Alvain, S., Bopp, L., Hirata, T., Lima, I., Sailley, S., and Doney, S. C.: Phytoplankton competition during the spring bloom in four plankton functional type models, Biogeosciences, 10, 6833–6850, doi:10.5194/bg-10-6833-2013, 2013.

Hauck, J., Völker, C., Wang, T., Hoppema, M., Losch, M., and Wolf-Gladrow, D.: Seasonally different carbon flux changes in the Southern Ocean in response to the Southern Annular Mode, Global Biogeochem. Cy., 27, 1–10, doi:10.1002/2013GB004600, 2013.

Hill, J., Popova, E. E., Ham, D. A., Piggott, M. D., and Srokosz, M.: Adapting to life: ocean biogeochemical modelling and adaptive remeshing, Ocean Sci., 10, 323–343, doi:10.5194/os-10-323-2014, 2014.

Hirata, T., Hardman-Mountford, N. J., Brewin, R. J. W., Aiken, J., Barlow, R., Suzuki, K., Isada, T., Howell, E., Hashioka, T., Noguchi-Aita, M., and Yamanaka, Y.: Synoptic relationships between surface Chlorophyll-*a* and diagnostic pigments specific to phytoplankton functional types, Biogeosciences, 8, 311–327, doi:10.5194/bg-8-311-2011, 2011.

Hohn, S.: Coupling and decoupling of biogeochemical cycles in marine ecosystems, Ph.D. thesis, Bremen University, Germany, 2009.

Holzer, M., Primeau, F. W., DeVries, T., and Matear, R.: The Southern Ocean silicon trap: data-constrained estimates of regenerated silicic acid, trapping efficiencies, and global transport paths, J. Geophys. Res., 119, 313–331, doi:10.1002/2013JC009356, 2014.

Hoppema, M., de Baar, H. J., Fahrbach, E., Hellmer, H. H., and Klein, B.: Substantial advective iron loss diminishes phytoplankton production in the Antarctic Zone, Global Biogeochem. Cy., 17, 1025, doi:10.1029/2002GB001957, 2003.

Jakobsson, M., Macnab, R., Mayer, L., Anderson, R., Edwards, M., Hatzky, J., Schenke, H. W., and Johnson, P.: An improved bathymetric portrayal of the Arctic Ocean: Implications for ocean modeling and geological, geophysical and oceanographic analyses, Geophys. Res. Lett., 35, L07602, doi:10.1029/2008GL033520, 2008.

Jin, X., Gruber, N., Dunne, J. P., Sarmiento, J. L., and Armstrong, R. A.: Diagnosing the contribution of phytoplankton functional groups to the production and export of particulate

organic carbon, $CaCO_3$, and opal from global nutrient and alkalinity distributions, Global Biogeochem. Cy., 20, GB2015, doi:10.1029/2005GB002532, 2006.

Johnson, G. C., McPhaden, M. J., and Firing, E.: Equatorial Pacific Ocean horizontal velocity, divergence, and upwelling, J. Phys. Oceanogr., 31, 839–849, doi:10.1175/1520-0485(2001)031<0839:EPOHVD>2.0.CO;2, 2001.

Kamatani, A.: Dissolution rates of silica from diatoms decomposing at various temperatures, Mar. Biol., 68, 91–96, doi:10.1007/BF00393146, 1982.

Key, R. M., Kozyr, A., Sabine, C. L., Lee, K., Wanninkhof, R., Bullister, J. L., Feely, R. A., Millero, F. J., Mordy, C., and Peng, T.-H.: A global ocean carbon climatology: Results from Global Data Analysis Project (GLODAP), Global Biogeochem. Cy., 18, GB4031, doi:10.1029/2004GB002247, 2004.

Kriest, I. and Oschlies, A.: On the treatment of particulate organic matter sinking in large-scale models of marine biogeochemical cycles, Biogeosciences, 5, 55–72, doi:10.5194/bg-5-55-2008, 2008.

Lam, P. J. and Bishop, J. K.: The continental margin is a key source of iron to the HNLC North Pacific Ocean, Geophys. Res. Lett., 35, L07608, doi:10.1029/2008GL033294, 2008.

Lancelot, C., de Montety, A., Goosse, H., Becquevort, S., Schoemann, V., Pasquer, B., and Vancoppenolle, M.: Spatial distribution of the iron supply to phytoplankton in the Southern Ocean: a model study, Biogeosciences, 6, 2861–2878, doi:10.5194/bg-6-2861-2009, 2009.

Large, W. G. and Yeager, S. G.: Diurnal to Decadal Global Forcing for Oceans and Sea-Ice Models: The Data Sets and Flux Climatologies, NCAR/TN-460+STR, Tech. rep., National Center for Atmos. Res., Boulder, Colorado, 2004.

Large, W. G. and Yeager, S. G.: The global climatology of an interannually varying air–sea flux data set, Clim. Dynam., 33, 341–364, doi:10.1007/s00382-008-0441-3, 2009.

Laws, E. A., Falkowski, P. G., Smith, W. O., Ducklow, H., and McCarthy, J. J.: Temperature effects on export production in the open ocean, Global Biogeochem. Cy., 14, 1231–1246, doi:10.1029/1999GB001229, 2000.

Le Quéré, C., Aumont, O., Monfray, P., and Orr, J.: Propagation of climatic events on ocean stratification, marine biology, and CO_2: Case studies over the 1979–1999 period, J. Geophys. Res., 108, 3375, doi:10.1029/2001JC000920, 2003.

Löscher, B. M., De Baar, H. J. W., De Jong, J. T. M., Veth, C., and Dehairs, F.: The distribution of Fe in the Antarctic circumpolar current, Deep-Sea Res. Pt. II, 44, 143–187, doi:10.1016/S0967-0645(96)00101-4, 1997.

Luo, C., Mahowald, N. M., and Del Corral, J.: Sensitivity study of meteorological parameters on mineral aerosol mobilization, transport, and distribution, J. Geophys. Res., 108, 4447, doi:10.1029/2003JD003483, 2003.

Mahowald, N., Luo, C., Del Corral, J., and Zender, C. S.: Interannual variability in atmospheric mineral aerosols from a 22-year model simulation and observational data, J. Geophys. Res., 108, 4352, doi:10.1029/2002JD002821, 2003.

Martin, J. H., Gordon, R. M., and Fitzwater, S. E.: The case for iron, Limnol. Oceanogr., 36, 1793–1802, 1991.

Moore, J. K. and Braucher, O.: Sedimentary and mineral dust sources of dissolved iron to the world ocean, Biogeosciences, 5, 631–656, doi:10.5194/bg-5-631-2008, 2008.

Moore, J. K., Abbott, M. R., and Richman, J. G.: Location and dynamics of the Antarctic Polar Front from satellite sea surface temperature data, J. Geophys. Res., 104, 3059–3073, 1999.

Moore, J. K., Doney, S. C., Glover, D. M., and Fung, I. Y.: Iron cycling and nutrient-limitation patterns in surface waters of the World Ocean, Deep-Sea Res. Pt. II, 49, 463–507, doi:10.1016/S0967-0645(01)00109-6, 2002.

Moore, J. K., Doney, S. C., and Lindsay, K.: Upper ocean ecosystem dynamics and iron cycling in a global three-dimensional model, Global Biogeochem. Cy., 18, GB4028, doi:10.1029/2004GB002220, 2004.

Najjar, R. G., Jin, X., Louanchi, F., Aumont, O., Caldeira, K., Doney, S. C., Dutay, J.-C., Follows, M., Gruber, N., Joos, F., Lindsay, K., Maier-Reimer, E., Matear, R. J., Matsumoto, K., Monfray, P., Mouchet, A., Orr, J. C., Plattner, G.-K., Sarmiento, J. L., Schlitzer, R., Slater, R. D., Weirig, M.-F., Yamanaka, Y., and Yool, A.: Impact of circulation on export production, dissolved organic matter, and dissolved oxygen in the ocean: results from Phase II of the Ocean Carbon-cycle Model Intercomparison Project (OCMIP-2), Global Biogeochem. Cy., 21, GB3007, doi:10.1029/2006GB002857, 2007.

Nevison, C., Keeling, R., Kahru, M., Manizza, M., Mitchell, B., and Cassar, N.: Estimating net community production in the Southern Ocean based on atmospheric potential oxygen and satellite ocean color data, Global Biogeochem. Cy., 26, GB1020, doi:10.1029/2011GB004040, 2012.

O'Neill, R. V., DeAngelis, D. L., Pastor, J. J., Jackson, B. J., and Post, W. M.: Multiple nutrient limitations in ecological models, Ecol. Model., 46, 147–163, doi:10.1016/0304-3800(89)90015-X, 1989.

Orr, J., Najjar, R., Sabine, C. L., and Joos, F.: Abiotic-HOWTO, Tech. rep., Internal OCMIP Report, LSCE/CEA Saclay, Gif-sur-Yvette, France, 1999.

Pacanowski, R. C. and Philander, S. G. H.: Parameterization of vertical mixing in numerical models of tropical oceans, J. Phys. Oceanogr., 11, 1443–1451, doi:10.1175/1520-0485(1981)011<1443:POVMIN>2.0.CO;2, 1981.

Parekh, P., Follows, M. J., and Boyle, E. A.: Decoupling of iron and phosphate in the global ocean, Global Biogeochem. Cy., 19, GB2020, doi:10.1029/2004GB002280, 2005.

Parkinson, C. L. and Washington, W. M.: A large-scale numerical model of sea ice, J. Geophys. Res., 84, 311–337, doi:10.1029/JC084iC01p00311, 1979.

Piggott, M. D., Gorman, G. J., Pain, C. C., Allison, P. A., Candy, A. S., Martin, B. T., and Wells, M. R.: A new computational framework for multi-scale ocean modelling based on adapting unstructured meshes, Int. J. Numer. Meth. Fl., 56, 1003–1015, doi:10.1002/fld.1663, 2008.

Redi, M.: Oceanic isopycnal mixing by coordinate rotation, J. Phys. Oceanogr., 12, 1154–1158, doi:10.1175/1520-0485(1982)012<1154:OIMBCR>2.0.CO;2, 1982.

Schlitzer, R.: Carbon export fluxes in the Southern Ocean: Results from inverse modeling and comparison with satellite-based estimates, Deep-Sea Res. Pt. II, 49, 1623–1644, doi:10.1016/S0967-0645(02)00004-8, 2002.

Schlitzer, R.: Export production in the equatorial and North Pacific derived from dissolved oxygen, nutrient and carbon data, J. Oceanogr., 60, 53–62, doi:10.1023/B:JOCE.0000038318.38916.e6, 2004.

Schneider, B., Bopp, L., Gehlen, M., Segschneider, J., Frölicher, T. L., Cadule, P., Friedlingstein, P., Doney, S. C., Behrenfeld, M. J., and Joos, F.: Climate-induced interannual variability of marine primary and export production in three global coupled climate carbon cycle models, Biogeosciences, 5, 597–614, doi:10.5194/bg-5-597-2008, 2008.

Schourup-Kristensen, V., Hauck, J., Wolf-Gladrow, D. A., and Völker, C.: Vertical supply of iron to the mixed layer of the Southern Ocean: The ocean model effect, J. Geophys. Res., in preparation, 2014.

SeaWIFS: available at: Ocean productivity home page, http://www.science.oregonstate.edu/ocean.productivity/index.php, last access: 1 December 2012.

Sidorenko, D., Danilov, S., Wang, Q., Huerta-Casas, A., and Schröter, J.: On computing transports in finite-element models, Ocean Model., 28, 60–65, doi:10.1016/j.ocemod.2008.09.001, 2009.

Sidorenko, D., Wang, Q., Danilov, S., and Schröter, J.: FESOM under coordinated ocean-ice reference experiment forcing, Ocean Dynam., 61, 881–890, doi:10.1007/s10236-011-0406-7, 2011.

Siegel, D. A., Buesseler, K. O., Doney, S. C., Sailley, S. F., Behrenfeld, M. J., and Boyd, P. W.: Global assessment of ocean carbon export by combining satellite observations and food-web models, Global Biogeochem. Cy., 28, 181–196, doi:10.1002/2013GB004743, 2014.

Steele, M., Morley, R., and Ermold, W.: PHC: A global ocean hydrography with a high-quality Arctic Ocean, J. Climate, 14, 2079–2087, doi:10.1029/2006GL026152, 2001.

Steinacher, M., Joos, F., Frölicher, T. L., Bopp, L., Cadule, P., Cocco, V., Doney, S. C., Gehlen, M., Lindsay, K., Moore, J. K., Schneider, B., and Segschneider, J.: Projected 21st century decrease in marine productivity: a multi-model analysis, Biogeosciences, 7, 979–1005, doi:10.5194/bg-7-979-2010, 2010.

Sunda, W. G. and Huntsman, S. A.: Iron uptake and growth limitation in oceanic and coastal phytoplankton, Mar. Chem., 50, 189–206, doi:10.1016/0304-4203(95)00035-P, 1995.

Tagliabue, A., Bopp, L., and Aumont, O.: Evaluating the importance of atmospheric and sedimentary iron sources to Southern Ocean biogeochemistry, Geophys. Res. Lett., 36, L13601, doi:10.1029/2009GL038914, 2009.

Tagliabue, A., Mtshali, T., Aumont, O., Bowie, A. R., Klunder, M. B., Roychoudhury, A. N., and Swart, S.: A global compilation of dissolved iron measurements: focus on distributions and processes in the Southern Ocean, Biogeosciences, 9, 2333–2349, doi:10.5194/bg-9-2333-2012, 2012.

Tagliabue, A., Sallée, J.-B., Bowie, A. R., Lévy, M., Swart, S., and Boyd, P. W.: Surface-water iron supplies in the Southern Ocean sustained by deep winter mixing, Nat. Geosci., 7, 314–320, doi:10.1038/ngeo2101, 2014.

Taylor, K. E.: Summarizing multiple aspects of model performance in a single diagram, J. Geophys. Res., 106, 7183–7192, doi:10.1029/2000JD900719, 2001.

Taylor, M. H., Losch, M., and Bracher, A.: On the drivers of phytoplankton blooms in the Antarctic marginal ice zone: A modeling approach, J. Geophys. Res., 118, 63–75, doi:10.1029/2012JC008418, 2013.

Timmermann, R., Danilov, S., Schröter, J., Böning, C., Sidorenko, D., and Rollenhagen, K.: Ocean circulation and sea ice distribution in a finite element global sea ice–ocean model, Ocean Model., 27, 114–129, doi:10.1016/j.ocemod.2008.10.009, 2009.

Timmermann, R., Le Brocq, A. M., Deen, T., J., Domack, E. W., Dutrieux, P., Galton-Fenzi, B., Hellmer, H. H., Humbert, A., Jansen, D., Jenkins, A., Lambrecht, A., Makinson, K., Niederjasper, F., Nitsche, F.-O., Nøst, O. A., Smedsrud, L. H., and Smith, W.: Antarctic ice sheet topography, cavity geometry, and global bathymetry (RTopo 1.0.5-beta), doi:10.1594/PANGAEA.741917, 2010.

Vichi, M. and Masina, S.: Skill assessment of the PELAGOS global ocean biogeochemistry model over the period 1980–2000, Biogeosciences, 6, 2333–2353, doi:10.5194/bg-6-2333-2009, 2009.

Vogt, M., Hashioka, T., Payne, M. R., Buitenhuis, E. T., Quéré, C. Le, Alvain, S., Aita, M. N., Bopp, L., Doney, S. C., Hirata, T., Lima, I., Sailley, S., and Yamanaka, Y.: The distribution, dominance patterns and ecological niches of plankton functional types in Dynamic Green Ocean Models and satellite estimates, Biogeosciences Discuss., 10, 17193–17247, doi:10.5194/bgd-10-17193-2013, 2013.

Wadley, M. R., Jickells, T. D., and Heywood, K. J.: The role of iron sources and transport for Southern Ocean productivity, Deep-Sea Res. Pt. I, 87, 82–94, doi:10.1016/j.dsr.2014.02.003, 2014.

Wagener, T., Guieu, C., Losno, R., Bonnet, S., and Mahowald, N.: Revisiting atmospheric dust export to the Southern Hemisphere ocean: Biogeochemical implications, Global Biogeochem. Cy., 22, GB2006, doi:10.1029/2007GB002984, 2008.

Wang, Q., Danilov, S., and Schröter, J.: Finite element ocean circulation model based on triangular prismatic elements, with application in studying the effect of topography representation, J. Geophys. Res., 113, C05015, doi:10.1029/2007JC004482, 2008.

Wang, Q., Danilov, S., Sidorenko, D., Timmermann, R., Wekerle, C., Wang, X., Jung, T., and Schröter, J.: The Finite Element Sea Ice–Ocean Model (FESOM) v.1.4: formulation of an ocean general circulation model, Geosci. Model Dev., 7, 663–693, doi:10.5194/gmd-7-663-2014, 2014.

Wang, S., Bailey, D., Lindsay, K., Moore, J. K., and Holland, M.: Impact of sea ice on the marine iron cycle and phytoplankton productivity, Biogeosciences, 11, 4713–4731, doi:10.5194/bg-11-4713-2014, 2014.

Wanninkhof, R.: Relationship between wind speed and gas exchange over the ocean, J. Geophys. Res., 97, 7373–7382, doi:10.1029/92JC00188, 1992.

Wekerle, C., Wang, Q., Danilov, S., Jung, T., and Schröter, J.: The Canadian Arctic Archipelago throughflow in a multiresolution global model: model assessment and the driving mechanism of interannual variability, J. Geophys. Res., 118, 4525–4541, doi:10.1002/jgrc.20330, 2013.

Wilhelm, S. W., King, A. L., Twining, B. S., LeCleir, G. R., DeBruyn, J. M., Strzepek, R. F., Breene, C. L., Pickmere, S., Ellwood, M. J., Boyd, P. W., and Hutchins, D. A.: Elemental quotas and physiology of a southwestern Pacific Ocean plankton community as a function of iron availability, Aquat. Microb. Ecol., 68, 185–194, doi:10.3354/ame01611, 2013.

Wolf-Gladrow, D. A., Zeebe, R. E., Klaas, C., Körtzinger, A., and Dickson, A. G.: Total alkalinity: the explicit conservative expression and its application to biogeochemical processes, Mar. Chem., 106, 287–300, 2007.

Yamanaka, Y. and Tajika, E.: The role of the vertical fluxes of particulate organic matter and calcite in the oceanic carbon cycle: studies using an ocean biogeochemical general circulation model, Global Biogeochem. Cy., 10, 361–382, doi:10.1029/96GB00634, 1996.

Yool, A., Popova, E. E., and Anderson, T. R.: Medusa-1.0: a new intermediate complexity plankton ecosystem model for the global domain, Geosci. Model Dev., 4, 381–417, doi:10.5194/gmd-4-381-2011, 2011.

PUBLICATION II

6

Vertical supply of iron to the mixed layer of the Southern Ocean: The ocean model effect

Vibe Schourup-Kristensen[1], Judith Hauck[1], Martin Losch[1], Dieter A. Wolf-Gladrow[1] and Christoph Völker[1]

[1] Alfred-Wegener-Institut Helmholtz-Zentrum für Polar und Meeresforschung, Postfach 12 01 61, 27515 Bremerhaven, Germany.

Submitted

Abstract In the Southern Ocean, the micronutrient iron plays a key role as a limiting nutrient for phytoplankton growth. Studies of the iron supply to the surface mixed layer have traditionally focused on the contribution from aeolian and sedimentary input, but recent work has highlighted the importance of the supply from below. We performed a model study in which the biogeochemical model REcoM2 was coupled to two different ocean models, the Finite Element Sea-ice Ocean Model (FESOM) and the MIT general circulation model (MITgcm). We analyzed the magnitude of the iron sources from below in the two models and assessed how the choice of ocean model impacts the iron fluxes across the base of the mixed layer and thereby also the modeled net primary and export production. Our results show a remarkable difference in terms of magnitude and mode of iron transport; the mean iron supply is four times higher in MITgcm than in FESOM, and the dominant pathway is through entrainment, whereas diffusion dominates in FESOM. This difference also has the effect that NPP is 48 % higher in FESOM than in MITgcm and that the export efficiency, the ratio between net primary production and export production, is smaller. In conclusion our study shows that the ocean model, and especially the mixed layer depth, has a key influence on the modeled iron fluxes into the surface mixed layer and thereby also on net primary and export production in the Southern Ocean.

6.1 INTRODUCTION

The Southern Ocean is known as one of the so-called High-Nutrient Low-Chlorophyll (HNLC) areas, characterized by low levels of chlorophyll *a* despite of high concentrations of macronutrients. Since the early 1990'ies it has been recognized that iron, which for instance is needed for phytoplankton photosynthesis and respiration, is an important limiting factor for primary production in the Southern Ocean (e.g. Martin, 1990; Martin et al., 1990; Martin et al., 1991).

Dissolved iron is supplied to the surface mixed layer by two mechanisms; remineralization of organic material (Boyd et al., 2010) and so-called new supply. The latter is provided by external sources such as dust deposition (e.g. Wagener et al., 2008), remineralization from the sediments (e.g. Blain et al., 2001), release from icebergs (Lin et al., 2011) and it is supplied from the deeper water by physical mechanisms such as upwelling, entrainment and diffusion (e.g. Tagliabue et al., 2014). The iron supply from the deep water plays an especially large role in the remote waters in the Southern Ocean (de Baar et al., 1995; Löscher et al., 1997) because the other sources tend to be localized in their distribution. The amount of iron supplied through the different sources is, however, not well quantified. Recent modeling studies have shown that the sediment source plays a larger role than the other external iron sources (Lancelot et al., 2009; Tagliabue et al., 2009), but studies regarding the impact of the supply from below are sparse.

In the Southern Ocean, large scale upwelling occurs south of the polar front (e.g. Speer et al., 2000), and it has been suggested that this contributes significantly to the total iron input to the surface water, with estimated average values ranging from 8 to 50 $\mu mol\, m^{-2}\, yr^{-1}$ (Watson et al., 2000; Hoppema et al., 2003; de Baar et al., 1995). But Tagliabue et al. (2014) argued that entrainment of iron through deepening of the mixed layer in the fall dominate the supply of iron from below, and that upwelling is of little importance when averaged over the entire Southern Ocean as it is cancelled out by the removal of iron through downwelling. The significance of diffusion likewise differs between studies; consistent with the findings of Tagliabue et al. (2014), Croot et al. (2007) showed that diffusion was of minor importance east of New Zealand, whereas Law et al. (2003) found that vertical eddy diffusion played a large role in the Antarctic Circumpolar Current (ACC) south of New Zealand. The effect of horizontal iron advection across the base of the mixed layer has been argued to play a role south of Australia (Ellwood et al., 2008), something that is induced by the combination of a southwards shoaling pycnocline and northwards wind-driven Ekman transport.

The flux of iron across the base of the mixed layer is dependent on the ocean mixing and circulation, which for example controls the depth of the mixed layer, the strength of the upwelling and the volume of entrained water. But it is likewise affected by the iron concentration just below the mixed layer and the iron gradient across the base of the mixed layer. The ferricline can be defined as the depth at which the iron gradient ($\partial Fe/\partial z$) has its highest value. The relative position of the ferricline to the base of the mixed layer has a large impact on the iron flux into the mixed layer; when the mixed layer depth (MLD) is shallower than the ferricline, only little iron can be supplied to the surface layer, and when the MLD comes below the ferricline a much larger supply can take place (Tagliabue et al., 2014).

In Ocean General Circulation Biogeochemical Models, a realistic ocean circulation and mixing is especially difficult to reproduce in the Southern Ocean (e.g. Downes et al., 2014), and this has the consequence that the export production (EP) estimated by the biogeochemical components varies widely in this region (Doney et al., 2004; Najjar et al., 2007). Models are, despite of this ambiguity, a tool routinely used to investigate the dynamics of export and primary production in the Southern Ocean (e.g. Taylor et al., 2013; Marinov et al., 2006), and although biogeochemical models are inherently simplistic and require strict validation (e.g. Assmann et al., 2010; Schourup-Kristensen et al., 2014), a large uncertainty regarding the vertical fluxes of iron is additionally introduced by the representation of ocean mixing and advection. Knowledge about the way the ocean model impacts the vertical iron fluxes is therefore crucial in order to interpret results regarding the complex interplay between physics and biology in the present, but also in future perturbations of the Southern Ocean.

In this paper we examine the impact of the Ocean General Circulation Model (OGCM) on the input of iron to the mixed layer of the Southern Ocean from below. We do this by comparing the results of two global OGCMs, the Finite Element Sea-ice Ocean Model (FESOM) and the Massachusetts Institute of Technology general circulation model (MITgcm), coupled to the same biogeochemical model, (The Regulated Ecosystem Model, REcoM2). We assess how the ocean model impacts the magnitude and spatial distribution of net primary production (NPP) as well as the amount of carbon that is exported to the deep ocean.

6.2 METHODS

6.2.1 *Experiment*

Two similar experiments were carried out with the coupled FESOM-REcoM2 (Schourup-Kristensen et al., 2014) and MITgcm-REcoM2 (Hauck et al., 2013) models. The ocean models were spun-up for 300 years after which the coupled REcoM2-OGCM runs were started and run for a total of 50 years. The CORE-I normal year forcing (Large and Yeager, 2009) was used throughout the runs, and the analysis carried out here is based on the last five years of the coupled runs.

6.2.2 *Ocean model I: FESOM*

The Finite Element Sea-Ice Ocean Model (FESOM) is a global ocean circulation model, solving the primitive equations using the hydrostatic and boussinesq approximations. It is coupled to a dynamic-thermodynamic sea-ice model, which operates on the same surface mesh. Discretization is carried out using the finite element method (Sidorenko et al., 2011; Wang et al., 2014).

The sub-grid scale processes of vertical mixing are parameterized using a Pacanowski-Philander type scheme, which ensures increased mixing as stratification weakens (Pacanowski and Philander, 1981). This is combined with additional mixing near the surface over a depth defined by the Monin-Obukhov length, following the suggestion of Timmermann and Beckmann (2004) to avoid unrealistically shallow summer mixed layers. The background vertical eddy diffusion is set to $1 \cdot 10^{-4}\ m^2\,s^{-1}$ for momentum and $1 \cdot 10^{-5}\ m^2\,s^{-1}$ for tracers, with a maximum value of $2 \cdot 10^{-2}\ m^2\,s^{-1}$.

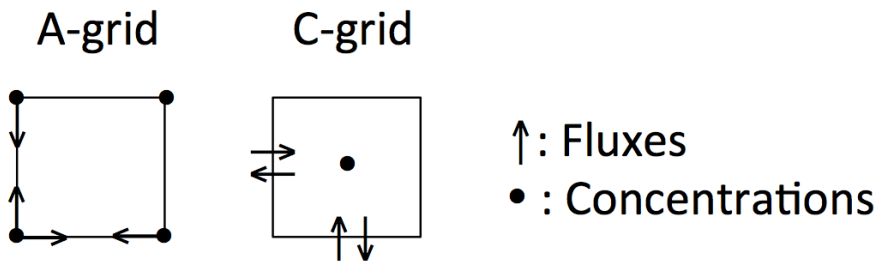

Figure 6.1: Location of concentrations and fluxes on A-grids and C-grids, respectively.

Horizontal mixing along neutral density slopes is incorporated following Redi (1982) and the eddy induced advection is implemented through the Gent and McWilliams scheme (Gent and Mcwilliams, 1990) with a critical neutral slope of 0.004.

For the spin-up, temperature and salinity fields were initialized with values from the PHC3.0 climatology (Steele et al., 2001) and the sea-ice was taken from a previous simulation. The sea surface salinity is restored towards the PHC3.0 climatology with a piston velocity of 10 m per 60 days. The version of FESOM used in the current run is presented by Sidorenko et al. (2011).

FESOM uses a prismatic mesh which is horizontally triangulated and unstructured, but vertically aligned, with the prisms divided into tetrahedra. Calculations are carried out on an A-grid (Arakawa and Lamb, 1977), with all fluxes and concentrations being calculated at nodes located in the corners of the prisms (Fig. 6.1). The mesh used here is similar to the one used by Schourup-Kristensen et al. (2014), with the horizontal resolution ranging from 15 km in the polar regions to 180 km in the central subtropical gyres. For a better description of the equatorial undercurrent and coastal processes, a resolution of 40 km was applied around the Equator and along the coasts. In the Southern Ocean the resolution ranges from 15 km close to the Antarctic to 150 km at 50°S. In the vertical, FESOM uses z-coordinates and the mesh has 32 levels. The resolution of the mesh increases towards the surface with 9 levels located in the upper 100 meters of the water column.

6.2.3 *Ocean model II: MITgcm*

As second general circulation model we use the Massachusetts Institute of Technology general circulation model (MITgcm, Marshall et al., 1997), which also solves the primitive equations under the Boussinesq approximation, in its hydrostatic mode. The model is discretized on a regular latitude-longitude-depth grid using the Arakawa C grid (Fig. 6.1). Longitudinal resolution is constant at 2°, while the latitudinal resolution varies from 0.38° to 2°, with higher resolution around the equator to better resolve the equatorial current systems, and increasing resolution southwards of the equator. In the vertical we use 30 layers, with 6 layers within the uppermost 100 m and layer thickness increasing with depth up to 500 m below a depth of 3700 m. The setup used here excludes the Arctic north of 80°N and we use the bathymetry of Timmermann et al. (2010).

Our setup includes a dynamic sea-ice model (Losch et al., 2010), a parameterization for sub-grid-scale mixing (Gent and Mcwilliams, 1990) with variable coefficient

and for density-driven downslope flows (Campin and Goosse, 1999). Vertical mixing within the mixed layer is parameterized using the *k*-profile parameterization (Large et al., 1994). The setup is described further by Hauck et al. (2013).

6.2.4 *Biogeochemical module: REcoM2*

The Regulated Ecosystem Model with two phytoplankton classes (REcoM2) belongs to the class of so-called quota models, in which the intracellular nutrient ratios are allowed to differ from the Redfield ratios within certain limits. Coupled to the MITgcm, different versions of REcoM have been used for carbon cycle research in the Southern Ocean (Hauck et al., 2013; Taylor et al., 2013; Losch et al., 2014), and it has recently been coupled to the Finite Element Sea-ice Ocean Model, which similarly operates in the global domain (Schourup-Kristensen et al., 2014).

REcoM2 has two phytoplankton classes, nanophytoplankton and diatoms, and one group of zooplankton. It describes the nutrients nitrogen, silicon and iron. The iron cycle is based on the work by Parekh et al. (2005). The concentration of dissolved iron is changed by uptake and release from phyto- and zooplankton, remineralization of detritus and by scavenging. The intracellular iron to carbon ratio is constant, and the biological uptake and release of iron is hence tied to the carbon cycle.

The aeolian input of iron is prescribed as monthly climatologies (Luo et al., 2003; Mahowald et al., 2003). We assume that the dust contains 3.5 % of iron, of which 1.5 % is instantly released in the surface ocean and the rest is lost. Iron is further added to the water from the sediments, where remineralization of iron is calculated based on the rate of carbon remineralization from the sediments to the ocean following Elrod et al. (2004). A full description of the version of REcoM2 used in this study, including parameter settings, can be found in Schourup-Kristensen et al. (2014).

REcoM2 is initialized with arbitrarily small values in all tracers except for dissolved iron (DFe), dissolved inorganic nitrogen (DIN), dissolved inorganic carbon (DIC), dissolved inorganic silicon (DSi) and Total Alkalinity (TA). TA and DIC are initialized with contemporary values from the GLODAP dataset (Key et al., 2004) and DSi and DIN with values from the Levitus World Ocean Atlas from 2005 (Garcia et al., 2006). So far, the measurements of iron profiles are too sparse to interpolate to a global field. We therefore initialize the field of dissolved iron with output from the earth system model PISCES (Aumont and Bopp, 2006), which has been modified in the Southern Ocean to the mean profiles presented by Tagliabue et al. (2012).

6.2.5 *Calculations*

We assess the mean flux of dissolved iron across the base of the mixed layer in the Southern Ocean south of 50°S, through vertical advection (up- and downwelling), horizontal advection, en- and detrainment and vertical eddy diffusion (Fig. 6.2). We define the mixed layer using the density threshold criteria of $0.03\,\mathrm{kg\,m^{-3}}$ following de Boyer Montegut et al. (2004).

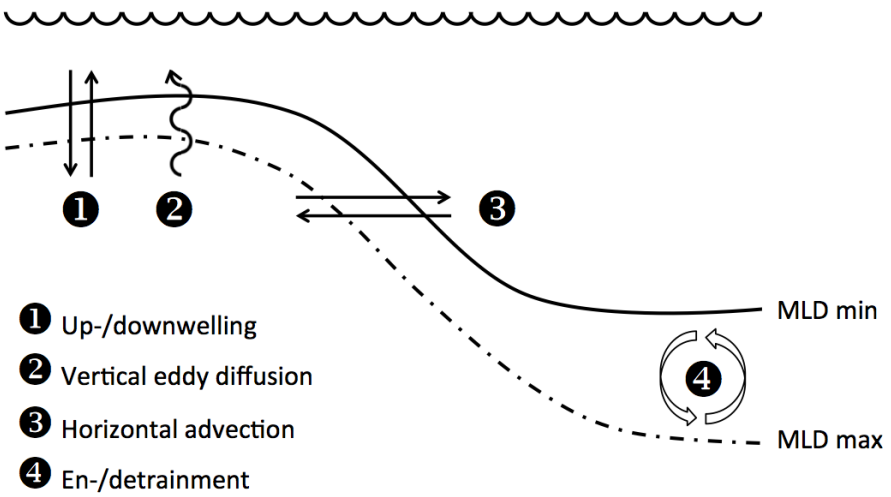

Figure 6.2: Schematics of the main physical processes responsible for bringing or removing iron to or from the mixed layer of the ocean (After Levy et al., 2013, Fig. 1b).

The flux of dissolved iron across the base of the mixed layer ($F(DFe)$) is calculated following Levy et al. (2013).

$$F(DFe) = \underbrace{-DFe_h \left(w_h + \mathbf{u}_h \cdot \nabla_H h + \frac{\partial h}{\partial t} \right)}_{\text{Subduction}} + \underbrace{\left(K_z \cdot \frac{\partial DFe}{\partial z} \right)_h}_{\text{Vertical eddy diffusion}} + \underbrace{\int_0^h E_{DFe}\, dz}_{\text{Eddy mixing}} \quad (6.1)$$

Here, the subscript h denotes the depth of the base of the mixed layer. The subduction term (i.e. Cushman-Roisin, 1987) entails the supply of iron from up-/downwelling ($DFe_h \cdot w_h$), from lateral advection across the sloping base of the mixed layer ($DFe_h \cdot \mathbf{u}_h \cdot \nabla_H h$) and from entrainment through the deepening/shoaling of the mixed layer over time ($DFe_h \cdot \partial_t h$). The variable DFe_h denotes the iron concentration at the base of the mixed layer and w_h and $\mathbf{u}_h = (u_h, v_h)$ are the vertical and horizontal velocity at the base of the mixed layer, respectively. The slope of the base of the mixed layer is defined as $\nabla_H h = (\partial h/\partial x, \partial h/\partial y)$ and $\partial h/\partial t$ is the change in the MLD with time.

The vertical eddy diffusion term covers the mixing from sub-grid scale turbulence, causing a transport of iron across the base of the mixed layer and is calculated online in both models. Here, the variable K_z denotes the diffusivity coefficient and $\partial DFe/\partial dz$ is the iron gradient, both at depth h.

The Eddy mixing term denotes the eddy mediated isopycnal transport of iron across the sloping base of the mixed layer. It is parameterized and is added to the advection term during online calculation in both models. We accordingly do not show explicit numbers of the iron supply through eddy mediated transport in the current study.

To obtain the yearly input of iron to the mixed layer from below, Eq. (6.1) is integrated over time. The model output has been saved with monthly intervals in both models, and the offline calculated iron fluxes are thus calculated for this time interval.

In models, the calculation of vertical fluxes is restricted by the finite nature of the model grids. Consequently, differences in the calculations of iron transport through up-/downwelling and diffusion occur due to the formulation of FESOM and MITgcm on an A-grid and C-grid respectively (Fig. 6.1).

For the up- and downwelling, the velocity and the iron concentration are defined in the same grid point in FESOM, whereas the iron concentration below or above the flux depth is used in the MITgcm, dependent on the direction of the vertical velocity.

For the vertical eddy diffusivity, the iron gradient at the point of the vertical eddy diffusion coefficient is needed. In FESOM, we used the gradient above the K_z-node due to the MLD definition. In MITgcm, the gradient is calculated as the difference between the concentration depth above and below the K_z, which is defined at the flux-points (Fig. 6.1).

For the horizontal advection, the result from FESOM is interpolated onto a regular $1° \times 1°$ grid, and calculations are performed using the centered difference gradient for both models.

6.3 RESULTS

6.3.1 *Yearly mean iron supply and biological production*

The mean supply of iron across the base of the mixed layer south of 50°S varies widely between the two models (Fig. 6.3), summing up to 20 $\mu mol\,Fe\,m^{-2}\,yr^{-1}$ in FESOM, and to 84 $\mu mol\,Fe\,m^{-2}\,yr^{-1}$ in MITgcm.

En- and detrainment transports iron into the surface layer during mixed layer deepening, and removes it during shallowing. It is important in both models, supplying 4.3 $\mu mol\,Fe\,m^{-2}\,yr^{-1}$, or 22 % of the mean iron supply from below, in FESOM, and in the MITgcm it is the largest of the iron sources with a total mean of 44 $\mu mol\,Fe\,m^{-2}\,yr^{-1}$, or 53 % of the iron supply (Fig. 6.3).

Vertical eddy diffusion across the base of the mixed layer occurs due to small-scale turbulent mixing brought on by energy cascading from for instance surface wind mixing. It is the dominant mechanism for vertical iron transport in FESOM, summing up to 13 $\mu mol\,Fe\,m^{-2}\,yr^{-1}$ and comprising 63 % of the total iron supply from below. In the MITgcm, the vertical eddy diffusion is the smallest of the sources taken into account, summing up to 2 $\mu mol\,Fe\,m^{-2}\,yr^{-1}$, or 2.5 % of the total mean supply (Fig. 6.3).

South of the Antarctic Polar Front upwelling dominates over downwelling, and in our study the mean upwelling south of 50 °S sums up to 29 Sv in FESOM and 27 Sv in the MITgcm ($1\,Sv = 10^6\,m^3\,s^{-1}$), both slightly lower than the 34 Sv estimated by Sloyan and Rintoul (2001). The net supply of iron to the mixed layer through upwelling is relatively small in both models, summing up 0.9 $\mu mol\,Fe\,m^{-2}\,yr^{-1}$, or 4 % of the total supply from below in FESOM and to 5.3 $\mu mol\,Fe\,m^{-2}\,yr^{-1}$, or 6 % in MITgcm (Fig. 6.3).

The pycnoclines, and hence also the MLD, shoal towards the south in the Southern Ocean, while the meridional flow of the surface water is in a northerly direction due to Ekman flow induced by the westerlies. This has the consequence that water is transported across the sloping base into the mixed layer, significantly contributing to the inflow of dissolved iron in both models (Fig. 6.3); in FESOM it comprises

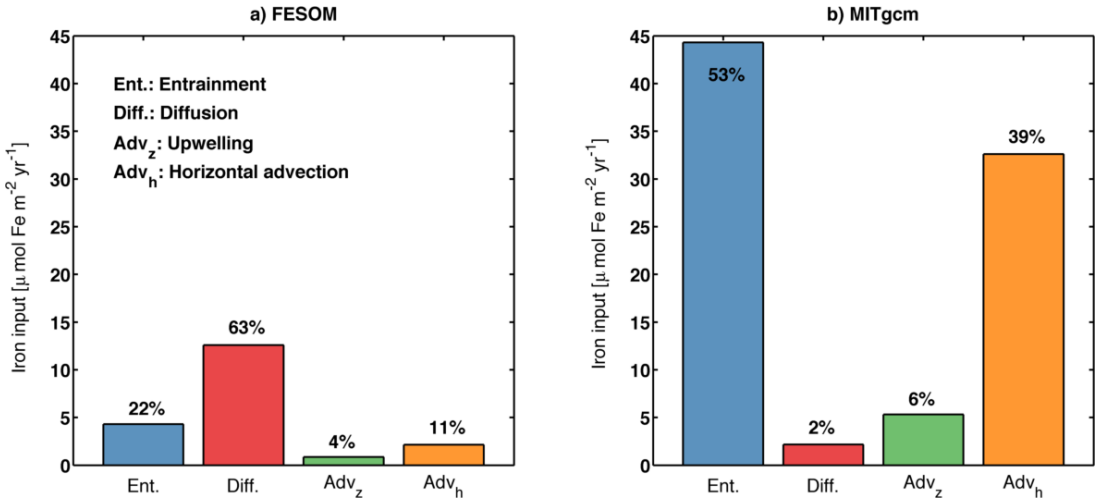

Figure 6.3: Mean upwards iron fluxes across the base of the mixed layer south of 50° S in the two models.: a) FESOM b) MITgcm. The percentage that each source contribute to the model in question is additionally marked.

2.1 μmol Fe m^{-2} yr^{-1}, or 11 % of the mean supply, and in MITgcm 33 μmol Fe m^{-2} yr^{-1} (39 %).

New iron is further supplied to the surface water through aeolian and sedimentary input in REcoM2. The input from dust south of 50°S comprises 1.29 μmol Fe m^{-2} yr^{-1} in both models, and the total supply from the sediment averages 0.43 and 0.45 μmol Fe m^{-2} yr^{-1} in FESOM and MITgcm, respectively.

The annual average NPP south of 50°S sums up to 3.1 Pg C yr^{-1} in FESOM, and in MITgcm it equals 2.1 Pg C yr^{-1} (Table 6.1). Despite of the difference in NPP between the models, both results are within the range of previous NPP estimates (e.g. Carr et al., 2006). The annual EP, calculated at a reference depth of 100 m, sums up to 1.12 and 1.22 Pg C yr^{-1} in FESOM and MITgcm, respectively, which is close to values from previous studies (Table 6.1).

For a model run in equilibrium, new production equals the export production, and we can consequently define the export efficiency as the ratio between the modeled EP and NPP. In FESOM, the mean export efficiency is 0.36 and in MITgcm it is 0.58 (Table 6.1). Previous studies (Boyd et al., 2005; Bowie et al., 2009; de Jong et al., 2012) show that the ratio between new and total NPP is highly variable, depending on the availability of iron, with measurements ranging from 0.05 to 0.6 EP/NPP (Table 6.1). The export efficiency in FESOM of 0.36 is thus within this range, while the MITgcm value of 0.58 is in the higher end, consistent with less iron limitation (e.g. Bowie et al., 2009).

6.3.2 *Seasonal cycle*

Mixed layer depth and ferricline

Consistent with observations (Sallée et al., 2010), the mean seasonal cycle of the mixed layer in the two models reaches the shallowest point in January and the deepest in August and September (Fig. 6.4). The MLD in FESOM is consistently shallower than in the observations, with the mean MLD_{max} being 21 m too shallow, whereas the MLD in MITgcm is too shallow from January to May, and too deep from June to

Table 6.1: Yearly NPP, EP and export efficiency south of 50°S for the two models as well as results from previous studies.

VALUE	UNIT	FESOM	MITGCM	OTHERS
NPP	$[\mathrm{Pg\,C\,yr^{-1}}]$	3.1	2.1	1.1 - 4.9[a]
EP	$[\mathrm{Pg\,C\,yr^{-1}}]$	1.1	1.22	1[b]
Export efficiency		0.36	0.58	0.05 - 0.6[c]

[a](Carr et al., 2006).

[b](Schlitzer, 2002; Nevison et al., 2012).

[c](Bowie et al., 2009; Boyd et al., 2005; de Jong et al., 2012).

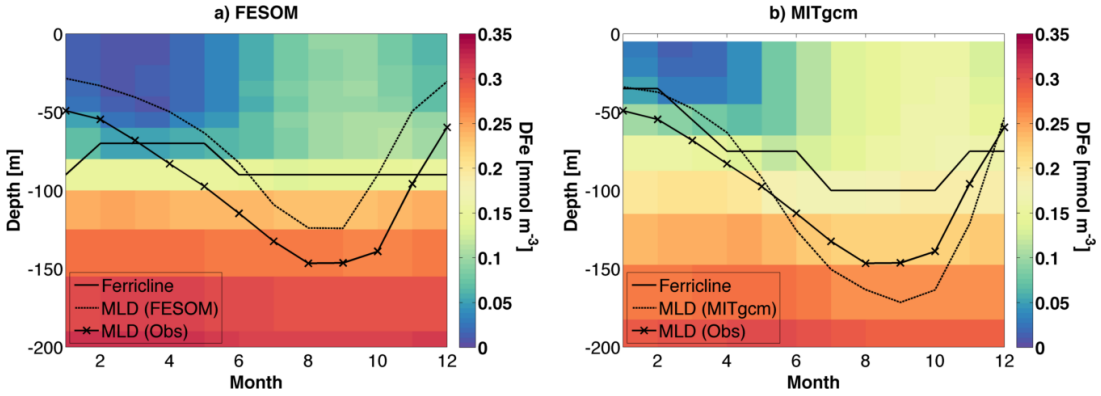

Figure 6.4: The seasonal development of the modeled mean iron profile south of 50 °S in the upper 200 meter. The depth of the modeled and observed mixed layer and the ferricline is likewise plotted. Observations of MLD from Sallée et al. (2010). a) FESOM b) MITgcm

November. The MITgcm's mean $\mathrm{MLD_{min}}$ is 20 m shallower than in the observations, and the $\mathrm{MLD_{max}}$ is 32 m deeper.

The depth of the mixed layer has a large impact on the vertical iron profile in the two models and hence also on the relative position of the MLD and the ferricline (Fig. 6.4). Following Tagliabue et al. (2014), the ferricline is defined as the depth where the maximum iron gradient occurs. In FESOM, the mean MLD is located well above the ferricline from January to April (Fig. 6.4a), and the iron concentration at the base of the mixed layer is consequently very low during these months. In MITgcm, the mean MLD is situated at approximately the same depth as the ferricline from January to May, and below it from June to November (Fig. 6.4b), and the mean iron concentration at the base of the mixed layer is consequently higher throughout the year in this model as compared to FESOM.

Iron supply

The iron supply through entrainment shows a clear seasonal cycle in both models, being large and positive during mixed layer deepening in the fall and large and negative in spring (Fig. 6.5a and b). The seasonal deepening of the MLD starts earlier in the MITgcm (Fig. 6.4), leading to a longer period of net entrainment in this model. Despite of the large detrainment in the spring in both models (Fig. 6.5a and b), the cumulative iron flux from entrainment is positive until October in FESOM (not shown),

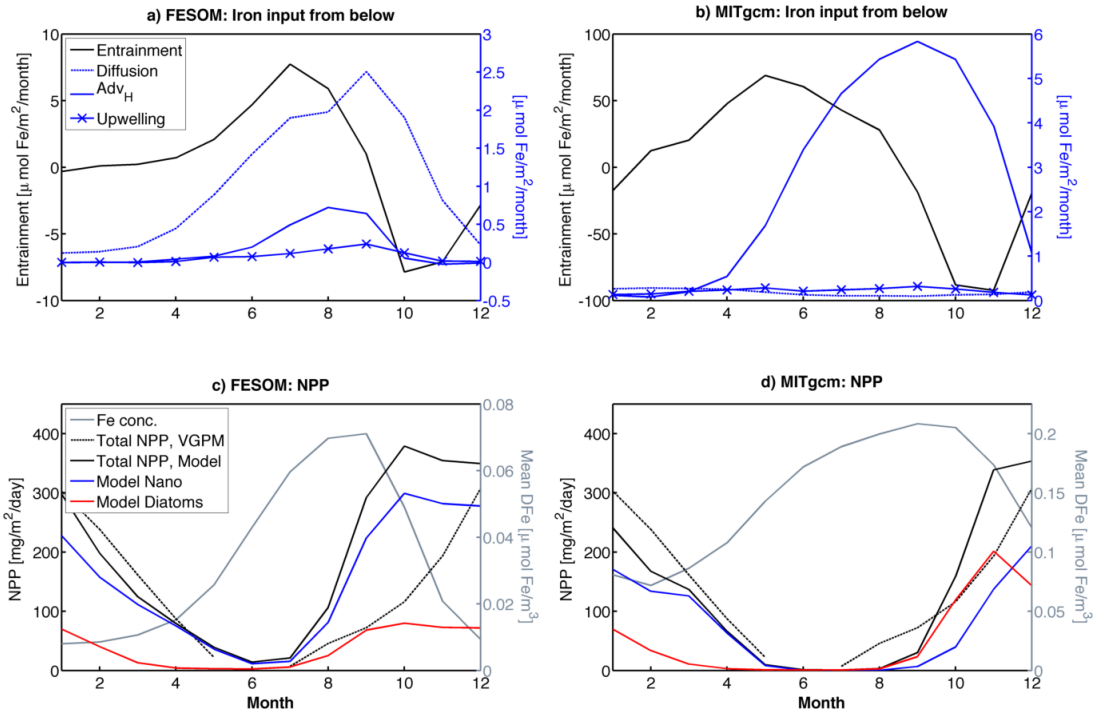

Figure 6.5: The monthly mean of iron supply to the mixed layer through entrainment, vertical eddy diffusion, horizontal advection and upwelling in a) FESOM and b) MITgcm. Notice the different axes and scales. The monthly mean of the iron concentration in the mixed layer, the total NPP as well as the contributions from nanophytoplankton and diatoms is plotted for c) FESOM and d) MITgcm. The seasonal cycle of the total NPP is calculated from the MODIS satellite and the VGPM algorithm (Behrenfeld and Falkowski, 1997).

with possible implications for the spring bloom as discussed below. In MITgcm, the positive cumulative iron flux from entrainment is positive from February onwards (not shown).

The magnitude of the iron flux from vertical eddy diffusivity differs greatly between the models (Fig. 6.3), and so does the timing of the supply; in FESOM the highest rate of supply occurs from June to November when the iron concentration at the base of the mixed layer is relatively high, whereas the major part of the supply from vertical eddy diffusion in MITgcm takes place from January to June during deepening of the mixed layer, as deepening leads to a higher diffusivity coefficient at the base of the mixed layer.

The maximum supply of iron through horizontal advection occurs in August in FESOM and in September in MITgcm, but the inflow starts two months earlier in MITgcm than in FESOM, due to the earlier deepening of the mixed layer (Fig. 6.5a and b).

The iron supply through upwelling is small in both models (Fig. 6.3), with the largest input occurring during winter and spring in both models (Fig. 6.5a and b). As the strength of the upwelling is similar in the two models, the larger mean flux in MITgcm (Fig. 6.3) can be attributed to the higher iron concentration at the base of the mixed layers (Fig. 6.7a and b).

Biological production

In FESOM, the timing of the spring bloom initialization is correct, but the maximum is reached two months earlier than in the observations (Fig. 6.5c). In MITgcm, the bloom is initiated slightly late, but the timing of the maximum fits well with the satellite-based estimates (Fig. 6.5d). FESOM thus has a better date of initialization and MITgcm a better peak timing, but both models have too steep increases in NPP during the spring bloom. The difference between the models shows that the circulation and mixing plays a role regarding the timing of the biological processes. One factor that may impact the timing of the spring bloom is the MLD, which is deeper in MITgcm than in FESOM north of 60°S. Less light thus reaches the phytoplankton in the mixed layer on average in MITgcm, pointing towards a larger role of light limitation in this model. This is further confirmed by MITgcm's higher iron concentration in the surface water (Fig. 6.4).

The iron concentration in the mixed layer is relatively low in FESOM (Fig. 6.5c). As the nanophytoplankton have a smaller demand for iron through a smaller half saturation constant, they dominate production in this model (Fig. 6.5c). The larger amount of nanophytoplankton in FESOM further has the effect that a larger degree of remineralization takes place in the mixed layer, sustaining NPP in November and December (Fig. 6.5c). In MITgcm, the deeper mixed layer keeps the production light limited longer, and the iron concentration in the mixed layer higher. In August and September production is dominated by diatoms, which have a higher maximum growth rate in the model. When the iron surface concentration decreases towards the end of the year, the fraction of diatoms likewise decrease due to their higher half saturation constant (Fig. 6.5d).

The average composition of the NPP differs significantly between the two models; nanophytoplankton is responsible for 79 % of the Southern Ocean NPP in FESOM, whereas they comprise 33 % of the NPP in MITgcm. In a study based on satellite observations, Hirata et al. (2011) show that diatoms comprise less than 20 % of the biomass in the Southern Ocean (Fig. 1 in Vogt et al., 2013), in agreement with FESOM. Bracher et al. (2009) conversely show that diatoms dominate production in the South-

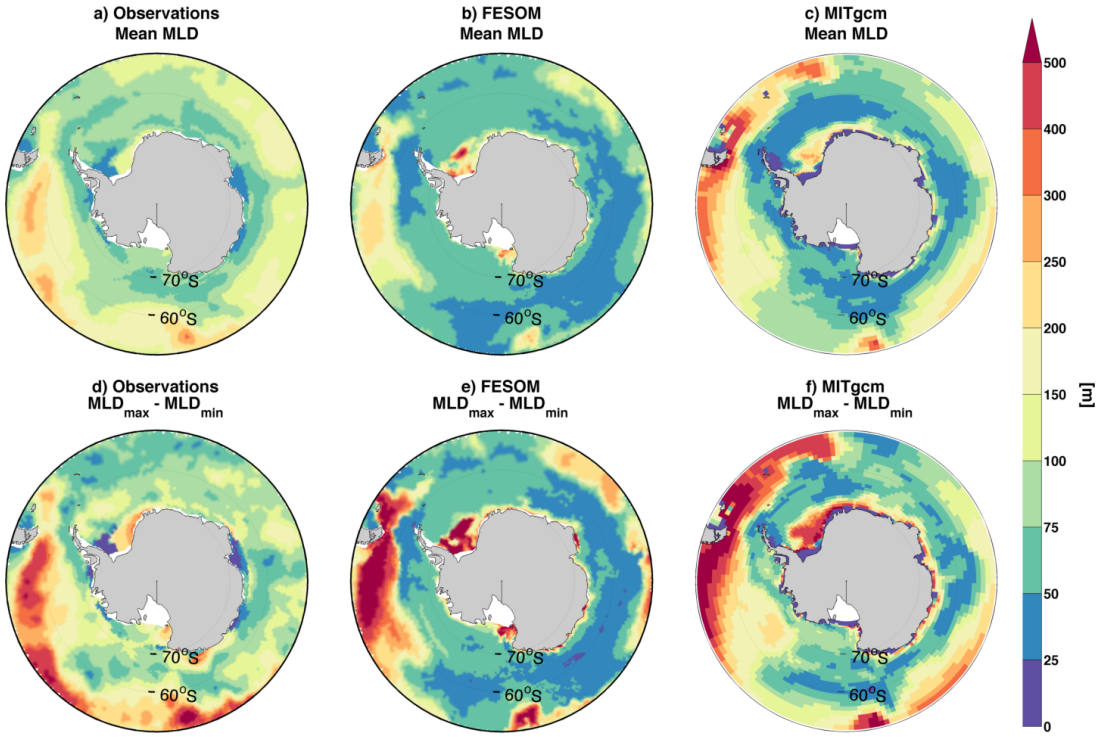

Figure 6.6: The yearly averaged MLD: a) based on observations (Sallée et al., 2010) b) FESOM c) MITgcm. The seasonal amplitude of the MLD (MLD_{max} and MLD_{min}): d) based on observations (Sallée et al., 2010) e) FESOM f) MITgcm.

ern Ocean, which is in line with Hoffmann et al. (2008) who argued that diatoms are responsible for up to 75 % of the NPP, and fits well with the result from MITgcm. The amount of diatoms in the Southern Ocean varies widely between model studies as shown by Vogt et al. (2013). Our study suggests that part of the explanation for this large difference could lie in the OGCMs and their representation of the vertical iron supply.

6.3.3 *Spatial distribution*

Mixed layer depth and ferricline

In FESOM, the yearly averaged MLD is shallower than in the observations in the whole Southern Ocean (Fig. 6.6a and b), though the spatial distribution with deeper mixed layers near the Polar Front and shallower in the temporarily ice-covered zone (TICZ) is captured. In MITgcm, the yearly averaged MLD is slightly shallow in the area of the TICZ, approximately south of 60°S (Fig. 6.6c). The deeper MLD in the area between 50 and 60°S is also captured in this model, though it becomes too deep in the Pacific and especially in the Atlantic sector of the Southern Ocean.

The seasonal amplitude of the MLD especially affects the amount of the entrained iron (Eq. 6.1). In FESOM, the amplitude is captured, and is even slightly high compared to observations, north of 60°S (Fig. 6.6d and e). But it is smaller than in the observations in the TICZ south of 60°S. The amplitude is closer to the observations in MITgcm (Fig. 6.6d and f), though it again becomes too large in the Atlantic and eastern Pacific Southern sectors of the Southern Ocean.

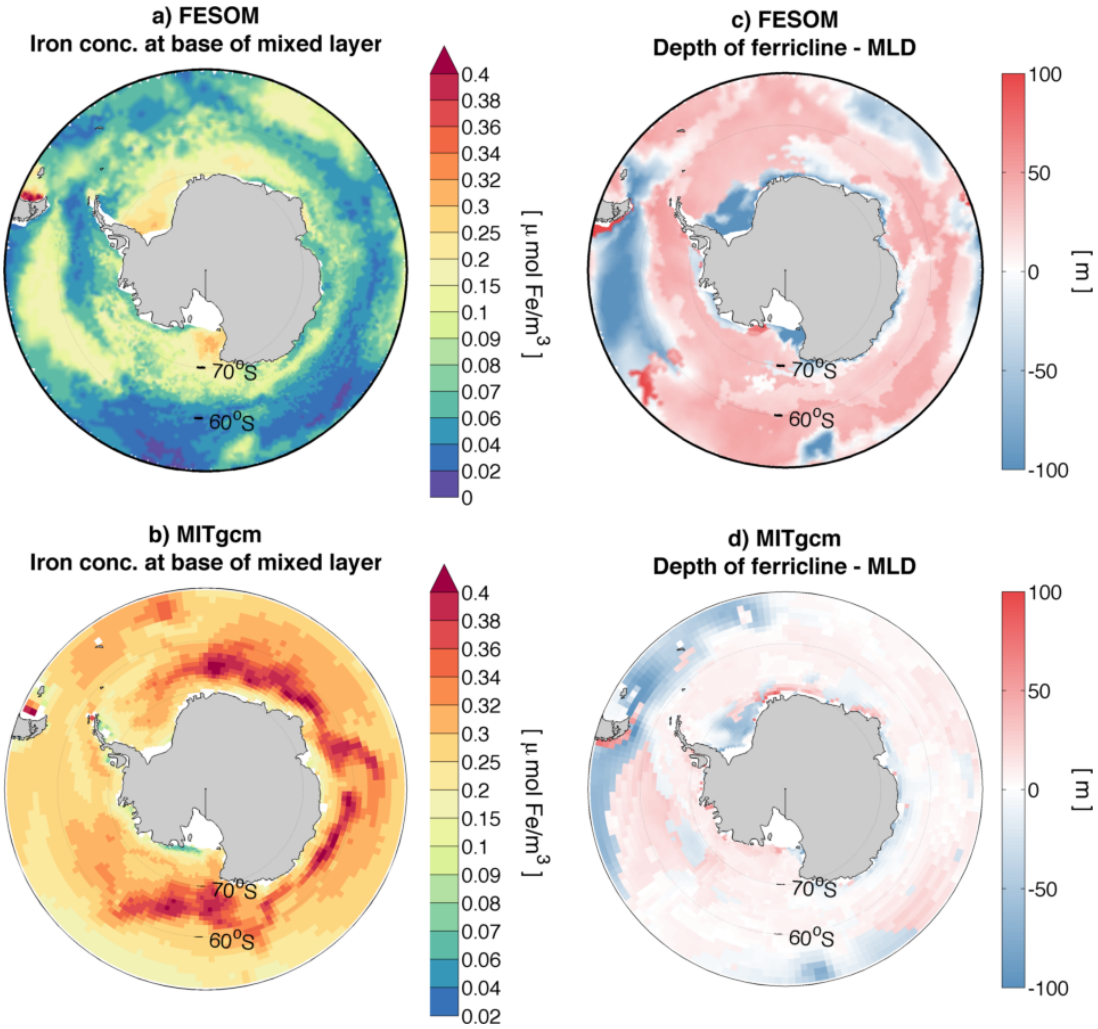

Figure 6.7: Mean iron concentration at the base of the mixed layer (a, b). Depth difference between the MLD and the ferricline averaged over time, positive numbers denote that the MLD is shallower than the ferricline, negative that it is deeper (c, d). a, c) FESOM. b, d) MITgcm.

The mean iron concentration at the base of the mixed layer shows how much iron is available for supply to the surface mixed layer. In FESOM, the mean iron concentration at the base of the mixed layer is below 0.1 µmol Fe m^{-3} in large areas of the Southern Ocean (Fig. 6.7a). The highest concentrations, ranging from 0.1 to 0.3 µmol Fe m^{-3}, occur in the Weddell and Ross Gyres as well as in the areas of deep winter mixed layers in the eastern Pacific and Indian Oceans. The mean iron concentration at the base of the mixed layer in the MITgcm range from 0.1 to 0.3 µmol Fe m^{-3} in the majority of the Southern Ocean, and reaches as high as 0.4 µmol Fe m^{-3} in the upwelling region south of 60°S (Fig. 6.7b).

The distance between the ferricline and the MLD highly affects the amount of iron that is supplied to the mixed layer (Tagliabue et al., 2014), and the spatial distribution of this field confirms that the MLD on average is located above the ferricline in FESOM (Fig. 6.7c). It is only in the area between 50 and 60°S and in the coastal convection zones, the places characterized by deep mixed layers (Fig. 6.6b) and high mean iron concentrations (Fig. 6.7a), that the mean MLD is located deeper than the ferricline in this model, leading to the relatively low iron concentration at the base of the mixed

layer. In MITgcm, the MLD is located below the ferricline north of 60°S (Fig. 6.7d), and south of 60°S the MLD and the ferricline are much closer to each other than in FESOM. The iron concentration at the base of the mixed layer is consequently higher in MITgcm (Fig. 6.7b).

Iron supply

In FESOM, entrainment mainly occurs north of 60°S (Fig. 6.8a). It is highly correlated with the seasonal amplitude of the MLD (Fig. 6.6e), with the higher rate of entrainment occurring in the areas of a larger MLD amplitude. This happens as the deep mixing has the effect that the MLD is located closer to or below the ferricline (Fig. 6.7c), leading to a higher iron concentration at the base of the mixed layer (Fig. 6.7a), thereby increasing the magnitude of the iron entrainment.

In MITgcm, a large degree of entrainment takes place north of 60°S (Fig. 6.8b). South of 60°S, MITgcm likewise has positive entrainment in large areas (Fig. 6.8b), brought on by the deeper mixed layer (Fig. 6.6c), the larger seasonal amplitude of the MLD (Fig. 6.6f) and the smaller distance between the MLD and the ferricline in MITgcm than in FESOM (Fig. 6.7c and d). In this model, there is no close relationship between the dynamics of the mixed layer (Fig. 6.6c and f) and the strength of the entrainment. This is due to the overall larger seasonal amplitude and larger depth of the mixed layer, causing the MLD to be below or close to the ferricline on average in the majority of the Southern Ocean (Fig. 6.7c and d).

The input of iron to the mixed layer through horizontal advection mainly occurs north of 60°S (Fig. 6.8c and d), where the meridional slope of the mixed layer depth is largest (Fig. 6.6b and e). Both models have a large input in the eastern Pacific part of the Southern Ocean and south of Tasmania (Fig. 6.8c and d). But where MITgcm additionally has input in the Indian sector, FESOM has a flux of iron out of the mixed layer here, with the consequence that the net mean supply through this mechanism becomes smaller. These negative fluxes are caused by the zonal flow of water, and thereby also iron, out of the mixed layer in the affected areas (not shown).

In FESOM, the higher iron fluxes from vertical eddy diffusion take place in a zone around Antarctica, providing the largest iron input to the TICZ, as well as to the areas of deep winter mixing (Fig. 6.8e). In this model, a high degree of vertical eddy diffusion occurs intermittently when the water column is unstable and when the wind mixing induces deeper mixed layers, and this intermittent nature is also visible in the spatial distribution. In MITgcm, the average input from vertical eddy diffusion can be disregarded due to its small contribution (Fig. 6.3), but the vertical eddy diffusion rate is higher in the temporary ice zone, especially in the Indian and Pacific sectors of the Southern Ocean. The supply north of 60°S is very small (Fig. 6.8f).

The largest input through upwelling occurs south of 60°S in both models (Fig. 6.8g and h), where the iron concentration is highest (Fig. 6.7a and b).

Net primary production

In FESOM the highest rates of NPP take place in the area between 60 and 50°S, where the strength of the entrainment is highest (Fig. 6.8a) and the mixed layer is deepest (Fig. 6.6b). South of 60°S the highest production occurs in the areas where the vertical eddy diffusion is highest.

The total NPP is higher in FESOM than in MITgcm (Table 6.1), and the differences in the rate of NPP are also evident in the spatial distribution (Fig. 6.9), especially where

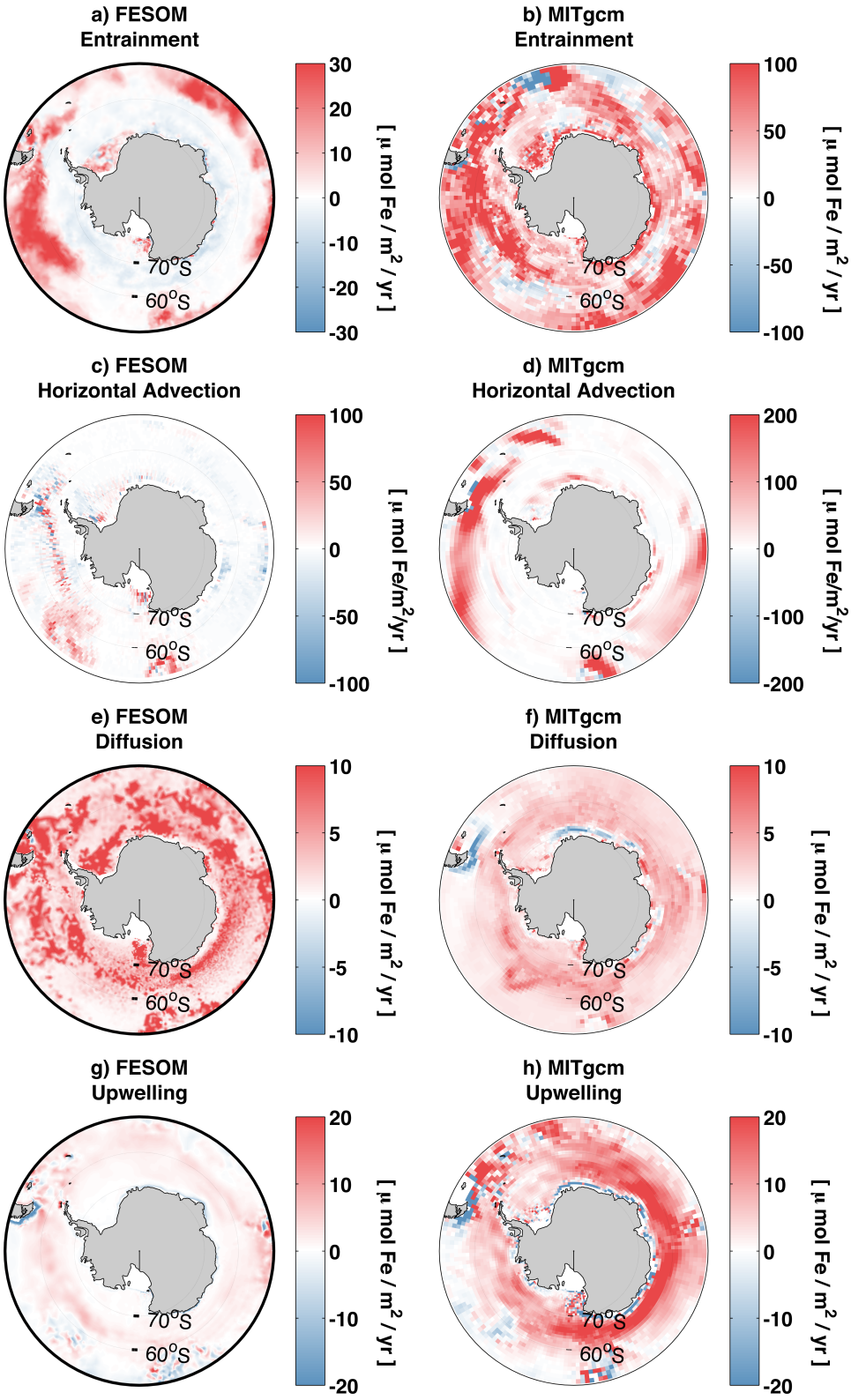

Figure 6.8: Spatial distribution of the input of iron through entrainment (a and b), horizontal advection (c and d), vertical eddy diffusion (e and f) and upwelling (g and h) in FESOM and MITgcm, respectively. Notice the different scales.

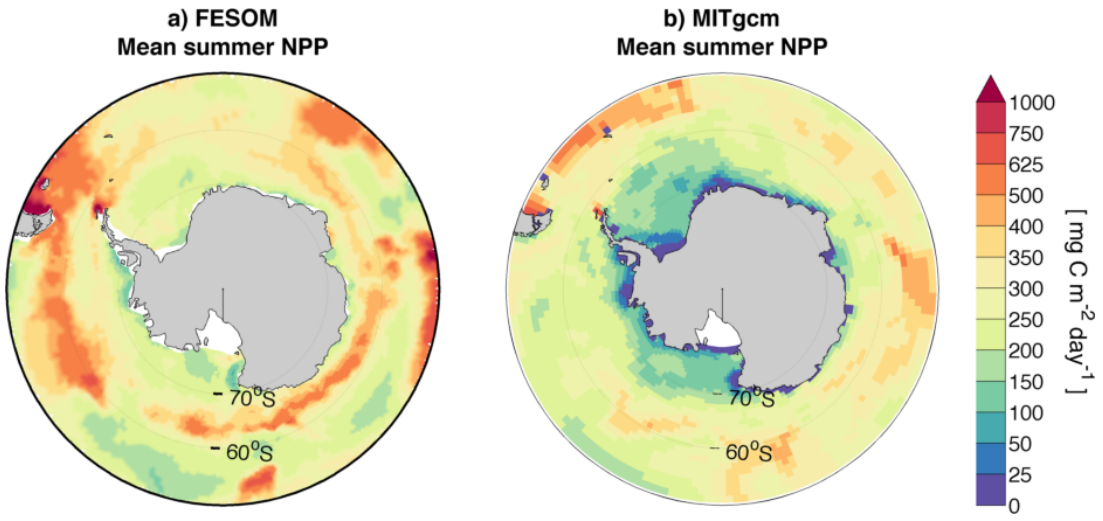

Figure 6.9: Spatial distribution of the mean rate of summer (October to March) NPP in the Southern Ocean. a) FESOM, b) MITgcm.

FESOM has a larger production in the area of the deep winter mixed layers (Fig. 6.6c). In MITgcm the connection between the iron supply and the NPP is much less obvious. The pattern of the distribution does, however, show similarities between the two models; the main areas of elevated production occur north of 60°S and especially east of the Patagonian shelf in the Atlantic sector of the Southern Ocean in both models, as is also the case in reality (e.g. Arrigo et al., 2008).

6.4 DISCUSSION

6.4.1 *Mixed layer depth*

The differences we observe in the iron dynamics of our two model runs shows that the state of the ocean model, including the representation of the mixed layer, has a large impact on the biogeochemical results.

The mixed layer in the Southern Ocean is affected by a number of interconnected processes, such as wind mixing and buoyancy forcing, and it is particularly difficult to constrain in models (e.g. Sallée et al., 2013; Downes et al., 2014). The parameterization of the vertical mixing is one component that has a large impact on the MLD. The KPP scheme, which is used in MITgcm, is known to allow for deeper mixing when a stable thermocline is present (Large et al., 1994). This explains some of the difference between the models. Additionally, the MLD in FESOM has been improved in version 1.4, in which the KPP scheme is used (Downes et al., 2014). The slope of the pycnoclines, and thereby the strength of the stratification, is affected by the GM-parameterization of the eddy induced transport in both models. The strength of this transport may however differ between the two models due to tuning. A steeper slope of the pycnoclines in MITgcm likewise allows for deeper mixing than in FESOM. Lastly the difference in spatial resolution between the two models may also impact the MLD.

Another important physical factor is the strength of the large scale overturning circulation in the OGCMs, which largely controls the southward transport of iron into the Southern Ocean, and thereby the iron supply to and the iron fluxes across the

base of the mixed layer. The impact of the ocean circulation and mixing on the biogeochemical results is, however, highly complex, and made even more complicated by the internal feedbacks of the biogeochemical model. This study can thus not point to the exact reason for the differences in the biogeochemical results, but it highlights that the OGCM has a large impact on the biogeochemical results, and that the vertical iron supply can explain a large part of these differences.

6.4.2 *Iron supply from below*

Due to the large seasonal amplitude of the mixed layer (Fig. 6.5b), the iron supply through entrainment dominates the supply in MITgcm. As the average seasonal amplitude is overestimated compared to the observations, it is likely that the entrainment likewise is somewhat overestimated in this model. For FESOM, the mean seasonal amplitude is well represented (Fig. 6.5a), but the MLD is too shallow throughout the season, leading to a lower iron concentration at the base of the mixed layer and thereby less input through entrainment. It is thus likely that the entrainment is underestimated in this model and entrainment does most likely play a significant role in the Southern Ocean in reality, especially in the areas of deep wind mixing. This fits well with the study by Tagliabue et al. (2014), where they concluded that the entrainment contributed the most to the flux of iron to the mixed layer in the Southern Ocean. In the their analyzed observations, the flux of iron supplied through entrainment was 21 $\mu mol\,Fe\,m^{-2}\,yr^{-1}$ (Tagliabue et al., 2014), a value between the results in this study (Fig. 6.3). The range provided by Tagliabue et al. (2014) are closest to the results from FESOM in the area north of 60°S, despite of the better fit regarding iron concentration and MLD in MITgcm. It must however be noted that the observed profiles in Tagliabue et al. (2014) are sparse and do not give a complete picture of the Southern Ocean.

Tagliabue et al. (2014) found that the supply of iron through vertical eddy diffusion was very small across the observation sites, similar to MITgcm, whereas Law et al. (2003) showed that vertical eddy diffusion played a significant role in the highly iron depleted waters south of New Zealand, agreeing more with the results from FESOM. The fact that vertical eddy diffusion dominates the supply of iron from below in FESOM also fits well with the results from an eddy-permitting model study by Dufour et al. (2013) who found that vertical eddy diffusion dominated the supply of DIC to the mixed layer of the Southern Ocean.

Previous studies focussing on the supply of iron through upwelling have usually calculated the flux by using the magnitude of the water transport multiplied by a constant iron concentration, such as 0.3 to 0.4 $\mu mol\,Fe\,m^{-3}$ (e.g. Watson et al., 2000; Hoppema et al., 2003). This results in a higher supply through upwelling than what is the case in the present study, and points to the important role the mixed layer plays in determining the vertical fluxes. Tagliabue et al. (2014) argued that the upwelling of iron on average is of minor importance in the Southern Ocean as it is cancelled out by downwelling north of the Polar Front, something that is true in both of our models. But despite of the insignificance of the upwelling for the iron flux into the mixed layer, it must be noted that this mechanism plays a large role regarding the supply of iron to the base of the mixed layer, from where it is brought upwards through other mechanisms. As the the iron concentration at the base of the mixed layer varies significantly between our models, this mechanism may be very important.

6.4.3 *Other iron sources*

In the Southern Ocean iron is supplied through several other sources including aeolian deposition, sedimentary input and release from icebergs and sea-ice. In FESOM, the average iron input from the sediment and the aeolian sources, is smaller than, or on the order of, the vertical sources considered in the current study, but likely important locally. Regarding MITgcm, the external sources comprises a much smaller fraction of the sources considered here and their impact on production is thus likewise much smaller. The size of the sediment source is, however, not well constrained and varies widely between models, with the models used in the current study having a source that is in the smaller end of the range normally used (Aumont and Bopp, 2006; Moore and Braucher, 2008). It is thus possible that the sediment source in reality plays a larger role than what our study indicates. Models are routinely used to quantify the magnitude of the external iron sources in the Southern Ocean (e.g. Lancelot et al., 2009; Wadley et al., 2014). The sediment source has been shown to play a significant role regarding the iron supply, especially in the Atlantic sector of the Southern Ocean and locally in proximity to islands (e.g. Lancelot et al., 2009; Tagliabue et al., 2009; Pollard et al., 2007).

In previous studies the supply of iron from below is normally disregarded. The current study does however highlight how the supply from below affects the total NPP and the phytoplankton composition in the Southern Ocean. Our study thus suggests that the performance of the ocean model, and thereby the iron supply from below, must be evaluated before assessing the importance of the external sources.

6.4.4 *Biological production*

Remote sensing products of Southern Ocean ocean color (e.g. Arrigo et al., 2008) have revealed that high primary production occurs in certain places. This includes areas downwind of the continents (e.g. Jickells et al., 2005), downstream of islands, continental shelves and topographic features (e.g. Blain et al., 2001; de Jong et al., 2012) and along the receding ice edge (Arrigo et al., 2008). This distribution of NPP indicates that the input of iron from external sources such as dust and sediments indeed play a large role in the Southern Ocean, concurring with model studies (e.g. Lancelot et al., 2009; Tagliabue et al., 2009). While we recognize the role of external iron sources locally in the Southern Ocean, we do argue that the vertical iron fluxes are important for maintaining the iron concentration in the Southern Ocean, especially in remote areas and below sea-ice.

6.4.5 *Export efficiency*

The value of the export efficiency denotes the fraction of exported NPP, and is therefore a key number regarding the model's carbon cycle. For a model in equilibrium, the amount of nutrients supplied to the mixed layer must be balanced by the amount exported through sinking of organic material. The export ratio is consequently expected to be larger in a system with a larger input of nutrients.

After deriving export efficiencies (*fe*-ratios) from iron measurements in the strongly iron limited area south-west of New Zealand, Boyd et al. (2005) argued that a realistic range for the export efficiency in the area was 0.05 to 0.48. The higher ratios here

were connected to higher iron inputs. In line with this, de Jong et al. (2012) found an even higher export ratio of 0.59 in the Atlantic sector of the Southern Ocean where iron limitation is less severe. This connection between iron availability and export efficiency is also observed in our study, where MITgcm has the larger efficiency (Table 6.1).

In a measurement-based study, Bowie et al. (2009) found low export efficiencies (*fe*-ratios) in the severely iron depleted area south of Australia and remarked that regenerated iron must be important for production in this region. In FESOM, where production is dominated by the less iron demanding nanophytoplankton (Fig. 6.5a), the continued production in the summer is most likely likewise fueled by regenerated iron. As the turnover rate is higher for nanophytoplankton this iron "source" is most likely higher in FESOM than in MITgcm where diatoms dominate production (Fig. 6.5b).

Maiti et al. (2013) presented a collection of previous estimates of the export efficiency from the Southern Ocean, showing that they vary widely but that the export efficiency generally decreases with increasing NPP. This latter feature is also seen in our study, where FESOM has a higher NPP, but lower export efficiency than MITgcm. In MITgcm, the ratio of diatom production is higher than in FESOM, and as diatoms have a smaller remineralization rate this leads to the larger export efficiency in this model. This may indicate that models with diatom dominance have a higher export efficiency, something that again must be kept in mind when evaluating model runs regarding the marine carbon-cycle.

6.4.6 *Future iron supply*

The response of the Southern Ocean mixed layer depth to climate change is not fully understood. Two counteracting mechanisms can be predicted; shallowing due to stronger stratification (e.g. Sallée et al., 2013) and deepening due to stronger winds (e.g. Meijers, 2014). The current study shows that the direction of change could greatly impact the iron supply to the mixed layer, and thereby the biological production and export in the area. As the reproduction of a realistic mixed layer depth is already a challenge for ocean models under current forcing (e.g. Meijers, 2014; Downes et al., 2014), the modeled response of marine NPP and EP to climate change could be strongly influenced by unidentified biases in the ocean model, with large implications for the predicted carbon fluxes in the model.

6.5 CONCLUSION

Our study clearly shows that special care must be taken to adequately represent the ocean circulation and mixing in coupled biogeochemical ocean models, both in contemporary and in future runs, as it has a large effect on the modeled iron fluxes across the base of the mixed layer, and thereby the net primary production and the export efficiency.

Differences in the ocean state led to the sources of iron from below being very different in our two models, both in magnitude and in terms of what source dominates the iron supply. In FESOM, the supply of iron was lower than in MITgcm and the vertical eddy diffusion dominated the overall supply, while entrainment was important north of 60°S and during the spring bloom. Entrainment dominated the iron supply

in MITgcm due to a larger variability of the mixed layer in this model. Horizontal advection also plays a role in MITgcm.

The net primary production in both models was reasonable compared to satellite-based observations, but the species composition differed significantly between them, with diatoms being responsible for 67 % of the NPP in MITgcm and 21 % in FESOM. MITgcm's larger iron supply from below, and thereby also higher mixed layer iron concentrations, caused the larger and more iron demanding diatoms to thrive in this model. The larger supply of iron in MITgcm also led to a higher export efficiency of 0.58, as opposed to 0.36 in FESOM. The ocean state, and thereby the mixed layer dynamics, of the ocean general circulation model is thus of major importance for studies of the carbon cycle in the Southern Ocean.

REFERENCES

Arakawa, A. and V. R. Lamb (1977). "Computational design of the basic dynamical processes of the UCLA general circulation model." *M. Comp. P.* (17), pp. 173–265.

Arrigo, K. R., G. L. van Dijken, and S. Bushinsky (2008). "Primary production in the Southern Ocean, 1997–2006." *J. Geophys. Res.* (113) C8. DOI: 10.1029/2007JC004551.

Assmann, K., M. Bentsen, J. Segschneider, and C. Heinze (2010). "An isopycnic ocean carbon cycle model." *Geosci. Model Dev.* (3), pp. 143–167. DOI: 10.5194/gmd-3-143-2010.

Aumont, O. and L. Bopp (2006). "Globalizing results from ocean in situ iron fertilization studies." *Global Biogeochem. Cy.* (20) GB2017. DOI: 10.1029/2005GB002591.

Behrenfeld, M. J. and P. G. Falkowski (1997). "Photosynthetic rates derived from satellite-based chlorophyll concentration." *Limnol. Oceanogr.* (42) 1, pp. 1–20.

Blain, S., P. Tréguer, S. Belviso, E. Bucciarelli, M. Denis, S. Desabre, M. Fiala, V. Martin Jézéquel, J. Le Fèvre, P. Mayzaud, J.-C. Marty, and S. Razouls (2001). "A biogeochemical study of the island mass effect in the context of the iron hypothesis: Kerguelen Islands, Southern Ocean." *Deep Sea Res. Pt. I* (48) 1, pp. 163–187. DOI: 10.1016/S0967-0637(00)00047-9.

Bowie, A. R., D. Lannuzel, T. A. Remenyi, T. Wagener, P. J. Lam, P. W. Boyd, C. Guieu, A. T. Townsend, and T. W. Trull (2009). "Biogeochemical iron budgets of the Southern Ocean south of Australia: Decoupling of iron and nutrient cycles in the subantarctic zone by the summertime supply." *Global Biogeochem. Cy.* (23) GB4034. DOI: 10.1029/2009GB003500.

Boyd, P. W., E. Ibisanmi, S. G. Sander, K. A. Hunter, and G. A. Jackson (2010). "Remineralization of upper ocean particles: Implications for iron biogeochemistry." *Limnol. Oceanogr.* (55) 3, p. 1271. DOI: 10.4319/lo.2010.55.3.1271.

Boyd, P. W., C. S. Law, D. A. Hutchins, E. R. Abraham, P. L. Croot, M. Ellwood, R. D. Frew, M. Hadfield, J. Hall, S. Handy, C. Hare, J. Higgins, P. Hill, K. A. Hunter, K. LeBlanc, M. T. Maldonado, R. M. McKay, C. Mioni, M. Oliver, S. Pickmere, M. Pinkerton, K. Safi, S. Sander, S. A. Sanudo-Wilhelmy, M. Smith, R. Strzepek, A. Tovar-Sanchez, and S. Wilhelm (2005). "FeCycle: Attempting an iron biogeochemical budget from a mesoscale SF6 tracer experiment in unperturbed low iron waters." *Global Biogeochem. Cy.* (19) GB4S20. DOI: 10.1029/2005GB002494.

Bracher, A., M. Vountas, T. Dinter, J. Burrows, R. Röttgers, and I. Peeken (2009). "Quantitative observation of cyanobacteria and diatoms from space using PhytoDOAS

on SCIAMACHY data." *Biogeosciences* (6), pp. 751–764. DOI: 10.5194/bg-6-751-2009.

Campin, J.-M. and H. Goosse (1999). "Parameterization of density-driven downsloping flow for a coarse-resolution ocean model in z-coordinate." *Tellus A* (51) 3, pp. 412–430. DOI: 10.1034/j.1600-0870.1999.t01-3-00006.x.

Carr, M.-E., M. A. Friedrichs, M. Schmeltz, M. Noguchi Aita, D. Antoine, K. R. Arrigo, I. Asanuma, O. Aumont, R. Barber, and M. Behrenfeld (2006). "A comparison of global estimates of marine primary production from ocean color." *Deep-Sea Res. Pt. II* (53) 5, pp. 741–770. DOI: 10.1016/j.dsr2.2006.01.028.

Croot, P., R. Frew, S. Sander, K. Hunter, M. Ellwood, S. Pickmere, E. Abraham, C. Law, M. Smith, and P. Boyd (2007). "Physical mixing effects on iron biogeochemical cycling: FeCycle experiment." *J. Geophys. Res.* (112) C6. DOI: 10.1029/2006JC003748.

Cushman-Roisin, B. (1987). "Subduction." In: *Dynamics of the oceanic surface mixed layer*. Ed. by P. Muller and D. Henderson. Manoa, Hawaii: Univ. of Hawaii at Manoa, pp. 181–196.

De Baar, H. J. W., J. T. M. de Jong, D. C. E. Bakker, B. M. Löscher, C. Veth, U. Bathmann, and V. Smetacek (1995). "Importance of iron for plankton blooms and carbon dioxide drawdown in the Southern Ocean." *Nature* (373). DOI: 10.1038/373412a0.

De Boyer Montegut, C., G. Madec, A. S. Fischer, A. Lazar, and D. Iudicone (2004). "Mixed layer depth over the global ocean: An examination of profile data and a profile-based climatology." *J. Geophys. Res.* (109) C12003. DOI: 10.1029/2004JC002378.

De Jong, J., V. Schoemann, D. Lannuzel, P. Croot, H. de Baar, and J.-L. Tison (2012). "Natural iron fertilization of the Atlantic sector of the Southern Ocean by continental shelf sources of the Antarctic Peninsula." *J. Geophys. Res.* (117) G1. DOI: 10.1029/2011JG001679.

Doney, S. C., K. Lindsay, K. Caldeira, J.-M. Campin, H. Drange, J.-C. Dutay, M. Follows, Y. Gao, A. Gnanadesikan, N. Gruber, A. Ishida, F. Joos, G. Madec, E. Maier-Reimer, J. C. Marshall, R. J. Matear, P. Monfray, A. Mouchet, R. Najjar, J. C. Orr, G. K. Plattner, J. L. Sarmiento, R. Schlitzer, R. D. Slater, I. J. Totterdell, M. F. Weirig, Y. Yamanaka, and A. Yool (2004). "Evaluating global ocean carbon models: The importance of realistic physics." *Global Biogeochem. Cy.* (18) GB3017. DOI: 10.1029/2003GB002150.

Downes, S., R. Farneti, P. Uotilac, S. M. Griffies, S. Marsland, D. Bailey, E. Behrens, M. Bentsen, D. Bi, A. Biastoch, C. Böning, A. Bozec, E. Chassignet, G. Danabasoglu, S. Danilov, N. Diansky, H. Drange, P. G. Fogli, A. Gusev, A. Howard, M. Illicak, T. Jung, M. Kelley, W. G. Large, A. Leboissetiero, M. Long, J. Lu, S. Masina, A. Mishra, A. Navarra, A. J. G. Nurserp, L. Patara, B. L. Samuels, D. Sidorenko, P. Spence, H. Tsujino, Q. Wang, and S. G. Yeager (2014). "An assessment of Southern Ocean water masses and sea-ice during 1988-2007 in a suite of inter-annual CORE-II simulations." *submitted to Clim. Dynam.*

Dufour, C. O., J. L. Sommer, M. Gehlen, J. C. Orr, J.-M. Molines, J. Simeon, and B. Barnier (2013). "Eddy compensation and controls of the enhanced sea-to-air CO_2 flux during positive phases of the Southern Annular Mode." *Global Biogeochem. Cy.* (27) 3, pp. 950–961. DOI: 10.1002/gbc.20090.

Ellwood, M. J., P. W. Boyd, and P. Sutton (2008). "Winter-time dissolved iron and nutrient distributions in the Subantarctic Zone from 40–52S; 155–160E." *Geophys. Res. Lett.* (35) L11604. DOI: 10.1029/2008GL033699.

Elrod, V. A., W. M. Berelson, K. H. Coale, and K. S. Johnson (2004). "The flux of iron from continental shelf sediments: A missing source for global budgets." *Geophys. Res. Lett.* (31) L12307. DOI: 10.1029/2004GL020216.

Garcia, H., R. Locarnini, T. Boyer, and J. Antonov (2006). *In World Ocean Atlas 2005, Volume 4: Nutrients (phosphate, nitrate, silicate),(ed. S. Levitus)*. Tech. rep. Washington, DC: NOAA Atlas NESDIS.

Gent, P. R. and J. C. Mcwilliams (1990). "Isopycnal mixing in ocean circulation models." *J. Phys. Oceanogr.* (20) 1, pp. 150–155. DOI: 10.1175/1520-0485(1981)011<1443:POVMIN>2.0.CO;2.

Hauck, J., C. Völker, T. Wang, M. Hoppema, M. Losch, and D. A. Wolf-Gladrow (2013). "Seasonally different carbon flux changes in the Southern Ocean in response to the Southern Annular Mode." *Global Biogeochem. Cy.* (27), pp. 1–10. DOI: 10.1002/2013GB004600.

Hirata, T., N. J. Hardman-Mountford, R. J. W. Brewin, J. Aiken, R. Barlow, K. Suzuki, T. Isada, E. Howell, T. Hashioka, M. Noguchi-Aita, and Y. Yamanaka (2011). "Synoptic relationships between surface Chlorophyll-a and diagnostic pigments specific to phytoplankton functional types." *Biogeosciences* (8) 2, pp. 311–327. DOI: 10.5194/bg-8-311-2011.

Hoffmann, L., I. Peeken, and K. Lochte (2008). "Iron, silicate, and light co-limitation of three Southern Ocean diatom species." *Polar Biol.* (31) 9, pp. 1067–1080. DOI: 10.1007/s00300-008-0448-6.

Hoppema, M., H. J. W. de Baar, E. Fahrbach, H. H. Hellmer, and B. Klein (2003). "Substantial advective iron loss diminishes phytoplankton production in the Antarctic Zone." *Global Biogeochem. Cy.* (17) 1. DOI: 10.1029/2002GB001957.

Jickells, T. D., Z. S. An, K. K. Andersen, A. R. Baker, G. Bergametti, N. Brooks, J. J. Cao, P. W. Boyd, R. A. Duce, K. A. Hunter, H. Kawahata, N. Kubilay, J. LaRoche, P. S. Liss, N. Mahowald, J. M. Prospero, A. J. Ridgwell, I. Tegen, and R. Torres (2005). "Global iron connections between desert dust, ocean biogeochemistry, and climate." *Science* (308) 5718, pp. 67–71. DOI: 10.1126/science.1105959.

Key, R. M., A. Kozyr, C. L. Sabine, K. Lee, R. Wanninkhof, J. L. Bullister, R. A. Feely, F. J. Millero, C. Mordy, and T.-H. Peng (2004). "A global ocean carbon climatology: Results from Global Data Analysis Project (GLODAP)." *Global Biogeochem. Cy.* (18) GB4031. DOI: 10.1029/2004GB002247.

Lancelot, C., A. de Montety, H. Goosse, S. Becquevort, V. Schoemann, B. Pasquer, and M. Vancoppenolle (2009). "Spatial distribution of the iron supply to phytoplankton in the Southern Ocean: a model study." *Biogeosciences* (6) 12, pp. 2861–2878. DOI: 10.5194/bg-6-2861-2009.

Large, W. G. and S. G. Yeager (2009). "The global climatology of an interannually varying air–sea flux data set." *Clim. Dynam.* (33) 2-3, pp. 341–364. DOI: 10.1007/s00382-008-0441-3.

Large, W. G., J. C. McWilliams, and S. C. Doney (1994). "Oceanic vertical mixing: A review and a model with a nonlocal boundary layer parameterization." *Rev. Geophys.* (32) 4, pp. 363–403. DOI: 10.1029/94RG01872.

Law, C. S., E. R. Abraham, A. J. Watson, and M. I. Liddicoat (2003). "Vertical eddy diffusion and nutrient supply to the surface mixed layer of the Antarctic Circumpolar Current." *J. Geophys. Res.* (108) C8. DOI: 10.1029/2002JC001604.

Levy, M., L. Bopp, P. Karleskind, L. Resplandy, C. Ethe, and F. Pinsard (2013). "Physical pathways for carbon transfers between the surface mixed layer and the ocean interior." *Global Biogeochem. Cy.* (27), pp. 1001–1012. DOI: DOI:10.1002/gbc.20092.

Lin, H., S. Rauschenberg, C. R. Hexel, T. J. Shaw, and B. S. Twining (2011). "Free-drifting icebergs as sources of iron to the Weddell Sea." *Deep-Sea Res. Pt. II* (58) 11, pp. 1392–1406. DOI: 10.1016/j.dsr2.2010.11.020.

Löscher, B. M., H. J. W. de Baar, J. T. M. de Jong, C. Veth, and F. Dehairs (1997). "The distribution of Fe in the Antarctic circumpolar current." *Deep Sea Re. Pt. II* (44) 1, pp. 143–187. DOI: 10.1016/S0967-0645(96)00101-4.

Losch, M., D. Menemenlis, J.-M. Campin, P. Heimbach, and C. Hill (2010). "On the formulation of sea-ice models. Part 1: Effects of different solver implementations and parameterizations." *Ocean Model.* (33) 1, pp. 129–144. DOI: 10.1016/j.ocemod.2009.12.008.

Losch, M., V. Strass, B. Cisewski, C. Klaas, and R. G. Bellerby (2014). "Ocean state estimation from hydrography and velocity observations during EIFEX with a regional biogeochemical ocean circulation model." *J. Mar. Sys.* (129), pp. 437–451. DOI: 10.1016/j.jmarsys.2013.09.003.

Luo, C., N. M. Mahowald, and J. Del Corral (2003). "Sensitivity study of meteorological parameters on mineral aerosol mobilization, transport, and distribution." *J. Geophys. Res* (108) D15. DOI: 10.1029/2003JD003483.

Mahowald, N., C. Luo, J. Del Corral, and C. S. Zender (2003). "Interannual variability in atmospheric mineral aerosols from a 22-year model simulation and observational data." *J. Geophys. Res* (108) D12. DOI: 10.1029/2002JD002821.

Maiti, K., M. A. Charette, K. O. Buesseler, and M. Kahru (2013). "An inverse relationship between production and export efficiency in the Southern Ocean." *Geophys. Res. Lett.* (40), pp. 1557–1561. DOI: 10.1002/grl.50219.

Marinov, I., A. Gnanadesikan, J. Toggweiler, and J. Sarmiento (2006). "The Southern Ocean biogeochemical divide." *Nature* (441) 7096, pp. 964–967. DOI: 10.1038/nature04883.

Marshall, J., A. Adcroft, C. Hill, L. Perelman, and C. Heisey (1997). "A finite-volume, incompressible Navier Stokes model for studies of the ocean on parallel computers." *J. Geophys. Res.* (102) C3, pp. 5753–5766. DOI: 10.1029/96JC02775.

Martin, J. H., S. E. Fitzwater, and R. M. Gordon (1990). "Iron deficiency limits phytoplankton growth in Antarctic waters." *Global Biogeochem. Cy.* (4) 1, pp. 5–12. DOI: 10.1029/GB004i001p00005.

Martin, J. H. (1990). "Glacial-interglacial CO_2 change: The iron hypothesis." *Paleoceanography* (5) 1, pp. 1–13. DOI: 10.1029/PA005i001p00001.

Martin, J. H., R. M. Gordon, and S. E. Fitzwater (1991). "The case for iron." *Limnol. Oceanogr.* (36) 8.

Meijers, A. J. S. (2014). "The Southern Ocean in the Coupled Model Intercomparison Project phase 5." *Philos. Trans. R. Soc. A* (372) 2019. DOI: 10.1098/rsta.2013.0296.

Moore, J. K. and O. Braucher (2008). "Sedimentary and mineral dust sources of dissolved iron to the world ocean." *Biogeosciences* (5) 3, pp. 631–656. DOI: 10.5194/bg-5-631-2008.

Najjar, R. G., X. Jin, F. Louanchi, O. Aumont, K. Caldeira, S. C. Doney, J.-C. Dutay, M. Follows, N. Gruber, F. Joos, K. Lindsay, E. Maier-Reimer, R. J. Matear, K. Matsumoto, P. Monfray, A. Mouchet, J. C. Orr, G.-K. Plattner, J. L. Sarmiento, R. Schlitzer, R. D. Slater, M.-F. Weirig, Y. Yamanaka, and A. Yool (2007). "Impact of circulation on export production, dissolved organic matter, and dissolved oxygen in the ocean: Results from Phase II of the Ocean Carbon-cycle Model Intercomparison Project (OCMIP-2)." *Global Biogeochem. Cy.* (21) GB3007. DOI: 10.1029/2006GB002857.

Nevison, C., R. Keeling, M. Kahru, M. Manizza, B. Mitchell, and N. Cassar (2012). "Estimating net community production in the Southern Ocean based on atmospheric potential oxygen and satellite ocean color data." *Global Biogeochem. Cy.* (26) GB1020. DOI: 10.1029/2011GB004040.

Pacanowski, R. C. and S. G. H. Philander (1981). "Parameterization of vertical mixing in numerical models of tropical oceans." *J. Phys. Oceanogr.* (11) 11, pp. 1443–1451. DOI: 10.1175/1520-0485(1981)011<1443:POVMIN>2.0.CO;2.

Parekh, P., M. J. Follows, and E. A. Boyle (2005). "Decoupling of iron and phosphate in the global ocean." *Global Biogeochem. Cy.* (19) GB2020. DOI: 10.1029/2004GB002280.

Pollard, R., R. Sanders, M. Lucas, and P. Statham (2007). "The Crozet natural iron bloom and export experiment (CROZEX)." *Deep-Sea Res. Pt. II* (54) 18, pp. 1905–1914. DOI: 10.1016/j.dsr2.2007.07.023.

Redi, M. H. (1982). "Oceanic isopycnal mixing by coordinate rotation." *J. Phys. Oceanogr.* (12) 10, pp. 1154–1158. DOI: 10.1175/1520-0485(1982)012<1154:OIMBCR>2.0.CO;2.

Sallée, J.-B., E. Shuckburgh, N. Bruneau, A. Meijers, T. Bracegirdle, and Z. Wang (2013). "Assessment of Southern Ocean mixed-layer depths in CMIP5 models: Historical bias and forcing response." *J. Geophys. Res.* (118), pp. 1845–1862. DOI: 10.1002/jgrc.20157.

Sallée, J.-B., K. Speer, S. Rintoul, and S. Wijffels (2010). "Southern Ocean thermocline ventilation." *J. Phys. Oceanogr.* (40) 3, pp. 509–529. DOI: 10.1175/2009JPO4291.1.

Schlitzer, R. (2002). "Carbon export fluxes in the Southern Ocean: Results from inverse modeling and comparison with satellite-based estimates." *Deep-Sea Res. Pt. II* (49) 9, pp. 1623–1644. DOI: 10.1016/S0967-0645(02)00004-8.

Schourup-Kristensen, V., D. Sidorenko, D. A. Wolf-Gladrow, and C. Völker (2014). "A skill assessment of the biogeochemical model REcoM2 coupled to the Finite Element Sea-Ice Ocean Model (FESOM 1.3)." *Geosci. Model Dev.* (7) 6, pp. 2769–2802. DOI: 10.5194/gmd-7-2769-2014.

Sidorenko, D., Q. Wang, S. Danilov, and J. Schröter (2011). "FESOM under coordinated ocean-ice reference experiment forcing." *Ocean Dynam.* (61) 7, pp. 881–890. DOI: 10.1007/s10236-011-0406-7.

Sloyan, B. M. and S. R. Rintoul (2001). "The Southern Ocean Limb of the Global Deep Overturning Circulation*." *J. Phys. Oceanogr.* (31) 1, pp. 143–173. DOI: 10.1175/1520-0485(2001)031<0143:TSOLOT>2.0.CO;2.

Speer, K., S. R. Rintoul, and B. Sloyan (2000). "The diabatic Deacon Cell*." *J. Phys. Oceanogr.* (30) 12, pp. 3212–3222. DOI: 10.1175/1520-0485(2000)030<3212:TDDC>2.0.CO;2.

Steele, M., R. Morley, and W. Ermold (2001). "PHC: A global ocean hydrography with a high-quality Arctic Ocean." *J. Climate* (14) 9, pp. 2079–2087. DOI: 10.1029/2006GL026152.

Tagliabue, A., L. Bopp, and O. Aumont (2009). "Evaluating the importance of atmospheric and sedimentary iron sources to Southern Ocean biogeochemistry." *Geophys. Res. Lett.* (36) L13601. DOI: 10.1029/2009GL038914.

Tagliabue, A., T. Mtshali, O. Aumont, A. R. Bowie, M. B. Klunder, A. N. Roychoudhury, and S. Swart (2012). "A global compilation of dissolved iron measurements: focus on distributions and processes in the Southern Ocean." *Biogeosciences* (9) 6, pp. 1–17. DOI: 10.5194/bg-9-2333-2012.

Tagliabue, A., J.-B. Sallée, A. R. Bowie, M. Lévy, S. Swart, and P. W. Boyd (2014). "Surface-water iron supplies in the Southern Ocean sustained by deep winter mixing." *Nat. Geosci.* (7), pp. 314–320. DOI: 10.1038/ngeo2101.

Taylor, M. H., M. Losch, and A. Bracher (2013). "On the drivers of phytoplankton blooms in the Antarctic marginal ice zone: A modeling approach." *J. Geophys. Res* (118), pp. 63–75. DOI: 10.1029/2012JC008418.

Timmermann, R. and A. Beckmann (2004). "Parameterization of vertical mixing in the Weddell Sea." *Ocean Model.* (6) 1, pp. 83–100. DOI: 10.1016/S1463-5003(02)00061-6.

Timmermann, R., A. M. Le Brocq, T. J. Deen, E. W. Domack, P. Dutrieux, B. Galton-Fenzi, H. H. Hellmer, A. Humbert, D. Jansen, A. Jenkins, A. Lambrecht, K. Makinson, F. Niederjasper, F.-O. Nitsche, O. A. N?st, L. H. Smedsrud, and W. Smith (2010). *Antarctic ice sheet topography, cavity geometry, and global bathymetry (RTopo 1.0.5-beta)*. DOI: 10.1594/PANGAEA.741917.

Vogt, M., T. Hashioka, M. R. Payne, E. T. Buitenhuis, C. L. Quéré, S. Alvain, M. N. Aita, L. Bopp, S. C. Doney, T. Hirata, I. Lima, S. Sailley, and Y. Yamanaka (2013). "The distribution, dominance patterns and ecological niches of plankton functional types in Dynamic Green Ocean Models and satellite estimates." *Biogeosciences Discuss.* (10) 11, pp. 17193–17247. DOI: 10.5194/bgd-10-17193-2013.

Wadley, M. R., T. D. Jickells, and K. J. Heywood (2014). "The role of iron sources and transport for Southern Ocean productivity." *Deep Sea Res. Pt I* (87), pp. 82–94. DOI: DOI:10.1016/j.dsr.2014.02.003.

Wagener, T., C. Guieu, R. Losno, S. Bonnet, and N. Mahowald (2008). "Revisiting atmospheric dust export to the Southern Hemisphere ocean: Biogeochemical implications." *Global Biogeochem. Cy.* (22) GB2006. DOI: 10.1029/2007GB002984.

Wang, Q., S. Danilov, D. Sidorenko, R. Timmermann, C. Wekerle, X. Wang, T. Jung, and J. Schröter (2014). "The Finite Element Sea Ice-Ocean Model (FESOM) v.1.4: formulation of an ocean general circulation model." *Geosci. Model Dev.* (7) 2, pp. 663–693. DOI: 10.5194/gmd-7-663-2014.

Watson, A. J., D. C. E. Bakker, A. J. Ridgwell, P. W. Boyd, and C. S. Law (2000). "Effect of iron supply on Southern Ocean CO_2 uptake and implications for glacial atmospheric CO_2." *Nature* (407) 6805, pp. 730–733. DOI: 10.1038/35037561.

PUBLICATION III

7

Sensitivity of Southern Ocean phytoplankton composition to changes in model iron scavenging and sediment supply

Vibe Schourup-Kristensen[1], Dieter A. Wolf-Gladrow[1] and Christoph Völker[1]

[1] Alfred-Wegener-Institut Helmholtz-Zentrum für Polar und Meeresforschung, Postfach 12 01 61, 27515 Bremerhaven, Germany.

To be submitted

Abstract One way to study the impact of the Southern Ocean iron sources on biological production is by using ocean general circulation biogeochemical models (OGCBMs). Most of such studies agree that the sediment source is the most important of the external iron sources to the Southern Ocean. Neither this benthic iron flux nor the removal trough scavenging of iron onto organic particles are, however, well constrained by measurements, and these fluxes thus vary widely between models. While many OGCBMs produce relatively similar numbers for the total net primary production (NPP) in the Southern Ocean, it is not clear to what extend the large differences in the iron supply and iron removal affects the modeled phytoplankton composition and opal export in the Southern Ocean.

We are presenting a sensitivity study, in which the strength of the benthic iron flux was varied simultaneously with the counteracting scavenging of iron in the water. We show that while changing the benthic iron flux substantially, it is possible to recreate both the mean iron profiles and the total NPP in the Southern Ocean by choosing an appropriate scavenging rate. The changed iron input does, however, change the spatial distribution of the NPP along with the amount of NPP from diatoms. A benthic shelf iron flux of 1.2 μmol Fe m^{-2} day^{-1}, leading to a total input of 2.14 $\times$ 10^9 mol Fe yr^{-1} to the Southern Ocean, leads to the best results when evaluating against knowledge of iron fluxes, as well as diatom distributions and opal export. Given the large degree of freedom regarding the modeled strength of the benthic iron flux and the scavenging rate, this study highlights the importance of evaluating the total NPP against observations, but in particular also against observations of diatom abundance and opal export. Data for both of these are, however, scarce, and the study thus shows how additional data collection regarding the Southern Ocean phytoplankton composition is necessary to further improve the evaluation of OGCBMs.

7.1 INTRODUCTION

Iron is thought to be the main limiting factor of biological production in 30 to 50 % of the world's surface ocean (Moore et al., 2002; Aumont et al., 2003; Dutkiewicz et al., 2005). The main known areas are the so-called High-Nutrient Low-Chlorophyll (HNLC) regions: The Southern Ocean (Martin et al., 1990; Boyd et al., 2000), the Equatorial Pacific (Kolber et al., 1994; Behrenfeld et al., 1996) and the Northern Pacific (Martin and Fitzwater, 1988).

Traditionally, the most important external iron source to the ocean has been thought to be aeolian dust input (e.g. Jickells et al., 2005), but several studies have shown that the sediment source likewise plays an important role. An increase in the water's concentration of dissolved iron towards the coast and shelf areas was first documented by Johnson et al. (1997) and has later been widely confirmed (e.g. Johnson et al., 2003; Moore and Braucher, 2008). Studies showing that coastally derived iron was carried far into the Pacific Ocean from the Aleutians (Lam et al., 2006) and Kamchatka (Lam and Bishop, 2008) further indicated that this source can not be ignored in large scale iron budgets.

Determining the origin of the dissolved iron in the water is, however, difficult. A new method for this, based on the stable isotopes of iron in seawater, has recently been developed (John and Adkins, 2010; Conway et al., 2013). The stable isotope technique has confirmed the importance of the sediment source of iron; Conway and John (2014) showed that sediment derived iron was advected far from its source region in the Equatorial Atlantic, and Radic et al. (2011) found that iron in the eastern equatorial Pacific originated in the sediments of Papua New Guinea.

In the Southern Ocean, the aeolian iron input supplies a significant amount of new iron in the areas downwind of Patagonia and Australia (e.g. Cassar et al., 2007), but since half of the atmospheric supply is lost on a length scale of 1500 km (Prospero et al., 1989) much less reaches the remoter areas of this ocean leading to widespread iron limitation. Satellite-based measurements of Southern Ocean chlorophyll nevertheless show consistent patches of high concentrations downstream of islands such as South Georgia (e.g. Korb and Whitehouse, 2004), the Kerguelen (e.g. Blain et al., 2001) and Crozet Island (e.g. Pollard et al., 2009). One explanation for these blooms is that the sediment source of iron also plays a role in the Southern Ocean, where released iron can travel relatively far when it is transported in the fast flowing jet streams of the Antarctic Circumpolar Current (de Baar et al., 1995; Croot et al., 2004a). Several model studies have confirmed the importance of the sediment source of iron, both in the Southern Ocean (Tagliabue et al., 2009; Lancelot et al., 2009; Wadley et al., 2014) and on the global scale (Moore and Braucher, 2008). The strength of the sediment source is, however, not well constrained by measurements and both the total supply and the parameterization of iron from the sediments therefore varies widely between models (e.g. Aumont and Bopp, 2006; Moore and Braucher, 2008; Lancelot et al., 2009). A large variation in the strength of the sediment source of iron is possible because the magnitude of the removal of iron through particle scavenging is not well known either, and modelers thus have a large degree of freedom regarding the tuning of the strength of the iron sources parallel with the particle scavenging.

In the Southern Ocean, the iron availability affects the phytoplankton composition (e.g. Takeda, 1998; Hoffmann et al., 2006; Wang et al., 2014b), which has an impact on the mean intracellular ratio between silicate and carbon in diatoms (Baines et al.,

2010; Assmy et al., 2013). Changes in the strength of the sediment source of iron and the scavenging rate are thus likely to impact the model's representation of diatoms and opal export, especially in the Southern Ocean where diatoms play a comparably large role (e.g. Soppa et al., 2014)

In this paper, we investigate how simultaneous changes in the strength of the sediment source and the scavenging of iron impact the phytoplankton productivity and composition in the Southern Ocean in a coupled biogeochemical ocean model. We further determine the optimal setting of parameters that determine the strength of the benthic iron flux and the scavenging rate by evaluating the changes in the phytoplankton composition compared to observations.

7.2 METHODS

7.2.1 *Ocean model*

For the current study we are using the Finite Element Sea-ice Ocean Model (FESOM) version 1.4 (Wang et al., 2014a) coupled to the biogeochemical model REcoM2 described below.

FESOM is a global sea-ice ocean model, which solves the hydrostatic equations under the commonly applied Boussinesq approximations using the finite element method. FESOM 1.4 is an update from the version used in previous work with REcoM2 (Schourup-Kristensen et al., 2014b; Schourup-Kristensen et al., 2014a). Important improvements include a change of the parameterization of the diapycnal mixing from the Pacanowski-Philander parameterization (PP, Pacanowski and Philander, 1981) to the *k*-profile parameterization (KPP, Large et al., 1994). This ensures that vertical turbulent mixing occurs to a larger degree in stable stratified water. Secondly, the Gent-McWilliams parameterization (Gent and Mcwilliams, 1990), which controls the eddy-induced horizontal advection, has been tuned to improve the slope of the isopycnals in the Southern Ocean, something that has a large impact on the mixed layer depth (MLD) in the area. And finally, the background vertical mixing coefficient now increases with depth, where it was previously constant. A full description of the current model version can be found in Wang et al. (2014a).

FESOM runs on a grid that is horizontally triangulated and unstructured, and vertically stratified. In the Southern Ocean south of 35°S, the grid used for the current study contains 16.000 surface nodes and a total of almost 477.000 nodes. The horizontal resolution ranges from 15 km along the coast of the Ross Sea to around 160 km on the southern edge of the subtropical gyres (Fig. 7.1). The bottom topography south of 60°S is based on the Rtopo-1 dataset (Timmermann et al., 2010) and in the rest of the Southern Ocean it is based on data from the General Bathymetric Chart of the Ocean (www.gebco.net). Both datasets have 1 minute resolution. The grid is similar to the one used in Schourup-Kristensen et al. (2014b).

7.2.2 *Biogeochemical model*

The Regulated Ecosystem Model (REcoM2) is a so-called Nutrient-Phytoplankton-Zooplankton-Detritus model (e.g. Hauck et al., 2013; Schourup-Kristensen et al., 2014b). The limiting nutrients include nitrogen, silicate and iron and the model additionally describes the cycling of carbon. It has two phytoplankton classes, nanophy-

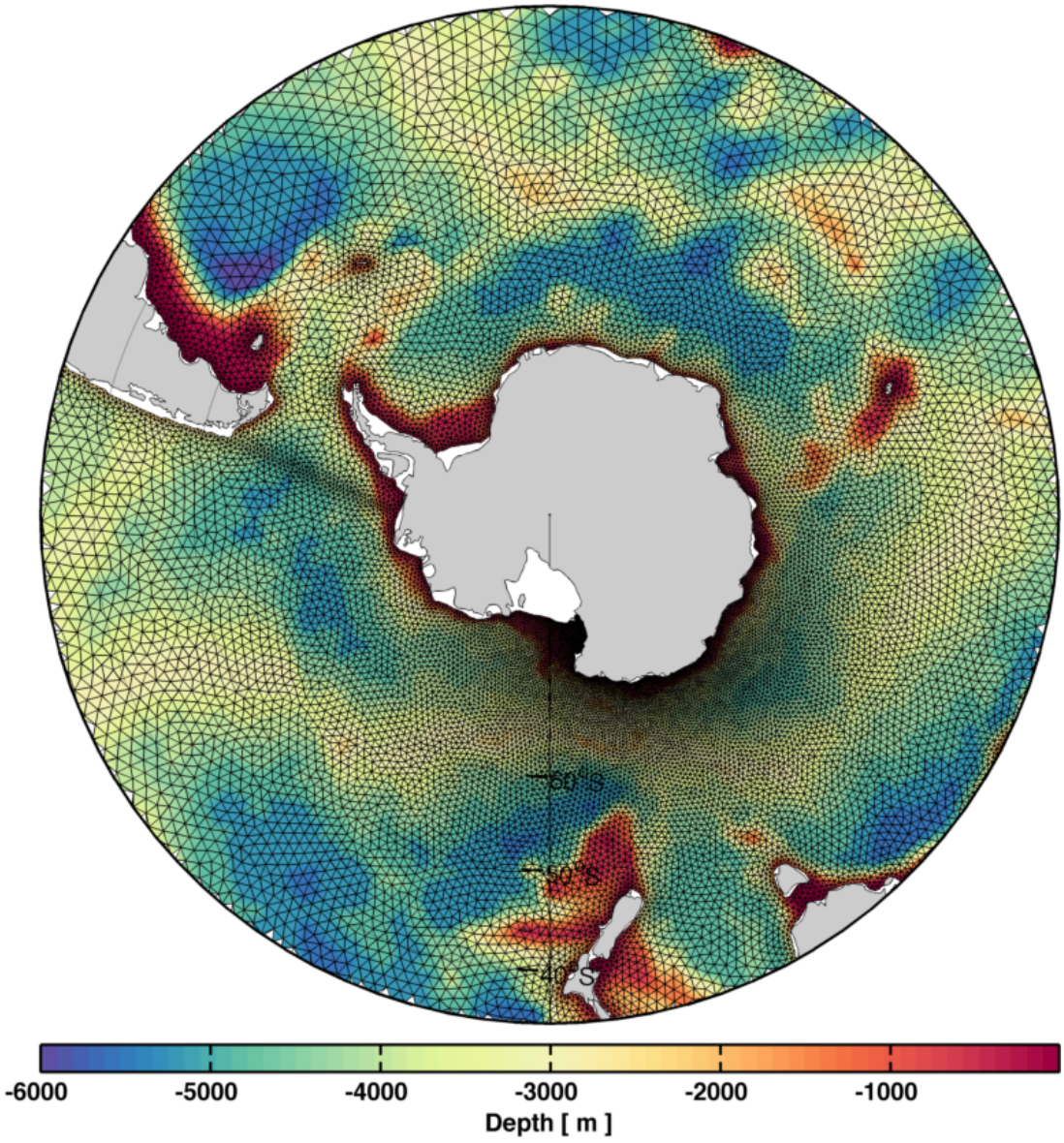

Figure 7.1: The horizontally triangulated grid used in the study, overlaid the bottom topography.

toplankton and diatoms and one class of zooplankton. The detritus is contained in one class and has a sinking velocity that increases with depth following Kriest and Oschlies (2008). REcoM2 employs variable stoichiometry between carbon and the macronutrients following Geider et al. (1998).

The concentration of dissolved iron in the water is increased through remineralization of phytoplankton and detritus, as well as by zooplankton excretion and respiration. Iron is removed from the water by phytoplankton growth and scavenging. The intracellular concentration of iron is linearly correlated with the intracellular carbon concentration, with a Fe:C ratio of 0.005 $\mu mol\,Fe\,(mmol\,C)^{-1}$ following Sunda and Huntsman (1995), and uptake limitation is calculated using Michaelis-Menten kinetics.

The calculation of the scavenging rate is based on Parekh et al. (2005), where only a fraction of the dissolved iron is available for scavenging as the rest is bound to ligands. It has been altered to make scavenging linearly correlated with the concentration of detritus in the water column, with the effect that the scavenging rate becomes higher in areas of high biological production, and lower in low production areas. The scavenging rate ($Scav$) is calculated as follows:

$$Scav = \kappa_{Fe} \cdot DetC \cdot DFe' \quad \left[\mu mol\,Fe\,m^{-3}\,day^{-1}\right] \tag{7.1}$$

Here, DFe' ($\mu mol\,Fe\,m^{-3}$) denotes the concentration of the dissolved iron that is not bound to ligands, $DetC$ ($mmol\,C\,m^{-3}$) is the detritus concentration and κ_{Fe} ($(mmol\,C\,m^{-3})^{-1}\,day^{-1}$) is the mass specific scavenging rate.

The removal of iron by scavenging is balanced by aeolian and sedimentary iron inputs in the model. The dust field applied in REcoM2 (Mahowald et al., 2003; Luo et al., 2003) is assumed to contain 3.5 % of iron by weight, of which 1.5 % dissolves immediately in the surface ocean upon deposition and the rest is lost from the system.

The input of dissolved iron from the sediments is calculated following Elrod et al. (2004), so the iron flux from the benthos to the bottom water ($BenF_{Fe}$) is proportional to the release of inorganic carbon from the sediments:

$$BenF_{Fe} = \frac{BenthosC \cdot q_{sed}^{Fe:C}}{\rho_C^{ben}} \quad \left[\mu mol\,Fe\,m^{-2}\,day^{-1}\right] \tag{7.2}$$

The vertically integrated carbon concentration in the benthos is denoted by $BenthosC$ ($mmol\,C\,m^{-2}$), $\rho_C^{ben} = 200\,day$ is the remineralization time scale for benthos carbon and $q_{sed}^{Fe:C}$ ($\mu mol\,Fe\,mmol\,C^{-1}$) is the benthic iron to carbon release ratio. The Fe:C ratio in the sediments can become higher than in organic material in general as lithogenic iron in the sediments is mobilized under anoxic conditions. In the current study it is the mass specific scavenging rate (κ_{Fe}) and iron to carbon concentration in the benthos ($q_{sed}^{Fe:C}$) that are varied as described next.

7.2.3 *Experiments*

For the current study we have performed a total of nine model runs, using REcoM2-FESOM 1.4; one control run and eight sensitivity runs (Table 7.1). For all runs the ocean model was spun-up for 300 years under the CORE-I normal year forcing (Large and Yeager, 2009), after which the biogeochemical model was started and run for 50

Table 7.1: Experiments performed, including the values of the Fe:C-ratio in the sediment ($q_{sed}^{Fe:C}$) and mass specific scavenging rate (κ_{Fe}).

MODEL RUN	SEDIMENT FE:C-RATIO [μmol Fe mmol C^{-1}]	MASS SPECIFIC SCAVENGING RATE [$(\text{mmol C m}^{-3})^{-1}\,\text{day}^{-1}$]
CTRL	0.01	0.0312
SED1.1	0.10	0.312
SED1.2	0.10	0.156
SED1.3	0.10	0.078
SED1.4	0.10	0.039
SED2.1	0.68	1.061
SED2.2	0.68	0.531
SED2.3	0.68	0.266
SED2.4	0.68	0.133

years, likewise under CORE-I forcing. The results presented here are the averages of the last 10 years of the runs.

To investigate the effect of the strength of the sediment source of iron on the biological production in the Southern Ocean south of 35°S, two sets of experiments were performed (Experiment 1 and 2), each with a constant benthic Fe:C release ratio ($q_{sed}^{Fe:C}$, Eq. 7.2). In experiment 1, the benthic Fe:C release ratio was ten times higher than in the CTRL run, and in experiment 2, it was set to 0.68 μmol Fe mmol C^{-1} as estimated by Elrod et al. (2004).

For the two experiments, the scavenging rate was increased as compared to the CTRL run to account for the additional iron input. For each experiment, four different scavenging rates were tested (κ_{Fe}, Eq. 7.1), leading to total of four sensitivity runs in each experiment. These runs were named SED1.1 to 1.4 and SED2.1 to 2.4 in experiment 1 and 2, respectively (Table 7.1).

7.3 RESULTS

7.3.1 *Sensitivity study*

Iron

In REcoM2, the magnitude of the released iron from the sediments depend on the prescribed benthic Fe:C release ratio as well as the carbon concentration within the sediments (Eq. 7.2). The release consequently differs between all of the model runs, with the total input to the Southern Ocean south of 35°S ranging from 0.22×10^9 mol Fe yr^{-1} in the CTRL run to 15.8×10^9 mol Fe yr^{-1} in SED2.3 (Table 7.2). The benthic Fe:C ratio has a large impact on the amount of iron released from the sediments, and the total iron input varies with almost a factor 10 between experiment 1 and 2, whereas the intra-experiment difference, brought on by differences in the scavenging rate, is small (Table 7.2). The total iron release nevertheless increases with decreased scavenging rate in the first three studies (1.1 to 1.3 and 2.1 to 2.3), but

Table 7.2: Total iron input to the Southern Ocean south of 35°S from the sediments in all runs, the mean iron flux into the water on the upper 500 m of the water column and the percentage of the external iron input contributed by the sediments. Input from dust: 0.28×10^9 mol Fe yr^{-1}.

RUN	IRON INPUT [10^9 mol Fe yr^{-1}]	MEAN FLUX [μmol Fe $m^{-2} day^{-1}$]	BENTHIC INPUT [%]
CTRL	0.22	0.12	44.0
SED1.1	2.00	1.33	87.7
SED1.2	2.10	1.30	88.2
SED1.3	2.14	1.20	88.4
SED1.4	2.00	0.96	87.7
SED2.1	13.8	9.60	98.0
SED2.2	14.9	9.70	98.2
SED2.3	15.8	9.42	98.3
SED2.4	15.1	7.83	98.2

then decreases again (Table 7.2). The increase happens as less scavenging means that more iron is available in the water for biological production, which leads to more carbon sinking into the sediments, thereby increasing the iron release (Eq. 7.2). This biological feedback mechanism will be discussed further below.

Turning to the vertical distribution of the mean benthic iron flux per unit area, it is largest in the sediments shallower than 500 m, with the maximum iron input occurring at a depth of 50 m in all runs (Fig. 7.2). The strength of the mean iron flux in the upper 500 m of the ocean differs greatly between experiment 1 and 2, concurring with the total iron input to the Southern Ocean (Table 7.2 and Fig. 7.2). The small intra-experimental dependence of the mean iron flux in the upper 500 m on the scavenging can be explained by the fact that the removal of iron through scavenging is less important in areas where iron is continuously supplied, such as the shelf area. The supply allows for biological production to continue in coastal regions despite of a high scavenging rate, and the organic carbon maintains the benthic iron release.

In contrast to the mean sediment flux, the mean iron profile in the Southern Ocean does not change substantially between the CTRL run, experiment 1 and experiment 2, but it changes slightly when the scavenging is changed (Fig. 7.3). On the shelves (> -1000 m, Fig. 7.3a and b), decreased scavenging leads to increased iron concentrations throughout the water column (Fig. 7.3a and b). The largest increases in the iron concentration on the shelves occur in the runs with the highest benthic Fe:C ratio, as more iron is delivered to the water in these runs (Fig. 7.3b). In the open water (< -1000 m, Fig. 7.3c and d), the same pattern occurs, with higher iron concentrations in the runs with less scavenging, though the effect is less clear in the deep water than in the shallow water. One thing that stands out is the fact that it is possible to virtually produce the open ocean iron profile of the CTRL run in both experiment 1 and 2 (Fig. 7.3c and d). Compared to the observations, all of the model runs have too low surface iron concentrations in the open ocean, whereas the deep iron concentrations

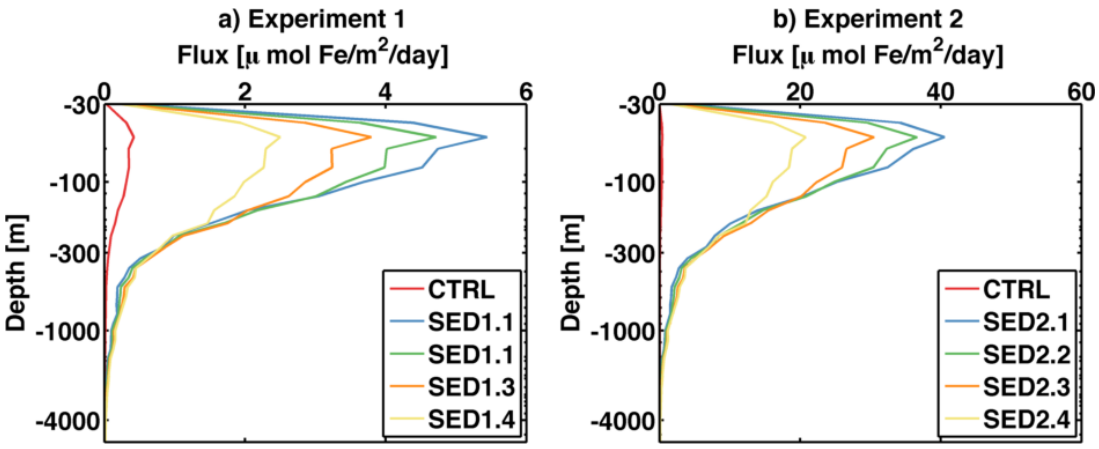

Figure 7.2: Vertical profiles of the mean flux from the sediment into the water calculated south of 35°S. a) Experiment 1 (Fe:C_{sed} = 0.1 µmol Fe mmol C^{-1}), and CTRL run. b) Experiment 2 (Fe:C_{sed} = 0.68 µmol Fe mmol C^{-1}), and CTRL run.

become too high, especially in SED2.1 to 2.4 where the sediment input is highest. For the shelves, the modeled iron profiles are closer to the observations than in the open ocean (Fig. 7.3).

Residence time of iron

The residence time of iron in the model (T_{res}) is calculated using the removal rate of iron, which depends on the scavenging of iron onto particles and on the sinking speed of iron-containing detritus. The residence time is calculated for the Southern Ocean south of 35°S for the upper 500 m and for the whole water column (Table 7.3).

$$\begin{aligned} T_{res} &= \frac{Fe_V}{\text{Fe removal rate}_V} \\ &= \frac{Fe_V}{Scav_V + 0.005\,\mu\text{mol Fe mmol C}^{-1} \cdot Det_V \cdot w_{Det} \cdot H^{-1}} \end{aligned} \tag{7.3}$$

Here the term Fe_V denotes the water's iron inventory (µmol Fe), $Scav_V$ denotes the total scavenging loss as described in Eq. (7.1) multiplied by the water volume (µmol Fe day^{-1}). Det_V is the water's inventory of detritus (mmol C), w_{det} is the sinking speed of the detritus and H is the depth of the water column considered.

The residence time in the model is clearly affected by the rate of scavenging, both in the upper 500 m of the water column and in the whole water column of the Southern Ocean. The longest upper ocean residence time of 18 years occurs in the CTRL run where the scavenging rate is the lowest, and the shortest residence time occurring in SED2.1 where the scavenging is highest (Table 7.3). The scavenging rate controls the residence time directly by removing iron from the water, but it also controls it indirectly as less scavenging leads to higher iron concentrations in the water, which in turn leads to more biological production and thereby also a higher export of iron through the sinking of detritus. In the CTRL run, the scavenging component and the sinking component of Eq. (7.3) are of equal magnitude, but as scavenging is increased in experiment 1 and 2, the scavenging becomes more important. In experiment 2 the scavenging is on average 50 times higher than the removal of iron through sinking of detritus.

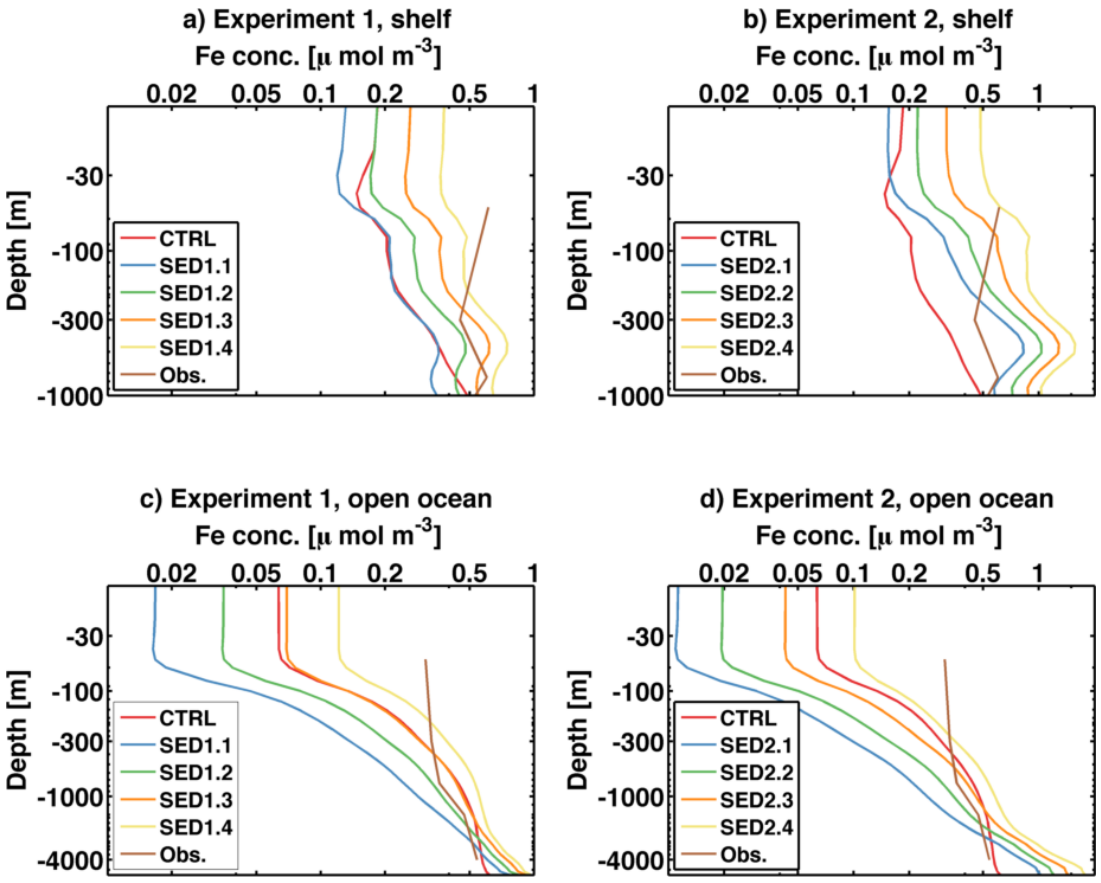

Figure 7.3: Vertical profiles of the mean iron concentration in the Southern Ocean south of 35°S. a) Experiment 1, mean iron profiles on the shelves (> -1000 m). b) Experiment 2, mean iron profiles on the shelves (> -1000 m). c) Experiment 1, mean iron profiles in the open ocean (< -1000 m). d) Experiment 2, mean iron profiles in the open ocean (< -1000 m). All subplots additionally have the vertical profile from the CTRL run and from the observations from Tagliabue et al. (2012), Table 1. Notice the double log-scale.

Table 7.3: Residence time of iron in the Southern Ocean south of 35° for the entire water column and waters shallower than 500 m.

RUN	UPPER 500 M	WHOLE WATER COLUMN
CTRL	18.1 years	266.8 years
SED1.1	2.5 years	45.2 years
SED1.2	3.6 years	53.0 years
SED1.3	5.5 years	68.3 years
SED1.4	9.2 years	101.7 years
SED2.1	3.6 months	7.8 years
SED2.2	5 months	8.6 years
SED2.3	7.2 months	9.8 years
SED2.4	13 months	13.4 years

The residence time is consistently higher when calculated for the whole water column than when calculated for the upper 500 m of the water column. This is because the iron concentration is highest in the deep water (e.g. Fig. 7.3) and because the detritus concentration decreases with depth leading to less removal of iron through both sinking and scavenging.

Biology
The total NPP south of 35°S in the nine runs ranges from 4.9 $\mathrm{Pg\,C\,yr^{-1}}$ in run SED2.1 to 10.3 $\mathrm{Pg\,C\,yr^{-1}}$ in run SED1.4 (Fig. 7.4a). For both experiment 1 and 2, the total NPP increases with decreasing scavenging, as decreased scavenging means that more iron is available for biological production. The NPP from diatoms is especially dependent on the water's iron concentration as diatoms have a higher requirement for iron than the smaller nanophytoplankton due to their higher half saturation constant. But when iron is available, diatoms also have a higher growth rate than the nanophytoplankton, and all in all this leads to larger differences in the fraction of NPP from diatoms within the experiments. The NPP from diatoms is largest in run SED1.4 and 2.4.

The intracellular Si:C ratio in the diatoms has been shown to increase under iron limitation (e.g. Takeda, 1998). This dependence is build into the REcoM2 code and when the Si:C ratio is averaged for the Southern Ocean south of 35°S, this ratio indicates in which runs the diatoms are more iron stressed. The intracellular ratio is allowed to vary between set limits of 0.004 to 0.8 $\mathrm{mmol\,Si\ mmol\,C^{-1}}$ in REcoM2, and in all runs, the mean Southern Ocean Si:C ratio lies between 0.5 and 0.8. The ratio does, however, decrease with decreased scavenging rate, as this means that more iron is available in the mixed layer (Fig. 7.3).

Another quantity that is related to iron limitation is export of biogenic silica (opal). A large fraction of the global export of opal, takes place in the Southern Ocean (e.g. Dunne et al., 2007). In REcoM2, the total export of opal is, not surprisingly, highly correlated with the diatom fraction of the NPP (Fig. 7.4), and thus increases with decreasing scavenging in the water. Of the sensitivity runs, only SED1.4 has a larger opal export than the CTRL run.

In our study it is clear that the mean state of the biology is dependent on the rate of scavenging and the resulting iron availability, but less on the magnitude of the sediment source. It is interesting to note that the CTRL is very similar to the run SED1.3 regarding the NPP and the mean Si:C ratio (Fig. 7.4a, b and c), whereas they differ regarding the export of opal (Fig. 7.4d). Regarding experiment 2, the NPP of the CTRL run lies between the result of SED2.3 and SED2.4.

7.3.2 *Spatial distribution*

For the spatial distribution we compare the CTRL run with SED1.3, as these runs produce a similar result regarding the total NPP, but not for the contribution of diatoms to NPP and the opal export. Regarding experiment 2, the NPP in the CTRL run lies between the results from SED2.3 and SED2.4 (Fig. 7.4) and we will to compare to run SED2.3.

Iron fields
In the CTRL run, the mean iron concentration in the upper 100 m is highest in the belt between 40 and 60°S, with the highest concentrations occurring downstream

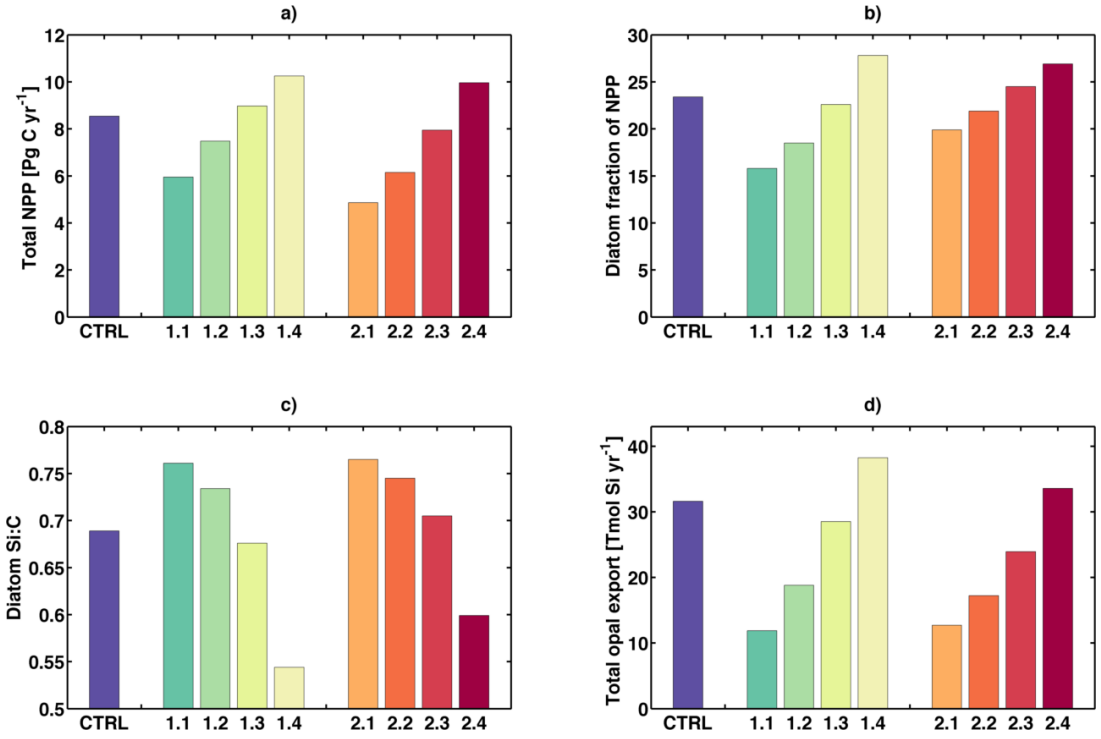

Figure 7.4: a) Total NPP south of 35°S for every run. b) The mean percentage of NPP by diatoms south of 35°S in all runs. c) Mean intracellular C:Si-ratio in diatoms south of 35°S in all runs. d) Total export of opal south of 35°S in all runs. The values written above the bars in subplot a) and c) denote the total NPP and opal export south of 50°S, respectively.

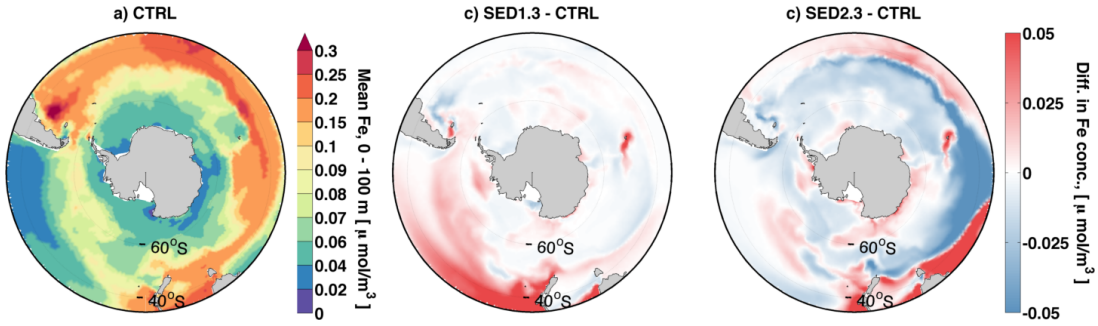

Figure 7.5: a) Mean surface iron concentration in the upper 100 m south of 50°S in the CTRL run, b) The difference in the mean iron concentration in the upper 100 m between SED1.3 and CTRL. c) The difference in the iron concentration in the upper 100 m between SED2.3 and CTRL

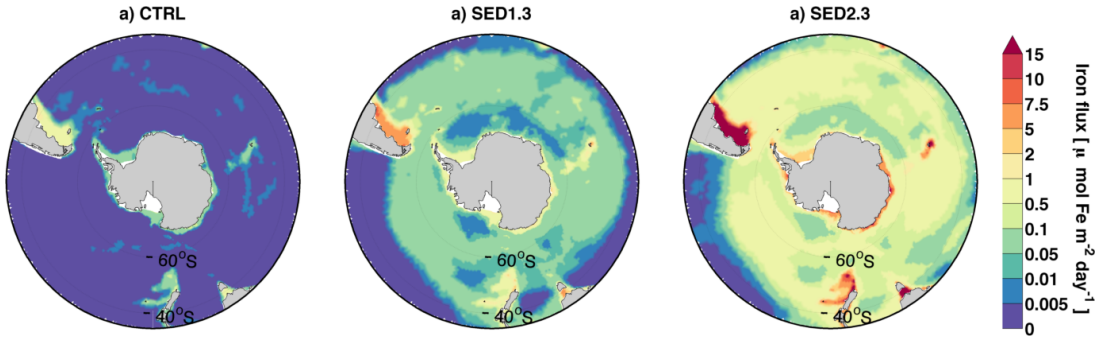

Figure 7.6: a) Mean benthic input of iron in the Southern Ocean south of 50°S in model run a) CTRL, b) SED1.3, c) SED2.3. Notice the nonlinear scale.

of Patagonia, South Africa and Australia (Fig. 7.5a), where iron is supplied through dust and from the sediments (Fig. 7.6a). The CTRL run has a small input from the shelves around the Antarctica (Fig. 7.6a), but not enough to increase the iron concentration here (Fig. 7.5a), possibly because it is immediately removed from the surface by coastal downwelling or utilized for phytoplankton growth.

In SED1.3, the increased iron flux from the shelf of New Zealand increases the iron concentration in the Pacific sector of the Southern Ocean (Fig. 7.5b), the area with the lowest iron concentration in the CTRL run. The second place of elevated iron concentrations is around the Kerguelen Plateau, where the sediment flux also is relatively high (Fig. 7.5b and 7.6b). The open ocean part of the Southern Ocean does, however, also have areas with slightly lower iron concentrations in SED1.3 compared to the CTRL run due to the higher scavenging rate in SED1.3.

The much higher benthic input in SED2.3 along with the higher scavenging rate creates a strong off-shore gradient, with high concentrations close to the shore and very low in the open ocean (Fig. 7.5c).

Net primary production

The spatial distribution of the NPP is correlated with the iron concentration in the upper 100 m of the water column in the CTRL run, with higher rates between 40 and 60°S, especially in the Atlantic and Indian sectors of the Southern Ocean (Fig. 7.7a). When the sedimentary iron input is increased in SED1.3 and SED2.3, the total NPP is

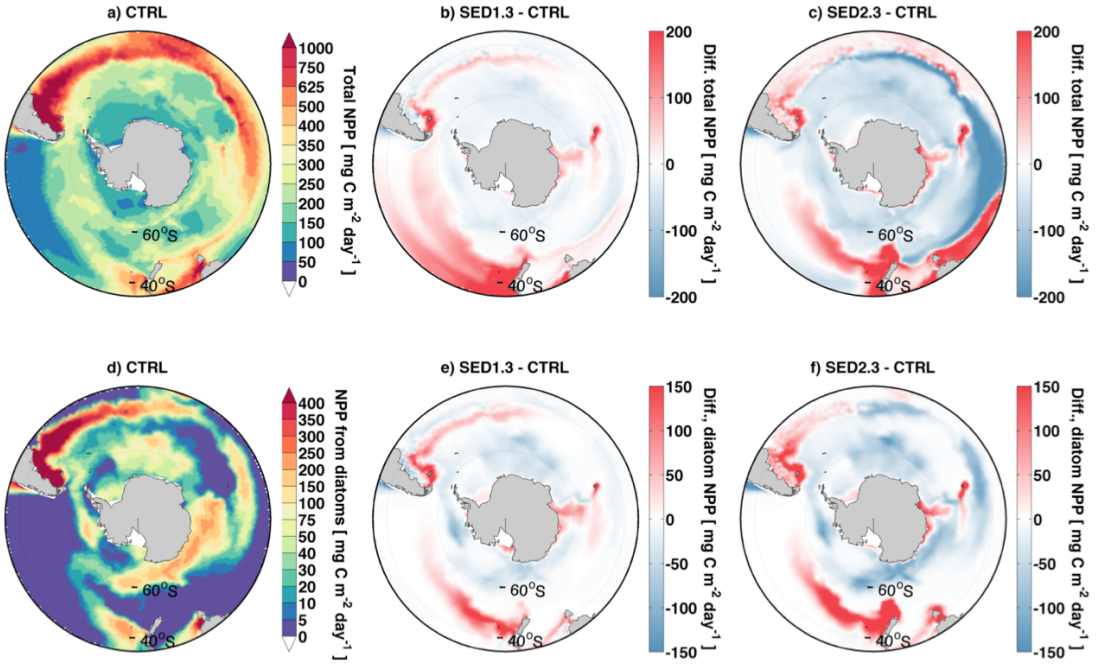

Figure 7.7: a) Mean NPP in CTRL run. b) Difference in the rate of total NPP between CTRL and SED1.3. c) Difference in the rate of total NPP between CTRL and SED2.3. d) Mean NPP from diatoms in CTRL run. e) Difference in the rate of diatom NPP between CTRL and SED1.3. f) Difference in the rate of diatom NPP between CTRL and SED2.3.

increased downstream of the Patagonian shelf, in the Pacific sector of the Southern Ocean, downstream of New Zealand and around the Kerguelen plateau, where the iron concentrations were also elevated, but it is decreased in the rest of the Southern Ocean (Fig. 7.7b and c). The magnitude of the changes in both directions are largest in SED2.3 as both the near-shore iron input and the off-shore iron removal is the largest in this model run (Fig. 7.5).

Regarding the NPP from the diatoms in the CTRL run, it mainly takes place downstream of the Patagonian shelf, where iron is added from the dust and the sediments, but it also occurs in the Indian sector of the Southern Ocean south of 60°S, where iron must be supplied from below (Fig. 7.7d). When the sediment source is increased, the diatom growth is increased downstream of shelves, especially in the Pacific Ocean, and on the shelves of Patagonia, Kerguelen and along the Antarctic coast (Fig. 7.7e and f). In the open ocean south of 50°S, the production of diatoms is, however, decreased, especially in SED2.3 where the scavenging is strongest. The similarity in the patterns between the change in the total NPP and the NPP from the diatoms show that diatoms are to a large degree responsible for the changes in the NPP between the runs, especially south of 40°S.

Silicon

Due to a slow dissolution rate of biogenic silica, the export of opal is highly correlated with the diatom production in the CTRL run, with the largest export occurring downstream of New Zealand and the Patagonian shelf. A large export, however, also takes place south of 50°S where the external iron input is much smaller (Fig. 7.7a and 7.8a). When the benthic flux and scavenging rate of iron is increased in SED1.3 and

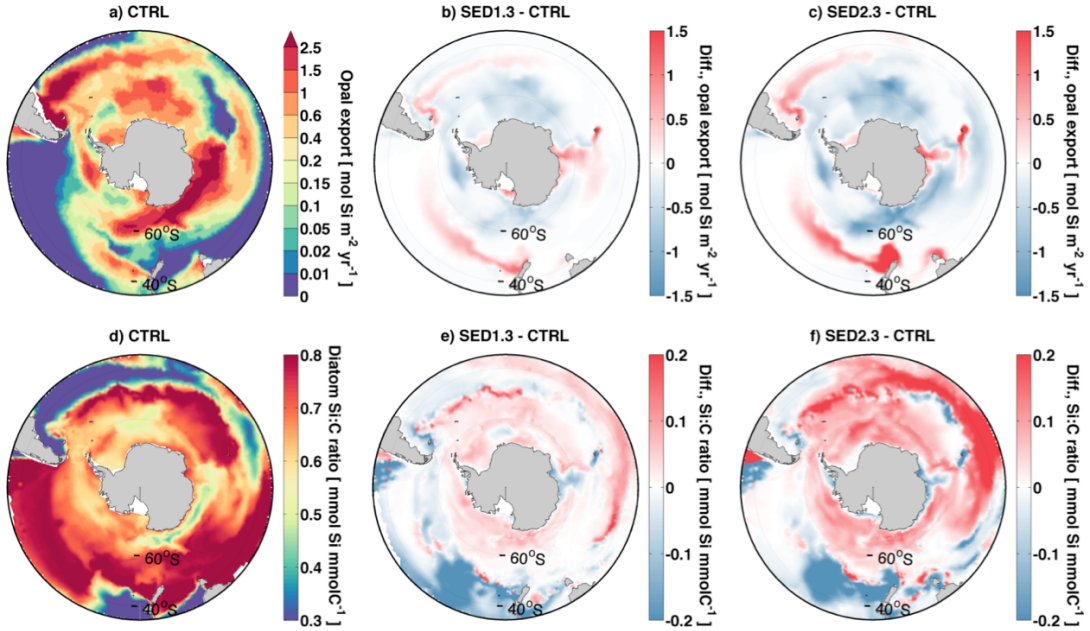

Figure 7.8: a) Mean opal export across 100 m. b) Difference in opal export between SED1.3 and CTRL runs. c) Difference in opal export between SED2.3 and CTRL run. d) Mean intracellular Si:C ratio in CTRL run. e) Difference in intracellular Si:C ratio between SED1.3 and CTRL. f) Difference in intracellular Si:C ratio between SED2.3 and CTRL.

2.3, the opal export increases downstream of the main shelves, but decreases south of 50°S, similar to NPP from diatoms (Fig. 7.8b and c).

The diatom intracellular ratio between silicon and carbon affects the export of the two compounds. In the CTRL, low diatom Si:C ratios clearly occur in the same areas where the production from diatoms is high, but not necessarily where the iron concentrations are high. This indicates that the Si:C ratio is a proxy for good growth conditions for the diatoms, rather than for iron concentrations. The dependence of the Si:C ratio on the iron concentration is clear when we examine the changes between the CTRL run and SED1.3 and 2.3, as the ratio decreases south of 60°S, where the iron concentration also decreases and it increases downstream of the shelfs where the iron concentration is increased (Fig. 7.8e and f).

7.4 DISCUSSION

7.4.1 *Magnitude of the sediment flux*

Measurements of the flux of iron into the water on the Southern Ocean continental shelves cover a large range of values. In the lower end, a newer study found an average iron flux of 0.36 µmol m^{-2} day^{-1} for the Ross Sea (Marsay et al., 2014), whereas Blain et al. (2008) measured 136 µmol Fe m^{-2} day^{-1} on the Kerguelen plateau. These fluxes represent single sites, while our values are averaged over time and space (Table 7.2). While our CTRL run flux of 0.12 µmol m^{-2} day^{-1} is relatively close to the value found by Marsay et al. (2014), the mean value of the flux south of 35°S should most likely be somewhat higher than the value in the Ross Sea, and the value

of 136 μmol Fe m^{-2} day^{-1}, measured on the highly productive Kerguelen Plateau during the peak of iron release, is too high as a mean for the area south of 35°S. In between these is the mean value of 9.2 μmol m^{-2} day^{-1} found by de Jong et al. (2012) measured on the continental shelves in the Atlantic sector of the Southern Ocean, which is very similar to our mean values from experiment 2 (Table 7.2). Their value represents several sites and could indicate that the flux in our experiment 2 is realistic, thereby implying that the scavenging scheme should be changed in REcoM2 to deal with the increased iron input from such a large flux. A global mean flux of 4.3 μmol m^{-2} day^{-1} based on shelf fluxes was suggested by Elrod et al. (2004), and falls between our mean shelf fluxes in experiment 1 and 2 (Table 7.2). Since many of the observations Elrod et al. (2004) based their number on were located in high-productivity areas such as the Californian upwelling zone, it is probably too high as a mean for the Southern Ocean, where biological production generally is lower. This dataset thus points towards the flux in experiment 1 as the more realistic one.

The strength of the iron flux in experiment 1 (Table 7.2) also fits well with that used by some other OGCBMs; Moore et al. (2004) used a constant value of 2 μmol m^{-2} day^{-1} in areas shallower than 1100 m, whereas Aumont and Bopp (2006) used a depth dependent release rate of iron that was set to a maximum of 1 μmol m^{-2} day^{-1}. The parameterization of the iron release used in the current study (Elrod et al., 2004), which leads to a spatially varying iron release, has also been used by Moore and Braucher (2008) and Wadley et al. (2014). In the CESM model (Moore and Braucher, 2008), it lead to an input rate ranging from 0 to 16.5 μmol Fe m^{-2} day^{-1}, very similar to the values in our SED2.3 model run (Fig. 7.6), and not unreasonable compared to the measurements mentioned above. But as is the case for the observations, the modeled fluxes vary significantly.

In the current study, the total input of iron to the Southern Ocean varied with more than an order of magnitude, from 0.22×10^9 mol Fe yr^{-1} in the CTRL run to 15.8×10^9 mol Fe yr^{-1} in SED2.3 (Table 7.2). Observation-based estimates of the total iron input do not exist, but it is possible to compare the iron input in REcoM2 to other OGCBMs. Tagliabue et al. (2009) had an input of 1.34×10^9 mol Fe yr^{-1} in a model study covering the area south of 35°S. This is slightly lower than the input of 2.00 to 2.14×10^9 mol Fe yr^{-1} we see in our experiment 1 (Table 7.2). In another model study, Lancelot et al. (2009) had a total input of 0.38×10^9 mol Fe yr^{-1} from the sediments south of 60°S. This is very similar to the input in our SED1.3 run, in which the input was 0.36×10^9 mol Fe yr^{-1} in the same area.

7.4.2 *Iron concentration and scavenging*

The modeled mean iron profiles tend to have low surface iron concentrations and high deep iron concentrations compared to the mean profile of the observations, especially in the open ocean (Fig. 7.3). This shows that while most of the iron from the sediments is added from depths shallower than 500 m (Fig. 7.2), most of the scavenging, which is dependent on the detritus concentration, also removes iron in the upper part of the water column. In reality, the maximum mean values are generally close to 0.6 μmol Fe m^{-3}, though it varies between the major ocean basins (e.g. Johnson et al., 1997; Moore and Braucher, 2008; Tagliabue et al., 2012). The modeled deep water concentrations close to 1 μmol Fe m^{-3} are thus likely overestimated. Johnson et al. (1997)

suggested that the scavenging rate of iron increases when the concentration reaches 0.6 μmol Fe m^{-3}, thereby explaining this apparent maximum. In REcoM2, binding of dissolved iron to ligands decreases scavenging when the iron concentration is lower than 1 μmol Fe m^{-3}. Decreasing the assumed ligand concentration would be a way to increase the scavenging rate in the model, something that could be necessary for realistic runs with an increased sediment source, especially when the strength is high as in experiment 2.

Regarding the surface iron concentrations, Klunder et al. (2011) observed a northward increase in the Atlantic sector of the Southern Ocean, ranging from 0.15 μmol Fe m^{-3} in the Weddell Gyre to 0.25 μmol Fe m^{-3} at 55°S. In the Indian sector of the Southern Ocean, Grand et al. (2015), on the contrary, found that the surface iron concentrations decreased northwards from Antarctica, with maximum coastal values of 1.7 μmol m^{-3}, and the concentration falling to 0.2 μmol m^{-3} north of the Polar Front. In our runs, the iron concentration north of 60°S fit well with these results, and the surface iron concentration increases from south to north similar to the result from Klunder et al. (2011) (Fig. 7.5). Towards the south, the modeled iron concentrations are, however, relatively low, and while the coastal iron input is increased in SED1.3 and SED2.3 (Fig. 7.6b and c), the iron concentration around Antarctica has not increased towards the values from Grand et al. (2015).

In experiment 2, the combination of low surface mixed layer iron concentrations and high deep water iron concentration compared to the observations (Fig. 7.3) indicate that the value of 0.68 μmol Fe (mmol C^{-1}) for the benthic Fe:C ratio is too high for our model setup. In the open ocean that is not downstream from shelves, the iron concentration has been decreased in many areas in SED1.3 when compared to the CTRL run, and for SED2.3, the changes in the spatial distribution makes it clear that the scavenging needed to keep the sediment input in check is simply too large to be realistic as it removes too much dissolved iron in the open ocean.

One thing that might change the effect of the scavenging rate is the aeolian iron deposition. In the CTRL run, the sediment source make up 44 % of the total external iron input, whereas it comprises approximately 88 and 98 % in experiment 1 and 2, respectively. In the model study by Lancelot et al. (2009), the sediment source comprised 90 % of the iron input south of 60°S, concurrent with SED1.3, whereas the sediment source comprised 72 % of the input south of 35°S in the study by Tagliabue et al. (2009). For the global ocean, the sediment source made up 58 % of the total iron supply in the study by Moore and Braucher (2008). Provided that these numbers are reasonable, and we do not know if they are, our CTRL run and experiment 1 have the more reasonable ratios between the sediment input and the dust input (Table 7.2).

7.4.3 *Residence time of iron*

The residence time of iron in the ocean is much lower than that of the macronutrients and also lower than the time scale of the thermohaline circulation (Johnson et al., 1997). The residence time can be calculated through the rate of iron removal or the rate of the input. As the flux of the iron input and associated scavenging varies widely between models, so does the residence time. At the higher end of the range lies the global mean residence time of 233 years found be Parekh et al. (2005). In this model, the only external iron source was aeolian, and the residence time in our CTRL run (267 years, Table 7.3) is relatively close to their result as this run only has

a small sedimentary iron input. Moore and Braucher (2008) conversely calculated a global mean residence time of 12 years in a model with a relatively large input of iron from external sources, and also a higher scavenging rate. Their surface water residence time estimate ranged from 5 months in high-input areas to 1.4 years in areas with less iron input. The sediment input in this model is, on the global scale, approximately similar to ours in experiment 2, and the calculated residence time of the current study fits relatively well with their estimates, both for the surface water and for the whole ocean (Table 7.3). Iron removal or input rates are, however, difficult to constrain and measurement-based estimates of the residence time therefore also differ significantly.

In a study based on measurements, Bruland et al. (1994) estimated a residence time of iron in the central North Pacific deep water ranging from 70 to 140 years. In the North Atlantic deep water, the residence time has been found to be 270 years, while it was estimated to be one to five months in the surface water (Bergquist and Boyle, 2006). In the Equatorial Atlantic the surface residence time is similarly short, ranging from 280 days to 10.5 years have been found in the Equatorial Atlantic, which is under influence from the Saharan dust plume (Croot et al., 2004b). These studies cover the whole range of residence times calculated in the current study (Table 7.3). In this study, the residence time is based on removal of iron, which is strongly controlled by the scavenging. Decreasing the assumed concentration of ligands in the model could move the high scavenging towards the coast, thereby reducing it in the open ocean. This in turn would impact the residence time. But the processes are complex and difficult to predict, and in order to utilize the residence times to optimize the iron cycle in the model a more in depth study would be necessary.

7.4.4 *Biological production*

The higher values for NPP occur in the runs SED1.3 and 1.4 along with SED2.3 and 2.4, in which the iron scavenging is relatively small and the surface iron concentrations high. The fraction of the total NPP that is carried out by diatoms has previously been shown to be dependent on the available iron (Wang et al., 2014b), and we also see how the diatoms become more abundant in the runs where the iron concentration is higher in the mixed layer (Fig. 7.4c). The increase in diatoms does, however, occur downstream of islands and continental shelfs, while diatoms decrease in abundance in the open ocean (Fig. 7.7e and f). This means that it is only in the runs SED1.4, 2.3 and 2.4 that the diatom make up a larger fraction of the total NPP than in the CTRL run (Fig. 7.4c). In a study based on satellite-based measurements, Bracher et al. (2009) showed that diatoms dominate production in the Southern Ocean south of 30°S, whereas other studies have shown less production by diatoms (e.g. Alvain et al., 2005; Hirata et al., 2011). In a study focussing on the Southern Ocean, Soppa et al. (2014) show that diatoms dominate in areas with high iron input, especially downstream of the Patagonian shelf and in the Atlantic sector of the Southern Ocean in general, but also south of Australia, and east of New Zealand and the Kerguelen Plateau. In our study, the spatial distribution of the diatom production broadly follows the same pattern (Fig. 7.7), but diatom productivity in the Atlantic sector of the Southern Ocean is relatively low, most likely due to too little sedimentary input from the shelves around the Antarctic Peninsula and South Georgia (Fig. 7.5 and 7.6). One factor that plays a role in this, is the resolution of the model grid, which is increased

in coastal regions in FESOM (Fig. 7.1), but not enough to capture the narrow shelves adequately in both of these regions and especially around South Georgia (Fig. 7.1). We do consequently not capture the South Georgia bloom or the bloom downstream of the Antarctic Peninsula, which shows up in high-resolution runs (e.g. Wadley et al., 2014). If these blooms were captured, they would likely contain a large degree of diatoms as is the case in the Kerguelen bloom and downstream of the other major shelves (Fig. 7.7e and f).

In commonly used OGCBMs, the fraction of the biomass from diatoms in the Southern Ocean ranges from 20 to 100 % (Vogt et al., 2013), and thereby differs widely, but they have in common that the diatoms are more abundant in areas with higher iron availability. Diatoms do not dominate production in any of our runs, with the highest percentage of NPP from diatoms occurring in SED1.4, where they comprise 28 % of the total NPP. Our model results are thus at the lower end of what other models have found, especially SED1.1 and 1.2 (Fig. 7.4b), but close to the results by Alvain et al. (2005), as described above.

One thing that can help constrain the appropriate amount of diatom primary production in the Southern Ocean is by comparing the amount of vertically exported opal in our model to the amount found in previous studies. While our higher values of opal export fit well with the results in the lower end of the range from Dunne et al. (2007), the low opal export in the runs SED1.1 and 1.2 as well as SED2.1 to 2.3 show that too little iron is available in these runs to make them realistic (Fig. 7.4). As diatoms are dependent on a higher iron concentration than the nanophytoplankton to grow, the low open ocean surface iron concentrations in SED2.3 (Fig. 7.5c) along with the changes that occur in the spatial distribution of the diatom NPP (Fig. 7.7f) make it clear that although the NPP from diatoms has increased downstream of the major shelves in SED2.3, where the surface iron concentration has been increased, it has decreased in the open ocean due to the larger scavenging that occurs here, leading to a relatively small opal export.

Another factor affecting the silicon export is the intracellular Si:C ratio of the diatoms. In REcoM2, this number decreases with increasing iron availability, varying from 0.544 mol Si $(\text{mol C})^{-1}$ in SED1.4 to 0.76 mol Si $(\text{mol C})^{-1}$ in SED1.1 and 2.1 (Fig. 7.4). On a global scale, the Si:C ratio has been shown to vary with a factor of 4 to 5, with the mean value being 0.11 mol Si mol C^{-1} (e.g. Sarthou et al., 2005). Compared to the other major oceans, the Southern Ocean is, however, highly silicified, with measured values of the Si:C ratio ranging from 0.31 to 0.6 mol Si mol C^{-1}, dependent on the iron availability (e.g. Brzezinski et al., 2003; Hoffmann et al., 2007; Baines et al., 2010). The mean numbers for the Si:C ratios in REcoM2 are rather high compared to observed estimates, and consistent with a highly iron limited regime.

7.5 CONCLUSION

We have shown, that given different strengths of the sediment source of iron, combined with an appropriate rate of iron removal from the water through scavenging, it is possible to create virtually identical mean iron profiles for the Southern Ocean along with reasonable numbers for the total NPP. The phytoplankton composition and the spatial distribution of the NPP did, however, change with changed strengths

of the iron flux. When choosing a combination of the benthic iron influx and scavenging rate in a model it is therefore necessary to evaluate the model's NPP from diatoms along with the amount of opal exported against previous studies, as these are highly dependent on the iron availability in the model. While our CTRL run produced reasonable values for the biogeochemistry, the sediment source of iron is relatively small in this run, and the NPP from diatoms is most likely also too small. Based on the knowledge we have about the benthic iron flux, as well as the above mentioned parameters, we found that our model run SED1.3 gave better results, with a mean shelf iron input of 1.2 μmol Fe m^{-2} yr$-$1, leading to a total benthic iron influx of 2.14 $\times$ 10^9 mol Fe yr^{-1} to the Southern Ocean. The open ocean NPP is, however, still relatively small in this run, as is the fraction of the NPP from diatoms and the export of biogenic silicon. Further sensitivity runs with different parameterizations of the scavenging could improve this by decreasing the off-shore iron gradient.

REFERENCES

Alvain, S., C. Moulin, Y. Dandonneau, and F. Bréon (2005). "Remote sensing of phytoplankton groups in case 1 waters from global SeaWiFS imagery." *Deep Sea Res. Pt. I* (52) 11, pp. 1989 –2004. DOI: 10.1016/j.dsr.2005.06.015.

Assmy, P., V. Smetacek, M. Montresor, C. Klaas, J. Henjes, V. H. Strass, J. M. Arrieta, U. Bathmann, G. M. Berg, E. Breitbarth, B. Cisewski, L. Friedrichs, N. Fuchs, G. J. Herndl, S. Jansen, S. Krägefsky, M. Latasa, I. Peeken, R. Röttgers, R. Scharek, S. E. Schüller, S. Steigenberger, A. Webb, and D. Wolf-Gladrow (2013). "Thick-shelled, grazer-protected diatoms decouple ocean carbon and silicon cycles in the iron-limited Antarctic Circumpolar Current." *Proc. Natl. Acad. Sci. U.S.A* (110) 51, pp. 20633–20638. DOI: 10.1073/pnas.1309345110.

Aumont, O. and L. Bopp (2006). "Globalizing results from ocean in situ iron fertilization studies." *Global Biogeochem. Cy.* (20) GB2017. DOI: 10.1029/2005GB002591.

Aumont, O., E. Maier-Reimer, S. Blain, and P. Monfray (2003). "An ecosystem model of the global ocean including Fe, Si, P colimitations." *Global Biogeochem. Cy.* (17) 2. DOI: 10.1029/2001GB001745.

Baines, S. B., B. S. Twining, M. A. Brzezinski, D. M. Nelson, and N. S. Fisher (2010). "Causes and biogeochemical implications of regional differences in silicification of marine diatoms." *Global Biogeochem. Cy.* (24) 4. DOI: 10.1029/2010GB003856.

Behrenfeld, M. J., A. J. Bale, Z. S. Kolber, J. Aiken, and P. G. Falkowski (1996). "Confirmation of iron limitation of phytoplankton photosynthesis in the equatorial Pacific Ocean." *Nature* (383), pp. 508–511. DOI: 10.1038/383508a0.

Bergquist, B. A. and E. A. Boyle (2006). "Dissolved iron in the tropical and subtropical Atlantic Ocean." *Global Biogeochem. Cy.* (20) 1. DOI: 10.1029/2005GB002505.

Blain, S., G. Sarthou, and P. Laan (2008). "Distribution of dissolved iron during the natural iron-fertilization experiment KEOPS (Kerguelen Plateau, Southern Ocean)." *Deep Sea Res. Pt. II* (55) 5, pp. 594–605. DOI: 10.1016/j.dsr2.2007.12.028.

Blain, S., P. Tréguer, S. Belviso, E. Bucciarelli, M. Denis, S. Desabre, M. Fiala, V. Martin Jézéquel, J. Le Fèvre, P. Mayzaud, J.-C. Marty, and S. Razouls (2001). "A biogeochemical study of the island mass effect in the context of the iron hypothesis: Kerguelen Islands, Southern Ocean." *Deep Sea Res. Pt. I* (48) 1, pp. 163–187. DOI: 10.1016/S0967-0637(00)00047-9.

Boyd, P. W., A. J. Watson, C. S. Law, E. R. Abraham, T. Trull, R. Murdoch, D. C. E. Bakker, A. R. Bowie, K. O. Buesseler, H. Chang, M. Charette, P. Croot, K. Downing, R. Frew, M. Gall, M. Hadfield, J. Hall, M. Harvey, G. Jameson, J. LaRoche, M. Liddicoat, R. Ling, M. T. Maldonado, R. M. McKay, S. Nodder, S. Pickmere, R. Pridmore, S. Rintoul, K. Safi, P. Sutton, R. Strzepek, K. Tanneberger, S. Turner, A. Waite, and J. Zeldis (2000). "A mesoscale phytoplankton bloom in the polar Southern Ocean stimulated by iron fertilization." *Nature* (407) 6805, pp. 695–702. DOI: 10.1038/35037500.

Bracher, A., M. Vountas, T. Dinter, J. Burrows, R. Röttgers, and I. Peeken (2009). "Quantitative observation of cyanobacteria and diatoms from space using PhytoDOAS on SCIAMACHY data." *Biogeosciences* (6), pp. 751–764. DOI: 10.5194/bg-6-751-2009.

Bruland, K. W., K. J. Orians, and J. P. Cowen (1994). "Reactive trace metals in the stratified central North Pacific." *Geochim. Cosmochim. Ac.* (58) 15, pp. 3171–3182. DOI: 10.1016/0016-7037(94)90044-2.

Brzezinski, M. A., M.-L. Dickson, D. M. Nelson, and R. Sambrotto (2003). "Ratios of Si, C and N uptake by microplankton in the Southern Ocean." *Deep Sea Res. Pt. II* (50) 3, pp. 619–633. DOI: 10.1016/S0967-0645(02)00587-8.

Cassar, N., M. L. Bender, B. A. Barnett, S. Fan, W. J. Moxim, H. Levy, and B. Tilbrook (2007). "The Southern Ocean biological response to aeolian iron deposition." *Science* (317) 5841, pp. 1067–1070. DOI: 10.1126/science.1144602.

Conway, T. M., A. D. Rosenberg, J. F. Adkins, and S. G. John (2013). "A new method for precise determination of iron, zinc and cadmium stable isotope ratios in seawater by double-spike mass spectrometry." *Anal. Chim. Acta* (793), pp. 44–52. DOI: 10.1016/j.aca.2013.07.025.

Conway, T. M. and S. G. John (2014). "Quantification of dissolved iron sources to the North Atlantic Ocean." *Nature* (511) 7508, pp. 212–215. DOI: 10.1038/nature13482.

Croot, P. L., K. Andersson, M. Öztürk, and D. R. Turner (2004a). "The distribution and speciation of iron along 6°E in the Southern Ocean." *Deep Sea Res. Pt. II* (51) 22, pp. 2857–2879.

Croot, P. L., P. Streu, and A. R. Baker (2004b). "Short residence time for iron in surface seawater impacted by atmospheric dry deposition from Saharan dust events." *Geophys. Res. Lett.* (31) 23. DOI: 10.1029/2004GL020153.

De Baar, H. J. W., J. T. M. de Jong, D. C. E. Bakker, B. M. Löscher, C. Veth, U. Bathmann, and V. Smetacek (1995). "Importance of iron for plankton blooms and carbon dioxide drawdown in the Southern Ocean." *Nature* (373). DOI: 10.1038/373412a0.

De Jong, J., V. Schoemann, D. Lannuzel, P. Croot, H. de Baar, and J.-L. Tison (2012). "Natural iron fertilization of the Atlantic sector of the Southern Ocean by continental shelf sources of the Antarctic Peninsula." *J. Geophys. Res.* (117) G1. DOI: 10.1029/2011JG001679.

Dunne, J. P., J. L. Sarmiento, and A. Gnanadesikan (2007). "A synthesis of global particle export from the surface ocean and cycling through the ocean interior and on the seafloor." *Global Biogeochem. Cy.* (21) GB4006. DOI: 10.1029/2006GB002907.

Dutkiewicz, S., M. J. Follows, and P. Parekh (2005). "Interactions of the iron and phosphorus cycles: A three-dimensional model study." *Global Biogeochem. Cy.* (19) 1. DOI: 10.1029/2004GB002342.

Elrod, V. A., W. M. Berelson, K. H. Coale, and K. S. Johnson (2004). "The flux of iron from continental shelf sediments: A missing source for global budgets." *Geophys. Res. Lett.* (31) L12307. DOI: 10.1029/2004GL020216.

Geider, R. J., H. L. MacIntyre, and T. M. Kana (1998). "A dynamic regulatory model of phytoplanktonic acclimation to light, nutrients, and temperature." *Limnol. Oceanogr.* (43) 4, pp. 679–694. DOI: 10.4319/lo.1998.43.4.0679.

Gent, P. R. and J. C. Mcwilliams (1990). "Isopycnal mixing in ocean circulation models." *J. Phys. Oceanogr.* (20) 1, pp. 150–155. DOI: 10.1175/1520-0485(1981)011<1443:POVMIN>2.0.CO;2.

Grand, M. M., C. I. Measures, M. Hatta, W. T. Hiscock, W. M. Landing, P. L. Morton, C. S. Buck, P. M. Barrett, and J. A. Resing (2015). "Dissolved Fe and Al in the upper 1000 m of the eastern Indian Ocean: a high-resolution transect along 95°E from the Antarctic margin to the Bay of Bengal." *Global Biogeochem. Cy.* DOI: 10.1002/2014GB004920.

Hauck, J., C. Völker, T. Wang, M. Hoppema, M. Losch, and D. A. Wolf-Gladrow (2013). "Seasonally different carbon flux changes in the Southern Ocean in response to the Southern Annular Mode." *Global Biogeochem. Cy.* (27), pp. 1–10. DOI: 10.1002/2013GB004600.

Hirata, T., N. J. Hardman-Mountford, R. J. W. Brewin, J. Aiken, R. Barlow, K. Suzuki, T. Isada, E. Howell, T. Hashioka, M. Noguchi-Aita, and Y. Yamanaka (2011). "Synoptic relationships between surface Chlorophyll-a and diagnostic pigments specific to phytoplankton functional types." *Biogeosciences* (8) 2, pp. 311–327. DOI: 10.5194/bg-8-311-2011.

Hoffmann, L., I. Peeken, K. Lochte, P. Assmy, and M. Veldhuis (2006). "Different reactions of Southern Ocean phytoplankton size classes to iron fertilization." *Limnol. Oceanogr.* (51) 3, pp. 1217–1229. DOI: 10.4319/lo.2006.51.3.1217.

Hoffmann, L. J., I. Peeken, and K. Lochte (2007). "Effects of iron on the elemental stoichiometry during EIFEX and in the diatoms Fragilariopsis kerguelensis and Chaetoceros dichaeta." *Biogeosciences* (4) 4, pp. 569–579. DOI: 10.5194/bg-4-569-2007.

Jickells, T. D., Z. S. An, K. K. Andersen, A. R. Baker, G. Bergametti, N. Brooks, J. J. Cao, P. W. Boyd, R. A. Duce, K. A. Hunter, H. Kawahata, N. Kubilay, J. LaRoche, P. S. Liss, N. Mahowald, J. M. Prospero, A. J. Ridgwell, I. Tegen, and R. Torres (2005). "Global iron connections between desert dust, ocean biogeochemistry, and climate." *Science* (308) 5718, pp. 67–71. DOI: 10.1126/science.1105959.

John, S. G. and J. F. Adkins (2010). "Analysis of dissolved iron isotopes in seawater." *Mar. Chem.* (119) 1, pp. 65–76. DOI: 10.1016/j.marchem.2010.01.001.

Johnson, K. S., V. A. Elrod, S. E. Fitzwater, J. N. Plant, F. P. Chavez, S. J. Tanner, R. M. Gordon, D. L. Westphal, K. D. Perry, J. Wu, et al. (2003). "Surface ocean-lower atmosphere interactions in the northeast Pacific Ocean gyre: Aerosols, iron, and the ecosystem response." *Global Biogeochem. Cy.* (17) 2.

Johnson, K. S., R. M. Gordon, and K. H. Coale (1997). "What controls dissolved iron concentrations in the world ocean?" *Mar. Chem.* (57) 3, pp. 137–161. DOI: 10.1016/S0304-4203(97)00043-1.

Klunder, M. B., P. Laan, R. Middag, H. J. W. de Baar, and J. C. Van Ooijen (2011). "Dissolved iron in the Southern Ocean (Atlantic sector)." *Deep Sea Res. Pt. II* (58) 25, pp. 2678–2694. DOI: 10.1016/j.dsr2.2010.10.042.

Kolber, Z. S., R. T. Barber, K. H. Coale, S. E. Fitzwateri, R. M. Greene, K. S. Johnson, S. Lindley, and P. G. Falkowski (1994). "Iron limitation of phytoplankton photosynthesis in the equatorial Pacific Ocean." *Nature* (371) 6493, pp. 145–149. DOI: 10.1038/371145a0.

Korb, R. E. and M. Whitehouse (2004). "Contrasting primary production regimes around South Georgia, Southern Ocean: Large blooms versus high nutrient, low chlorophyll waters." *Deep Sea Res. Pt. I* (51) 5, pp. 721–738. DOI: 10.1016/j.dsr.2004.02.006.

Kriest, I. and A. Oschlies (2008). "On the treatment of particulate organic matter sinking in large-scale models of marine biogeochemical cycles." *Biogeosciences* (5) 1, pp. 55–72. DOI: 10.5194/bg-5-55-2008.

Lam, P. J. and J. K. B. Bishop (2008). "The continental margin is a key source of iron to the HNLC North Pacific Ocean." *Geophys. Res. Lett.* (35) Lo7608. DOI: 10.1029/2008GL033294.

Lam, P. J., J. K. B. Bishop, C. C. Henning, M. A. Marcus, G. A. Waychunas, and I. Y. Fung (2006). "Wintertime phytoplankton bloom in the subarctic Pacific supported by continental margin iron." *Global Biogeochem. Cy.* (20) GB1006. DOI: 10.1029/2005GB002557.

Lancelot, C., A. de Montety, H. Goosse, S. Becquevort, V. Schoemann, B. Pasquer, and M. Vancoppenolle (2009). "Spatial distribution of the iron supply to phytoplankton in the Southern Ocean: a model study." *Biogeosciences* (6) 12, pp. 2861–2878. DOI: 10.5194/bg-6-2861-2009.

Large, W. G. and S. G. Yeager (2009). "The global climatology of an interannually varying air–sea flux data set." *Clim. Dynam.* (33) 2-3, pp. 341–364. DOI: 10.1007/s00382-008-0441-3.

Large, W. G., J. C. McWilliams, and S. C. Doney (1994). "Oceanic vertical mixing: A review and a model with a nonlocal boundary layer parameterization." *Rev. Geophys.* (32) 4, pp. 363–403. DOI: 10.1029/94RG01872.

Luo, C., N. M. Mahowald, and J. Del Corral (2003). "Sensitivity study of meteorological parameters on mineral aerosol mobilization, transport, and distribution." *J. Geophys. Res* (108) D15. DOI: 10.1029/2003JD003483.

Mahowald, N., C. Luo, J. Del Corral, and C. S. Zender (2003). "Interannual variability in atmospheric mineral aerosols from a 22-year model simulation and observational data." *J. Geophys. Res* (108) D12. DOI: 10.1029/2002JD002821.

Marsay, C. M., P. N. Sedwick, M. S. Dinniman, P. M. Barrett, S. L. Mack, and D. J. McGillicuddy (2014). "Estimating the benthic efflux of dissolved iron on the Ross Sea continental shelf." *Geophys. Res. Lett.* (41), pp. 7576–7583. DOI: 10.1002/2014GL061684.

Martin, J. H., R. M. Gordon, and S. E. Fitzwater (1990). "Iron in Antarctic waters." *Nature* (345), pp. 156–158. DOI: 10.1038/345156a0.

Martin, J. H. and S. Fitzwater (1988). "Iron deficiency limits phytoplankton growth in the north-east Pacific subarctic." *Nature* (331), pp. 341–343. DOI: 10.1038/331341a0.

Moore, J. K. and O. Braucher (2008). "Sedimentary and mineral dust sources of dissolved iron to the world ocean." *Biogeosciences* (5) 3, pp. 631–656. DOI: 10.5194/bg-5-631-2008.

Moore, J. K., S. C. Doney, and K. Lindsay (2004). "Upper ocean ecosystem dynamics and iron cycling in a global three-dimensional model." *Global Biogeochem. Cy.* (18) GB4028. DOI: 10.1029/2004GB002220.

Moore, J. K., S. C. Doney, D. M. Glover, and I. Y. Fung (2002). "Iron cycling and nutrient-limitation patterns in surface waters of the World Ocean." *Deep-Sea Res. Pt. II* (49) 1, pp. 463–507. DOI: 10.1016/S0967-0645(01)00109-6.

Pacanowski, R. C. and S. G. H. Philander (1981). "Parameterization of vertical mixing in numerical models of tropical oceans." *J. Phys. Oceanogr.* (11) 11, pp. 1443–1451. DOI: 10.1175/1520-0485(1981)011<1443:POVMIN>2.0.CO;2.

Parekh, P., M. J. Follows, and E. A. Boyle (2005). "Decoupling of iron and phosphate in the global ocean." *Global Biogeochem. Cy.* (19) GB2020. DOI: 10.1029/2004GB002280.

Pollard, R. T., I. Salter, R. J. Sanders, M. I. Lucas, C. M. Moore, R. A. Mills, P. J. Statham, J. T. Allen, A. R. Baker, D. C. E. Bakker, M. A. Charette, S. Fielding, G. R. Fone, M. French, A. E. Hickman, R. J. Holland, J. A. Hughes, T. D. Jickells, R. S. Lampitt, P. J. Morris, F. H. Nedelec, M. Nielsdottir, H. Planquette, E. E. Popova, A. J. Poulton, J. F. Read, S. Seeyave, T. Smith, M. Stichcombe, S. Taylor, S. Thomalla, H. J. Venables, R. Williamson, and M. V. Zubkov (2009). "Southern Ocean deep-water carbon export enhanced by natural iron fertilization." *Nature* (457) 7229, pp. 577–580. DOI: 10.1038/nature07716.

Prospero, J. M., M. Uematsu, and D. L. Savoie (1989). *Chemical Oceanography*. Vol. 10. Academic Press, pp. 187–218. ISBN: 0-12-588610-1.

Radic, A., F. Lacan, and J. W. Murray (2011). "Iron isotopes in the seawater of the equatorial Pacific Ocean: new constraints for the oceanic iron cycle." *Earth Planet. Sc. Lett.* (306) 1, pp. 1–10. DOI: 10.1016/j.epsl.2011.03.015.

Sarthou, G., K. R. Timmermans, S. Blain, and P. Tréguer (2005). "Growth physiology and fate of diatoms in the ocean: a review." *J. Sea Res.* (53) 1, pp. 25–42. DOI: 10.1016/j.seares.2004.01.007.

Schourup-Kristensen, V., J. Hauck, D. A. Wolf-Gladrow, and C. Völker (2014a). "Vertical supply of iron to the mixed layer of the Southern Ocean: The ocean model effect." *submitted*.

Schourup-Kristensen, V., D. Sidorenko, D. A. Wolf-Gladrow, and C. Völker (2014b). "A skill assessment of the biogeochemical model REcoM2 coupled to the Finite Element Sea-Ice Ocean Model (FESOM 1.3)." *Geosci. Model Dev.* (7) 6, pp. 2769–2802. DOI: 10.5194/gmd-7-2769-2014.

Soppa, M. A., T. Hirata, B. Silva, T. Dinter, I. Peeken, S. Wiegmann, and A. Bracher (2014). "Global Retrieval of Diatom Abundance Based on Phytoplankton Pigments and Satellite Data." *Remote Sens.* (6) 10, pp. 10089–10106. DOI: 10.3390/rs61010089.

Sunda, W. G. and S. A. Huntsman (1995). "Iron uptake and growth limitation in oceanic and coastal phytoplankton." *Mar. Chem.* (50) 1, pp. 189–206. DOI: 10.1016/0304-4203(95)00035-P.

Tagliabue, A., L. Bopp, and O. Aumont (2009). "Evaluating the importance of atmospheric and sedimentary iron sources to Southern Ocean biogeochemistry." *Geophys. Res. Lett.* (36) L13601. DOI: 10.1029/2009GL038914.

Tagliabue, A., T. Mtshali, O. Aumont, A. R. Bowie, M. B. Klunder, A. N. Roychoudhury, and S. Swart (2012). "A global compilation of dissolved iron measurements: focus on distributions and processes in the Southern Ocean." *Biogeosciences* (9) 6, pp. 1–17. DOI: 10.5194/bg-9-2333-2012.

Takeda, S. (1998). "Influence of iron availability on nutrient consumption ratio of diatoms in oceanic waters." *Nature* (393) 6687, pp. 774–777. DOI: 10.1038/31674.

Timmermann, R., A. M. Le Brocq, T. J. Deen, E. W. Domack, P. Dutrieux, B. Galton-Fenzi, H. H. Hellmer, A. Humbert, D. Jansen, A. Jenkins, A. Lambrecht, K. Makinson, F. Niederjasper, F.-O. Nitsche, O. A. N?st, L. H. Smedsrud, and W. Smith (2010). *Antarctic ice sheet topography, cavity geometry, and global bathymetry (RTopo 1.0.5-beta)*. DOI: 10.1594/PANGAEA.741917.

Vogt, M., T. Hashioka, M. R. Payne, E. T. Buitenhuis, C. L. Quéré, S. Alvain, M. N. Aita, L. Bopp, S. C. Doney, T. Hirata, I. Lima, S. Sailley, and Y. Yamanaka (2013). "The distribution, dominance patterns and ecological niches of plankton functional types in Dynamic Green Ocean Models and satellite estimates." *Biogeosciences Discuss.* (10) 11, pp. 17193–17247. DOI: 10.5194/bgd-10-17193-2013.

Wadley, M. R., T. D. Jickells, and K. J. Heywood (2014). "The role of iron sources and transport for Southern Ocean productivity." *Deep Sea Res. Pt I* (87), pp. 82–94. DOI: DOI:10.1016/j.dsr.2014.02.003.

Wang, Q., S. Danilov, D. Sidorenko, R. Timmermann, C. Wekerle, X. Wang, T. Jung, and J. Schröter (2014a). "The Finite Element Sea Ice-Ocean Model (FESOM) v.1.4: formulation of an ocean general circulation model." *Geosci. Model Dev.* (7) 2, pp. 663–693. DOI: 10.5194/gmd-7-663-2014.

Wang, S., D. Bailey, K. Lindsay, J. K. Moore, and M. Holland (2014b). "Impact of sea ice on the marine iron cycle and phytoplankton productivity." *Biogeosciences* (11) 17, pp. 4713–4731. DOI: 10.5194/bg-11-4713-2014.

Part III

SYNTHESIS

8 DISCUSSION

Iron limitation of the Southern Ocean has been recognized as one of the main reasons for its High Nutrient Low Chlorophyll (HNLC) status since the early 1990'ies (e.g. Martin, 1990; Martin et al., 1990). Since then, substantial effort has gone into assessing the role of iron in the Southern Ocean. In the current thesis, the role of the iron supply from the sediments and from the deeper reservoirs has been assessed. It has in particular been explored how the representation of the Southern Ocean iron supply in large scale Ocean General Circulation Biogeochemical Models (OGCBMs) affect the prediction of the net primary and export production (NPP and EP) in these models, and what these results teach us about the the iron supply in nature.

Publication I documents the results of the coupling between the biogeochemical model REcoM2 to the Finite Element Sea-ice Ocean Model (FESOM). The modeled global biogeochemical surface fields capture the large scale features, with low production in the subtropical gyres and higher around the Equator and in the temperate regions. The model results are comparable to those of other non-eddy resolving OGCBMs, with the spatial distribution of the chlorophyll *a* and NPP being especially good. In the Southern Ocean, the NPP and EP fits well with satellite-based estimates and the results of other OGCBMs. Production here is strongly iron limited and dominated by nanophytoplankton.

Publication II and III, address the role of the iron input from the sediments and the vertical iron supply across the base of the mixed layer in the Southern Ocean. The ocean component of OGCBMs are known to have a large effect on the results for NPP and EP, especially in the Southern Ocean (e.g. Doney et al., 2004; Najjar et al., 2007). Publication II investigates how the vertical iron fluxes across the mixed layer, the NPP and the EP, differ between two model runs which only differ in the choice of Ocean General Circulation Model (OGCM) used; one was run with the Massachusetts Institute of Technology general circulation model (MITgcm) and one with FESOM. The study showed that the OGCM has a large impact on the vertical iron fluxes and the NPP. In MITgcm the total vertical flux is four times higher than in FESOM and the dominating pathway is entrainment, while it is diffusion in FESOM. The differences in the ocean circulation and mixing induce differences in the total NPP and the fraction of the NPP that is exported to the deep water. The study highlights the importance of assessing the the skill of the OGCM, and indicates that the vertical iron fluxes across the base of the mixed layer could play a large role regarding the differences in NPP and EP that has previously been established (e.g. Doney et al., 2004; Najjar et al., 2007).

The Southern Ocean is located far from major dust sources, and the sediment source of iron is thus thought to supply the bulk of new iron (e.g. Tagliabue et al., 2009a; Lancelot et al., 2009). The sediment source is, however, poorly constrained by measurements and thus varies widely between models, both in strength and in parameterization. Publication III presents a sensitivity study in which the sediment source of iron was varied significantly along with the scavenging rate. It shows that while the total NPP and the mean vertical iron profile can be recreated with very

Table 8.1: Overview of the model runs presented in this thesis, stating the differences between them. Each run is described in the associated publication.

PUBLICATION	RUN NAME	SEDIMENTARY FE:C	FESOM VERSION
I	Pub. I	0.01	1.3
II	Pub. II	0.01	1.3
III	Pub. III, CTRL	0.01	1.4
III	Pub. III, SED1.3	0.1	1.4
III	Pub. III, SED2.3	0.68	1.4

different strengths of the sediment source of iron, it also changes the spatial distribution of the NPP. The amount of NPP from diatoms and the resulting vertical export of opal to the deep ocean is likewise sensitive to the changed inputs in the iron supply.

In the following, the relative importance of the different iron sources in the Southern Ocean will first be discussed, and it will be debated how these sources may change in the a future ocean and what challenges modelers need to consider to take these changes into consideration. Secondly, advantages and typical applications of the new FESOM-REcoM2 are discussed, along with caveats and limitations. Finally, perspectives for future research areas and remaining open questions will be presented here.

8.1 IRON IN THE SOUTHERN OCEAN

8.1.1 *Current iron sources*

The model runs considered here are listed in Table (8.1), along with the factors that differ between them. The runs presented in publication I and II are identical, while the CTRL run in publication III use an updated version of FESOM. In the runs SED1.3 and SED2.3 from publication III, the sediment source was increased as compared to the other runs. Here, focus will mainly be on SED1.3 when the effect of the increased sediment source is discussed.

One strength of large scale OGCBMs is that they make it possible to upscale various processes to larger areas, such as the Southern Ocean. In the following, focus will be on the iron supply to the surface water of the Southern Ocean. Comparing the input of iron from the sediments (Pub. III) and the vertical flux across the base of the mixed layer (Pub. II) is, however, not straightforward, as the fluxes refer to different volumes of water. The vertical iron fluxes represent supply into the surface mixed layer, while the sediment derived input is calculated into the upper 500 m of the water column (Fig. 8.1). This makes the analysis somewhat inconsistent, but still gives an impression of the relative importance of the difference sources.

Total iron input to the Southern Ocean

In the model, the total input of iron to the surface mixed layer is approximately 14.5×10^8 mol Fe yr^{-1}, when counting the input from dust (0.5×10^8 mol Fe yr^{-1}, Pub. I, II and III), the vertical flux (9×10^8 mol Fe yr^{-1}, Pub. II) and the sedimentary input (5×10^8 mol Fe yr^{-1}, SED1.3, Pub. III) and while assuming that the iron added

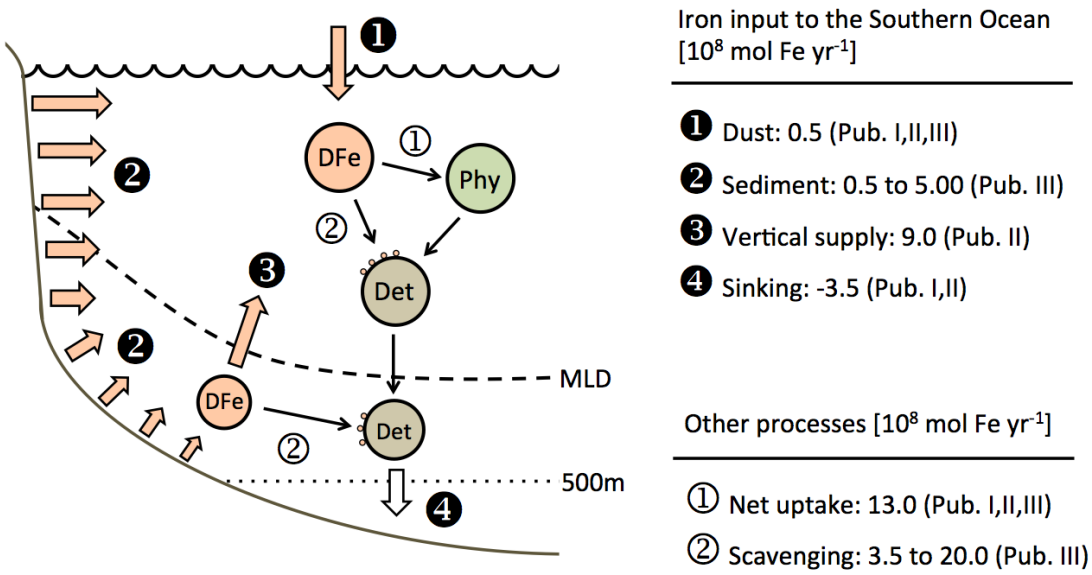

Figure 8.1: Conceptual plot of the iron fluxes in and out of the Southern Ocean surface water south of 50°S in FESOM-REcoM2. The input from the sediments and the scavenging is calculated for the upper 500 m of the water column. The uptake by phytoplankton is for the vertically integrated NPP. The dust input is identical in Pub. I, II and III. The numbers for the sediment source is from publication III, (CTRL and SED1.3), Table (7.2). The numbers for the vertical supply to the mixed layer is from publication II, Fig. 6.3, and counts entrainment, upwelling, horizontal advection and vertical eddy diffusion. Notice that dust is supplied to the surface ocean, the sediment flux takes place at the bottom at all depths, and the vertical fluxes are calculated across the base of the mixed layer. The plot gives a simplified view of the iron fluxes in the surface water of the Southern Ocean, and does not entail all fluxes represented in the model.

to the upper 500 m of the water column from the sediments is roughly equal to that added to the mixed layer (Fig. 8.1). For a total modeled NPP of 3.1 Pg C yr^{-1} in the Southern Ocean (Pub. I, II, III), the iron uptake is 13 $\times$ 10^8 mol Fe yr^{-1}. This number is very close to the 13.5 $\times$ 10^8 mol Fe yr^{-1}, which Boyd et al. (2012) argued biological production utilize in the Southern Ocean south of 50°S. The average iron input can thus on average sustain biological production in the Southern Ocean. Iron is, however, removed from the surface water through sinking of organic matter and through scavenging. The former accounts for a removal of 3.5 $\times$ 10^8 mol Fe yr^{-1} (Fig. 8.1), and the remainder of the iron in organic matter is thus remineralized above that depth. As scavenging of iron onto particles in the water account for a removal of 3.5 to 20 $\times$ 10^8 mol Fe yr^{-1} (CTRL and SED1.3, Pub. III), the remineralized iron also plays a role for production in the Southern Ocean.

The important role of the sediment source in supplying iron to the Southern Ocean is well established (e.g. Pollard et al., 2009; de Jong et al., 2012; Wadley et al., 2014) and confirmed in publication III. While the Southern Ocean NPP is very reasonable in publication I, II and the CTRL run of publication III, the surface iron concentrations were relatively low compared to measurements (e.g. Klunder et al., 2011; Grand et al., 2015) and the phytoplankton blooms downstream of islands such as South Georgia (e.g. Borrione and Schlitzer, 2013) and the Kerguelen Plateau (e.g. Blain et al., 2001) were missing, indicating that the sediment source of iron was too small. Increasing the strength of the sediment source tenfold from the CTRL run to the SED1.3 run, the total input to the upper 500 m of the water coumn of the Southern Ocean increased from 0.5 $\times$ 10^8 mol Fe yr^{-1} to 5 $\times$ 10^8 mol Fe yr^{-1} (Pub. III and Fig. 8.1). Both of these numbers are smaller than the sum of the vertical iron supply to the surface mixed layer of 9 $\times$ 10^8 mol Fe yr^{-1} (Pub. II and Fig. 8.1). As explained above, the numbers for the two sources do not refer to exactly the same water volume (Fig. 8.1), and a fraction of the input from the sediment source is most likely released below the mixed layer and transported upwards by the physical transport mechanisms, thereby being counted twice. The difference in the iron input from the sediments and the vertical flux is nevertheless large enough to show that the vertical iron supply is significant.

The sediment source of iron

One problem that commonly arises when a sediment source of iron is added to a large scale OGCBM is that the coastal resolution is relatively coarse compared to the width of the shelves in some areas, for example around Antarctica and along the west coast of the American continent. Despite of an increased resolution around the coast (40 km), the grid used in this thesis is still relatively coarse, with the consequence that the sediment source of iron is underestimated in some coastal areas. Moore and Braucher (2008) solved this by scaling the iron input in coastal grid cells by the fraction of the cell that would be on the shelf in reality, while a reasonable solution in FESOM would be to increase the coastal resolution, at least in studies focussing or relying especially on the sedimentary input of iron.

It is well established that recurrent phytoplankton blooms appear downstream of South Georgia and the Kerguelen Plateau in the Southern Ocean (Fig. 8.2a and e). In publication III it was argued that the diatom abundance and the vertical export of biogenic opal ought to be used to evaluate the skill of OGCBMs, while another approach would be to assess whether the island blooms are adequately captured with a given strength of the sedimentary iron source. In the CTRL run of publication III both the

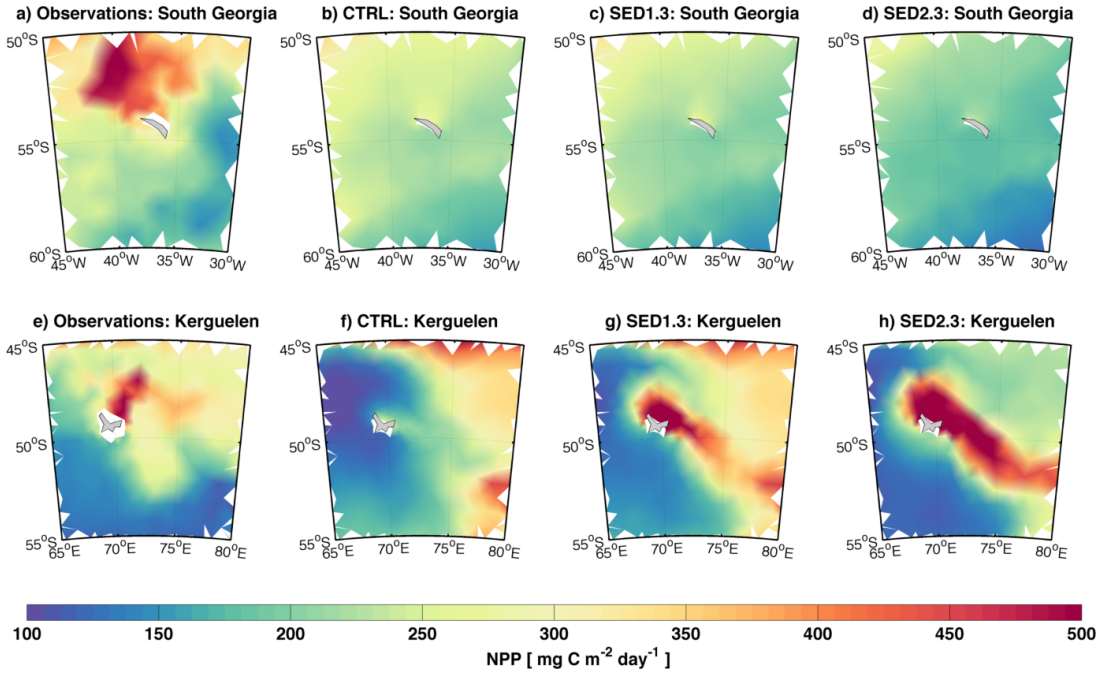

Figure 8.2: Mean NPP around South Georgia (a – d) and around Kerguelen Island (e - f), plotted using results from model run CTRL (b,f), SED1.3 (c,g) and SED2.3 (d,h) in publication III, along with satellite-based observations (a + d), (SeaWIFS and Behrenfeld and Falkowski, 1997)

South Georgia and Kerguelen blooms are missing (Fig.8.2b and f). While the modeled Kerguelen bloom increases with the increased strength of the sediment flux in run SED1.3 and 2.3 (Fig. 8.2f to h), the south Georgia bloom is not improved (Fig. 8.2b to d). North of the Kerguelen, the strength of the sediment source, combined with the size and depth of the shallow plateau fit together to produce a reasonable output, especially in SED1.3. For South Georgia, the missing bloom can be explained by the fact that the grid cells around South Georgia are all located at depths deeper than 1000 m (Fig. 7.1, Pub. III). At this depth only little iron is released (Fig 7.2, Pub. III), and a bloom fueled by the iron released from the sediments does not evolve. This illustrates the importance of developing the coastal grid suitable for the aim of the study, both regarding depth and resolution.

Vertical iron supply

The sedimentary iron source (Pub. III) and the vertical iron supply (Pub. II) are not entirely separable, but the fact that the vertical flux dominates the supply even when compared to model run SED1.3, where the sediment source is relatively large, indicates that the vertical iron supply is on average the most important in FESOM. Especially the input from entrainment is interesting as it has previously been shown to dominate the supply from below (Tagliabue et al., 2014) and to sustain the summer bloom in some remote parts of the Southern Ocean (Carranza and Gille, 2015). The magnitude of the modeled entrainment does, however, depend heavily on the ocean circulation and mixing as is demonstrated by the fact that the entrainment driven input of iron, which at 20.2×10^8 mol Fe yr^{-1}, is eight times higher in MITgcm-REcoM2 than in FESOM-REcoM2 (Pub. II). As the mean seasonal amplitude of the MLD is too small and the iron concentration at the base of the mixed layer low in FESOM as

compared to observations (Pub. II), the influx from entrainment is most likely underestimated in this model. In MITgcm, the mean seasonal amplitude is, on the other hand, too large, leading to the iron transport through entrainment probably being too high in this model. That the real entrainment should lie between the results from our study fits well with the observation-based result of 9.5×10^8 mol Fe yr^{-1} suggested by Tagliabue et al. (2014).

Due to the complexity of the processes controlling marine NPP, it is impossible to exactly pin-point which processes that are responsible for the differences in the two model runs presented in publication II. Since this study was carried out, REcoM2 has been coupled to an updated version of FESOM (Pub. III and App. A), which can help to give a better understanding of the effect of the different modeled processes. In the updated version, the mean seasonal cycle of FESOM's mixed layer depth is deeper and closer to both the observations and the MLD in MITgcm than before (Fig. 8.3). The entrainment of iron is also positive across the Southern Ocean, as is the case in MITgcm-REcoM2 (Fig. 6.8). But despite of these changes, all of the vertical iron fluxes are virtually identical in FESOM 1.3 (Pub. II, Fig. 6.3) and 1.4 (Fig. 8.3), and are thus still low compared to MITgcm (Pub. II). This shows, that even though the mixed layer indeed plays a role, especially for the entrainment and for the access to the deeper iron inventories, the iron supply across the base of the mixed layer is to a higher degree dependent on the supply of iron to the base of the mixed layer. The strength of the upwelling in the Southern Ocean, thus largely controls the iron fluxes into the surface mixed layer by delivering iron to the permanent thermocline, below which the MLD does not reach. The upwelling of iron to the base of the mixed layer is controlled by the iron concentration in the deep water and by the vertical velocity of the water. As only the circulation component differs between the two model runs in publication II, it is tempting to conclude that the vertical velocity, and thereby the different strengths of the meridional overturning circulation are responsible for the differences. But since the deep iron concentration is dependent on a number of processes, such as the sinking and remineralization of organic matter, which again are affected by the ocean circulation in multiple ways, this view is too simplified, though it is likely that the strength of the overturning circulation is a large part of the explanation for the differences in the vertical iron fluxes between the models.

Other iron sources

As the deep water iron concentrations are important for sustaining the vertical iron fluxes, the deeper iron sources could play an important role for the biological production in the Southern Ocean. These sources include the deeper sediment input, input from hydrothermal vents and the deep inflow of iron rich water to the deep Southern Ocean in the North Atlantic and Upper Circumpolar Deep Water. In models, it is thus both the implementation of the external sources into the code as well as a correct representation of the meridional overturning circulation and the mixed layer depth that is crucial for the amount of iron available for transport into the mixed layer from below. In the current study, the input from hydrothermal vents has not been considered, as they are most likely relatively unimportant on the timescale of the model runs presented here. On longer time scales they will, however, have noticeable effects, especially in the Pacific sector of the Southern Ocean where iron limitation is strongest (Tagliabue et al., 2010).

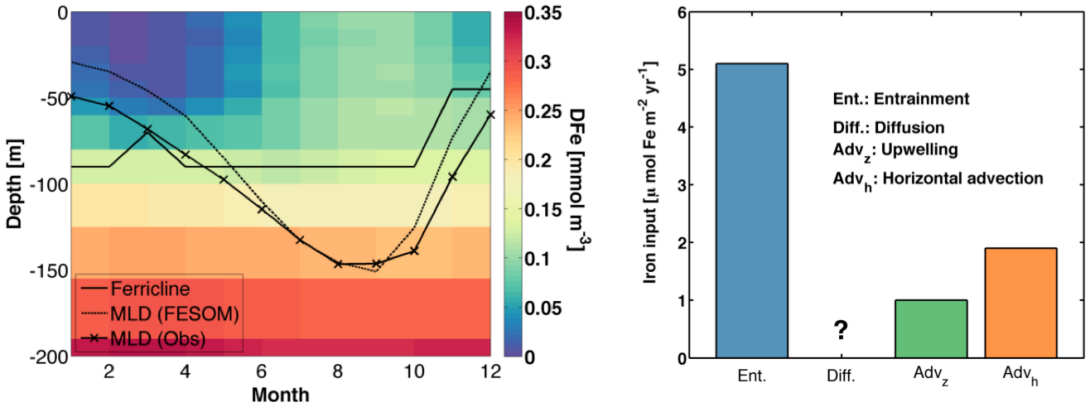

Figure 8.3: Plots illustrating the vertical iron supply, here plotted for the CTRL run, Pub. III. The CTRL run is similar to the run in Pub. II, except that FESOM has been updated to version 1.4. Left panel: The seasonal cycle of the mean vertical iron profile of the Southern Ocean south of 50°S, the mixed layer depth in FESOM and the mixed layer depth from observations (Sallée et al., 2010). Right panel: The mean iron input to the Southern Ocean south of 50°S through the different vertical transport mechanisms. Diffusion is left out as it was not calculated online during this model run.

8.1.2 *Iron supply in a changing climate*

Martin (1990) was the first to suggest that aeolian iron deposition to the Southern Ocean plays a crucial role in the global climate. The argument behind his "iron hypothesis" is that the large unused pool of macronutrients in the mixed layer of the Southern Ocean can be utilized for biological production when the aeolian deposition of iron is increased. This increased production leads to an increased drawdown of CO_2 from the atmosphere to the ocean, which reduces the atmospheric greenhouse effect and hence lowers the atmospheric temperature. Later studies have proven the correlation between aeolian dust deposition and changes in atmospheric CO_2 (e.g. Martínez-Garcia et al., 2011; Martínez-García et al., 2014) but it has also been argued that while dust indeed plays a role in the glacial/interglacial cycles, the changes in dust input are not large enough to be the controlling factor (e.g. Watson et al., 2000).

As the climate is currently changing more rapidly than ever before, the iron hypothesis becomes interesting again, as an increased temperature is likely to change the iron supply to the Southern Ocean in several ways; increased temperature will change the stratification and thereby the MLD (Rhein et al., 2013), changes in biological production may change the amount of iron released from the sediments (Elrod et al., 2004), changed circulation patterns will impact the transport of iron released by the sediments (Misumi et al., 2014) and a higher temperature will change the supply of iron from dust (Maher et al., 2010). These changes will affect biological production in the Southern Ocean and thereby also the feedbacks regarding the global carbon cycle and the climate (Boyd and Ellwood, 2010).

Ocean circulation and mixing

One consequence of a warmer ocean is that the mixed layer becomes shallower and the stratification stronger on a global scale, leading to decreased vertical mixing of

nutrients to the surface water along with increased light in the surface mixed layer (Rhein et al., 2013). The decreased nutrient supply leads to decreased NPP when averaged globally (e.g. Steinacher et al., 2010; Bopp et al., 2013). In the Southern Ocean, model studies, however, show that shallower mixed layers alleviate light limitation while nutrient supply is sustained by the large seasonal amplitude in the MLD, leading to a net increase in the NPP towards the end of the century (e.g. Bopp et al., 2001; Steinacher et al., 2010; Bopp et al., 2013; Misumi et al., 2014). The biogeochemical responses to 21st century forcing do, however, vary between models, especially in the Southern Ocean (Steinacher et al., 2010; Bopp et al., 2013).

One reason for the relatively deep mixed layers in the Southern Ocean are the subpolar westerlies, which have their maximum between the subtropical front and the polar front. The westerlies are expected to increase and move polewards over the coming century due to an increase in the index of the so-called Southern Annular Mode ((SAM) Sen Gupta et al., 2009; Zheng et al., 2013). This phenomenon acts against the strengthening of the stratification that warmer temperatures bring, and thus adds to the complexity of the future ocean circulation and mixing.

As shown in publication II, the ocean circulation and mixing differs greatly between OGCMs, even under similar prescribed forcing, with large effects on the modeled NPP. The response of OGCMs to the counteracting effects of the warming signal and the SAM-signal is thus bound to differ (e.g. Hauck et al., 2015), especially when forcing additionally differs between earth system models. Knowing the biases of the modeled ocean circulation and mixing under current forcing is thus critical for understanding it's response to future changes, though a large uncertainty is further introduced by the atmospheric component of the models.

Sedimentary supply

The strength of the iron release from the sediments depends on the redox state within the sediments, and thereby the amount of organic matter deposited on the sea bed (e.g. Elrod et al., 2004). As the rate of NPP is expected to increase over the next century in the Southern Ocean (e.g. Steinacher et al., 2010; Bopp et al., 2013), the supply of organic matter to the sediments will likely also increase, thereby increasing the release of iron from the sediments. Whether the additional iron supply from the sediments will have an effect on the biological production in the open ocean depends on the strength and location of the horizontal advection responsible for transport of the iron. As the subtropical gyres are currently expanding (Polovina et al., 2008), they will enter the Southern Ocean over the coming century, thereby transporting iron-rich water further towards the south (Misumi et al., 2014). The southwards shift of the subtropical gyres also intensifies the coastal currents, something that could increase the effect of the sedimentary supply of iron as they increase the off-shore transport from the shelfs. In large scale OGCMs the coastal currents are, however, not necessarily adequately captured. In these models, resolution thus impedes the representation of the sediment source two-fold; by not resolving the shelves from which the major part of the sediment derived iron is released, and also by not representing the strong surface currents necessary for advection adequately. Here, FESOM has the advantage of the unstructured grid that makes it possible to resolve the shelves in future studies regarding the sediment derived iron input to the ocean.

Other iron sources

Dependent on the changes in land use and climate, the dust supply is likely to

increase in the future (e.g. Maher et al., 2010). Large parts of the Southern Ocean are, however, located far from land sources, and the input of iron from the sediments is still likely to dominate the input in spite of enhanced aeolian iron inputs (Tagliabue et al., 2009a), especially if the sediment source also increases.

As sea-ice forms, it incorporates and up-concentrates iron from the underlying sea water, while iron supplied by dust is also stored in the ice (van der Merwe et al., 2011). The sea-ice mainly acts to change the location and timing of the iron-input to the water, and its primary effect is to change the phytoplankton composition (e.g. Wang et al., 2014b). Recently, the calving of ice bergs has been shown to increase in the Southern Ocean (Mouginot et al., 2014). Icebergs transport iron to relatively remote areas of the Southern Ocean, releasing iron as they melt (Raiswell et al., 2008; Lin et al., 2011). While the iron input from ice is most likely small compared to other iron sources (Table 1.1) it is likely to directly impact biological production locally, and can potentially be investigated with FESOM-REcoM2 as will be discussed in section (8.4.1).

Irradiance and temperature

Future changes in radiation and temperature do not just change the iron sources directly, but also the conversion of Fe(III) to the more bioavailable Fe(II) (Fig. 1.5). Using an OGCBM, Tagliabue et al. (2009b) showed that including the irradiance in the modeled iron cycle increases the amount of bioavailable iron by up to 53 % in the Southern Ocean, while including the effect of temperature on the iron speciation decreased the amount of available iron slightly. Commonly used OGCBMs do take the changed availability of light for phytoplankton growth into account (e.g. Steinacher et al., 2010), but the direct effect on the iron cycle is so far only considered in a single model (Tagliabue et al., 2009b; Tagliabue and Völker, 2011). This direct effect of irradiance on the bioavailable iron should thus be tested in a larger amount of models and in runs covering the next century in order to gain a better understanding of the coming changes in the Southern Ocean. As studies already suggest that the iron concentration in the Southern Ocean surface water will increase in the coming century (e.g. Misumi et al., 2014), this effect could either be enhanced or decreased as changes in the MLD also affects the average irradiation in the surface mixed layer and thereby the iron availability.

8.2 GLOBAL IRON SUPPLY

As FESOM is a global model, the different iron inputs must result in an adequate representation of the biogeochemical fields for the global ocean. During the initial coupling of REcoM2 to FESOM, iron was not released to the water from the sediments. Test runs did, however, indicate that large parts of the Arctic Ocean, which in reality receives iron from the broad shelves among the Siberian coastline (e.g. Klunder et al., 2012; Hioki et al., 2014), became iron limited in the absence of the sediment source. A relatively weak sediment source was consequently added. In the Pacific Ocean, the iron limitation is, however, strong, both in publication I and when FESOM was updated (App. A, Fig. A.8). One explanation for this is the very narrow coastal shelf along the west coast of South and North America, which are not captured in the current grid, thus diminishing the sediment source in the region. Another explanation is that scavenging removes iron from deep water, thereby reducing the Fe:N

ratio in the upwelled water. Based on measurements of iron's isotopic composition, it has recently been argued that the sediment input from Papua New Guinea is transported across the Pacific Ocean and sustains biological production in the eastern Pacific (Radic et al., 2011). Increasing the sediment source tenfold in publication III does increase the surface iron concentrations in the western Pacific Ocean as iron is brought eastwards from the coast of Japan and New Zealand, again showing that an increased strength of the sediment source improves the skill of REcoM2. Whether the sedimentary iron input from Papua New Guinea plays a role in supplying iron to the surface water of the modeled Pacific Ocean is, however, an open question.

8.3 TWO DIFFERENT OCEAN MODELS

Coupling a biogeochemical model to a new ocean model requires a significant amount of effort and time, both regarding the actual work of the coupling, but even more so for the process of tuning the coupled model to obtain reasonable results when compared to observations or satellite-based estimates of the state variables. The current thesis presents the results of such an effort, with the coupling of the biogeochemical model REcoM2 to the Finite Element Sea-ice Ocean Model (FESOM). The question is, however: When is it reasonable to choose FESOM-REcoM2 for a study, considering that REcoM2 already runs coupled to the MITgcm in a successful set-up?

FESOM's main strength is the capability to highly resolve certain areas with seamless transition to areas of lower resolution. This feature has not been fully utilized in the current study, but should be further investigated in the future. As a higher resolution is likely to improve the skill of the ocean model, it is probable that it will also affect the biogeochemical results (e.g. Doney et al., 2004; Najjar et al., 2007; Sinha et al., 2010). The effect of resolution was investigated by McKiver et al. (2014) who showed that a higher resolution especially improved the distribution of surface chlorophyll *a* due to a better description of the vertical velocity and MLD in the OGCM.

While it is in theory easy to change the mesh in FESOM, it does in reality require a lot of work to first create a mesh and then tune it for the ocean. Further, when running the coupled FESOM-REcoM2 model it may be necessary to tune the biogeochemical model again. It is therefore relevant to look for tested configurations of FESOM before embarking on a new study with FESOM-REcoM2. An additional advantage of using a tested configuration is that knowledge about the ocean state exists, and as shown in publication II, the ocean circulation and mixing is key for successful biogeochemical modeling. For FESOM, several tuned configurations with specialized grids exist. One example is a mesh in which the resolution is scaled towards eddy activity, which would for instance make it possible to examine the role of mesoscale eddy transport of nutrients into the mixed layer. Other possibilities include using a high resolution Arctic Ocean or a mesh where the equatorial region is highly resolved. Another aspect to keep in mind when using a grid with local high resolution is its increased computational demand. This is due to the larger amount of nodes that such a mesh has, and to the smaller time step that is necessary in the whole model domain. Higher resolution thus increases the runtime of the model.

The complexity of FESOM's grid is an advantage for resolving complicated topography, but it demands more of the people that process the output in terms of mathematical and programming abilities. The complexity of the grid thus also increases the risk of simple mathematical errors during processing.

The MITgcm-setup used with REcoM2 is in contrast to FESOM relatively simple to work with as calculations are performed on a regular grid. The MITgcm also comes with extensive experience and support in forms of a very large user group with associated output in forms of papers and knowledge of the model's behavior under different circumstances. The drawback of this model is that REcoM2 runs on a single grid of relatively coarse resolution that is not easily changed.

When choosing which model to use for a certain research question it thus makes sense to look at the question at hand; does it require a high resolution in a certain area, does a grid exist for this area for FESOM and is the length of the planned model run reasonable compared to the required runtime of FESOM? Otherwise, it is most likely a good idea to choose to work with MITgcm-REcoM2.

8.4 FUTURE DIRECTIONS FOR FESOM-RECOM2

8.4.1 *Iron sources*

In publication III, the model's sensitivity to the strength of the sediment source was investigated, but to learn more about its effect, a mesh with higher resolution on the continental shelves would be necessary. Higher coastal resolution would make it possible to examine the role of the sediment source in generating the increased NPP downstream of islands as well as the distance travelled by the iron from the coast.

Resolving the area of the ACC would make it possible to look into the frontal role for the iron distribution, and whether frontal activity increases the iron supply by vertical mixing as argued by Sokolov and Rintoul (2007). If resolution permits, the role of the horizontal eddy transport could also be investigated.

Another possibility is to add iron to the surface water from melting icebergs (e.g. Raiswell et al., 2008; Lancelot et al., 2009). An iceberg transport model has been coupled to FESOM (Rackow, 2011; Wesche et al., 2013) and ongoing work adds a realistic amount of calved icebergs to the Southern Ocean. As the melt rate is calculated in the iceberg model, iron could be added to this melt water in realistic concentrations and thereby be added to the water. As the iron supply from icebergs is small relative to the other source (E.g. Table 1.1), it most likely has a local effect, and such a study would be more reasonable if performed using a relatively high spatial resolution, as is possible in FESOM.

8.4.2 *The Arctic Ocean*

The current global version of FESOM (Wang et al., 2014a) has been used for a number of studies regarding the Arctic Ocean (e.g. Wang et al., 2012; Wekerle et al., 2013). Due to the rapidly decreasing sea-ice extent in the Arctic Ocean, with associated changes in mixed layer depth and light availability, NPP is also likely to change drastically in the area. While contemporary model runs show that the NPP predicted by the models agrees relatively well with the satellite-based observations, the controlling limitation factors of light and nutrient concentrations differ widely between models (Popova et al., 2012). The modeled biogeochemistry of the Arctic Ocean also is thus also sensitive to the performance of the ocean model. As a consequence, the models respond differently to the retreat of sea-ice over the coming century, with

the Arctic NPP increasing in some models while decreasing in others (Vancoppenolle et al., 2013).

As grids with a high resolution in the Arctic Ocean and associated tuned ocean states exist for FESOM, it would be logical to investigate how FESOM-REcoM2 describes the biogeochemistry in the Arctic. An important factor in the future Arctic Ocean is the representation of sea-ice and associated biogeochemistry (e.g. Vancoppenolle et al., 2013). FESOM does a good job in modeling the seasonal and interannual extent of Arctic sea-ice (Wekerle et al., 2013), but the biogeochemistry within the sea-ice is not incorporated into the REcoM2 code, and the light penetration through the sea-ice is crudely parameterized. The impact of these two factors would be interesting to further investigate with FESOM-REcoM2.

8.4.3 *Climate runs*

The model runs in the present thesis have all been performed with the prescribed CORE-I and II forcing (Large and Yeager, 2004; Large and Yeager, 2009), which is a good choice here as it reduces the complexity of the model set-up and it makes hind cast experiments and thereby skill assessment against existing observational data possible.

Currently, it is not possible to perform runs covering future climate changes with FESOM-REcoM2, as the interannually varying CORE-II forcing data set ends in 2008 (Large and Yeager, 2009). For climate runs over climate relevant time scales, different forcing must thus be considered. One option is to use the output from an atmospheric model and use it as prescribed forcing. This method was used by Hauck et al. (2015) to force the MITgcm-REcoM2 to the end of the 21st century. Another option is to use an interactive atmospheric model component. For FESOM this has become a realistic possibility after its coupling to the atmospheric model ECHAM6 (Sidorenko et al., 2015; Rackow et al., 2014). In a coupled model, ocean and atmosphere are fully interactive and inconsistencies from prescribed forcing are thus avoided. The free interaction, however, adds to the degrees of freedom, with the consequence that larger errors between the modeled and observed fields may occur as the model develops its own equilibrium state. Running FESOM-REcoM2 with an interactive atmosphere is interesting in relation to the current work, as it could shed light on the effect of future changes in the MLD on the vertical iron supply to the Southern Ocean, and its impact on EP and NPP. For studies regarding the Arctic Ocean, it would further be interesting to see how the high resolution of FESOM-REcoM2 would change the model's reaction to future climate change. But, as highlighted in publication II of the current thesis, such studies will, not give a definitive answer to the future changes in net primary production, as biogeochemical changes are highly dependent on the ocean model.

When running future scenarios with FESOM-REcoM2, it is necessary to first evaluate the carbon cycle in the model When evaluating the skill of FESOM-REcoM2 in publication I, the carbon cycle was not considered as it was not yet in equilibrium due to the relatively short runtime. A logical next step is thus to assess the skill of the model with respect to Dissolved Inorganic Carbon (DIC), Total Alkalinity (TA), pH and calcium carbonate export as done by Yool et al. (2013). This would open for the opportunity to investigate the atmosphere-ocean flux of CO_2 and the effect of ocean acidification on the phytoplankton communities.

REFERENCES

Behrenfeld, M. J. and P. G. Falkowski (1997). "Photosynthetic rates derived from satellite-based chlorophyll concentration." *Limnol. Oceanogr.* (42) 1, pp. 1–20.

Blain, S., P. Tréguer, S. Belviso, E. Bucciarelli, M. Denis, S. Desabre, M. Fiala, V. Martin Jézéquel, J. Le Fèvre, P. Mayzaud, J.-C. Marty, and S. Razouls (2001). "A biogeochemical study of the island mass effect in the context of the iron hypothesis: Kerguelen Islands, Southern Ocean." *Deep Sea Res. Pt. I* (48) 1, pp. 163–187. DOI: 10.1016/S0967-0637(00)00047-9.

Bopp, L., P. Monfray, O. Aumont, J.-L. Dufresne, H. Le Treut, G. Madec, L. Terray, and J. C. Orr (2001). "Potential impact of climate change on marine export production." *Global Biogeochem. Cy.* (15) 1, pp. 81–99. DOI: 10.1029/1999GB001256.

Bopp, L., L. Resplandy, J. Orr, S. C. Doney, J. P. Dunne, M. Gehlen, P. Halloran, C. Heinze, T. Ilyina, R. Séférian, et al. (2013). "Multiple stressors of ocean ecosystems in the 21st century: projections with CMIP5 models." *Biogeosciences* (10) 10, pp. 6225–6245. DOI: 10.5194/bg-10-6225-2013.

Borrione, I. and R. Schlitzer (2013). "Distribution and recurrence of phytoplankton blooms around South Georgia, Southern Ocean." *Biogeosciences* (10) 1, pp. 217–231. DOI: 10.5194/bg-10-217-2013.

Boyd, P. W., K. R. Arrigo, R. Strzepek, and G. L. Dijken (2012). "Mapping phytoplankton iron utilization: Insights into Southern Ocean supply mechanisms." *J. Geophys. Res.* (117) C06009. DOI: 10.1029/2011JC007726.

Boyd, P. W. and M. J. Ellwood (2010). "The biogeochemical cycle of iron in the ocean." *Nat. Geosci.* (3) 10, pp. 675–682. DOI: 10.1038/ngeo964.

Carranza, M. M. and S. T. Gille (2015). "Southern Ocean wind-driven entrainment enhances satellite chlorophyll-a through the summer." *J. Geophys. Res.* (120), pp. 304–323. DOI: 10.1002/2014JC010203.

De Jong, J., V. Schoemann, D. Lannuzel, P. Croot, H. de Baar, and J.-L. Tison (2012). "Natural iron fertilization of the Atlantic sector of the Southern Ocean by continental shelf sources of the Antarctic Peninsula." *J. Geophys. Res.* (117) G1. DOI: 10.1029/2011JG001679.

Doney, S. C., K. Lindsay, K. Caldeira, J.-M. Campin, H. Drange, J.-C. Dutay, M. Follows, Y. Gao, A. Gnanadesikan, N. Gruber, A. Ishida, F. Joos, G. Madec, E. Maier-Reimer, J. C. Marshall, R. J. Matear, P. Monfray, A. Mouchet, R. Najjar, J. C. Orr, G. K. Plattner, J. L. Sarmiento, R. Schlitzer, R. D. Slater, I. J. Totterdell, M. F. Weirig, Y. Yamanaka, and A. Yool (2004). "Evaluating global ocean carbon models: The importance of realistic physics." *Global Biogeochem. Cy.* (18) GB3017. DOI: 10.1029/2003GB002150.

Elrod, V. A., W. M. Berelson, K. H. Coale, and K. S. Johnson (2004). "The flux of iron from continental shelf sediments: A missing source for global budgets." *Geophys. Res. Lett.* (31) L12307. DOI: 10.1029/2004GL020216.

Grand, M. M., C. I. Measures, M. Hatta, W. T. Hiscock, W. M. Landing, P. L. Morton, C. S. Buck, P. M. Barrett, and J. A. Resing (2015). "Dissolved Fe and Al in the upper 1000 m of the eastern Indian Ocean: a high-resolution transect along 95°E from the Antarctic margin to the Bay of Bengal." *Global Biogeochem. Cy.* DOI: 10.1002/2014GB004920.

Hauck, J., C. Völker, and D. A. Wolf-Gladrow (2015). "A multi-model study on Souther Ocean CO_2 uptake and the role of the biological carbon pump in the 21st century." *submitted to Global Biogeochem. Cy.*

Hioki, N., K. Kuma, Y. Morita, R. Sasayama, A. Ooki, Y. Kondo, H. Obata, J. Nishioka, Y. Yamashita, S. Nishino, T. Kikuchi, and M. Aoyama (2014). "Laterally spreading iron, humic-like dissolved organic matter and nutrients in cold, dense subsurface water of the Arctic Ocean." *Sci. Rep.* (4) 6775. DOI: 10.1038/srep06775.

Klunder, M., P. Laan, R. Middag, H. d. Baar, and K. Bakker (2012). "Dissolved iron in the Arctic Ocean: Important role of hydrothermal sources, shelf input and scavenging removal." *J. Geophys. Res.* (117) C04014. DOI: 10.1029/2011JC007135.

Klunder, M. B., P. Laan, R. Middag, H. J. W. de Baar, and J. C. Van Ooijen (2011). "Dissolved iron in the Southern Ocean (Atlantic sector)." *Deep Sea Res. Pt. II* (58) 25, pp. 2678–2694. DOI: 10.1016/j.dsr2.2010.10.042.

Lancelot, C., A. de Montety, H. Goosse, S. Becquevort, V. Schoemann, B. Pasquer, and M. Vancoppenolle (2009). "Spatial distribution of the iron supply to phytoplankton in the Southern Ocean: a model study." *Biogeosciences* (6) 12, pp. 2861–2878. DOI: 10.5194/bg-6-2861-2009.

Large, W. G. and S. G. Yeager (2004). *Diurnal to Decadal Global Forcing for Oceans and Sea-Ice Models: The Data Sets and Flux Climatologies, NCAR/TN-460+STR*. Tech. rep. Boulder, Colorado: National Center for Atmospheric Research.

Large, W. G. and S. G. Yeager (2009). "The global climatology of an interannually varying air–sea flux data set." *Clim. Dynam.* (33) 2-3, pp. 341–364. DOI: 10.1007/s00382-008-0441-3.

Lin, H., S. Rauschenberg, C. R. Hexel, T. J. Shaw, and B. S. Twining (2011). "Free-drifting icebergs as sources of iron to the Weddell Sea." *Deep-Sea Res. Pt. II* (58) 11, pp. 1392–1406. DOI: 10.1016/j.dsr2.2010.11.020.

Maher, B., J. Prospero, D. Mackie, D. Gaiero, P. Hesse, and Y. Balkanski (2010). "Global connections between aeolian dust, climate and ocean biogeochemistry at the present day and at the last glacial maximum." *Earth-Sci. Rev.* (99) 1, pp. 61–97.

Martin, J. H., R. M. Gordon, and S. E. Fitzwater (1990). "Iron in Antarctic waters." *Nature* (345), pp. 156–158. DOI: 10.1038/345156a0.

Martin, J. H. (1990). "Glacial-interglacial CO_2 change: The iron hypothesis." *Paleoceanography* (5) 1, pp. 1–13. DOI: 10.1029/PA005i001p00001.

Martínez-Garcia, A., A. Rosell-Melé, S. L. Jaccard, W. Geibert, D. M. Sigman, and G. H. Haug (2011). "Southern Ocean dust-climate coupling over the past four million years." *Nature* (476) 7360, pp. 312–315. DOI: 10.1038/nature10310.

Martínez-García, A., D. M. Sigman, H. Ren, R. F. Anderson, M. Straub, D. A. Hodell, S. L. Jaccard, T. I. Eglinton, and G. H. Haug (2014). "Iron fertilization of the Subantarctic Ocean during the last ice age." *Science* (343) 6177, pp. 1347–1350. DOI: 10.1126/science.1246848.

McKiver, W. J., M. Vichi, T. Lovato, A. Storto, and S. Masina (2014). "Impact of increased grid resolution on global marine biogeochemistry." *J. Mar. Sys.* DOI: 10.1016/j.jmarsys.2014.10.003.

Misumi, K., K. Lindsay, J. K. Moore, S. C. Doney, F. O. Bryan, D. Tsumune, and Y. Yoshida (2014). "The iron budget in ocean surface waters in the 20th and 21st centuries: projections by the Community Earth System Model version 1." *Biogeosciences* (11) 1, pp. 33–55. DOI: 10.5194/bg-11-33-2014.

Moore, J. K. and O. Braucher (2008). "Sedimentary and mineral dust sources of dissolved iron to the world ocean." *Biogeosciences* (5) 3, pp. 631–656. DOI: 10.5194/bg-5-631-2008.

Mouginot, J., E. Rignot, and B. Scheuchl (2014). "Sustained increase in ice discharge from the Amundsen Sea Embayment, West Antarctica, from 1973 to 2013." *Geophys. Res. Lett.* (41), pp. 1576–1584. DOI: 10.1002/2013GL059069.

Najjar, R. G., X. Jin, F. Louanchi, O. Aumont, K. Caldeira, S. C. Doney, J.-C. Dutay, M. Follows, N. Gruber, F. Joos, K. Lindsay, E. Maier-Reimer, R. J. Matear, K. Matsumoto, P. Monfray, A. Mouchet, J. C. Orr, G.-K. Plattner, J. L. Sarmiento, R. Schlitzer, R. D. Slater, M.-F. Weirig, Y. Yamanaka, and A. Yool (2007). "Impact of circulation on export production, dissolved organic matter, and dissolved oxygen in the ocean: Results from Phase II of the Ocean Carbon-cycle Model Intercomparison Project (OCMIP-2)." *Global Biogeochem. Cy.* (21) GB3007. DOI: 10.1029/2006GB002857.

Pollard, R. T., I. Salter, R. J. Sanders, M. I. Lucas, C. M. Moore, R. A. Mills, P. J. Statham, J. T. Allen, A. R. Baker, D. C. E. Bakker, M. A. Charette, S. Fielding, G. R. Fone, M. French, A. E. Hickman, R. J. Holland, J. A. Hughes, T. D. Jickells, R. S. Lampitt, P. J. Morris, F. H. Nedelec, M. Nielsdottir, H. Planquette, E. E. Popova, A. J. Poulton, J. F. Read, S. Seeyave, T. Smith, M. Stichcombe, S. Taylor, S. Thomalla, H. J. Venables, R. Williamson, and M. V. Zubkov (2009). "Southern Ocean deep-water carbon export enhanced by natural iron fertilization." *Nature* (457) 7229, pp. 577–580. DOI: 10.1038/nature07716.

Polovina, J. J., E. A. Howell, and M. Abecassis (2008). "Ocean's least productive waters are expanding." *Geophys. Res. Lett.* (35) L03618. DOI: 10.1029/2007GL031745.

Popova, E. E., A. Yool, A. C. Coward, F. Dupont, C. Deal, S. Elliott, E. Hunke, M. Jin, M. Steele, and J. Zhang (2012). "What controls primary production in the Arctic Ocean? Results from an intercomparison of five general circulation models with biogeochemistry." *J. Geophys. Res.* (117) C8. DOI: 10.1029/2011JC007112.

Rackow, T. (2011). "Modellierung der Eisbergdrift als Erweiterung eines Finite-Elemente-Meereis-Ozean-Modells." PhD thesis. Bremen University, Germany.

Rackow, T., H. F. Goessling, T. Jung, S. Sidorenko, T. Semmler, D. Barbi, and D. Handorf (2014). "Towards multi-resolution climate modeling with ECHAM6-FESOM. Part II: climate variability." *Submitted to Clim. Dyn.*

Radic, A., F. Lacan, and J. W. Murray (2011). "Iron isotopes in the seawater of the equatorial Pacific Ocean: new constraints for the oceanic iron cycle." *Earth Planet. Sc. Lett.* (306) 1, pp. 1–10. DOI: 10.1016/j.epsl.2011.03.015.

Raiswell, R., L. G. Benning, M. Tranter, and S. Tulaczyk (2008). "Bioavailable iron in the Southern Ocean: the significance of the iceberg conveyor belt." *Geochem. Trans* (9) 7, p. 9. DOI: 10.1186/1467-4866-9-7.

Rhein, M., S. R. Rintoul, S. Aoki, E. Campos, D. Chambers, R. A. Feely, S. Gulev, G. C. Johnson, S. A. Josey, A. Kostianoy, C. Mauritzen, D. Roemmich, L. D. Talley, and F. Wang (2013). "Observations: Ocean." In: *Climate Change 2013: The Physical Science Basis. Contribution of Working Group I to the Fifth Assessment Report of the Intergovernmental Panel on Climate Change*. Ed. by T. F. Stocker, D. Qin, G.-K. Plattner, M. Tignor, S. K. Allen, J. Boschung, A. Nauels, Y. Xia, V. Bex, and P. M. Midgley. Cambridge, United Kingdom and New York, NY, USA: Cambridge University Press, pp. 255–316. DOI: 10.1017/CBO9781107415324.010.

Sallée, J.-B., K. Speer, S. Rintoul, and S. Wijffels (2010). "Southern Ocean thermocline ventilation." *J. Phys. Oceanogr.* (40) 3, pp. 509–529. DOI: 10.1175/2009JPO4291.1.

Sen Gupta, A., A. Santoso, A. S. Taschetto, C. C. Ummenhofer, J. Trevena, and M. H. England (2009). "Projected changes to the Southern Hemisphere ocean and sea ice in the IPCC AR4 climate models." *J. Climate* (22) 11, pp. 3047–3078. DOI: 10.1175/2008JCLI2827.1.

Sidorenko, D., T. Rackow, T. Jung, T. Semmler, D. Barbi, S. Danilov, K. Dethlof, W. Dorn, K. Fieg, H. Goessling, D. Handorf, S. Harig, W. Hiller, S. Juricke, M. Losch, J. Schröter, D. V. Sein, and Q. Wang (2015). "Towards multi-resolution global climate modeling with ECHAM6-FESOM. Part I: Model formulation and mean climate." *Clim. Dynam.* (44) 3-4, pp. 757–780. DOI: 10.1007/s00382-014-2290-6.

Sinha, B., E. T. Buitenhuis, C. L. Quéré, and T. R. Anderson (2010). "Comparison of the emergent behavior of a complex ecosystem model in two ocean general circulation models." *Progr. Ocean.* (84) 3, pp. 204–224. DOI: 10.1016/j.pocean.2009.10.003.

Sokolov, S. and S. R. Rintoul (2007). "On the relationship between fronts of the Antarctic Circumpolar Current and surface chlorophyll concentrations in the Southern Ocean." *J. Geophys. Res.* (112) C7. DOI: 10.1029/2006JC004072.

Steinacher, M., F. Joos, T. L. Frölicher, L. Bopp, P. Cadule, V. Cocco, S. C. Doney, M. Gehlen, K. Lindsay, J. K. Moore, B. Schneider, and J. Segschneider (2010). "Projected 21st century decrease in marine productivity: a multi-model analysis." *Biogeosciences* (7) 3, pp. 979–1005. DOI: 10.5194/bg-7-979-2010.

Tagliabue, A., L. Bopp, and O. Aumont (2009a). "Evaluating the importance of atmospheric and sedimentary iron sources to Southern Ocean biogeochemistry." *Geophys. Res. Lett.* (36) L13601. DOI: 10.1029/2009GL038914.

Tagliabue, A., L. Bopp, O. Aumont, and K. R. Arrigo (2009b). "Influence of light and temperature on the marine iron cycle: From theoretical to global modeling." *Global Biogeochem. Cy.* (23) GB2017. DOI: 10.1029/2008GB003214.

Tagliabue, A., L. Bopp, J.-C. Dutay, A. R. Bowie, F. Chever, P. Jean-Baptiste, E. Bucciarelli, D. Lannuzel, T. Remenyi, G. Sarthou, O. Aumont, M. Gehlen, and C. Jeandel (2010). "Hydrothermal contribution to the oceanic dissolved iron inventory." *Nat. Geosci.* (3) 4, pp. 252–256. DOI: 10.1038/ngeo818.

Tagliabue, A. and C. Völker (2011). "Towards accounting for dissolved iron speciation in global ocean models." *Biogeosciences* (8) 10, pp. 3025–3039.

Tagliabue, A., J.-B. Sallée, A. R. Bowie, M. Lévy, S. Swart, and P. W. Boyd (2014). "Surface-water iron supplies in the Southern Ocean sustained by deep winter mixing." *Nat. Geosci.* (7), pp. 314–320. DOI: 10.1038/ngeo2101.

Vancoppenolle, M., L. Bopp, G. Madec, J. P. Dunne, T. Ilyina, P. R. Halloran, and N. Steiner (2013). "Future Arctic Ocean primary productivity from CMIP5 simulations: Uncertain outcome, but consistent mechanisms." *Global Biogeochem. Cy.* (27) 3, pp. 605–619. DOI: 10.1002/gbc.20055.

Van der Merwe, P., D. Lannuzel, A. R. Bowie, C. M. Nichols, and K. M. Meiners (2011). "Iron fractionation in pack and fast ice in East Antarctica: Temporal decoupling between the release of dissolved and particulate iron during spring melt." *Deep Sea Res. Pt. II* (58) 9, pp. 1222–1236. DOI: 10.1016/j.dsr2.2010.10.036.

Wadley, M. R., T. D. Jickells, and K. J. Heywood (2014). "The role of iron sources and transport for Southern Ocean productivity." *Deep Sea Res. Pt I* (87), pp. 82–94. DOI: DOI:10.1016/j.dsr.2014.02.003.

Wang, Q., S. Danilov, D. Sidorenko, R. Timmermann, C. Wekerle, X. Wang, T. Jung, and J. Schröter (2014a). "The Finite Element Sea Ice-Ocean Model (FESOM) v.1.4: formulation of an ocean general circulation model." *Geosci. Model Dev.* (7) 2, pp. 663–693. DOI: 10.5194/gmd-7-663-2014.

Wang, S., D. Bailey, K. Lindsay, J. K. Moore, and M. Holland (2014b). "Impact of sea ice on the marine iron cycle and phytoplankton productivity." *Biogeosciences* (11) 17, pp. 4713–4731. DOI: 10.5194/bg-11-4713-2014.

Wang, X., Q. Wang, D. Sidorenko, S. Danilov, J. Schröter, and T. Jung (2012). "Long-term ocean simulations in FESOM: evaluation and application in studying the impact of Greenland Ice Sheet melting." *Ocean Dynam.* (62) 10-12, pp. 1471–1486. DOI: 10.1007/s10236-012-0572-2.

Watson, A. J., D. C. E. Bakker, A. J. Ridgwell, P. W. Boyd, and C. S. Law (2000). "Effect of iron supply on Southern Ocean CO_2 uptake and implications for glacial atmospheric CO_2." *Nature* (407) 6805, pp. 730–733. DOI: 10.1038/35037561.

Wekerle, C., Q. Wang, S. Danilov, T. Jung, and J. Schröter (2013). "The Canadian Arctic Archipelago throughflow in a multiresolution global model: Model assessment and the driving mechanism of interannual variability." *J. Geophys. Res* (118), pp. 4525–4541. DOI: 10.1002/jgrc.20330.

Wesche, C., T. Rackow, and W. Dierking (Sept. 2013). "Iceberg drift in the eastern Weddell Sea: observed and modeled." In: *Proceedings of ESA Living Planet Symposium, EdinESA Special Publication SP-722*. European Space Agency.

Yool, A., E. E. Popova, and T. R. Anderson (2013). "MEDUSA-2.0: an intermediate complexity biogeochemical model of the marine carbon cycle for climate change and ocean acidification studies." *Geosci. Model Dev.* (6) 5, pp. 1767–1811. DOI: 10.5194/gmd-6-1767-2013.

Zheng, F., J. Li, R. T. Clark, and H. C. Nnamchi (2013). "Simulation and projection of the Southern Hemisphere annular mode in CMIP5 models." *J. Climate* (26) 24, pp. 9860–9879. DOI: 10.1175/JCLI-D-13-00204.1.

9 CONCLUSION

In this thesis, the results of the coupling between the biogeochemical model REcoM2 and the Finite Element Sea-ice Ocean Model (FESOM) were first documented. Secondly, the new model was used to gain a better understanding of the sources providing iron to the surface mixed layer of the Southern Ocean. The work in particular focussed on the input of iron from the sediment and from the deeper reservoirs through vertical transport across the base of the mixed layer, and how these sources, and their model parameterization and strength, affect the net primary production in the Southern Ocean.

The coupled FESOM-REcoM2 model captures the main spatial surface patterns of the global biogeochemical fields, with relatively low biological production in the subtropical gyres and higher in the temperate regions. The results are comparable to those of other non-eddy resolving Ocean General Circulation Biogeochemical Models (OGCBMs), with the spatial distribution of the chlorophyll *a* and net primary production (NPP) being in the better end of previous results.

The thesis shows that the representation of the ocean circulation and mixing in the Ocean General Circulation Model (OGCM) has a large impact on the vertical supply of iron to the surface mixed layer. The vertical iron supply in turn affects the representation of net primary and export production as well as the phytoplankton composition in the models, though other factors from the OGCM, such as irradiance in the water, also plays a role. As coupled Ocean General Circulation Biogeochemical Models (OGCBMs) are routinely used to investigate the carbon cycle in the Southern Ocean, the study highlight the importance of evaluating the skill of the OGCM in order to understand the biogeochemical results.

The input of iron to the water from the sediments is thought to play an important role in the Southern Ocean, but measurements provide a large range of flux rates. The strength of the sediment source thus varies widely between OGCBMs. In FESOM-REcoM2 it is possible to vary the strength of the sediment source considerably, and still obtain reasonable and similar results for the surface iron concentration in the Southern Ocean. The strength of the sediment source does, however, impact the phytoplankton composition and its spatial distribution in the model, especially downstream of shelf regions, as well as the magnitude of the opal export. One way to constrain the rate of iron release from the sediments is thus to evaluate the model's results regarding diatom production and opal export to previous estimates of these factors.

In conclusion, OGCBMs are useful tools to gain an understanding of the marine biogeochemical cycles. Their results are, however, dependent on the representation of the physical and biogeochemical processes in the models and these must therefore be critically addressed. In this thesis this has been done with a focus on the representation of iron limitation in the Southern Ocean.

Part IV

APPENDIX

A

RESULTS OF RECOM2 COUPLED TO FESOM 1.4

A.1 INTRODUCTION

The Regulated Ecosystem Model with two phytoplankton classes (REcoM2) was presented in a set-up with the Finite Element Sea-ice Ocean Model (FESOM) in publication I. For publication III FESOM was updated to the newest version (v. 1.4, Wang et al., 2014).

Here, the the results of the CTRL run of publication III are compared to observational data in a manner similar to what was done in publication I, starting with the physical fields, then the nutrients and ending with the biological production. Focus is on the mean surface fields, calculated based on the last ten years of 50-year simulations as described in publication III.

The results are first presented in Taylor diagrams (Taylor, 2001), in which the model results are compared to observations. A number of plots additionally illustrate the bias between modeled and observed surface fields. For the mixed layer depth (MLD) and net primary production (NPP) we additionally show the seasonal cycle in the individual ocean basins illustrated in Fig. A.1. The data we compare the model results to is listed in Table 1 (Pub. I) along with its temporal extend and resolution.

A.2 RESULTS

A.2.1 *Physics: Mixed Layer Depth*

The MLD was calculated using the density threshold criteria of $0.03\,\mathrm{kg\,m^{-3}}$ as suggested by de Boyer Montegut et al. (2004). The correlation between the observed and the modeled mean MLD equals 0.73 (Fig. A.2a), and has thus been improved from the correlation of 0.68 found by (Schourup-Kristensen et al., 2014).

Overall, the spatial distribution of the $\mathrm{MLD_{max}}$ is well captured, with the shallower MLD in the tropics and deeper in the temperate areas (Fig. A.3). In the Southern Ocean, the deep mixed layers in the Indian and Pacific sectors are captured, though their meridional extend is somewhat off. Close to the Antarctic, the $\mathrm{MLD_{max}}$ is too shallow as was also the case in the previous model version (Fig. A.3).

Taking the spatial distribution of each month into account, the correlation between the observed and the modeled mean MLD is 0.58 (Fig. A.2b). The seasonal cycle of the individual ocean basins illustrated in Fig. (A.1) all have significant correlations with the observations (Fig. A.4). Additionally, all ocean basins, except for the North Indian and Equatorial Pacific Basins, have correlations that are higher than 0.9. In the Southern Ocean, the depth of the MLD over the year has been improved compared to the previous version of FESOM, as the bias between the modeled and the observed MLD has become smaller. Overall, FESOM does a good job in reproducing the seasonal cycle of the MLD.

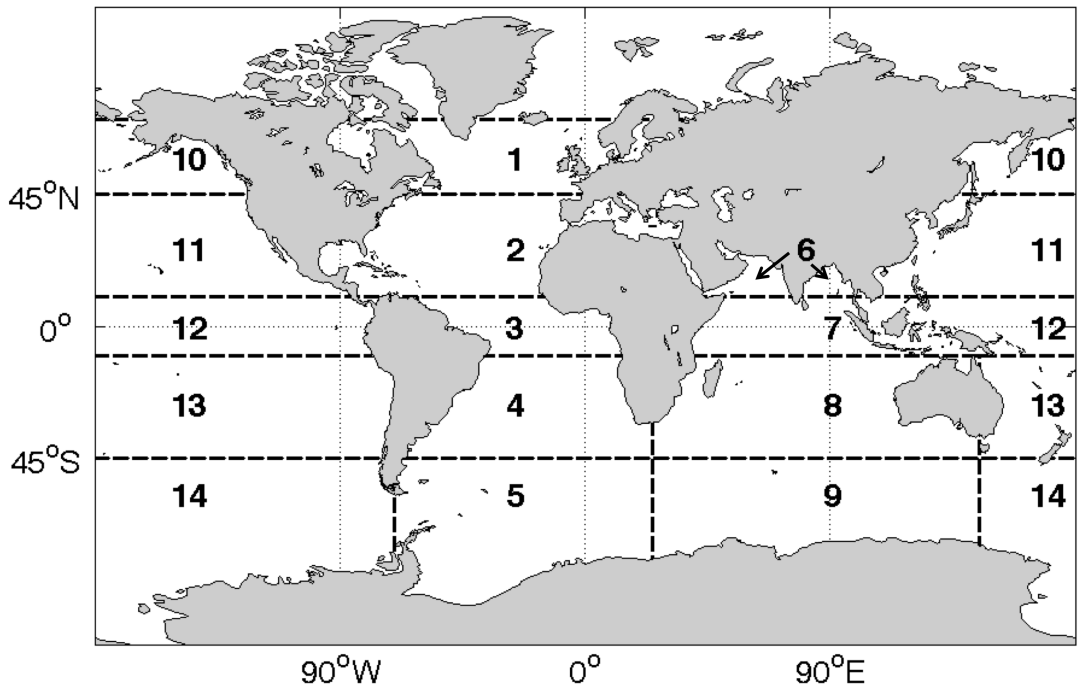

Figure A.1: Division of the global surface ocean into individual basins used to show the seasonal cycle of the MLD and NPP.

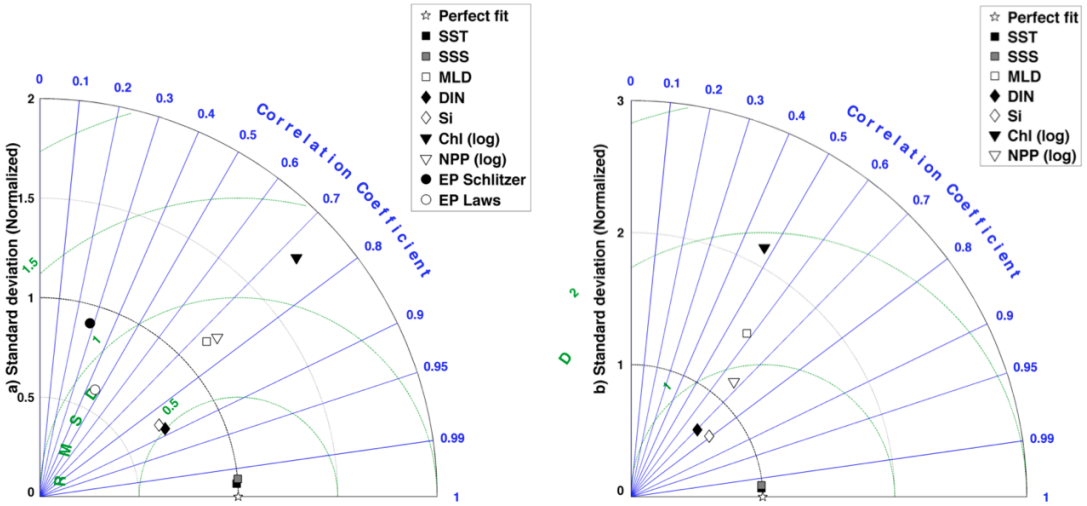

Figure A.2: Taylor diagrams (Taylor, 2001) showing correlation, normalized standard deviation and the normalized root mean square error between values of the model results and observations (Table 1, Schourup-Kristensen et al., 2014), weighted by area. a) Spatial distribution. b) Spatial-seasonal distribution.
All values are surface values, except the mixed layer depth and the vertically integrated NPP. All fields have been interpolated to a 1° by 1° grid, using linear interpolation.

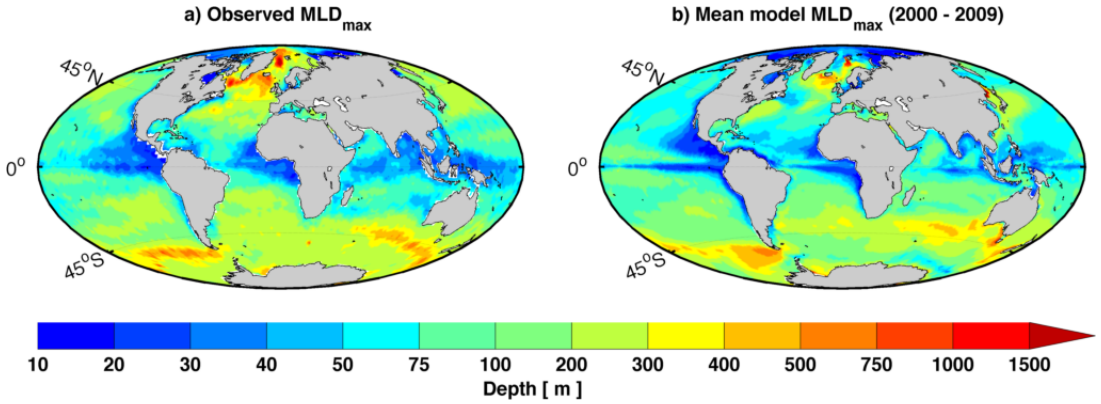

Figure A.3: Mean MLD_{max} for a) observations (de Boyer Montegut et al., 2004), b) model.

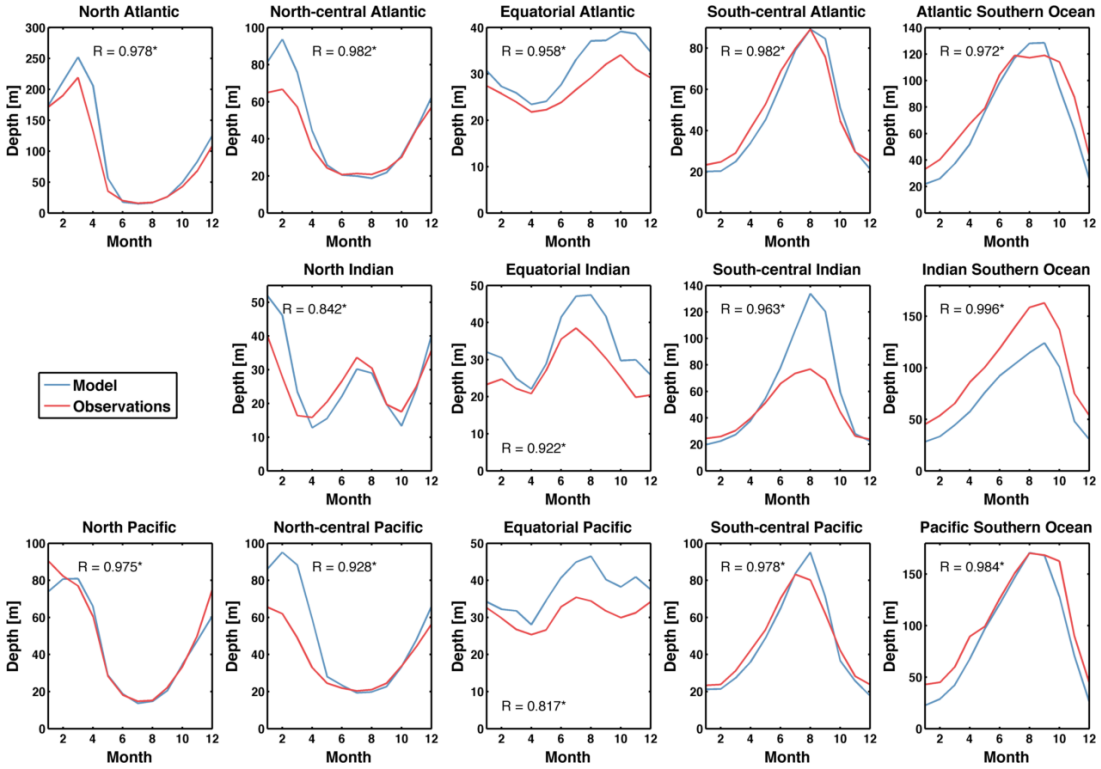

Figure A.4: Mean MLD over the year in the basins depicted in Fig. A.1 for the model results and observations de Boyer Montegut et al. (2004). The correllation coefficient between model results and observations is written in each subplot, and the statistically significant correlations (p values < 0.05) are marked with *.

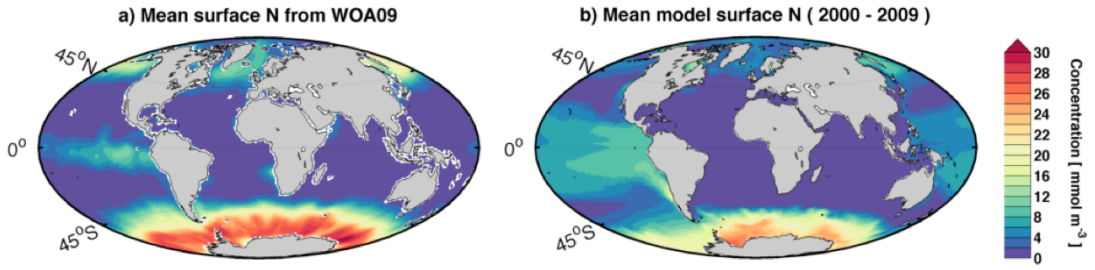

Figure A.5: Mean surface concentration of dissolved inorganic nitrogen (DIN) for a) observations (Garcia et al., 2010), b) model.

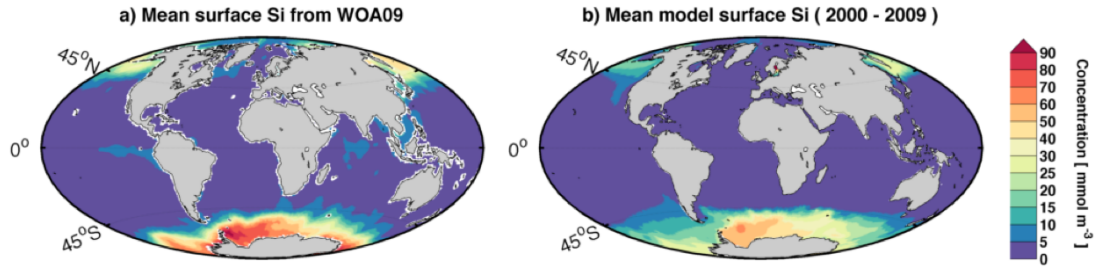

Figure A.6: Mean surface concentration of dissolved inorganic nitrogen (DIN) for a) observations (Garcia et al., 2010), b) model.

A.2.2 *Nutrients and nutrient limitation*

For dissolved inorganic nitrogen (DIN) and silicon (DSi), the correlations between the spatial distribution of the observations and the model results are 0.88 and 0.86, respectively. These relatively high correlations occur as the main distribution with high concentrations of DIN and DSi in the Southern Ocean and the northern seas, along with low concentrations in the subtropical gyres are captured in the model (Fig. A.5 and A.6). For DIN, the surface concentrations are, however, too high in the tropical Pacific Ocean, as was also the case when REcoM2 was coupled to FESOM 1.3.

Due to scarcity of iron measurements, the water's concentration of dissolved iron can not be directly compared to a climatology of observations. The spatial distribution of surface iron nevertheless appears reasonable, with the highest concentrations in the Equatorial Atlantic and Indian Oceans, which are under influence of the dust plume from the Sahara. The lowest concentrations occur in the Pacific Ocean, whereas the Southern Ocean has intermediate surface iron concentrations (Fig. A.7). When comparing to mean values for various ocean basins it is apparent that the modeled iron field is closest to the observations in the Atlantic and Indian Oceans, while the mean concentrations are too low, especially in the Pacific, but also in the Southern Ocean (Table A.1).

The relatively low iron concentrations in the Pacific and Southern Ocean lead to iron being the most limiting nutrient in these areas, both for nanophytoplankton and diatoms (Fig. A.8). Nanophytoplankton is on average limited by iron in 57 % of the global ocean, while the number for diatoms is 54 %. These are relatively high numbers, showing that the iron limitation is relatively strong in the model, especially

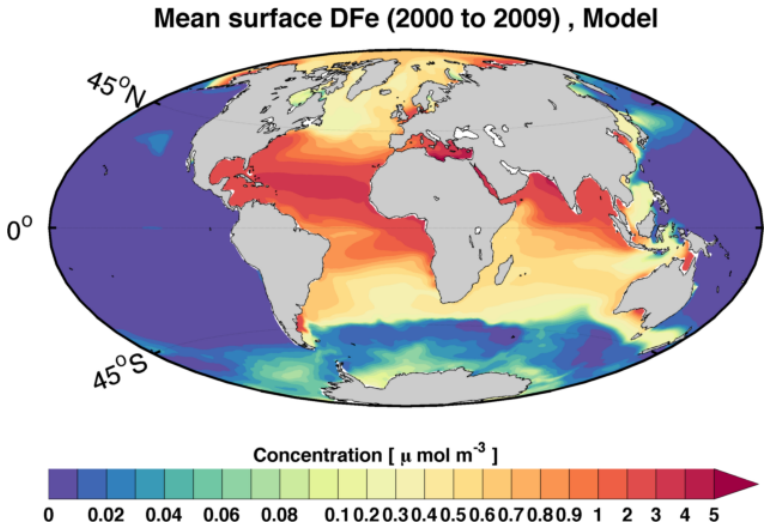

Figure A.7: Mean surface concentration of dissolved iron. Plotted to the scale of Schneider et al. (2008)

Table A.1: Modeled mean surface iron concentrations (0–100 m) in the different ocean basins shown in Fig. A.1. Observed values are from Moore and Braucher (2008), except those marked with *, which are from Tagliabue et al. (2012), Table 2. The latter is the mean of the values given for the Antarctic and Subantarctic regions.

BASIN	LATITUDINAL EXTEND	MODEL	OBS.
North Atlantic	45 – 70° N	0.42	0.68
North-central Atlantic	10 – 45° N	1.25	0.68
South-central Atlantic	45 – 10° S	0.86	0.44
North Indian	45 – 10° S	1.37	1.21
North Pacific	45 – 70° N	0.14	0.31
Equatorial Pacific	10° S – 10° N	0.02	0.84
South-central Pacific	45 – 10° S	0.02	0.31
Atlantic Southern Ocean	90 – 45° S	0.13	0.39*
Indian Southern Ocean	90 – 45° S	0.07	0.33*
Pacific Southern Ocean	90 – 45° S	0.07	0.15*

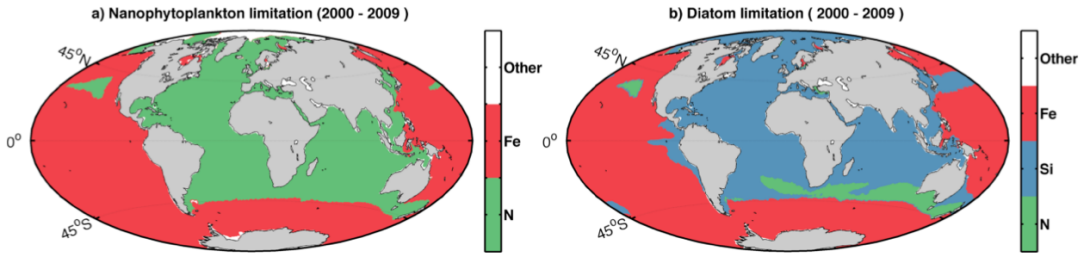

Figure A.8: Annual mean limiting nutrients calculated following Schneider et al. (2008). a) Nanophytoplankton (Fe = 56.8 %, DIN = 41.3 % of total area. b) Diatoms (Fe = 53.9 %, DSi = 40.6 % and DIN = 5.5 % of total area.))

Table A.2: Net primary and export production for the global domain and south of 50°S in FESOM-REcoM2 and in the literature.

NPP_{GLO} [Pg C yr^{-1}]	EP_{GLO} [Pg C yr^{-1}]	$OPAL_{GLO}$ [Tmol Si yr^{-1}]	NPP_{SO} [Pg C yr^{-1}]	EP_{SO} [Pg C yr^{-1}]	$OPAL_{SO}$ [Tmol Si yr^{-1}]
32.4	5.9	67.4	3.1	1.2	21.2

in the Pacific Ocean. For diatoms, silicon is dominating the nutrient limitation in the remainder of the global ocean.

A.2.3 *Biological production*

The global NPP is 32.4 Pg C yr^{-1} and the export production (EP) 5.9 Pg C yr^{-1}, very similar to the numbers in the previous version of FESOM-REcoM2. The global export of biogenic silicon (opal) sums up to 67 Tmol Si yr^{-1}.

For the spatial distribution of chlorophyll *a* and NPP, the correlation between the model results and the satellite-based estimates are 0.73 and 0.75, respectively. For both fields, the spatial distribution, with low concentrations in the subtropical gyres and higher between 40 and 70°S and N, is captured (Fig. A.9 and A.10). But especially the surface chlorophyll concentrations are too low in the gyres, and both fields have too low concentrations in the Pacific Ocean due to the strong iron limitation here (Fig. A.8).

The seasonal cycle of NPP is plotted in Fig. (A.11) for the ocean basins shown in Fig. (A.1). The seasonal cycle of the modeled NPP has significant correlations with the satellite based estimates in eight of the fourteen basins, and the best seasonal cycles are found in the subtropical gyres. North and south of 45°N and S, respectively, the spring bloom starts earlier in the model than in the satellite-based estimates, and in the Pacific Ocean it is again clear that the modeled NPP is relatively low.

For export production (EP), the correlations are 0.28 and 0.46 when compared to the fields from Schlitzer (2004) and Laws et al. (2000), respectively. Export production is, however, difficult to measure, and the fields we compare to are thus uncertain. Looking at the spatial distribution, the modeled EP (Fig. A.12) is highly correlated with the NPP (Fig. A.10), with large export rates occurring in the upwelling zones around the Equator, in the Southern Ocean and in the north Atlantic. As indicated by the correlation coefficients, this is closest to the EP-field from Laws et al. (2000),

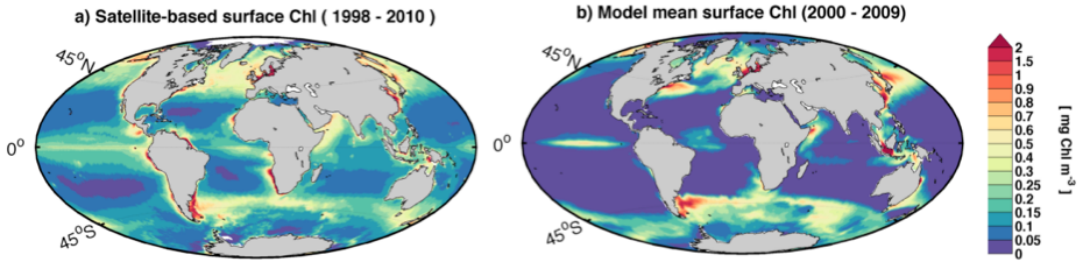

Figure A.9: Spatial distribution of the mean surface concentration of chlorophyll *a* plotted to the scale of Schneider et al. (2008). a) Satellite-based estimate (www.globcolour.info). b) Modeled mean.

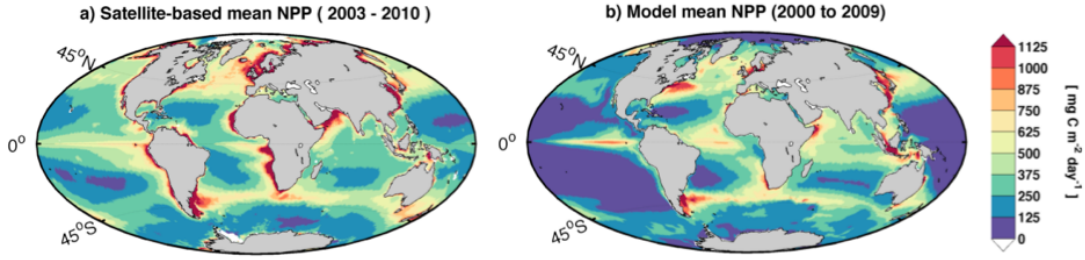

Figure A.10: Spatial distribution of the vertically integrated net primary production plotted to the scale of Schneider et al. (2008). a) Satellite-based estimate (SEAWIFS and Behrenfeld and Falkowski (1997)). b) Modeled mean.

while the field from Schlitzer (2004) has less export in the North Atlantic and more in the coastal zones.

A.3 CONCLUSION

The biogeochemical model REcoM2 has been coupled to the newest version of the Finite Element Sea-ice Ocean Model (FESOM, v. 1.4). The results of the new model are very similar to those of REcoM2 coupled to FESOM,1.3. The largest differences occur in the Southern Ocean, where the mixed layer has improved from the previous version, leading to more production in the Pacific sector of the Southern Ocean, and generally to higher levels of chlorophyll *a* in the surface water.

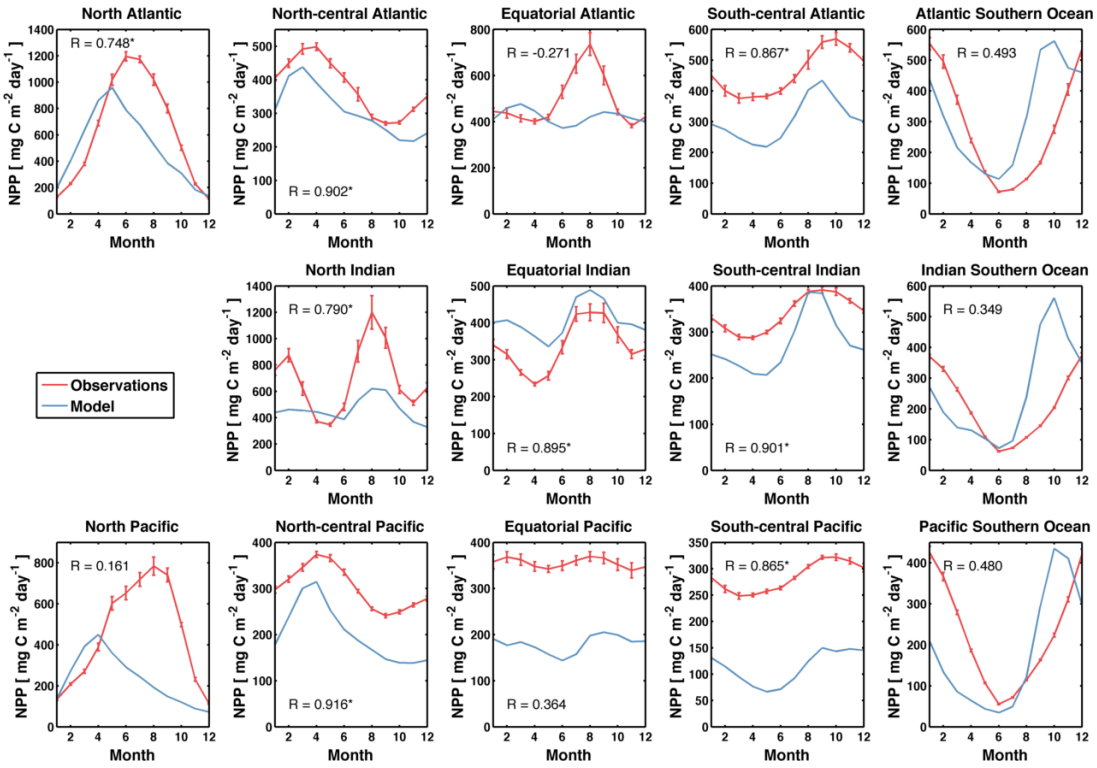

Figure A.11: Mean NPP over the year in the basins depicted in Fig. A.1 plotted for the model mean and satellite-based observation (SeaWIFS and Behrenfeld and Falkowski (1997)). The correllation coefficient between model results and observations is written in each subplot, and the statistically significant correlations (p values < 0.05) are marked with *

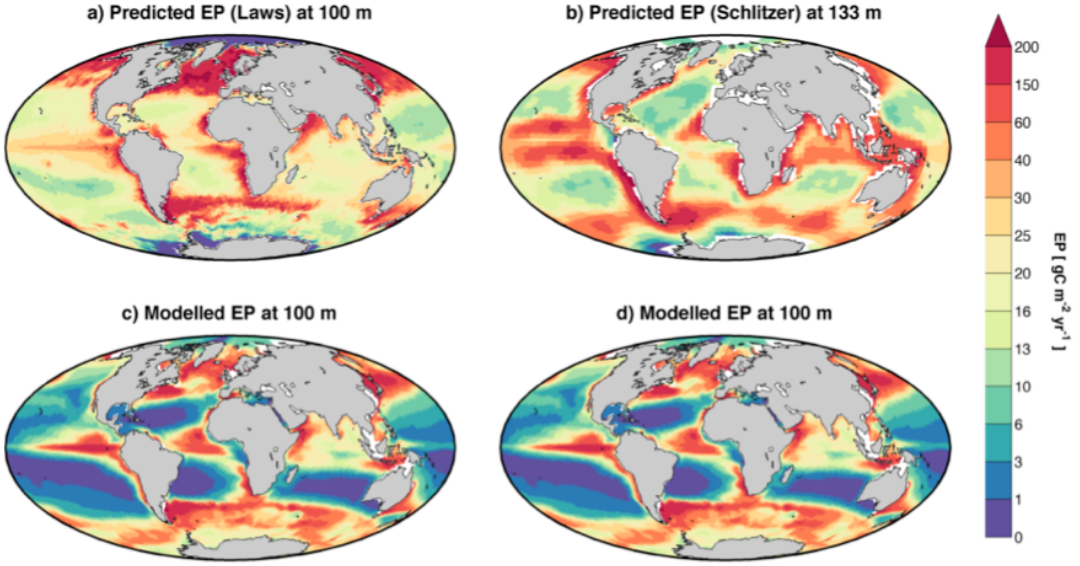

Figure A.12: Spatial distribution of the export production. a) Satellite-based estimate (Laws et al., 2000). b) Inverse model based estimate (Schlitzer, 2004) c + d) Modeled EP.

REFERENCES

Behrenfeld, M. J. and P. G. Falkowski (1997). "Photosynthetic rates derived from satellite-based chlorophyll concentration." *Limnol. Oceanogr.* (42) 1, pp. 1–20.

De Boyer Montegut, C., G. Madec, A. S. Fischer, A. Lazar, and D. Iudicone (2004). "Mixed layer depth over the global ocean: An examination of profile data and a profile-based climatology." *J. Geophys. Res.* (109) C12003. DOI: 10.1029/2004JC002378.

Garcia, H., R. Locarnini, T. Boyer, J. Antonov, M. Zweng, O. Baranova, and D. Johnson (2010). *World Ocean Atlas 2009, Volume 4: Nutrients (phosphate, nitrate, silicate),(ed. S. Levitus)*. Tech. rep. Washington, DC: NOAA Atlas NESDIS.

Laws, E. A., P. G. Falkowski, W. O. Smith, H. Ducklow, and J. J. McCarthy (2000). "Temperature effects on export production in the open ocean." *Global Biogeochem. Cy.* (14) 4, pp. 1231–1246. DOI: 10.1029/1999GB001229.

Moore, J. K. and O. Braucher (2008). "Sedimentary and mineral dust sources of dissolved iron to the world ocean." *Biogeosciences* (5) 3, pp. 631–656. DOI: 10.5194/bg-5-631-2008.

Schlitzer, R. (2004). "Export production in the equatorial and North Pacific derived from dissolved oxygen, nutrient and carbon data." *J. Oceanogr.* (60) 1, pp. 53–62. DOI: 10.1023/B:JOCE.0000038318.38916.e6.

Schneider, B., L. Bopp, M. Gehlen, J. Segschneider, T. L. Frölicher, P. Cadule, P. Friedlingstein, S. C. Doney, M. J. Behrenfeld, and F. Joos (2008). "Climate-induced interannual variability of marine primary and export production in three global coupled climate carbon cycle models." *Biogeosciences* (5), pp. 597–614. DOI: 10.5194/bg-5-597-2008.

Schourup-Kristensen, V., D. Sidorenko, D. A. Wolf-Gladrow, and C. Völker (2014). "A skill assessment of the biogeochemical model REcoM2 coupled to the Finite Element Sea-Ice Ocean Model (FESOM 1.3)." *Geosci. Model Dev.* (7) 6, pp. 2769–2802. DOI: 10.5194/gmd-7-2769-2014.

Tagliabue, A., T. Mtshali, O. Aumont, A. R. Bowie, M. B. Klunder, A. N. Roychoudhury, and S. Swart (2012). "A global compilation of dissolved iron measurements: focus on distributions and processes in the Southern Ocean." *Biogeosciences* (9) 6, pp. 1–17. DOI: 10.5194/bg-9-2333-2012.

Taylor, K. E. (2001). "Summarizing multiple aspects of model performance in a single diagram." *J. Geophys. Res* (106) D7, pp. 7183–7192. DOI: 10.1029/2000JD900719.

Wang, Q., S. Danilov, D. Sidorenko, R. Timmermann, C. Wekerle, X. Wang, T. Jung, and J. Schröter (2014). "The Finite Element Sea Ice-Ocean Model (FESOM) v.1.4: formulation of an ocean general circulation model." *Geosci. Model Dev.* (7) 2, pp. 663–693. DOI: 10.5194/gmd-7-663-2014.